

11-10-87  
P-231

# Rheological Behavior and Microstructure of Ceramic Particulate/Aluminum Alloy Composites

by

Hee-Kyung MOON

B.S., Seoul National University (1980)

M.S., Seoul National University (1982)

SUBMITTED IN PARTIAL FULFILLMENT  
OF THE REQUIREMENTS FOR THE  
DEGREE OF

DOCTOR OF PHILOSOPHY  
IN MATERIALS SCIENCE AND ENGINEERING

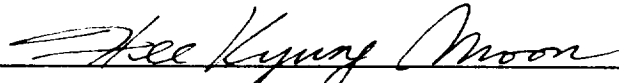
at the

MASSACHUSETTS INSTITUTE OF TECHNOLOGY

September 1990

© Massachusetts Institute of Technology 1990

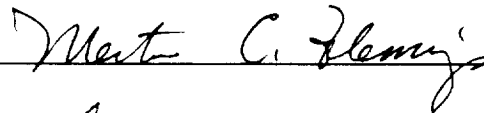
Signature of Author



Department of Materials Science and Engineering

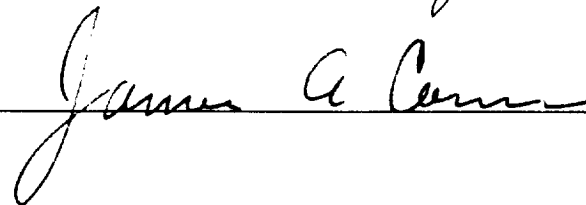
August 10, 1990

Certified by



Merton C. Flemings  
Thesis Supervisor

Certified by



James A. Cornie  
Thesis Supervisor

Accepted by

Linn W. Hobbs

Chairman, Departmental Committee on Graduate Students

(NASA-CR-190036) RHEOLOGICAL BEHAVIOR AND  
MICROSTRUCTURE OF CERAMIC  
PARTICULATE/ALUMINUM ALLOY COMPOSITES Ph.D.  
Thesis Final Technical Report (MIT) 231 p

N92-27542

Unclass  
0075754

G3/26

**RHEOLOGICAL BEHAVIOR AND MICROSTRUCTURE OF CERAMIC  
PARTICULATE/ALUMINUM ALLOY COMPOSITES**

by

HEE-KYUNG MOON

JAMES A. CORNIE

MERTON C. FLEMINGS

MASSACHUSETTS INSTITUTE OF TECHNOLOGY  
Cambridge, MA 02139

Final Technical Report  
Grant NAG 3-808  
MIT/OSP 99328

Prepared for

NASA Lewis Research Center  
Cleveland, Ohio 44135

# Rheological Behavior and Microstructure of Ceramic Particulate/Aluminum Alloy Composites

by

Hee-Kyung MOON

Submitted to the Department of Materials Science and Engineering  
on August 10, 1990 in partial fulfillment of the requirements for  
the degree of Doctor of Philosophy in Materials Engineering

## ABSTRACT

The rheological behavior and microstructure were investigated using a concentric-cylinder viscometer for three different slurries: a) semi-solid alloy slurries of a matrix alloy, Al-6.5wt%Si, b) composite slurries, SiC<sub>p</sub>(8.5  $\mu$ m)/Al-6.5wt%Si, with the same matrix alloy in the fully molten state, and c) composite slurries of the same composition with the matrix alloy in the semi-solid state. The pseudoplasticity (or shear-thinning behavior) of these slurries was obtained by step changes of shear rate from a given initial shear rate. To study the thixotropic behavior of the system, a slurry was allowed to rest for different periods of time, prior to shearing at a given initial shear rate.

In the continuous cooling experiments the viscosities of these slurries were dependent on shear rate, cooling rate, volume fraction of primary solid of matrix alloy, and volume fraction of silicon carbide.

In the isothermal experiments, all three kinds of slurries exhibited non-Newtonian behavior, depending on the volume fraction of solid particles. When a sample was sheared after a period of rest, the viscosity displayed a characteristic transient state. The steady state viscosity was also dependent on initial shear rate, and amount and size of the solid phase. A composite slurry in the fully molten state showed a higher viscosity than the alloy slurry with equivalent fraction solid. The composite slurry with a semi-solid matrix, however, exhibited a lower viscosity than the alloy slurry with equivalent total volume fraction solid. These differences in steady state viscosities were explained in terms of the microstructures of quenched samples. The composite slurries with 20 and 30 vol%SiC and an alloy slurry with 40 vol% of primary solid exhibited obvious pseudoplasticity up to a critical shear rate, beyond which a Newtonian behavior was obtained.

The non-deformable silicon carbide particulates were considered to contribute not only to the reduction in the viscosity of composite slurries, but to the refinement of the primary solid phase of the matrix alloy by inhibiting particle agglomeration.

Thesis Supervisor: Merton C. Flemings  
Title: Toyota Professor of Materials Processing,  
Head, Department of Materials Science and Engineering

Thesis Supervisor: James A. Cornie  
Title: Director, Laboratory for the Processing and Evaluation of Inorganic  
Matrix Composites

# TABLE OF CONTENTS

<u>CHAPTER</u>	<u>Page</u>
TITLE PAGE	1
ABSTRACT	2
TABLE OF CONTENTS	3
LIST OF FIGURES	6
LIST OF TABLES	14
ACKNOWLEDGMENTS	15
1. INTRODUCTION	16
2. LITERATURE REVIEW	18
2.1. The Rheology of Suspensions of Rigid Particles	18
2.1.1. Newtonian Behavior of Suspensions	18
2.1.2. Non-Newtonian Behavior of Suspensions	28
2.1.3. Thixotropy	35
2.2. Rheological Behavior of Alloy and Composite Slurries	43
2.2.1. Introduction	43
2.2.2. Castings of Semi-Solid Slurries	44
2.2.3. Viscosity of Liquid Metal	46
2.2.4. Alloy Slurry Systems	48
2.2.5. Composite Slurries	59
2.2.6. Theoretical Treatments	61
2.2.7. Fluidity of Slurries	62
3. EXPERIMENTAL METHODS	65
3.1. Materials	65
3.1.1. Matrix Alloy	65
3.1.2. Ceramic Particulates	66
3.1.3. Composite Preparation	66
3.2. Experimental Apparatus	68
3.3. Viscometer	70
3.4. Experimental Approaches	73
3.4.1. Continuous Cooling Condition	74

3.4.2. Isothermal Condition: Isothermal "Steady State"	74
3.4.3. Approach for Non-Newtonian Behavior	75
3.4.4. Thixotropic Behavior of Slurries	76
4. RHEOLOGICAL BEHAVIOR OF ALLOY SLURRIES IN THE SEMI-SOLID STATE	79
4.1. Introduction	79
4.2. Experimental Procedures for Matrix Alloy	79
4.3. Continuous Cooling Conditions	81
4.3.1. Apparent Viscosity	81
4.3.2. Microstructures	82
4.4. Isothermal Conditions	82
4.5. Non-Newtonian Properties of Semi-Solid Alloy Slurries	84
4.5.1. Pseudoplasticity	84
4.5.2. Effect of Rest Time and Thixotropy	85
4.6. Discussion	86
4.7. Summary of Results	91
5. RHEOLOGICAL BEHAVIOR OF COMPOSITE SLURRIES WITH THE MATRIX ALOY IN THE MOLTEN STATE	93
5.1. Introduction	93
5.2. Experimental Procedures for Composite ( $T > T_L$ )	94
5.3. Results	95
5.3.1. Constant Shear Rate Experiments	95
5.3.2. Step Change of Shear Rate: Structure Curves	97
5.4. Discussion	99
5.4.1. Rate of Thixotropic Recovery in the Transient Stage	99
5.4.2. Comparison with Semi-Solid Alloy Slurry	101
5.4.3. Comparison of Experimental Data with Theoretical Models	101
5.5. Summary of Results	102
6. RHEOLOGICAL BEHAVIOR OF COMPOSITE SLURRIES WITH THE MATRIX ALLOY IN THE SEMI-SOLID STATE	104
6.1. Introduction	104
6.2. Experimental Procedures for Composites ( $T_E < T < T_L$ )	105

6.3. Results	106
6.3.1. Continuous Cooling of Composite Slurry	106
6.3.2. Isothermal Shearing of Composite Slurry	109
6.4. Discussion	111
6.5. Summary of Results	111
7. CONCLUSION	113
8. SUGGESTIONS FOR FUTURE RESEARCH	116
APPENDICES	117
A1. Calculation of Fraction Solid of Matrix Alloy	117
A2. Couette Concentric Cylinder Viscometry	120
FIGURES	127
TABLES	209
BIBLIOGRAPHY	221
BIOGRAPHICAL NOTE	230

## LIST OF FIGURES

<u>FIGURE</u>	<u>Page</u>
Fig. 2.1	127
<p>Comparison of an asymptotic relation for the relative viscosity by Frankel-Acrivos [14] with various models of Rutgers [12], Thomas [13], Einstein [8], and Guth-Simha [31].(a) relative viscosity versus reduced concentration, <math>\phi/\phi_m</math>, (b) relative viscosity versus concentration.</p>	
Fig. 2.2	128
<p>At high concentrations, suspensions may have viscosities between the low shear limiting and high shear limiting values, depending on applied shear rate. The suspension shown here has a pseudoplasticity in which the relative viscosity decreases with increasing shear rate. The difference between the two limiting values may become greater as the concentration of a suspension is higher [37].</p>	
Fig. 2.3	129
<p>Schematic flow curve at steady state, <math>\log \eta</math> versus <math>\log \dot{\gamma}</math>: (a) for a pseudoplastic (shear-thinning) suspension, and (b) for a dilatant (shear-thickening) suspension. N1 and N2 are Newtonians in the low and high shear rate ranges, respectively. P denotes pseudoplasticity and D is for dilatancy.</p>	
Fig. 2.4	130
<p>Equilibrium, structure, and initial shear stress curves for a thixotropic suspension of colloidal alumina [67]. All these curves, together with time dependent parameters, are required to understand fully the complicated rheological behavior of thixotropic suspensions.</p>	
Fig. 2.5	131
<p>The functional forms of <math>\alpha</math> and <math>\beta</math> in Cheng's structural equations can be obtained by experiments [53].</p>	
Fig. 2.6	132
<p>Rheocasting process [71].</p>	
Fig. 2.7	133
<p>Viscosity of some aluminum alloys in liquid state [148].</p>	
Fig. 2.8	134
<p>Effect of shear rate on viscosity [72].</p>	
Fig. 2.9	135
<p>Shear-thinning behavior of a semi-solid alloy slurry. Note the effect of the initial shear rate on viscosity [72].</p>	

Fig. 2.10	Effect of cooling rate on viscosity [72].	136
Fig. 2.11	Effect of shear rate and cooling rate on the solid-liquid surface area and primary particle size, $d$ [108].	137
Fig. 2.12	Experimentally determined hysteresis loops of 0.45 volume fraction solid slurry of Sn-15%Pb alloy and some well-known nonmetallic thixotropic materials [72].	138
Fig. 2.13	(a) Time dependence of shear stress after a time of rest for Al-15%Cu at $f_s = 0.4$ . The alloy slurry exhibits the "ultimate shear strength," $T_{max}$ , before a new steady state. (b) The shape of primary solid of the alloy affects the value of the maximum stress. Also stress is a strong function of the rest time [94].	139
Fig. 2.14	The fluidity of an alloy in semi-solid state decreases with increase of volume fraction solid and decrease in shear rate: (1) Al-10%Cu [86] and (2) Sn-15%Pb [85].	140
Fig. 2.15	Spiral fluidity of alumina particulate/Al-11Si composite slurry [144].	141
Fig. 3.1	(a) Phase diagram of Al-Si alloy [162]. (b) Volume fraction solid of primary phase for Al-6.51wt%Si alloy.	142
Fig. 3.2	Scanning electron micrograph of high purity silicon carbide (SiC) particulates at different magnifications.	143
Fig. 3.3	Size distribution of silicon carbide particulates analyzed by a Coulter counter. The average size of the batch is 8.5 $\mu m$ .	144
Fig. 3.4	Ceramic particulates and matrix alloy packed into an alumina crucible for pressure infiltration.	145
Fig. 3.5	Pressure-infiltration equipment used for the preparation of high density composite compact.	146
Fig. 3.6	Sketch of apparatus for the dilution of compact.	147
Fig. 3.7	(a) Optical micrograph of Al-6.5wt%Si alloy, conventionally cast without stirring during solidification (b) Optical micrograph of a pressure-infiltrated SiC <sub>p</sub> /Al-6.5wt%Si composite compact.	148
Fig. 3.8	Sketch of experimental apparatus for the rheological study of alloy and composite slurries.	149



Fig. 3.9	Optical torque transducer: Vibrac® model T3.	150
Fig. 3.10	Rotating concentric cylinder viscometer used in this study, often called the Searle-type viscometer.	151
Fig. 3.11	Plot of measured apparent viscosity of S-600 standard oil and standard values.	152
Fig. 3.12	Experimental procedures for (a) Continuous cooling and (b) Isothermal experiments	153
Fig. 3.13	Step change method to obtain structure curves. $\lambda_o$ , $\lambda_i$ , and $\lambda_j$ are the individual structures corresponding to the shear rates $\dot{\gamma}_o$ , $\dot{\gamma}_i$ , and $\dot{\gamma}_j$ , respectively.	154
Fig. 3.14	Experimental procedure for measuring the effect of rest time on the transient curve and microstructure.	155
Fig. 4.1	Plot of apparent viscosity of Al-6.5wt%Si alloy versus volume fraction solid at cooling rate 0.075 K/s with shear rates of 180, 540, and 900 s <sup>-1</sup> .	156
Fig. 4.2	Plot of apparent viscosity of Al-6.5wt%Si alloy versus volume fraction solid at cooling rate of 0.0083 K/s with shear rates of 180, 540, and 900 s <sup>-1</sup> .	157
Fig. 4.3	Cross-sectional microstructures of continuously cooled samples of Al-6.5wt%Si alloy in the gap of the viscometer: the average shear rates were (a) 180 and (b) 900 s <sup>-1</sup> and the average cooling rate was 0.075 K/s for both. The final volume fraction solid is 0.52, calculated by the Scheil equation.	158
Fig. 4.4	Change in apparent viscosity of Al-6.5wt%Si alloy during isothermal shearing: apparent viscosity was increasing to a maximum level in the early period of isothermal shearing, and then slowly decreased to a steady state level.	159
Fig. 4.5	Plot of apparent viscosity of Al-6.5wt%Si alloy at an isothermal steady state versus volume fraction solid of the primary solid phase under different initial shear rates, $\dot{\gamma}_o$ .	160
Fig. 4.6 (a)	Plot of isothermal shear stress at steady state versus initial shear rate for volume fractions solid of 0.2 and 0.4 in Al-6.5wt%Si alloy.	161

Fig. 4.6 (b)	Plot of isothermal apparent viscosity at steady state versus initial shear rate for volume fractions solid of 0.2 and 0.4 in Al-6.5wt%Si alloy.	162
Fig. 4.7 (a)	Pseudoplasticity of an alloy slurry with volume fraction solid of 0.4, sheared at an initial shear rate of $900 \text{ s}^{-1}$ . (a) plot of shear stress versus shear rate,	163
Fig. 4.7 (b)	Pseudoplasticity of an alloy slurry with volume fraction solid of 0.4, sheared at an initial shear rate of $900 \text{ s}^{-1}$ . (b) plot of apparent viscosity versus shear rate.	164
Fig. 4.8(a,b)	Microstructural evolution during the rest of a slurry of Al-6.5wt%Si with $g_{s(\alpha)}=0.4$ : The initial microstructure was formed by shearing isothermally at the initial shear rate of $180 \text{ s}^{-1}$ for two hours. The rest time was (a) 0 (the initial structure), and (b) 3 hours, respectively.	165
Fig. 4.8(c,d)	Microstructural evolution during the rest of a slurry of Al-6.5wt%Si with $g_{s(\alpha)}=0.4$ : The initial microstructure was formed by shearing isothermally at the initial shear rate of $180 \text{ s}^{-1}$ for two hours. The rest time was (c) 6 hours, and (d) 24 hours, respectively.	166
Fig. 4.9	Transient curves of apparent viscosity with time when shearing of a slurry of Al-6.5wt%Si alloy was resumed after a rest.	167
Fig. 4.10	Plot of initial peak viscosity after resumption of shearing versus rest time.	168
Fig. 4.11	Plot of time for new equilibrium versus rest time.	169
Fig. 4.12	The coefficient B' in eqn.(48) of Al-6.5wt%Si alloy versus shear rate at cooling rates of 0.075 and 0.0083 K/s.	170
Fig. 4.13	The coefficient A' in eqn.(48) of Al-6.5wt%Si alloy versus shear rate at cooling rates of 0.075 and 0.0083 K/s.	171
Fig. 4.14	The coefficient B' in eqn.(48) of Al-6.5wt%Si alloy versus cooling rate at shear rates of 180, 540, and $900 \text{ s}^{-1}$ .	172
Fig. 4.15	Plot of change of viscosity relative to the steady state and shearing time after different periods of rest: 30, 300, and 4980 seconds.	173
Fig. 4.16	Plot of thixotropic recovery rate and rest time.	174

Fig. 5.1	Optical micrograph of 20vol%SiC/Al-6.5wt%Si composite cast in a graphite mold.	175
Fig. 5.2	Change of apparent viscosity of 20vol%SiC/Al-6.5wt%Si composite with time, sheared at different shear rates after a rest at 700°C (transient curves).	176
Fig. 5.3	Change of apparent viscosity of 10, 20, and 30vol%SiC/Al-6.5wt%Si composite with time, sheared at 900 s <sup>-1</sup> after a rest at 700°C (transient curves).	177
Fig. 5.4	Plot of shear stress at steady state and initial shear rate for composite slurries with 10, 20, and 30 vol% SiC/Al-6.5 wt%Si at 700°C (equilibrium curves).	178
Fig. 5.5	Plot of apparent viscosity at steady state and initial shear rate for composite slurries with 10,20 and 30vol% SiC/Al-6.5 wt%Si at 700 °C (equilibrium curves).	179
Fig. 5.6	Plot of apparent viscosity at steady state vs. volume fraction of SiC for composite slurries with 10, 20, and 30 vol% SiC/Al-6.5 wt%Si at 700 °C.	180
Fig. 5.7	Step change of shear rate: a composite slurry of 30vol%SiC/Al-6.5wt%Si at 700°C, initially sheared at 900 s <sup>-1</sup> .	181
Fig. 5.8 (a)	Plot of shear stress and shear rate of 20vol%SiC/Al-6.5wt%Si composite slurry at 700°C. Each sample was initially sheared at 180 and 900 s <sup>-1</sup> (structure curves).	182
Fig. 5.8 (b)	Plot of apparent viscosity and shear rate of 20vol% SiC/Al-6.5wt%Si composite slurry at 700°C. Each sample was initially sheared at 180 and 900s <sup>-1</sup> (structure curves).	183
Fig. 5.9 (a)	Plot of shear stress and shear rate of 10 and 20 vol% SiC/Al-6.5wt%Si composite slurries at 700°C. Both samples were initially sheared at 180 s <sup>-1</sup> (structure curves).	184
Fig. 5.9 (b)	Plot of apparent viscosity and shear rate of 10 and 20 vol%SiC/Al-6.5wt%Si composite slurries at 700°C. Both samples were initially sheared at 180 s <sup>-1</sup> (structure curves).	185
Fig. 5.10(a)	Plot of shear stress and shear rate of 20 and 30 vol%SiC/Al-6.5wt%Si composite slurries at 700°C. Both	

	samples were initially sheared at $900 \text{ s}^{-1}$ (structure curves).	186
Fig. 5.10(b)	Plot of apparent viscosity and shear rate of 20 and 30 vol%SiC/Al-6.5wt%Si composite slurries at $700^{\circ}\text{C}$ . Both samples were initially sheared at $900 \text{ s}^{-1}$ (structure curves).	187
Fig. 5.11	Plot of change of viscosity relative to the steady state and shearing time after a rest, sheared at different shear rates for 20vol%SiC/Al-6.5wt%Si composite slurry at $700^{\circ}\text{C}$ .	188
Fig. 5.12	Plot of change of viscosity relative to the steady state and shearing time after a rest, sheared at $900 \text{ s}^{-1}$ for 20 and 30 vol%SiC/Al-6.5wt%Si composite slurries at $700^{\circ}\text{C}$ .	189
Fig. 5.13	Comparison of apparent viscosity of an alloy slurry with $g_{s(\alpha)}=0.2$ in the semi-solid state and a composite slurry with $g_{s(\text{SiC})}=0.2$ at $700^{\circ}\text{C}$ .	190
Fig. 5.14	Plot of low shear limit viscosity and high shear limit viscosity and volume fraction of SiC.	191
Fig. 6.1	Change of apparent viscosity of a composite with 20 vol%SiC, continuously cooled at $0.075 \text{ K/s}$ at shear rates of 180 and $540 \text{ s}^{-1}$ . The fraction solid is from the primary solid of the matrix alloy, equivalent to the temperature.	192
Fig. 6.2	Change of apparent viscosity of composite slurries with 0, 10, and 20 vol%SiC, continuously cooled at $0.075 \text{ K/s}$ at shear rates of $180 \text{ s}^{-1}$ . Note that there is a clear cross-over in temperature for a composite with 20 vol%SiC, below which the viscosity of the composite is lower than that of the matrix alloy.	193
Fig. 6.3	Change of apparent viscosity of composite slurries with 0, 10, and 20 vol%SiC, continuously cooled at $0.075 \text{ K/s}$ at shear rates of $180 \text{ s}^{-1}$ . Note that volume fraction solid is expressed in total solid amount, including SiC and primary solid, calculated by eqn. (53).	194
Fig. 6.4	Comparison of difference in the viscosities of a composite slurry with 20vol%SiC and the matrix alloy of the composite, both sheared at 180 and $540 \text{ s}^{-1}$ .	195

Fig. 6.5	Optical micrographs of samples, continuously cooled at 0.075 K/s, and sheared at $900 \text{ s}^{-1}$ (x75): (a) Al-6.5wt%Si matrix alloy ( $R_A=2.8$ ), (b) 20 vol%SiC/Al-6.5wt%Si composite ( $R_A=2.5$ ).	196
Fig. 6.6	Effect of cooling rate on the microstructures of composites (20 vol%SiC/Al-6.5wt%Si), sheared at 180, and continuously cooled at (a) $\epsilon = 0.075 \text{ K/s}$ ( $R_A=3.6$ ), and (b) $\epsilon = 0.0083 \text{ K/s}$ ( $R_A=2.8$ ) (x75).	197
Fig. 6.7	Effect of shear rate on the microstructures of composites (20 vol%SiC/Al-6.5wt%Si), continuously cooled at 0.075 K/s (x37.5). Shear rate was (a) $180 \text{ s}^{-1}$ ( $R_A=3.6$ ), and (b) $900 \text{ s}^{-1}$ ( $R_A=2.7$ ), respectively.	198
Fig. 6.8	Comparison of the apparent viscosity of a composite with total 0.36 fraction solid (i.e., a mixture of $g_{s(\alpha)}=0.20$ and $g_{s(\text{SiC})}=0.2$ ) and an alloy slurry with 0.36 fraction solid of primary particles only. Note that the apparent viscosity of the composite is lower than that of the alloy slurry.	199
Fig. 6.9	Optical microstructures of a composite with (i.e., a mixture of $g_{s(\alpha)}=0.20$ and $g_{s(\text{SiC})}=0.2$ ), isothermally sheared at (a) $180 \text{ s}^{-1}$ and (b) $900 \text{ s}^{-1}$ , respectively, (x75).	200
Fig. 6.10	Plot of shear stress and shear rate of 20 vol%SiC/Al-6.5wt%Si at a temperature for $g_{s(\alpha)}=0.2$ . Each sample was initially sheared at 180 and $900 \text{ s}^{-1}$ (structure curves).	201
Fig. 6.11	Plot of apparent viscosity and shear rate of 20 vol%SiC/Al-6.5wt%Si at a temperature for $g_{s(\alpha)}=0.2$ . Each sample was initially sheared at 180 and $900 \text{ s}^{-1}$ (structure curves).	202
Fig. 6.12	Plot of shear stress and shear rate of 20 vol%SiC/Al-6.5wt%Si at a temperature for $g_{s(\alpha)}=0.2$ and a matrix alloy with $g_{s(\alpha)}=0.4$ . Both samples were initially sheared at $900 \text{ s}^{-1}$ (structure curves).	203
Fig. 6.13	Plot of apparent viscosity and shear rate of 20 vol%SiC/Al-6.5wt%Si at a temperature for $g_{s(\alpha)}=0.2$ and a matrix alloy with $g_{s(\alpha)}=0.4$ . Both samples were initially sheared at $900 \text{ s}^{-1}$ (structure curves).	204

Fig. 6.14	Plot of peak viscosity after resumption of shearing versus rest time for 20 vol%SiC/Al-6.5wt%Si at a temperature for $g_{s(\alpha)}=0.2$ . The initial shear rate was $180\text{s}^{-1}$ .	205
Fig. 6.15	Optical micrograph of 20 vol%SiC/Al-6.5wt%Si at a temperature for $g_{s(\alpha)}=0.2$ , initially sheared at $180\text{ s}^{-1}$ for two hours, followed by resting for $10^4\text{ s}$ .	206
Fig. A1	Comparison of weight fractions solid calculated from the lever rule and the Scheil equation.	207
Fig. A2	Velocity distribution in the annulus between two concentric, rotating cylinders [160]. (a) Case I : inner cylinder rotating; outer cylinder at rest (b) Case II:inner cylinder at rest; outer cylinder rotating	208
Fig. A3	Taylor vortices between two concentric cylinders: inner cylinder rotating, the outer cylinder at rest [160].	208

## LIST OF TABLES

<u>TABLE</u>		<u>Page</u>
Table 2.1	Relationship between relative viscosity and concentration of suspension.	209
Table 2.2	Maximum packing volume concentration in suspensions of uniform hard spheres [1].	210
Table 2.3	Effect of process parameters on rheocast structure and viscosity.	211
Table 3.1	Chemical analysis of Al-6.5wt%Si binary alloy.	212
Table 3.2	Chemical analysis of high purity silicon carbide particulates.	213
Table 4.1	Effect of cooling rate, initial shear rate and volume fraction solid on the apparent viscosity of continuously cooled Al-6.5wt%Si alloy slurries (viscosity unit in Pa·s).	214
Table 4.2	Effect of shear rate and volume fraction solid on the apparent viscosity at "steady state" of isothermally held Al-6.5wt%Si alloy slurries (viscosity unit in Pa·s).	215
Table 5.1	Apparent viscosity and shear stress at steady state for molten composite slurry and molten matrix at 700°C.	216
Table 5.2	The measured values of $n$ and high shear rate limit viscosity for SiC/Al-6.5wt%SiC composites at 700°C.	217
Table 6.1	The comparison of apparent viscosities for a alloy slurry and a composite slurry with the same total solid fraction (at steady state, isothermally sheared for two hours).	218
Table A1.	Dimensions of rotors and constants for rheological equations.	219
Table A2.	Stability criteria for the flow in concentric cylinder viscometer (Searle-type viscometer).	220

## ACKNOWLEDGMENTS

I would like to thank my thesis supervisor, Professor Merton C. Flemings, for his encouragement and support throughout my graduate work at MIT. My special thanks are also due to my thesis co-supervisor, Dr. James A. Cornie, who has advised me with many ideas and gourmet Espresso coffee. I am grateful to the members of the Solidification and Metal Matrix Composites Processing Group for their help and friendship. I would like to thank Maria Wehrle Due for her technical assistance as well as encouragement. I am grateful to Professor Theodoulos Z. Kattamis, who has taken part in helpful discussions. I wish to thank Dr. Seyong Oh for many discussions and his special care in my early years at MIT. I owe my thanks to Dr. Thomas J. Piccone for the proof reading of my thesis.

This thesis is dedicated to my wife, Jeong-Hae, and my son, Michael Han-Gi who was born during my study. I wish to express my dearest love and appreciation to her for never-ending support, love, and sacrifice, and also for raising our son. I would like to thank my parents for their constant care and encouragement.

I am grateful to my company, POSCO (Pohang Iron & Steel Co. Ltd., Pohang, Korea) for supporting my study and allowing me to complete this long-term work. This research was sponsored by NASA Lewis Research Center (contract no. NAG 3-808) in its beginning, and continued by the the funding from ONR/IST-SDIO (contract no. N00014-85-K-0645). An interim support was also provided by the MIT-Industrial Consortium for the Processing and Evaluation of Inorganic Matrix Composites.



## CHAPTER 1.

# INTRODUCTION

The solidification processings of metal matrix composites (MMCs) have drawn much attention because these prospective materials could be manufactured at lower cost than by other processing methods such as hot isostatic pressing, powder metallurgical processing, etc. Recently, the ceramic particulate-reinforced MMCs are being produced on a commercial scale via some proprietary casting processes.

In most casting methods, except pressure casting, the reinforcement is added and mixed by stirring in the molten and/or semi-solid state of the matrix alloy. The first physical problem in these casting processes is to overcome the poor wettability of ceramic particulates with molten matrix alloy. Secondly, when the ceramic particulates or other reinforcements are incorporated into the molten matrix metal, the composite slurry would exhibit viscosity which is dependent on the shear rate and/or time. In general, with higher volume fraction of reinforcement, composite slurries become more viscous and more dependent on stirring conditions. Hence, understanding of the rheological behavior of such slurries is an important factor in the successful processing of cast composites.

The relationships of apparent viscosity of semi-solid alloy slurries with processing and material parameters have been understood by combining microstructural features and viscosity. On the other hand, the study of rheological behavior in composite slurries is still in its initial stage,

while the interest in these composite materials is growing rapidly. The major objectives of this thesis are to investigate the following:

- (a) Non-Newtonian behavior and thixotropy of composite slurries with silicon carbide particulates (8.5  $\mu\text{m}$ ) with the matrix alloy, Al-6.5wt%Si, in the fully molten and semi-solid state.
- (b) Comparison of these composite slurries with the semi-solid unreinforced alloy slurries of the matrix, and
- (c) Understanding the role of a non-deformable ceramic particulate in the rheological behavior and microstructure.

## CHAPTER 2.

# LITERATURE BACKGROUND

### 2.1. The Rheology of Suspensions of Rigid Particles

A physical mixture of a liquid in a liquid is referred to as an emulsion, and a mixture of a solid in a liquid as a suspension. Hence, slurries of solid metal particles in equilibrium with liquid metal and of ceramic particles in a metallic liquid are suspensions. Suspensions in many cases have to be treated as non-Newtonian fluids whose rheological flow properties are controlled by a large number of variables. The question is why such non-Newtonian behavior occurs and how the variables influence the viscosity of suspensions [1-7]. This review focuses only on those suspensions with rigid solids in Newtonian fluids.

#### 2.1.1. Newtonian Behavior of Suspensions

##### *A. Theoretical Works*

The theoretical calculation of the viscosity of suspensions of solid particles can be approached in several ways. Firstly, the viscosity may be determined from the velocity gradient:

$$\tau_{ik} = -\eta \left( \frac{\partial u_i}{\partial x_k} + \frac{\partial u_k}{\partial x_i} \right) dV \quad (1)$$

and, secondly, from energy dissipation in the bulk of the liquid:

$$E_v = - \eta \int_v \frac{\partial u_i}{\partial x_k} \left( \frac{\partial u_i}{\partial x_k} + \frac{\partial u_k}{\partial x_i} \right) dV \quad (2)$$

where  $\tau_{ik}$  is the shear stress on the plane  $i$  in the direction  $k$ , the  $u$ 's are the velocities at the locations  $x$ , and  $E_v$  is the energy dissipated in the bulk of the fluid by viscous forces.

The variables should include the shape and size distribution of the particles, the presence of electrical charges, and the type of flow being experienced, as well as the volume fraction of particles in the suspension. Exact theoretical calculations of viscosity have been successfully completed only for dilute suspensions. As the volume fraction of the particles increases, it becomes more difficult to predict the rheological behavior because of complicated interaction among many variables.

### **(1) Effect of Concentration**

For the case of extremely dilute suspensions, less than 0.01 in volume fraction solid, the following relationship has been accepted to since Einstein theoretically derived the classical equation [8]:

$$\eta_r = \eta_s / \eta_m = 1 + k_1 \phi + \dots \quad (3)$$

where  $\eta_r$  is the relative viscosity,  $\eta_s$  the viscosity of the suspension,  $\eta_m$  the viscosity of the suspending medium and  $\phi$  is the volume fraction of

particles. The value of  $k_1$  varies with the shape of the particles : 2.5 for spheres, and higher than 2.5 for ellipsoidal. The assumptions made in the equation are:

- (i) The diameter of rigid spherical particles of uniform size is large compared with that of the suspending medium molecules, but small compared with the smallest dimension of the rheometer,
- (ii) also, the particles are far enough apart to be treated as independent of each other, or the concentration is small,
- (iii) the flow around particles is at steady state, without inertial, concentration gradient, or wall slip effects, and
- (iv) the liquid medium perfectly adheres to the particles.

With more concentrated suspensions, it is necessary to account for the hydrodynamic interaction of particles, particle rotations, collisions between particles, mutual exclusion, doublet and higher order agglomerate formation, and, ultimately, mechanical interference between particles as packed bed concentrations are approached. The difficulties in arriving at a theory for these concentrated suspensions lie in the fact that the random structure of the suspension cannot be represented by a simple model.

Simha [9] used a cell model of a hard sphere suspension, placing the particles in the centers of spherical shells with radii, inversely proportional to  $\phi$ , and dependent on hydrodynamic interactions.

$$\eta_{r.o.} = 1 + [\eta]_s \eta_o' \phi \quad (4)$$

where

$$\eta_o' = f \{ (\phi_m/\phi)^{-1/3} \}$$

Mooney [10], using some global considerations about the filling of the suspension volume by particles, derived a formula,

$$\eta_{r,o} = \exp \left( \frac{2.5 \phi}{1 - k \phi} \right) \quad (5)$$

In the equation, the subscript o indicates zero rate of shear,  $k$  is a parameter to be determined by experiment, which is constrained by  $1.35 \leq k \leq 1.91$  according to his theory. The constant  $k$  is considered to be equivalent to the inverse of the maximum packing volume fraction of particles,  $\phi_m$ . For uniform hard spheres in random packing, the intrinsic viscosity is 2.5 and the maximum packing volume fraction is 0.62 in experiments. For non-uniform spheres, these variables should be determined by curve fitting or experiments. Brodnyan [11] extended Mooney's treatment to concentrated suspensions of ellipsoids and obtained, by a combination of theoretical considerations and empirical curve fitting,

$$\eta_{r,o} = \exp \left\{ \frac{[2.5 + 0.399 (p - 1)]^{1.48} \phi}{1 - k \phi} \right\} \quad (6)$$

where  $k$  is the crowding factor ( $1 < k < 2$ ), and  $p$  the aspect ratio of the ellipsoid. All these equations, however, fail to fit experimental data for the concentrations over 10%.

At higher volume fractions, particle interactions become significant, and the relationship between viscosity and concentration becomes non-linear. These results were summarized by Rutgers [12]. A simple attempt to correlate the data of many experiments was made by Thomas [13]. In

both cases, the final curves were largely arbitrary and did not agree with each other. Thomas selected some of most reliable data, and examined them after correcting for particle size and shear rate. Up to  $\phi = 0.6$ , his semi-empirical curve could be represented quite accurately by a reduced equation:

$$\eta_{r,\infty} = 1 + 2.5\phi + 10.05 \phi^2 + A \exp(B\phi) \quad ; \quad A=0.00273, B=16.6 \quad (7)$$

In this curve, viscosity shows a slow increase at low fraction and a fast rise when  $\phi$  is high. The first three terms take into account the hydrodynamic interaction; the last term is only to be added at concentrations higher than  $\phi = 0.25$  and takes care of the rearrangement of particles in the suspension. The equation, however, is limited by the maximum packing since it predicts a finite viscosity even when  $\phi = 1$ .

For highly concentrated suspensions, some other equations are of interest. For a suspension of uniform solid spheres, Frankel and Acrivos [14] used an asymptotic technique in the limit as the concentration approaches its maximum value or maximum packing volume concentration. They started from the hydrodynamic interaction of neighboring spheres and obtained the asymptotic rate of viscous dissipation of energy, finally to reach the following equation with no empirical constants.

$$\eta_r = 1 + \frac{9}{8} \left\{ \frac{(\phi/\phi_m)^{1/3}}{(1-\phi/\phi_m)^{1/3}} \right\} \quad \text{as } \phi/\phi_m \rightarrow 1 \quad (8)$$

Comparing their equation to the equations of Rutgers and Thomas, they found that their equation fitted well both of the two previous equations using a different value of  $\phi_m$  for the volume concentrations greater than eight-tenths of the maximum volume concentration (Fig. 2.1 [14]). Hence, they presumed that collision, segregation, and inertial effects were of minor importance in the usual apparatus such as the Couette-type viscometer. Still, their equation is limited by the shape of the particles.

Mori and Ototake [15] derived an equation for the relative viscosity of a suspension without limiting the shape of particles. They used a specific volume concept to overcome the shape of particles. They also considered the maximum packing concentration and used the concept that the particles in the same stratum in flow had the same velocity and did not change their mutual distances. They derived an equation for the relative viscosity of a general suspension as:

$$\eta_r = 1 + \frac{\bar{d} S_r}{2 \Phi}, \quad \Phi = \frac{1}{\phi} - \frac{1}{\phi_m} \quad (9)$$

where  $\bar{d}$  is the effective average diameter of particles,  $S_r$  is the total surface area of particles per unit volume of the particles,  $\phi$  is the volume concentration and  $\phi_m$  is the limiting concentration at the fully-packed state. Hence, the shape factor was considered in  $S_r$  with more flexibility than in other formulations. In the limit of extreme dilution of spheres, the equation reduces to a form quite close to the Einstein-type equation:  $\eta_r = 1 + 3 \phi$ . As the concentration approaches the limiting concentration, then the relative viscosity increases to infinity.



Numerous formulas for the relationship between the relative viscosity and volume concentration are listed in Table 2.1. Some values of the maximum packing volume concentration of uniform hard spheres given in Table 2.2 [1].

## **(2) Effect of Particle Size**

The viscosity of a suspension may increase or decrease as the particle size increases, depending on the system. The data do not permit an isolated conclusion of the effect of particle size to be drawn but indicate that, whenever particles are not spherical, the relative viscosity is higher than that of a suspension of spheres and increases with increasing particle size [26].

## **(3) Effect of Particle Size Distribution**

When the particles are separated but the volume fraction of particles is too large for the effects of neighboring particles on each other to be ignored, the dispersity of the particles becomes important ( $\phi \geq 0.2$ ). It is experimentally, as well as theoretically, found that a suspension of poly-sized spheres has a lower viscosity than a similar monodisperse suspension with the same total volume fraction. The distribution of particle size contributes directly to the maximum packing volume fraction,  $\phi_m$ . Any increase in  $\phi_m$  reduces  $\eta_{r,0}$  at a constant value of  $\phi$  by tailoring the distribution of spherical particles. Several methods for maximization have been proposed to reduce viscosity. For example, McGeary [27] proposed the following equation for the N-generation of spheres.

$$\phi_{m,N}(\infty) = \phi_{m,N-1}(\infty) + [1 - \phi_{m,N-1}(\infty)] \phi_{m,N-1}(\infty) \quad (10)$$

with  $R^N$  to an infinity, where  $R$  is the ratio of the size of largest particle to that of smallest particle. For random packing of binary sized spheres, the dependence of  $\phi_m$  on  $R$  can be expressed as

$$\phi_{m,2} = \phi_{m,2}(\infty) \{ 1 - \exp[ a_0 + a_1 \exp(-a_2 R) ] \} \quad (11)$$

where the  $a_i$  are parameters. Parkinson et al. [28], combining equations from Farris [29] and Mooney [10], derived the relative viscosity of polydispersed suspension:

$$\eta_{r,o} = \prod_i \exp [ 2.5 \phi_i / ( 1 - k_i \phi_i ) ] \quad (12)$$

$$k_i = 0.168 d_i^{-1.0072}$$

where  $\phi_i$  is the volume fraction of each generation of spherical particles, and  $k_i$  depends on the particle diameter,  $d_i$ , given by an empirical relation.

#### (4) Effect of Particle Shape

At the onset of shearing, non-spherical particles begin to rotate with a period

$$t_p = 2 \pi ( p + p^{-1} ) / \dot{\gamma} \quad (13)$$

where  $p$  is the aspect ratio ( $= d_{\max} / d_{\min}$ ). Due to these orientation effects,  $[\eta]_s$  is a periodic function of time, gradually damped to reach a steady state

value [30]. The equations of Einstein type are no longer true for suspensions of anisometric particles, where crowding and mode of deformation affects the orientation.

In the region of infinite dilution ( $p^{-2} > \phi$ ), the particle rotates freely without being affected by the presence of other particles. Accordingly, the intrinsic viscosity of anisometric particles,  $[\eta]_a$ , is a measure of particle hydrodynamic value defined by its geometry. For rigid dumb-bells, Simha [31] derived

$$[\eta]_a = 3 (L/d)^2 / 2 \quad (14)$$

where  $L$  is sphere separation and  $d$  is sphere diameter. For ellipsoids of rotation and rigid rods, Simha [32] also derived

$$[\eta]_a = \frac{14}{15} + \frac{p^2}{5} \left[ \frac{1}{3 (\ln 2p - \sigma)} + \frac{1}{\ln 2 - \sigma + 1} \right] \quad (15)$$

where  $\sigma$  is a numerical constant;  $\sigma = 1.5$  for ellipsoids of rotation, and  $\sigma = 1.8$  for rigid rods. This equation holds for  $p > 20$  and provides the upper bound for freely rotating particles.

For time-averaged optimum orientation, Goldsmith and Mason [33] proposed

$$[\eta]_a = p^3 / [3 (\ln 2p - \sigma) (p + 1)^2] \quad (16)$$

Harber and Brenner [34] derived a general relation for  $[\eta]_a$  of triaxially anisometric ellipsoids.

In the semi-concentrated region ( $p^{-2} < \phi < p^{-1}$ ), movement takes place in two dimensions. This results in a decrease of the apparent hydrodynamic volume of the particles. One can postulate that the two-body interactions can be expressed by

$$\eta_o' = 1 + k_H [\eta]_a \phi + \dots \quad (17)$$

where the Huggins constant,  $k_H$ , expresses the particle-particle interactions. For hard sphere suspensions,  $k_H = 5/16 \phi_m$ . For anisometric particles,  $k_H$  depends on the type of flow, on shape, and on orientation.

As  $\phi$  approaches the maximum packing value ( $\phi > p^{-1}$ ),  $\eta_r$  should rapidly increase toward infinity. Experimentally, a series of complicating factors are involved. All of these led to highly non-Newtonian behavior and the zero-shear viscosity can be extracted only after a series of correcting procedures. Pragmatically, the relation between  $[\eta]_a$  and  $\phi_m$  on the aspect ratio  $p$  for discs and rods can be approximated by

$$[\eta]_a \text{ or } \phi_m = a_0 + a_1 p^2 \quad (18)$$

with the  $a_i$  being parameters.

### ***B. Empirical Works***

Many experiments were performed to find a more complicated formula for the relative viscosity as a function of  $\phi$ :  $\eta_r = \eta_r(\phi)$ . Experimental difficulties for suspensions include:

- Continuum theory assumptions; A concentration gradient must exist between the bulk of the sample and the layer near the wall [35]. A rule of thumb requires that the smallest dimension of the measuring device should be at least 10 times larger than the largest diameter of the flowing particles [36]
- Generation of well-dispersed suspensions; Theory requires that particles be separated and randomly oriented, but due to strong solid-solid interactions, and low limit of the dilute, free-tumbling region, this requirement is seldom attained. The presence of aggregates and/or orientation invariably leads to non-Newtonian behavior.
- Non-deformable particles; The particles are assumed to be rigid or non-breakable. The latter requirement is particularly difficult to observe when measuring suspensions of rigid fibers in viscous media.

### **2.1.2. Non-Newtonian Behavior of Suspensions**

Many other problems arise as the viscosity of some suspensions, including semi-solid alloy slurries, are found to be dependent on shear rate, and on particle size, shape, and distribution. The Newtonian behavior of suspensions presented as in the Einstein-type relationship is limited to very low concentrations of particles. As the concentration of suspension increases, the particle interaction becomes more significant and the behavior of such suspensions is in most cases non-Newtonian. Other reasons for this are: wall effects in capillary viscometers, slip at particle surfaces, insufficient dispersion, adsorption, turbulence, sedimentation, etc.

### **(1) Effect of Concentration**

Many suspensions exhibit shear-thinning behavior typically above a concentration of 0.20. The viscosity, then, ranges between two limiting values  $\eta_0$  and  $\eta_\infty$  at low and high shear rates, respectively, as shown in Fig. 2.2 [37]. The figure also indicates that the suspensions are Newtonian up to the concentration of 0.20 with a slope of 2.7, which is very close to that in Einstein-type models; they start to exhibit shear-rate dependence above this concentration. Since the Thomas equation was obtained after an extrapolation to infinite rate of shear, the equation is applicable to the corresponding high shear limit viscosity. The parameters  $[\eta]$  and  $p$  in the Krieger-Dougherty model [21] are regarded as shear-dependent and the equation has been used to represent both  $\eta_\infty$  and  $\eta_0$ . At higher concentrations,  $\eta_0$  may be many times greater than  $\eta_\infty$  and the ( $\eta_0$  vs.  $\phi$ ) relationship may be correspondingly more complicated. Most of proposed equations in Table 2.1 imply this shear rate dependence.

### **(2) Shear Rate Dependences with No Time-Dependence**

On a flow curve, or shear stress versus shear rate, the slope, which is defined as viscosity, decreases as shear rate increases. This is called shear-thinning or pseudoplastic behavior. The case opposite to shear-thinning is called shear-thickening or dilatant behavior [38]: viscosity increases with shear rate. Suspensions of particles in the size of 0.10 to 230 microns can exhibit either pseudoplastic or dilatant types of behavior, depending on the viscosity of the suspending medium and the shear rate. At both high and low shear rates, a suspension can be Newtonian, in which

the corresponding viscosity remains constant within those ranges,  $\eta_{\infty}$  or  $\eta_0$ , respectively. As illustrated in Fig. 2.3, viscosity values of a suspension at a concentration ranges within these two limits.

For non-Newtonian suspensions, the viscosity or shear stress can be expressed as a function of shear rate. The power law equation is best suited for many pseudoplastic and dilatant systems:

$$\tau = k \dot{\gamma}^n \quad (19)$$

$$\eta = k' \dot{\gamma}^{n-1} \quad (20)$$

The constant  $n$  ( $0 < n < 1$  for pseudoplasticity, and  $1 < n$  for dilatancy) is a measure of the degree of non-Newtonian behavior, and the greater the departure from unity the more pronounced are the non-Newtonian properties of the material. The constant  $k$  is a measure of the consistency of the material; the higher the  $k$ , the more viscous it is. The physical interpretation of pseudoplasticity is that with increasing shear rate the anisometric particles are progressively aligned in the direction of flow. The viscosity continues to decrease with increasing shear rate until no further alignment along the streamlines is possible and the flow becomes Newtonian at the high shear limit.

The most frequently used semi-empirical equations to describe viscosity versus shear rate dependence are the four-parameter Cross dependence [39]

$$\frac{\eta - \eta_{\infty}}{\eta_0 - \eta_{\infty}} = \frac{1}{(1 + a_0 \dot{\gamma}^{a_1})} \quad (21)$$

and the three-parameter Williamson relation [40]

$$\frac{\eta - \eta_o}{\eta_o - \eta_\infty} = \frac{1}{(1 + a_2 \sigma_{12})} \quad (22)$$

where  $\eta_\infty$  and  $\eta_o$  are Newtonian viscosities at the high and low shear limits, respectively, and the  $a_i$  are parameters. Another four-parameter relation has been recently proposed [41]. All three equations are valid for Newtonian-pseudoplastic-Newtonian cases, as shown in Fig.2.3 (a), without showing yield.

When a suspension exhibits a yield stress, the yield effect should be first be subtracted. Among several methods for determining  $\tau_y$ , the modified Casson equation [42] is

$$\sqrt{\tau_{12}} = k_0 + k_1 \sqrt{\left(\frac{\eta_a}{\eta_o}\right) \dot{\gamma}} \quad (23)$$

where  $k_0$  and  $k_1$  are parameters,  $\tau_{12}$  is shear stress,  $\eta_a$  is the apparent viscosity of the dispersing liquid. The yield stress is also dependent on the concentration, and the dependence can be expressed in either power law or exponential form of the concentration [43].

### (3) Effect of Agglomeration

A suspension in which the particles have formed pairs, or aggregates, can be considered to be a suspension of single particles of a new shape, and as such must be expected to show different properties from a suspension in which the particles remain separated. The aggregation can



be due to inter-particle thermodynamic interactions, chemical bonding, or crowding in simple geometric terms. The latter prevails in shear flows of suspensions of anisometric particles. Aggregation of particles always results in higher viscosity [44]. This can be attributed primarily to the increase of effective volume fraction solid as more and more liquid is entrapped in the aggregates.

#### (4) Other Effects

##### *Settling and non-settling suspensions*

The major problem in studying the rheology of settling suspension is to avoid sedimentation and plug flow. In general, when the density of the solid particles is greater than that of the suspending medium, the viscosity increases with increasing particle density. An empirical relationship between  $K$  and the difference in density,  $\Delta\rho$ , was found by Ward [45].

$$K = (1.6 \times 10^{-3}) \Delta\rho / \eta_0 \quad (24)$$

$$\eta_r = (1 - k_1 \phi - K)^{-1} \quad (25)$$

Clarke [46] attributed this phenomenon to the decreased viscous drag forces experienced by colliding particles. The particles easily move around and rebound from one another, increasing the number of interactions, the total energy dissipated, and therefore the viscosity.

##### *Type of Flow*

Particles in suspension, even spherical ones, will be distributed anisotropically in many flows. Most proposed models for calculating

effective viscosities have assumed isotropic conditions, which is one reason why they have failed to explain non-Newtonian behavior. The flow can also either promote or inhibit the formation of structures by the particles. Clays, for example, are suspensions in which, when there is no flow, the particles flocculate and form continuous structures; thus they exhibit thixotropy and a yield stress.

#### *Non-Hydrodynamic Forces*

It has been known that non-hydrodynamic forces act on particles in suspension. These forces are listed in the Deryagin-Landau-verwey-Overbeek theory of colloid stability [47,48] and consists of thermal (Brownian) forces, electrical forces and London-van der Waals forces [3].

All non-hydrodynamic forces cause non-Newtonian behavior in suspensions because there is a competition between them and hydrodynamic forces, resulting in viscosity.

#### **(5) Mechanism of Non-Linear Behavior**

The non-linear behavior of a dispersed system can be explained by the fact that suspended particles interfere with the mobility of part of the suspended medium. There are two sorts of interference: Disturbance and immobilization [49].

##### *Disturbance*

This is a hydrodynamic problem defined as interference experienced by the suspending medium as it moves by the particles of the suspension. If anisometric particles rotate, the volume of fluid displaced in their rotation

can be much larger than their own volume. The particle motion is then equivalent to the motion of a sphere of larger diameter and the effective volume fraction is much higher than the actual. One thus can explain why suspensions of elongated particles are more viscous. At rest, all the angles of particles orientation to the direction of flow are equally possible. This determines a certain viscosity, which is the low limit viscosity,  $\eta_0$ . Without the Brownian movement at lower temperature or with very high rate of shear, the particles may ultimately become completely oriented or directed to the flow of liquid. This determines another value of viscosity, which is often called the high shear limit viscosity,  $\eta_\infty$ . Generally, there will be at every temperature and every rate of shear a dynamic equilibrium between the forces of diffusion and orientation, with a corresponding viscosity  $\eta$ , where  $\eta_0 > \eta > \eta_\infty$ . With disturbance theory, one can explain why some suspensions made of attracting particles are more viscous than those of non-attracting particles at equivalent fraction solid.

### *Immobilization*

This is due to the fact that suspended particles generally bind part of the suspending medium so that an larger effective particle is formed, which is suspended as a whole in the suspending medium. Immobilization can be an important contributing factor to the viscosity of a suspension [45]. The effect of shear rate on immobilization is generally time-dependent. As shear forces are increased, aggregates break up and release entrapped liquid. Yet the number of collisions increases with increasing shear, thus increasing the probability of aggregate formation. Very often a dynamic equilibrium is reached between the rate of breakup and the rate of buildup [50]. It will take a finite amount of time for this

equilibrium to be attained, resulting in time dependent rheological properties.

### **2.1.3. Thixotropy**

In modern rheology it has been generally agreed to define thixotropy as the continuous decrease of apparent viscosity with time under shear and the subsequent recovery of viscosity when shearing is discontinued. The early history of thixotropy has been reviewed by Bauer and Collins [51]. More recent reviews were performed by Mewis [52].

In a thixotropic material the shear stress or viscosity at a given shear rate is also a function of time of shearing, and depends on the material. The shear stress decreases from its initial peak value with shearing to an equilibrium level. The more complex problem is that the equilibrium stress level and the time to reach equilibrium are strongly dependent on the previous shear history of the material, which affects the structure of the solid/liquid mixture. Although thixotropy has long been recognized in many suspensions and emulsions, there has still been no universal rule to elucidate this phenomenon. Every theoretically or empirically functional expression is applied to these materials with certain limitations [53].

### ***A. Theoretical Works on Thixotropy***

#### **(1) Generalized Continuum Mechanics**

This is the first approach to develop a theoretical description for thixotropic materials. The Reiner-Rivlin constitutive equation is

generalized by making the relation between stress and shear rate dependent on time as in Slibar and Paslay [54], where  $\tau_{crit}$  is made a function of the shear history. These approaches can only explain thixotropy qualitatively with many assumptions. Hence, very few comparisons with experiments have been made.

## (2) Structural Kinetics

The idea of this approach is that the change of rheological parameter with time is caused by changes in the internal structure of the material, The non-linear, time-dependent behavior can then be described by a set of two equations. The first gives the instantaneous stress as a function of the instantaneous kinematics for every possible degree of structure. The second is a kinetic equation, which describes the rate of the instantaneous value of the structure and the instantaneous kinematics. Cheng and Evans [55] have developed a general framework for these materials by taking a structural parameter  $\lambda$ :

$$\tau(t) = f[\lambda(t), \dot{\gamma}(t)] \quad (26)$$

$$\frac{d\lambda}{dt} = g[\lambda(t), \dot{\gamma}(t)] \quad (27)$$

After eliminating the structural parameter, Cheng [56, 57] later extended the concepts and gave a phenomenological approach to characterize these materials:

$$\frac{d\tau_{12}}{dt} = \alpha (\tau_{12}, \dot{\gamma}_{12}) \frac{d\dot{\gamma}_{12}}{dt} + \beta (\tau_{12}, \dot{\gamma}_{12}) \quad (28)$$

$$\alpha = \left( \frac{\partial \tau_{12}}{\partial \dot{\gamma}_{12}} \right) \quad \text{and} \quad \beta = \left( \frac{\partial \tau_{12}}{\partial \lambda} \right)_{\dot{\gamma}_{12}} \frac{d\lambda}{dt} \quad (29)$$

From the constant shear rate data ( $d\dot{\gamma}/dt = 0$ ),  $\beta$  can be readily obtained for a set of values of  $\tau$  and  $\dot{\gamma}$ .  $\alpha$  can be obtained in several ways: a) from constant shear stress data; b) from experiments with known  $d\dot{\gamma}/dt$ ; c) from experiments with step changes in shear rate, where  $(d\dot{\gamma}/dt)_\lambda$ , i.e.,  $\alpha$  can be directly computed.

### (3) Microstructural Approach

This approach starts from the microstructures to calculate rheological behavior. For thixotropic materials a few attempts have been made [58, 59]. The main difficulty with this is that detailed structural analyses of these materials are very incomplete and complicated.

### (4) Other Approaches

The analysis from Eyring's theory of rate processes has been suggested and used with some success [60]. It is based on the presence of various flow mechanisms. Each mechanism causes a Newtonian or a non-Newtonian contribution to the shear stress in proportion to the number of flow units of its kind. In a thixotropic material, flow units of one kind can

change to another kind. Empirical or semi-empirical procedures have also been proposed [61].

## ***B. Experimental Characterization of Thixotropy***

### **(1) Equivalent Flow Curve**

Alfrey [62] devised an experiment whereby one applies a constant stress to a material and measures the variations of shear rate as a function of time. For each new shear stress, a new curve,  $\dot{\gamma}$  versus time, is obtained. On each of these curves the initial rate of increase of the shear rate is measured (i.e., the shear rate at time zero). The experiment is repeated after leaving the system at rest for different times, and a surface in a three-dimensional space, shear rate, shear stress, and time, is generated. This method, however, has several disadvantages.

### **(2) Hysteresis Loop**

The most direct method of the different techniques developed to observe and measure the thixotropic behavior was proposed by Green and Weltman [63]. A rotational viscometer is employed to measure the hysteresis loop of a thixotropic material. The procedure commences with an up-curve, starting at the lowest rotational speed (shear rate), or zero speed if possible. The speed is increased continuously and rapidly while measuring the induced torque (shear stress). At some specified upper rotational limit, the speed is maintained constant, then reversed and a down-curve is measured. If the material is thixotropic, the up- and down-

curves of shear stress vs. shear rate when plotted together will not coincide, thus forming the loop. This condition is ascribed to a thixotropic breakdown. A large loop means considerable breakdown or large thixotropy.

### **(3) Step Shear Test**

The sample is sheared homogeneously until no further changes occur. At that stage a sudden change in stress or shear rate is applied. The material should be assumed to be in equilibrium prior to the application of the jump. If the changes are not completely reversible, no real equilibrium exists. In most viscometers the kinematics are controlled rather than the stresses. Hence experiments with step changes in shear rate appear more frequently than stress changes [64].

One particular kind of step function is of special interest. It consists of a sudden drop in shear rate from a finite value to zero. The reversibility of thixotropic decay under shear can also be verified. The standard procedure has been to start the flow again after a given time of rest and measure the overshoot stress. A diagram of this stress versus time of rest provides the curve for thixotropic recovery [65].

### **(4) Oscillatory Test**

This test is to use the triangular shear rate history, especially sine wave [66]. The amplitude is taken sufficiently large to extend into the non-Newtonian region. The stress-shear rate relation describes a time dependent hysteresis.



### ***C. Experimental Works***

Jones and Brodkey [67] reported thixotropic behavior of a colloidal suspension. They designed a suspension with which set structural levels could be produced and viscometric data could be obtained without changing the structural levels. Before the measurement, the liquid of 1.4 wight percent colloidal Baymal (DuPont's colloidal alumina) in 96.2 weight percent propylene glycol and 2.4 percent water was sitting for 8 hours for complete viscosity recovery of the fluid after shearing. These works were to determine the behavior of the fluid at various structural levels, which were determined by shearing the liquid until equilibrium was established at the selected shear rate. The shear rate was changed rapidly enough so that no structural change could take place during the changing time. After a new stress level was reached, the shear rate was changed back to the initial level and the liquid was sheared until equilibrium was again established. They noted that those structure curves, often called "down-curves," obtained by progressively lowering the shear rate in a stepwise manner, could imply the structural change during the process. The equilibrium, structure, and initial shear stress curves for this suspension are shown in Fig. 2.4.

Another example of experiments for the structural approach was given by Chavan et al. [53]. They measured viscosity and shear stress changes in bentonite in water (5-15 wt.%) and  $\text{TiO}_2$  in linseed oil (40-60 wt.%) at constant shear rates as well as by step changes in shear rates. Several model equations for the suspensions were compared. They also applied Cheng's structural equations to obtain  $\alpha$  and  $\beta$ , Fig. 2.5.

Triliskii et al. [68] analyzed the rheological data of thixotropic materials in rather different ways. From the shape of flow curves, they regarded an anomalous region in the curves as the structural part, which reflects thixotropic behavior of the materials. Then shear stress for suspensions was written in two parts:

$$\tau = \tau^* + \eta_{\infty} \dot{\gamma} = \eta^*(\dot{\gamma}) \dot{\gamma} + \eta_{\infty} \dot{\gamma} \quad (30)$$

$$\tau^* = \eta^*(\dot{\gamma}) \dot{\gamma} \quad (31)$$

$\tau^*$  is regarded as the structural component of total shear stress which arises due to rupture of the thixotropic bonds which exists between the structural elements. The second part is Newtonian behavior of the liquid phase (solvent) or dispersion medium. Then viscosity was expressed as

$$\frac{\eta - \eta_{\infty}}{\eta_0 - \eta_{\infty}} = \exp \left( - \frac{\beta' W^*}{RT} \right) \quad (32)$$

where

$$W^* = \int_0^{\gamma_e} \tau^* d\gamma_e = \int_0^{\gamma_e} (\eta - \eta_{\infty}) \dot{\gamma} d\gamma_e \quad (33)$$

where  $\beta'$  is the degree of heterogeneity of the structure in the flowing system,  $W^*$  is the value of energy of the reversible strain accumulated in the conditions of steady-state flow as a result of thixotropic structural changes,  $\eta_0$  is the highest Newtonian viscosity, and  $\gamma_e$  is the value of the reversible deformation. They examined their theory for non-Newtonian systems with different classes: a low-molecular weight plastic dispersion, solution of a polymer in oil, and a filled polymer.

Chiu and Don [69] derived kinetic equations for thixotropic systems, assuming that a) the rupture of aggregates is proportional to some power of shear rate, while b) the growth of aggregates is due to the surface forces among particles and is independent of shear rate. Assuming that  $\eta(\dot{\gamma}) = \eta_{\text{agg}}(\dot{\gamma}) + \eta_{\infty}$ , they calculated viscosity change as a function of time, which depends on the shear conditions.

$$\frac{\eta(t) - \eta_{\infty}}{\eta_0 - \eta_{\infty}} = P(t) \quad (34)$$

They also showed that their equations fitted well the experimental data for a suspension of salt in HTPB with mono-modal and bimodal distributions of salt particles.

## **2.2. Rheological Behavior of Alloy and Composite Slurries**

### **2.2.1. Introduction**

Rheological properties may play an important role in classical metallurgical practices such as casting or forging. This is equally true in processes which involve semi-solid material-either an alloy slurry of primary solid particles and liquid phase for an alloy or a composite slurry of ceramic particulates with liquid metal. In "rheocasting," primary solid particles of an alloy are modified in their shape from dendritic to globular by a vigorous shearing at a solid-liquid coexistence temperature. Since the viscosity of this semi-solid alloy slurry is greatly reduced by the shearing and accompanying structural modification of the solid phase, it becomes much easier to cast or forge such material, resulting in some improved properties. It is then very critical to understand and control the rheological properties and related microstructures of the semi-solid alloy slurry. For alloy slurries, there have been many experimental reports on the rheological behavior and structural evolution resulting from parameters of the material and of processing. However, the attempts to find relationships between the viscosity and experimental parameters have not yet found a general formulation.

Another rheological problem in metallurgical processing is the fabrication of discontinuously-reinforced metal matrix composites via either compocasting or liquid metallurgy. As the amount of reinforcement in either a semi-solid alloy slurry or molten metal increases, the whole composite slurry becomes more viscous. The composite slurry may also have non-Newtonian, time-dependent viscosity. Although the importance

of this class of composite material is increasing, there have been few reports on the rheological behavior and microstructure of the material.

In the early part of this review, a short look at semi-solid processing is provided, and then a review of the rheological behavior of these alloy and composite slurries will be presented. It should be noted that 'semi-solid slurry' is used as a general term for both the semi-solid alloy slurry, and the composite slurry in the fully molten state or semi-solid state of the matrix alloy.

### **2.2.2. Castings of Semi-Solid Slurries**

#### **(1) Rheocasting [70-117]**

Flemings and his colleagues [70-72,83,88,93] have pioneered a casting process of metallic alloys to produce a unique cast structure with non-dendritic, globular primary solid phase. In this process, vigorous shearing is applied to a molten alloy as it cools into the solidification range. The shearing "breaks" the dendrites into individual round particles, which become more-or-less spherical by coarsening. The process is termed "rheocasting" and a schematic description of it is shown in Fig. 2.6. A casting becomes stiff when the solid fraction of primary phase is about 15% in conventional casting. However, the rheocast slurry maintains very low viscosity at much higher solid fractions, depending on the shear rate and cooling rate. This enables the slurry to be cast at a lower temperature and provides many advantages over conventional liquid casting such as reduced hot cracking [117] and reduced shrinkage.

## **(2) Thixocasting and Thixoforging [118-123]**

When the rheocast ingot is reheated to a temperature at which it is semi-solid, it still maintains the cast shape and becomes soft enough for further processing. Then the reheated ingot may be die-cast or forged to final dimensions with better microstructure and properties than those obtained by conventional processings.

## **(3) Compocasting [124-141]**

The rheocasting technique was extended to produce metal matrix composites. Since reinforcements such as ceramic particulates, short fibers, or whiskers have poor wettability to molten metals, it is very difficult to fabricate such MMCs by mixing reinforcements and liquid metal. However, the reinforcement may be incorporated into a semi-solid alloy slurry of a matrix formed by rheocasting. Once the reinforcements are introduced into the semi-solid slurry, they are entrapped mechanically by primary solid particles. Then the chemical interaction between the reinforcements and liquid matrix proceeds with time, and finally the reinforcements stay in the composite slurry.

## **(4) Other Semi-Solid Slurry Processes**

### *Flow Casting*

In a method developed by the Centro Ricerche Fiat in Italy [142], a molten alloy passes through a static mixing device with a series of small elements shaped as alternating left- and right-hand helicals. An electro-

magnetic linear drive pump is employed to feed molten alloy into the mixer by Lorentz force. It was pointed out that the mixing action was independent of the flow velocity, the degree of mixing being the result of repeated stratification and not of turbulent transport phenomena.

In another method, grain refinement was achieved by utilizing the turbulence induced during pouring a semi-solid metal into a multiple channel [143].

### *Superstircasting*

This process is based on mechanical shearing at very high rotation speeds over 1000 rpm under vacuum. It is claimed that the refinement of primary solid particle can be accomplished, combining controlled cooling, with less porosity and with more homogeneous size distribution [112].

### *Vortex Method*

This is one of the methods for fabricating discontinuously-reinforced metal matrix composites. The reinforcement is fed into a molten matrix alloy by a vortex induced around a stirrer. The surface of the reinforcement should be treated in some way to improve the wettability with the molten metal [144-147].

## **2.2.3. Viscosity of Liquid Metal**

Metals behave as Newtonian fluids when in the completely molten state. Hence there is no dependence of viscosity on deformation rate. Instead, the viscosity of liquid metal is a function of chemical composition and temperature. The importance of the viscosity of a liquid phase in a

semi-solid slurry process can be explained as follows. As solidification proceeds during cooling below the liquidus, the liquid phase becomes enriched in solute when the partition coefficient  $k$  is smaller than unity; while the liquid phase loses solute when  $k$  is larger than unity. Hence, correction of the viscosity of a liquid alloy with temperature, as well as composition, may be required.

For some metallic systems, viscosity values can be found in the International Critical Tables. A classical measurement on aluminum alloys was made by Jones and Bartlett [148], Fig.2.7. Viscosity of aluminum alloys increased very little with decreasing temperature and rapidly increased just above the liquidus temperature. It is interesting that the addition of magnesium among alloying elements increased the viscosity of the alloy above that of pure aluminum; silicon addition reduced viscosity below that of pure aluminum.

Some theoretical predictions on the viscosity of molten metal have been suggested [149]. In general, the following relationship is known to predict the dependence of viscosity on temperature:

$$\eta_L (T) = C \exp (E_a/RT) \quad (35)$$

where  $\eta_L$  is viscosity of the liquid at temperature  $T$ ,  $C$  is a coefficient determined by the kind of alloy,  $E_a$  the activation energy for viscous flow, and  $R$  is the gas constant. Since the viscosity of pure metals and alloys in the liquid state ranges from 1 to 4 cP in most cases, most of the viscosity increase in the semi-solid state can be attributed to resistance to flow from the solid particles.



#### 2.2.4. Alloy Slurry Systems

Partially solidified, vigorously agitated slurries of tin-lead alloys were first studied by Flemings and his students at M.I.T. in the early 1970s [70-72]. Their works produced many pioneering results and provided a standard procedure for the rheological study of alloy slurries. When an alloy is cooled below the liquidus temperature with no agitation, its viscosity begins to increase very rapidly and it becomes almost like a solid when the volume fraction of primary phase of the alloy reaches about 0.15. If the alloy is sheared at a given deformation rate during solidification as in rheocasting, the alloy in the semi-solid state can then acquire quite a low viscosity. The deformation enhances the changes in morphology of solid phase. Hence, the resistance to the viscous flow, or viscosity, is greatly reduced. In the process, the viscosity of a alloy slurry is influenced by many variables, such as shear rate, cooling rate, solid fraction, shape and size of solid particles, shearing time, etc. In general, the apparent viscosity of a alloy slurry increases with increasing volume fraction solid, increasing cooling rate, and decreasing initial shear rate. Furthermore, the relative change in viscosity due to the variation of cooling rate and shear rate increases drastically at higher volume fraction solid. Moreover, these variables affect each other: for example, faster cooling results in smaller particle size with less sphericity, which increases viscosity. The qualitative effects of variables are summarized in Table 2.3. It should also be noted that the alloy slurries exhibit a complicated time-dependent phenomenon, which is called thixotropy.

### (1) Effect of Volume Fraction Solid on Viscosity

Many theories on the viscosity of suspensions can be expressed as a power series of volume fraction of second phase:

$$\eta_r = \eta_a / \eta_o = 1 + k_1 g_s + k_2 g_s^2 + \dots \quad (36)$$

where  $\eta_o$  is the viscosity of the suspending medium without particles, and  $\eta_r$  and  $\eta_a$  are the relative and apparent viscosities, respectively [13]. A plot of this expression shows a slow rise at low fraction solid and a fast rise at high fraction solid. The apparent viscosity can also be expressed by an equation of the form:

$$\eta_a = A \exp [B g_s] \quad (37)$$

For Sn-15%Pb this type of equation was fitted to continuous cooling data at fractions solid of over 0.2 and the coefficients A and B were dependent on cooling rate at a given shear rate [72,73,97]. This type of relationship is well known in conventional suspensions as part of the Thomas equation for the relative viscosity and concentration of suspensions.

Chijiwa and Fukuoka [76] measured the viscosity of Sn-15%Pb alloy in the semi-solid state. Up to a volume fraction solid of 0.4, they made an attempt to fit their data to an equation which they obtained from the suspensions of polyethylene pellets or glass beads in solvents of glycerol. Particle size ranged from 0.1 to 3 mm, which was reflected in the constants in the equation:

$$\eta_r = (1 - 2.5 \phi - a_1 \phi^2 + a_2 \phi^3)^{-1} \quad (38)$$

where  $\phi$  is volume fraction solid of the suspension. The constants were determined by experiments:  $a_1 = 0.171 \log d + 3.5$ ,  $a_2 = -0.85 d^{-1} + 13.3$ , and  $d$  is the particle diameter in millimeter. When a slurry of Sn-15%Pb at volume fraction solid of 0.4 to 0.8 was extruded, the liquid phase exuded.

## (2) Effect of Alloying Elements on Viscosity

The viscosities of metal alloys can be affected by the kind and amount of alloying elements [84,96]. The differences were attributed to cooling rates in the semi-solid region, crystallization rate, and the size and shape of primary solid particles. Another effect of alloying elements is the density difference of the solid and liquid phases of an alloy. In general, when the density of the solid particles is greater than that of the suspending medium, the viscosity increases with increasing particle density.

### *Hypoeutectic Alloys*

Shibutani et al. [84] reported the measurement of viscosity for various binary alloys with initial compositions, either below the solid solubility limit or between the solid solubility limit and the eutectic composition. Depending on the initial composition, the calculated volume fraction solid at the eutectic temperature,  $g_S(E)$ , by the Scheil equation can vary from 0.2 for the alloys with  $C_{SM} < C_o < C_E$ , such as Fe-4%C and Sn-45%Pb, up to 0.98 for those with  $C_o < C_{SM}$ , such as Sn-1.0%Pb. In the first case they showed that the fraction solid at which the viscosity rapidly increased was dependent on the initial composition or  $g_S(E)$ . They pointed out, however,

an exception that the viscosity of Sn-15%Pb alloy could increase more rapidly even under 0.4 of solid fraction. The viscosity for alloys with  $C_0 < C_{SM}$  increased very slow with cooling down to  $g_S = 0.5$ , and then rapidly increased at higher solid fractions. Under similar conditions of cooling rate and shear rate, the measured viscosity for Sn-1.0%Pb was about 1.0 poise and that for Sn-1.5%Pb was about 5 poise at the same fraction solid of 0.6.

The addition of copper in Al-Cu alloy also increased the viscosity of the semi-solid slurry of the alloy [80,105,112]. For Al-Si alloys [89], the primary solid became finer under shearing with increasing silicon content for  $C_{SM} < C_0 < C_E$ , and the viscosity increased with increasing silicon content. One question is why the same alloy system with different solute contents could show different viscosity in the semi-solid state at a given volume fraction solid, and more evidently at the higher fraction solid.

### *Eutectic Alloys*

Kayama et al. [77] reported that in the initial stage of the eutectic reaction the viscosity increase was very sluggish, then rapidly increased 10 min after reaching the eutectic temperature. Shibutani et al. [84] also observed the same trend in viscosity change at eutectic temperature. They attempted to calculate the solid fraction at which the rapid increase of viscosity occurred during the eutectic reaction. Yet the mechanism for this phenomenon is not clear.

For eutectic Al-Si alloy, the eutectic became massive and grew coarser as the eutectic reaction proceeded, and the torque value increased very slowly in the initial stage followed by a rapid increase in the later stage with the progression of the reaction [89,102].

### *Hypereutectic Alloys*

In the hypereutectic Al-Si alloys [89], the torque value remained at a low level, as for the fully liquid state as the volume fraction of Si crystals increased, and then rapidly increased in the later stage of the eutectic reaction. For hypereutectic Al-Cu alloys, the apparent viscosity decreased with increasing copper content [106].

### *Multi-Component Alloys*

For some multi-component alloys, few data have been reported, and yet the interpretation of data has not been clear [84]. The differences in viscosity due to various alloying elements were roughly attributed to cooling rates, the crystallization rate, and size of the primary solid [104]. When a grain refiner is added, the apparent viscosity increases due to the refinement of primary solid particles [106].

### **(3) Effect of Shear Rate and Shearing Time on Viscosity**

The viscosity of an alloy slurry decreases with increasing shear rate (Fig. 2.8). This behavior is known as pseudoplasticity or shear-thinning. The shear rate dependency of viscosity in thixotropic slurries results from the formation and breakdown of structural linkage between the particles of the slurry. At low shear rates, many bonds form between particles, and viscosity is high. At high shear rates, structural linkages between particles are broken down and resistance to flow is thereby reduced (shear thinning phenomenon). Moreover, under isothermal conditions, the viscosity decreases with time from an initial peak to an equilibrium level, which is called a steady state. At steady state, equilibrium exists between

the rate of formation and destruction of linkages between particles and viscosity is constant. At a given cooling rate, the solid particles in alloy slurry changes their size and shape with time by shearing. Hence the viscosity of the slurry is dependent on both shear rate and shearing time.

According to Joly and Mehrabian [72], the viscosity was more influenced by shear rate at higher cooling rates than at lower cooling rates in Sn-15%Pb slurry. The high viscosity of slowly stirred slurries compared with the much lower viscosities of rapidly stirred slurries was explained in terms of the buildup of clusters of solid particles at low shear rates and the breakup of these clusters when the shear rate was increased.

In metal slurries, the viscosity at a given volume fraction solid and cooling rate decreases with increasing shear rate [72,83,84,104,105]. This can be expressed by a classical power-law equation:

$$\eta_a = k' \dot{\gamma}^{n'} \quad (20)$$

where  $\dot{\gamma}$  is shear rate and  $n'$  is defined as  $n'=n-1$ , and  $-1 < n' < 0$  for a pseudoplastic material.  $n$  is also a function of solid fraction [83,108]. For Zn-27%Al slurries, values of  $n$  ranged from -0.5 to -0.7 [97]. Mori et al. [96] examined an Al-4.5%Cu alloy stirred during solidification with stirrers of two different shape: a paddle or a columnar rotor. The apparent viscosity,  $\eta_a$ , of the slurry was approximated by the following equation.

$$\eta_a = A N^{-1.8} \epsilon^{0.6} \exp(13g_s) \quad (39)$$

where  $A$  is a constant depending on stirrer shape (1.8 for paddle and 0.9 for columnar rotor),  $N$  is number of rotations per second,  $g_s$  is volume fraction

solid and  $\epsilon$  is cooling rate (K/s). As the rotation speed increased, the apparent viscosity decreased. Furthermore, the value of apparent viscosity in hypereutectic Al-Si alloys at high speeds above 30 rev/s remained almost unchanged to a certain level except a rapid change in the initial stage of solidification with cooling rate of 0.6 K/s [104].

The pseudoplasticity is also dependent on the initial shear rate as proven in Sn-15%Pb system and shown in Fig. 2.9 [72]. This means that the initial microstructure is determined by the initial shear rate. Since it is assumed that the structural feature should be preserved to obtain a structural curve for shear-thinning behavior, each curve reflects a different level of structure [67].

#### **(4) Effect of Cooling Rate on Viscosity**

In case of slurries of metal alloys, the cooling rate in the liquid-solid coexistence region is an important factor affecting viscosity. In general, the viscosity decreases as the cooling rate decreases, that is, as the total time spent in the liquid-solid region increases [72]. Furthermore, the change in viscosity due to variations in cooling rate and shear rate increases drastically with increasing volume fraction solid. At a given shear rate, the viscosity decreases as the cooling rate decreases, which is directly related to the increased total resident time spent in the liquid-solid region. To show the relative change in measured viscosity as a function of cooling rate, initial shear rate, and volume fraction solid, a composite plot of some the data from the above figures is presented in Fig. 2.10.

### **(5) Effect of Size and Shape of Solid Particles**

It has been well acknowledged that the viscosity of an alloy slurry is strongly dependent of the size and shape of the primary solid particles, which are resulting directly from shear rate or cooling rate, etc. [72,80,83,90,96]. The relationship of apparent viscosity with the shape and size of solid particles can be more simply explained in terms of the surface area per unit volume of solid particles,  $S_v$  [15,72,108]. As the value of  $S_v$  increases, the resistance of the particles to flow increases, so that the apparent viscosity of the system increases. An example of this parameter is given in Fig. 2.11 for Bi-17%Sn system [108].

#### *Effect of Shape of Solid*

Flemings and his colleagues [70-72] have shown that the viscosity of semi-solid slurries depends on the sphericity of the primary solid particles. Particles that are semi-dendritic produce slurries of higher viscosity than those that are more nearly rounded. The semi-dendritic particles have higher surface area/volume ratio than round particles. Although the size of a particle decreases as cooling rate increases, particles tend to retain the dendritic shape, which increases the viscosity at a given shear rate. Hence, the shear rate should also be high at higher cooling rates if spheroidal, or nearly spheroidal, particles are to be obtained.

Doherty et al. [79] observed that the shape of the primary solid phase in Al-20~30wt%Cu changed from conventional dendritic via rosette-type to a spherical structure with increasing shear rate and stirring period. This trend has been confirmed in other papers [72,103]. This proves that a coarsening process takes place during the isothermal hold, just as in the unsheared samples [94]. It was suggested that coarsening is accelerated by



faster solute transport that results from forced convection by shearing [79]. The amount of liquid entrapped in the particles decreases as the specific surface area of a particle decreases with coarsening [72]. This means that the relative volume of solid occupying the system becomes less and less, which, in fact, causes the same effect as decreased solid fraction, and reduces the apparent viscosity of the slurry.

#### *Effect of Size of Solid*

As cooling rate increases, particle diameter decreases at a rate roughly inversely proportional to the cube root of the time spent in the solid-liquid region. This results in an increase of the apparent viscosity of the slurry at a given shear rate due to higher values of the surface area/volume ratio than for larger particles at a given solid fraction [71]. Weltman and Green [150] also found that the viscosity of pigment suspensions rose with decreasing particle size for a fixed volume fraction of suspended particles. The size of primary solid particles increases with increasing volume fraction solid and decreasing cooling rate. Increasing shear rate always reduces the amount of entrapped liquid, possibly due to coarsening, within the primary solid particles, and reduces the size of primary solid particles in the case of slow cooling.

#### *Effect of aggregation*

Aggregation of particles always results in higher viscosity. This is primarily due to the increase of effective volume fraction solid as more and more liquid is entrapped in the aggregates. Mori et al. [96] treated the effect of coupling of primary solid particles on the viscosity in rheocasting of an Al-Cu alloy. They found that the viscosity increased as the the ratio of the

number of fine quasi-spherical primary solid particles to that of coupled particles increased.

#### **(6) Thixotropic Behavior**

Spencer et al. [70] reported that a partially solidified slurry of Sn-15%Pb exhibited a shear-thinning phenomenon, or pseudoplasticity. They explained this in terms of the size and shape of the primary solid particles in the slurry. It was found that with increasing shear rates these particles became ellipsoidal in shape and were oriented in the flow direction. While it was recognized that this phenomenon could be ascribed to the thixotropy of the material system, few controlled dynamic experiments were carried out to verify this fact.

These works were succeeded to Joly and Mehrabian [72] to verify, expand, and explain these previous observations. A model alloy of Sn-15%Pb was gradually brought to a specified temperature in the liquid-solid region. After the torque attained a constant steady state value, the hysteresis loops were generated to study the thixotropy of the system by using the Green-Weltmann method [63].

The viscosity decreases with increasing shear rate and is time-dependent. This behavior, in nonmetallic slurries, is usually assumed to result from a buildup of "structure" within the slurry [151]. In the case of partially solid metal slurries, it has been assumed that this is due to partial "welding" of the primary solid particles, which occurs to a greater extent the longer the time and the lower the shear rate. Fig. 2.12 shows experimentally determined hysteresis loops of a 0.45 volume fraction solid slurry of the alloy and some well-known nonmetallic thixotropic materials

[72]. The areas of the loop for honey and epoxy + 2.95%SiO<sub>2</sub> are of the same order of magnitude as that for the metal slurry (i.e., 10<sup>5</sup> to 10<sup>6</sup> dyne cm<sup>-2</sup> s<sup>-1</sup>).

Doherty et al. [94] observed that a alloy slurry of Al-15wt%Cu alloy at  $g_s=0.4$  exhibited an "ultimate shear strength,"  $T_{max}$ , before a new steady state (Fig. 2.13). The maximum stress was strongly dependent on the time of rest of the pre-sheared slurry. The shape of primary solid phase of the alloy affected the value of the maximum stress. The increase in the stress was interpreted from microstructural coarsening of solids during the rest. The clustering reaction was faster in a slurry with a larger amount of solid-liquid interface as in rosette-type solid particles.

## **(7) Theoretical Works**

For conventional suspensions, many theoretical models on thixotropy have been proposed [52]. In the case of alloy slurries, however, works have been mostly empirical. The difficulties in the latter slurry system result from the very complicated microstructural evolution in the system during shearing, which includes the change in the size and shape of the solid phase. Recently, the thixotropy of semi-solid alloy slurries was modeled by Brown [114]. He used a structural kinetic approach suggested originally by Cheng and Evans [55]. The essence of modeling a metallic semi-solid slurry lies in defining a constitutive equation for the structural evolution with readily available parameters.

### **2.2.5. Composite Slurries**

In compocasting or the vortex method, the incorporation of a poorly wettable reinforcement can be accomplished through very careful consideration of fluid flow of the stirred slurry or liquid. The viscosity of a slurry or liquid may affect: a) the introduction of the reinforcement into the flow, b) then, the retention of it in the flow, and c) the amount of porosity which is introduced by particles during the incorporation. Viscosity is more directly related to an optimum condition of fluid flow for the incorporation in the Reynolds number [147,152]. Although there have been many studies on viscosity in rheocasting, limited information is available on viscosity in compocasting. It was found [133,140,141] that the viscosity of the semi-solid slurry changes with volume fraction, shape, and size of the reinforcing phase in addition to those factors affecting viscosity in rheocasting, such as shear rate, stirring time, volume fraction, and cooling rate.

#### **(1) Metal Matrix Composite with the Matrix in Fully Molten State**

Recently, Girot [133] measured the apparent viscosity of aluminum alloys with and without SiC whiskers or short fibers. He confirmed that: a) there is a strong effect of the alloying elements on the viscosity, b) addition of the reinforcements leads to a significant increase in the viscosity of a composite slurry, and c) as the axial ratio of the ceramic particles becomes high, viscosity increases tremendously.

Loué and Kool [140] observed pseudoplasticity of the composite system 25wt%SiC(44 $\mu$ m)/Al-7%Si-0.3%Mg with the matrix in the fully molten state

while the fully molten matrix alloy behaved as a Newtonian fluid. Contrary to Loué and Kool's observation, Mada and Ajersch [141] commented that there was no shear rate dependence of viscosity when similar composites of 10 to 20  $\mu\text{m}$  SiC with 10 to 20% by volume were tested with the matrix in the fully molten state. They supposed that the particles of silicon carbide were very well dispersed, so that the aggregation of the particles was not a factor.

## **(2) Metal Matrix Composite with the Matrix in Semi-Solid State**

As a composite slurry is cooled into semi-solid region of the matrix alloy, the whole system becomes one having three components: primary solid phase of the matrix ( $\alpha$ ), matrix alloy liquid (L), and reinforcing particles (SiC). The primary solid particles are often hundreds of microns in diameter, while the reinforcing particles may be much smaller. Hence, it is very interesting to consider the effect of the presence of the smaller reinforcement on the morphology of the primary solid particles as well as on the rheological behavior of the total system. One possibility is that the much smaller reinforcement may be entrapped instead of liquid phase in the primary solid, which causes the same effect of decreasing total solid fraction and reducing viscosity.

Loué and Kool [140] reported a thixotropic behavior of an Al-7Si-0.3Mg alloy with or without SiC particulates of 44  $\mu\text{m}$  with the matrix alloy in the semi-solid state. Mada and Ajersch [141] investigated the rheological behavior of rheocast composites of Al-7%Si-0.3%Mg alloy (A356 aluminum alloy) with silicon carbide of 10 to 20  $\mu\text{m}$ . They supposed that the thixotropy of these materials was due to the changes in inter-particle and inter-aggregate bonding in the primary solid particles of the matrix. The

degradation of the bonds with shearing reduced the viscosity to a dynamic equilibrium value for a shear rate where the destruction and reconstruction of particle-agglomerate bonds reached a steady state. They also observed that the dynamic equilibrium was reached more rapidly with higher shear rates. The kinetics of the degradation of agglomerates were nearly independent of the concentration of silicon carbide particles, especially at high shear rates. The structural degradation of agglomerates, however, was highly dependent on the volume fraction of primary particles of the matrix.

#### **2.2.6. Theoretical Treatments**

The rheological behavior of discontinuously-reinforced composites in the fully-molten state can be treated in the same way as conventional suspensions. Contrary to fully molten metals, composite slurries in the fully molten state exhibit non-Newtonian behavior, which depends on the rate of deformation [140]. It should be noted that the reinforcing phase in the molten matrix metal maintains its shape and volume fraction, while primary solid particles in metallic slurries change their shape, size, and volume fraction with processing conditions as described in the previous chapter.

In the prediction of the dependence of viscosity on the volume fraction of particles, we may choose appropriate relationship(s) from among many equations. For very dilute suspensions, Einstein theoretically derived the relationship between the relative viscosity of a suspension and the volume fraction of solid particles suspended. Since the equation does not fit the experimental results for suspensions with higher volume fractions, many

other formulations have been proposed from theories or experiments. However, the equations do not agree with each other. Moreover, at very high concentration, the deviation of the equations from the observed values becomes so large that some other relationships have been more suggested. At high concentrations, the viscosity depends not only on the volume fraction, but also on the shape and size distribution of particles (e.g., eqn.(9)).

### 2.2.7. Fluidity of Slurries

#### (1) Metallic Slurries

From a practical point of view, the fluidity data of a rheocast slurry may be useful. Pai and Jones [85] measured the extent of solidification-limited flow of stirred Sn-15%Pb slurries along a defined channel under gravity. They found that the following relationship for the fluidity index of the alloy slurries.

$$Y_f = A \cdot g_L^2 \quad (40)$$

where  $Y_f$  is a fluidity index defined as the length of slurry flow in the channel,  $A$  is a constant, given by  $B \cdot t_D^p \cdot r_o^q$ ,  $t_D$  is delay time before pouring,  $r_o$  is mold radius, and  $g_L$  is volume fraction liquid. Their analysis, however, neglected the effect of stirring speed.

In another fluidity study by Assar et al. [86], more systematic measurements on the fluidity of Al-10%Cu alloy were performed. The fluidity was determined by the length of extracted bar in a copper tube.

Then, they obtained a modified relationship for the fluidity with an index  $n$  dependent on stirring speed,  $N$ , as shown in Fig. 2.14:

$$Y_f = (\text{constant}) f_L^m \quad \text{and} \quad m = (\text{constant}) N^{-2} \quad (41)$$

From the microstructures of the solidified rods, they concluded that the improvement in fluidity was due to the refinement of primary particles and reduction of agglomeration at high stirring speed.

It should be noted that the fluidity study is different from viscosity measurement since the first always involves complete solidification of slurry, while the latter does not. Also, the fluidity index taken in these experiments can not be the reciprocal of viscosity.

## **(2) Composite Slurries**

Surappa and Rohatgi [144] have observed that the spiral fluidity decreased as a result of additions of alumina, mica, and graphite particles of size 40 to 200  $\mu\text{m}$  to aluminum alloy melts. Also, the fluidity decreased with a decrease in the particle size for a given weight percentage of the particle. The decrease was attributed to the increased surface area of particulates, which provided more resistance to the flow. The fluidity,  $F$ , and the surface area of particulates,  $S$ , present in a unit weight of the composite were presented by a simple linear relationship:

$$F = a_1 - a_2 S \quad (42)$$



where  $a_1$  and  $a_2$  are constants determined by pouring temperature (Fig. 2.15). This figure also indicates that smaller particles induced more resistance to flow, and hence caused lower fluidity than the larger ones at a given volume concentration.

#### **2.2.8. Summary**

The viscosity of both an alloy in the semi-solid state and composite slurries is an important property for controlling of some processing methods such as rheocasting, thixocasting, and compocasting. These slurries exhibit non-Newtonian behaviors such as shear-thinning and thixotropy. The relationships of apparent viscosity of an alloy slurry with processing and material parameters have been understood by combining microstructural features and viscosity. On the other hand, the study of rheological behavior in composite slurry is still in its initial stage while interest in these composite materials is growing rapidly.

## CHAPTER 3.

# EXPERIMENTAL METHODS

### 3.1. Materials

#### 3.1.1. Matrix Alloy

As a model alloy, a nominal Al-7wt%Si binary alloy was chosen. The reasons for this choice are: (a) The reaction of silicon carbide with aluminum matrix alloy can be reduced by the presence of silicon in the liquid phase so that the chemical dissolution of silicon carbide is expected to be a minimum [153,154]; (b) The wettability of silicon carbide with liquid aluminum alloy could be improved [155]. These two factors are very important in the fabrication of the silicon carbide reinforced metal matrix composite; and finally, (c) The chemical composition is close to some commercially important aluminum alloys such as A356 or A357 other than a small addition of magnesium.

A pure binary Al-6.51wt%Si alloy was cast. The raw materials for the preparation were 99.9wt% pure aluminum and 99.9wt% pure silicon. The chemical analysis of Al-6.5wt%Si binary is listed in Table 3.1. The volume fraction of primary solid phase ( $\alpha$ ) was calculated by the Scheil equation (more detail in Appendix 1) and shown in Fig. 3.1 with the phase diagram of Al-Si binary alloy.

### **3.1.2. Ceramic Particulates**

High-purity silicon carbide (SiC) particulates were chosen as ceramic particulates. These ceramic particulates are the most prospective particulate reinforcements in metal matrix composites due to their low cost and beneficial properties. The shape of these particulates, provided by Norton Company in Worcester, Massachusetts, is shown in Fig. 3.2. A typical chemical analysis of the particulates is listed in Table 3.2. The analysis of particle size distribution was conducted by a Coulter counter TA II at Norton Company. Fig. 3.3 is a result of size analysis for HP 600 Grit particulates of average size 8.5  $\mu\text{m}$  by volume with monomodal size distribution.

### **3.1.3. Composite Preparation**

For the fabrication of ceramic particulate reinforced metal matrix composites, two different routes were taken: a) Compocasting method and b) Pressure infiltration/dilution method.

#### **(1) Compocasting Method [124]**

A semi-solid alloy slurry was prepared by vigorously stirring the alloy at a temperature between the liquidus and eutectic temperature of the alloy. Argon was used to cover the surface of the slurry during the process. Then a measured amount of silicon carbide particulate was fed at a fixed rate into the slurry. After finishing the particulate feeding, the slurry was continuously stirred for a certain time to enhance metal-to-ceramic wetting. Then, the composite slurry was superheated above the liquidus

temperature of the matrix while stirring was continuing. Finally, the molten composite slurry was cast into a bar in a graphite mold.

It was found from the casting practice that not all kinds of aluminum alloys were suitable for the compocasting method. In an Al-4.5wt%Cu alloy, for example, oxidation on the surface of the slurry caused extremely poor wetting of silicon carbide particulates with the matrix slurry. On the other hand, as expected from the wettability data sources, Al-Mg alloys were appropriate for this route.

## **(2) Pressure Infiltration/Dilution Method [156]**

This process consists of two stages: first, pressure infiltration of ceramic particulates compact to produce a highly-packed composite, and then dilution of the compact.

### *Step 1. Pressure Infiltration :*

Ceramic particulates and matrix alloy were weighed and packed into a mold (an alumina crucible), Fig. 3.4. The mold was put in a pressure chamber, Fig. 3.5. After sealing the chamber, it was evacuated during the heating cycle up to 730°C. Then a pressure of 1000 psi (6.9MPa) was applied inside the chamber by argon gas. The molten alloy was fully infiltrated into ceramic particulate-packed bed in a few minutes. While maintaining the initial pressure, the composite compact was cooled below the eutectic temperature of the matrix. In this cooling stage, the alumina crucible was put onto a chill at the bottom of the chamber to promote directional solidification. An example of the pressure-infiltrated SiC<sub>p</sub>/Al-7wt%Si compact is shown in Fig. 3.7(b). According to an area fraction measurement on the surface of these infiltrated composites, the volume fraction of ceramic particulates was about 55%.

### *Step 2. Dilution :*

The pressure-infiltrated composite compact was sectioned and weighed to make the final concentration of ceramic particulate after dilution with an addition of the matrix alloy. After a pre-measured amount of matrix alloy was molten, the high-concentration composite compact was added to the molten alloy. The slurry was sheared by an impeller to break down the compact until a satisfactorily fine dispersion of particulates was obtained. Then the diluted composite slurry was cast with a superheat. An apparatus for the dilution is shown in Fig. 3.6.

This process was tested with various aluminum alloys. An example of a diluted composite of 20 vol%SiCAl-7wt%Si is shown in Fig. 5.1. It was found that those compacts of SiC in a matrix such as Al-Cu or Al-Mg alloy were found to be too hard to be dispersed into a lower volume fraction. The composite compact of Al-7wt%Si matrix was relatively easy to be dispersed. The hardness of the composite compacts with various matrices was attributed to the formation of aluminum carbide caused by the dissolution of the silicon carbide particulates into silicon and carbon.

## **3.2. Experimental Apparatus**

A schematic description of experimental apparatus for the study of rheological behavior of the metallic and composite slurries is shown in Fig. 3.8. It consists of three major parts.

### **(1) Temperature Control**

Two resistance heaters were controlled separately to provide a more uniform thermal profile in the viscometer: 2-1/2-inch long and 6-inch long heating elements. The actual temperature of the sample material was measured by a thermocouple inserted into a gap through the wall of graphite crucible in the middle of the length of the inner cylinder. Hence the temperature measured by this thermocouple was close to the actual metal temperature within two degrees. In this way the sample temperature was controlled within  $\pm 1$  K in the case of isothermal conditions.

## **(2) Driving Part**

Two kinds of motors were used, depending on the speed of rotation. One was a series-wound direct-current motor (maximum 10,000 rpm) for high-speed operations and the other was a shunt-wound geared motor (15-500 rpm) for low speed operations. For the series motor the speed was controlled by a digital controller (Digi-Lok®) coupled with a magnetic pickup and teeth wheel. The speed of the motor was preset by a thumb wheel and the set speed was reached within less than five to ten seconds after switch-on. For the geared motor, a stroboscope was used to synchronize the speed of motor with the frequency of light pulses from the stroboscope. An optical torque transducer, shown in Fig. 3.9 (Vibrac® model T3), was used to measure the torque applied on the surface of the inner cylinder or the rotor. The maximum torque measurable by this transducer is  $2.26 \times 10^{-1}$  N·m with a safety factor of 100%. The optical torque transducer was connected to the shaft of the motor. The rotor is then connected to the torque transducer. Flexible couplings of stainless steel were used for the connections of the motor to the torquemeter and the

torquemeter to the rotor shaft. These couplings can compensate for minor misalignments along the rotating shafts. Two rotational bearings were used to reduce friction and wobbling from the shaft and rotor.

### **(3) Recordings**

A torsion detected by the optical torque transducer was transferred to a digital torque readout (Vibrac® model TM72-18) and then recorded on a chart recorder. The temperature from the monitor thermocouple inside the wall of the graphite crucible was also recorded on the same chart so that the changes in torque with time and temperature were simultaneously obtained.

## **3.3. Viscometer**

### **(1) Rotational Viscometer**

The rotational viscometer used for measurements of apparent viscosity (Searle-type viscometer) consists of two concentric cylinders, Fig. 3.10. A sample material was deformed by Couette shear. All the cylinders were made out of graphite (the most non-reactive material with aluminum alloy is zirconia). To prevent excessive oxidation of carbon at high operating temperatures, the viscometer chamber was filled with high-purity argon. The dimension of stationary outer cylinder (crucible) was fixed to  $4.0 \times 10^{-2}$  m in diameter and  $1.5 \times 10^{-1}$  m in height. Two diameters for the rotating inner cylinder (rotor) were used:  $3.2 \times 10^{-2}$  m and  $3.6 \times 10^{-2}$  m. Therefore, the ratios of the inner radius to the outer radius,  $\beta$ , were 0.8

and 0.9 for each dimension, respectively. These ratios were to provide fairly linear velocity profiles across the gap [160]. The average shear rate across the gap between the two cylinders was controlled by DC motor speed as well as by the size of the cylinder gap ( $4 \times 10^{-3}$  and  $2 \times 10^{-3}$  m). A case-hardened steel shaft of 1/4-inch diameter was connected to the inner cylinder. An alumina tube was put on the shaft to protect it from dissolving into the aluminum alloy. The shaft was then connected to an optical torque transducer. The twist angle of shaft was detected by an optical mechanism, and the signal was transferred to a digital readout and a chart recorder. The viscometer was calibrated with a U.S. National Institute of Standards and Technology oil (standard number S-600). The correlation factor between the standard and measured values was 0.95 between room temperature and 373 K, Fig. 3.11.

## **(2) Data Analysis**

The measured torque was considered to be that applied on the inner cylinder during shearing. Only the apparent viscosity was obtained from the measured torque and the given shear rate. The zero level of torque value was determined with the rotor rotating without a sample in the viscometer at operating temperature. In this way, the torque induced by causes other than the shearing of the sample material could be excluded from the torque measured with a sample. The shear stresses and average shear rates were calculated by using the following expressions derived from the Navier-Stokes equations for Newtonian fluid flow. (More details of the derivation are given in the Appendix 2):



Shear Stress: 
$$\tau = \frac{M_1}{2\pi R_1^2 L} \quad [\text{Pa}] \quad (43)$$

Average Shear Rate: 
$$\dot{\gamma} = \dot{\gamma}_{\text{average}} = \frac{2\beta}{1 - \beta^2} \Omega_1 \quad [\text{s}^{-1}] \quad (44)$$

Apparent Viscosity: 
$$\eta_a = \alpha \frac{\tau}{\dot{\gamma}_{\text{average}}} \quad [\text{Pa}\cdot\text{s}] \quad (45)$$

where  $M_1$  is the torque applied on the inner cylinder (N·m),  $R_1$  is the radius of the inner cylinder (m),  $L$  is the length of the inner cylinder (m),  $\beta$  is the ratio between the inner and the outer cylinder radii,  $\Omega_1$  is the angular speed of the inner cylinder in rad/s, and  $\alpha$  is the calibration factor for the viscosity, 0.95. The unit conversion for viscosity are  $1\text{Pa}\cdot\text{s} = 10 \text{ Poise} = 1000 \text{ cP}$ .

### (3) Major Sources of Error

#### (a) The dimension of shearing gap:

The clearance of the gap between the two cylinders is determined by the accuracy of the two radii and the stability of the rotation of the inner rotor. The rotor can be machined with the best accuracy while the instability of the gap clearance is unavoidable due to wobbling. The more difficult problem is the alignment of the rotating parts and crucible center. It was found that the gap width can vary  $\pm 5\%$  of the 2 mm around the rotor.

#### (b) Temperature profile in the shearing gap:

The length of the uniform temperature zone along the length of the gap may affect the local homogeneity of alloy slurry in terms of volume fraction of the primary solid phase. Under isothermal conditions, the temperature difference between the middle and top part of the gap was within two degrees, which may cause an error in the volume fraction solid of an alloy at a lower temperature range. When a sample is under continuous cooling, there may exist a temperature difference across the shearing gap. This is because the outer surface of the viscometer cools faster than the inside chamber.

(c) Readout Accuracy:

According to the manufacturer's manual for the digital torque readout (Vibrac® model TM72-18), the overall readout accuracy is  $\pm 0.5\%$  of full-scale and torque transducer accuracy. The overall accuracy of the torque transducer is  $\pm 1\%$  of full-scale.

### 3.4 Experimental Approaches

The rheological behavior of the alloy slurries in the semi-solid state and metal matrix composite with the matrix in the semi-solid state is greatly dependent on the thermal and shear history of the sample, as well as the material characteristics. By combining these histories, the rheological behavior of the slurries can be investigated. Hence, the experimental parameters should include:

(a) Material variables : the chemical composition of the matrix alloy, the volume fraction of primary solid phase, and the size and volume fraction of silicon carbide particulates.

(b) Process variables: average shear rate and initial shear rate, shearing time, temperature of the slurry, cooling rate, and the rest time of a sample after a shearing.

#### **3.4.1. Continuous Cooling Condition**

In the first type of thermal history, a molten sample alloy or composite was cooled continuously until it solidified at a fixed cooling rate from the molten state to the eutectic temperature with shearing, Fig. 3.12 (a). The average cooling rate was obtained by measuring the time from the liquidus temperature to the eutectic temperature of the alloy. In the present apparatus, the maximum average cooling rate was about 0.075 K/s when the power for the heating elements was turned off. Another average cooling rate of 0.0083 K/s was used for slow cooling by manually lowering the temperature in several steps. Three levels of average shear rates were applied: 180, 540, and 900 s<sup>-1</sup>. In the continuous cooling experiments, after a sample was sheared to the completion of solidification, the crucible was taken out and quenched. Metallographic samples were cut from the top, middle, and bottom parts and compared to check for settling of solid phase(s).

#### **3.4.2. Isothermal Condition: Isothermal "Steady State"**

After a sample alloy or composite was molten in the viscometer, the alloy was cooled at a fixed cooling rate with shearing, Fig. 3.12(b). The average cooling rate was obtained by measuring the time taken from the liquidus temperature to a specific temperature in the semi-solid region for

the alloy. After the target temperature was reached, shearing was continued until the shear stress level stabilized at a constant level, which is often called a "steady state" or equilibrium. The isothermal shearing time,  $t_2$ , was referred to the time for the shearing under isothermal conditions. Three levels of average shear rate were also taken to compare the effect of various shearing rates: 180, 540, and 900  $\text{s}^{-1}$ . It is referred to the "equilibrium curve" when the shear stress is plotted against the shear rate. In this plot each datum represents a structure of the slurry fully established at the steady state by the process variables taken.

In the isothermal experiments, a sample was sheared until a steady state, after which the rotor was raised and metallographic samples were taken.

### **3.4.3. Approach for Non-Newtonian Behavior**

To investigate the non-Newtonian pseudoplastic behavior of a slurry, it should be kept in mind that the microstructure of the slurry must be the same for each shear rate. Since the microstructure of a slurry can be determined by the initial shear rate,  $\dot{\gamma}_0$ , with other factors fixed, then the flow curve for the semi-solid slurry should be dependent on the initial shear rate, which determines the initial microstructure. Again, the equilibrium curve does not meet this condition to identify the shear rate dependency of viscosity. The most convenient way to preserve a steady structure of a slurry is as follows:

- First, a steady state is established after an initial transient stage at the initial shear rate,  $\dot{\gamma}_0$ .
- Then a new shear rate is applied without stopping shearing. The second shear rate can be higher or lower than the initial shear rate; however, a lower one is preferred since it disturbs the initial microstructure less than a higher new shear rate.
- After a short period, long enough to reach the new shear rate, the initial shear rate is returned.
- After the original steady state is re-established, another step change in shear rate is repeated in the same way.

This process is illustrated in Fig. 3.13. This process is called the "Step change method." The flow curve obtained from this process is considered to represent a constant microstructural level of the slurry established by the initial shear rate. Often this curve is called a "Structural curve," since such a curve represents one kind of shear history of a microstructure of the slurry. From this curve one can determine whether a slurry has pseudoplasticity or not. In the present study, this method has been adopted to obtain the pseudoplastic behavior of the slurries of metal and metal matrix composite.

#### **3.4.4. Thixotropic Behavior of Slurries**

Since thixotropy implies the time-dependency of viscosity, it can be expected that those measurements in the transient stages provide useful information. As mentioned in the background chapter, various

parameters will affect the time related functions. Three types of transient experiments have been proposed and reviewed by Mewis [52]:

- 1) A step change in shear rate or shear stress (step shear test)
- 2) A consecutive linear increase and decrease in shear rate (loop test)
- 3) A sinusoidal change in shear rate (oscillatory test)

Among these methods, the step shear test can readily be carried out [53, 159], and has been adopted in the present study.

The initial microstructure is important since thixotropy is also dependent on the microstructure, which is determined by the previous thermal and shear histories. The same initial condition of the slurry should be applied for each test. As the initial condition, the following procedures have been followed for each test:

(a) For metallic slurries:

A sample was melted and sheared while it was cooled to a target temperature. After steady state was reached, shearing was stopped and the sample was allowed to rest for a period of time. Then the initial shear rate was applied again to measure the transient curve of shear stress from the initial peak until it reached the initial steady state again.

(b) For metal matrix composite slurries:

(i) Above the liquidus of the matrix alloy

After a sample of composite was remelted, it was sheared at an initial shear rate until steady state was reached. Then the sample was rested for half an hour. After the rest, the initial shear rate was set again and the transient curve was obtained until the initial steady state.

(ii) In the semi-solid range of the matrix alloy

A sample was remelted and cooled to a temperature in the semi-solid range of the matrix alloy with shearing. After steady state was reached, the sample was rested for half an hour. Then the sample was sheared again at the same rate to obtain the transient curve.

There is a question as to how long time a sample should be rested before the resumption of shearing to set up an initial condition of the sample slurry for each test. Hence, it is required to investigate the effect of rest time on shear stress and microstructure of the slurry. As shown in Fig. 3.14, after a steady state for the initial shear rate was reached, the shearing was stopped and the sample was rested. After a period of time, the shearing was resumed at the same shear rate. The purpose of this resting was to find : (a) how the microstructure of the semi-solid slurry was changed with time during the rest: for example, the agglomeration of solid particles by coarsening, which was considered to be the main cause of the thixotropy of semi-solid alloy slurry; and (b) how fast the microstructure is restored to the initial one (kinetics of structural or thixotropic recovery).

## CHAPTER 4.

# RHEOLOGICAL BEHAVIOR OF ALLOY SLURRIES IN THE SEMI-SOLID STATE

### 4.1. Introduction

In this chapter, the rheological behavior of semi-solid alloy slurries of the matrix will be presented. Although the size and shape of the primary solid particles of the alloy slurries are quite different from those of composite slurry with ceramic particulates, this study on the metallic slurry would provide a good baseline for comparisons.

### 4.2. Experimental Procedures for Matrix Alloy

The matrix alloy, Al-6.5wt%Si, was remelted in the viscometer and maintained at 650°C. Then the following experiments were conducted:

#### (1) Continuous Cooling Conditions

The effects of cooling rate (0.5, 2.2, and 4.5 K/min or 0.0083, 0.037, and 0.075 K/s, respectively) and shear rate (180, 540, and 900 s<sup>-1</sup>) were investigated when the alloy was sheared in the semi-solid range of the alloy at a given cooling rate.



## (2) Isothermal Conditions

### *Steady state:*

The alloy was solidified with shearing to a specific temperature in the semi-solid range and the shearing was continued until the viscosity decreased to a constant level, which is called "steady state." The three levels of shear rate, the same as those in continuous cooling experiments, were employed.

### *Transient state :*

(i) After a steady state was obtained at an initial shear rate, the shearing was stopped and the slurry was allowed to rest for half an hour to provide an initial condition for samples. Then the same shear rate was applied again. The transient state induced from this re-shearing was investigated for the slurries with volume fractions solid of matrix alloy,  $g_{s(\alpha)}$ , of 0.2 and 0.4.

(ii) Step changes of shear rate were applied to obtain a structure curve for the slurries with 0.2 and 0.4 volume fraction solid. The initial shear rates were again 180, 540 and 900 s<sup>-1</sup>.

(iii) To study the effect of rest time on viscosity and microstructure, the slurries with 0.2 and 0.4 volume fraction solid were rested for a period of time from 15 seconds up to 24 hours. Then the initial shear rate was applied again. The initial up-peak was taken as to represent the microstructure established at the end of the rest.

### 4.3. Continuous Cooling Conditions

#### 4.3.1. Apparent Viscosity

When a metallic slurry is sheared and continuously cooled, the change in the apparent viscosity of the slurry with cooling can be expressed as a function of temperature or volume fraction of the primary solid phase, shear rate, and cooling rate:

$$\eta_a = f ( g_s, \dot{\gamma}, \epsilon ) \quad (46)$$

where  $g_s$  is volume fraction solid,  $\dot{\gamma}$  is shear rate, and  $\epsilon$  is the average cooling rate. The dependence of apparent viscosity on the volume fraction solid at the highest cooling rate in this study, 0.075 K/s is shown in Fig. 4.1. As the slurry was sheared at higher shear rates, the increase in the apparent viscosity with solidification was much slower than at lower shear rate. At a low shear rate of  $180 \text{ s}^{-1}$ , it was not possible to measure viscosity near the eutectic temperature. This can be attributed to the temperature difference across the gap in the viscometer: the outer portion of slurry in the gap solidifies while the inner part still contains liquid phase.

At a slower cooling rate of 0.0083 K/s, the apparent viscosity was much lower than that at the higher cooling rate, Fig. 4.2. At this cooling rate, it was possible to measure the apparent viscosity until the eutectic temperature was reached. The viscosity increased slowly in the earlier stage of solidification and rapidly increased when the slurry was cooled to near the eutectic temperature. In Table 4.1, the values of apparent viscosity at various shear rates for the two cooling rates were listed.

#### 4.3.2. Microstructures

The cross-sectional microstructures of the continuously cooled specimens are shown in Fig. 4.3 (a) and (b) : the average shear rates were 180 and 540 s<sup>-1</sup> and the average cooling rate was 0.075 K/s. The final volume fraction solid was 0.52, calculated by the Scheil equation. In both samples, most of the solid phase particles show the agglomeration of small particles to form large ones. At a shear rate of 180 s<sup>-1</sup>, the extent of the agglomeration seemed to be less than that at higher shear rate.

#### 4.4. Isothermal Conditions

As an alloy was cooled from the molten state to the semi-solid state, subsequent changes in apparent viscosity were observed as follows:

- In the liquid state, apparent viscosity remained almost constant.
- Near the liquidus temperature, the apparent viscosity started to increase very slowly.
- Then, as the alloy was cooled further into the semi-solid region, the increase in apparent viscosity became more rapid.
- When a target temperature was approached, the apparent viscosity was still increasing to a maximum level as shown in Fig. 4.4.
- Then, the apparent viscosity decreased very slowly to a constant level or a steady state after a long shearing at the isothermal condition.

The maximum values of viscosity in such curves were dependent on the cooling rate from the liquidus temperature to the target temperature, or fraction solid, and also on the shear rate. The viscosity data for the isothermal steady state were taken when the shear stress, measured as torque, reached a constant level after a period of isothermal shearing. It took often up to two hours for these metallic slurries to reach steady state. It was observed that the isothermal shearing time taken for the steady state was dependent on the initial shear rate, volume fraction solid of primary phase of the alloy, and the previous cooling rate before arriving at the target temperature. In general, at a given shear rate for some fraction solid, it took a longer time to reach a steady state when the sample was cooled faster before the isothermal temperature. At lower fraction solid, the time to reach a steady state was shorter than that at higher fraction solid. The dependence of the time on shear rate was not as obvious as the other factors.

Fig. 4.5 shows the dependence of the apparent viscosity of Al-6.5wt%Si alloy at isothermal steady states on the volume fraction of the primary solid phase under various initial shear rates. Some typical values of the apparent viscosity are listed in Table 4.2.

The flow curve, which is the plot of shear stress versus initial shear rate at steady state, is shown in Fig. 4.6(a) at different solid fractions. It should be noted that this steady state flow curve does not reveal the pseudoplasticity of the metallic slurry. In other words, these curves may not follow a typical relationship for pseudoplasticity such as the power law with a high shear limit viscosity term:

$$\eta = \eta_{\infty} + k' \dot{\gamma}^n \quad (47)$$

where  $k'$  and  $n'$  are constants dependent on the material and  $-1 < n' < 0$ ,  $n' = n - 1$  for pseudoplastic materials.

From a microstructural point of view, it is clear that the final microstructure at steady state is determined by initial shear rate. Each point in Fig. 4.6 may represent a different microstructure of the slurry. Hence, the pseudoplasticity of a slurry should be conducted by the step change of shear rate from the initial shear rate so that the initial microstructure could be unaltered. In Fig. 4.6 (b), the shear rate dependence of the viscosity data at isothermal steady state is shown for the different volume fractions solid. From this result it may be suggested that the higher the volume fraction solid, the more dependent is the viscosity of a slurry on shear rate.

## **4.5. Non-Newtonian Properties of Semi-Solid Alloy Slurries**

### **4.5.1. Pseudoplasticity**

From the step change of the shear rate after steady state at an initial shear rate, one can have a relationship of shear stress or viscosity and shear rate while the microstructure of the slurry is not significantly changed. Hence, the shear behavior of the slurry can be identified. One example is shown in Figures 4.8(a) and 4.8(b) for a sample of  $\phi_s(\alpha) = 0.4$ , initially sheared at  $900 \text{ s}^{-1}$ . After a steady state was established at the initial shear rate, the shear rate was suddenly dropped to a lower value. After a couple of minutes at the new shear rate, the initial shear rate was re-applied to set the initial steady state. The value of the down peak stress right after the new shearing was taken as a new stress level at the new

shear rate, while the original microstructure was considered to be unchanged. The results from this experiment suggest that:

- a) In the low shear rate range, the apparent viscosity decreased with increasing shear rate, which is referred to as pseudoplasticity.
- b) There seem to exist two limiting Newtonian behaviors in the very low and high limit of shear rates.
- c) Compared with the values of apparent viscosity at steady state, these new viscosities from the step change of shear rate were much lower at the same shear rate. This could be largely attributed to the different microstructures which resulted from the different shear histories of the slurries.

#### **4.5.2. Effect of Rest Time and Thixotropy**

After steady state at an initial shear rate of  $180 \text{ s}^{-1}$  was established, shearing was stopped to rest the slurry for a period of time. Then shearing was resumed at the initial shear rate. Samples for microstructures at the end of the resting period or before the start of re-shearing were taken and are shown in Fig. 4.8. The initial microstructure formed by the initial shear rate at steady state (isothermally sheared for 2 hours) is shown in Fig. 4.8(a). With a longer period of rest, solid particles agglomerated to form more spherical and larger particles. When the original shearing was resumed, the shear stress rose immediately to a peak value (up-peak) and subsequently decreased rapidly and then gradually to a steady state with time, Fig. 4.9. The initial up-peak level of shear stress or apparent viscosity was considered to be a result from the new microstructure built during the

rest period. Hence, the plot of up-peak viscosity versus rest time in the Fig. 4.10, suggests that:

- a) For longer rest times, the up-peak viscosity was higher.
- b) With a longer rest period, the increase of up-peak viscosity was slow.
- c) The increase in the corresponding viscosity seemed to reach a plateau after a long rest.

During the rest of a slurry, structural changes – the agglomeration or coarsening of the solid particles – proceed to give a new shear stress at the same initial shear rate. From the plot of time for the new steady state and rest time, Fig. 4.11, there also seemed to be a plateau at very long rest times. Loué et al. [157] reported the same result of the initial viscosity and rest time for Al-6%Cu and Al-7%Si-0.3%Mg at solid fractions of 0.40 and 0.35, respectively. In their method, the initial viscosity was obtained from the initial slope at the start of a hysteresis loop, i.e.,  $\eta_0$  at zero shear rate. Hence, the data in the present study are basically different from theirs. Yet, the general behavior of the rested slurry was the same. They did not cover data for long rest times as done in this study, so the plateau of viscosity at long resting times was not reported.

## 4.6. Discussion

### (1) Continuously cooled samples

In the range of  $0.2 < g_{s(\alpha)} < 0.45$ , the relationship between the apparent viscosity and volume fraction solid was obtained from a semi-log plot of apparent viscosity versus volume fraction solid. The plot revealed a straight line relationship in this range of volume fraction solid:

$$\eta_a = A' \exp(B' g_s) \quad (48)$$

where  $A'$  and  $B'$  are coefficients. This equation is in the same form as eqn.(7) by Thomas. For pseudoplastic materials, however, these coefficients are dependent on shear rate and cooling rate:  $A' \equiv f(\dot{\gamma}, \epsilon)$ ,  $B' \equiv g(\dot{\gamma}, \epsilon)$ . The coefficient  $B'$  implies the rate of viscosity increase with increasing volume fraction solid. These coefficients were determined by curve fitting. It was found that the coefficients  $A'$  and  $B'$  were dependent on the shear rate, as shown in Figures 4.12 and 4.13, respectively. The coefficient  $B'$  was strongly dependent on the shear rate, while the coefficient  $A'$  was rather small. The strong dependence of  $B'$  on the cooling rate is also shown in Fig. 4.14. With faster cooling, the apparent viscosity increased more rapidly during solidification.

In Fig. 4.3, there is no obvious difference in the size and shape of the primary solid particles. At the shear rate of  $180 \text{ s}^{-1}$ , however, the extent of agglomeration seemed to be less than that at a higher shear rate of  $540 \text{ s}^{-1}$ . The effective average size of the primary solid particles hence seemed to be smaller at lower shear rate than at higher shear rate. This may result in a larger surface area of agglomerated particles sheared at low shear rate, which increases the effective volume fraction of solid and consequently the resistance of a slurry to flow.

## **(2) Isothermally held samples**

### **Thixotropic property of metallic slurries**

Compared to the continuously cooled samples, the isothermally held samples showed much lower viscosity values at a given shear rate. This is



largely due to differences in the microstructure developed through the different thermal history. After the start of isothermal shearing, the shape and size of primary solid particles continue to be modified by Ostwald ripening, and finally they become more spherical and larger agglomerated particles. However, shearing would break the agglomerating particles. As the breakdown continues with time, the apparent viscosity decreases, as shown in Fig. 4.9. Eventually, an equilibrium between the breakup and agglomeration is established: a steady state where the viscosity remains constant. When shearing is stopped and the slurry is allowed to rest, only agglomeration occurs. The viscosity increases of an alloy slurry after a rest is thus strongly related with the microstructural evolution.

In both figures of Fig. 4.10 and 4.11, it is obvious that there exist plateaus of peak viscosity and time for a new equilibrium. This fact strongly suggest that the microstructural evolution, i.e., agglomeration, was saturated during a very long isothermal resting, so that there would be eventually no more agglomeration proceeding in the microstructure, e.g., Fig. 4.8(d). The solid particles were large and fairly spherical.

To study the rate of thixotropic recovery of a metallic slurry, the transient curves in Fig. 4.9 were re-plotted in Fig.4.15. These curves were well fitted to an equation of the type [158]:

$$\frac{\eta - \eta_{\text{steady}}}{\eta_{\text{peak}} - \eta_{\text{steady}}} = \exp(-k_t t) \quad (49)$$

where  $k_t$  is a coefficient dependent on the previous condition or rest time. The coefficient  $k_t$  can be termed the "thixotropic recovery rate," which

determines the rate of thixotropic recovery in the transient stage. In Fig. 4.16, this rate coefficient  $k_t$  was very high when the slurry was rested for shorter time and becomes lower with longer time period of rest.

#### Pseudoplasticity of alloy slurries

As mentioned earlier, the pseudoplastic behavior of a slurry can be identified only through a structure curve such as Fig. 4.7. From this curve several conclusions can be drawn:

- a) Up to a medium range of shear rate in the figure, the slurry exhibits pseudoplasticity, which allows application of the power law to the flow curve. The index  $n'$  in the power law,  $\eta = \eta_\infty + k' \dot{\gamma}^{n'}$ , was -0.85 when the initial shear rate was  $900 \text{ s}^{-1}$ .
- b) At the higher shear rates, the flow behavior turns to a Newtonian behavior, which is often called the "high (shear rate) limit Newtonian,"  $\eta_\infty$ .
- c) Also, another Newtonian behavior can be presumed at lower shear rates; often called the "low limit Newtonian,"  $\eta_0$ .

Hence, the metallic slurry at isothermal shearing exhibited a very typical pseudoplasticity. It should be noted that in almost every report on the pseudoplasticity of metallic slurries [72,96,140], the consistency of the microstructure from which the relation of viscosity versus shear rate was derived has not been even mentioned. Joly and Mehrabian [72] explained the pseudoplasticity of Sn-15%Pb with data obtained from the new steady state values at different shear rate. This experimental procedure could not provide constancy of microstructures. The consistency of microstructure is again a very important basis for such a non-Newtonian behavior of semi-solid alloy slurries, because the microstructures are dependent on the process variables and directly influence the rheological behavior.

### (3) Microstructures and Viscosity

Since the rheological behavior of a semi-solid metallic slurry is strongly dependent on the size and/or shape of primary solid particles, there have been several reports on this relationship.

Although the size of primary particles is determined by the process variables of shear rate, cooling rate, shearing time, etc., the shape factor is found to be much more important in the analysis of the viscosity of such slurries [140,157]. Then, the issue has been how to analyze the shape quantitatively. The first and most reasonable method was suggested by Joly and Mehrabian [72]. They proposed a volume fraction of "entrapped liquid" in an aggregate of primary solid particles,  $\phi_{Le}$ , and successfully explained the viscosity changes in Sn-15%Pb alloy slurry. Since the liquid phase entrapped in an aggregate would not contribute to the medium, the higher amount of entrapped liquid would result in a higher effective fraction solid to give higher viscosity.

Mori et al. [96] proposed the "particle coupling ratio,"  $R_n$ , which was defined as the ratio of the number per area of fine quasi-spherical particles,  $n_p$  (i.e., the number of large aggregates of many small single particles), and that of "complicated particles,"  $n_p'$  (i.e., the number of touching large aggregates, which are regarded as influencing the viscosity). Then, the ratio represents the degree of aggregation. They found that only  $R_n$  was related to the viscosity of Al-5%Cu alloy slurry in the form of  $\eta = C \cdot \exp(aR_n)$ . In their method, the concept of the entrapped liquid cannot be considered at all. Also, the those seemingly touching large aggregates may or may not contribute the flow behavior of the slurry.

In the present study, another way of quantitative analysis of agglomeration of primary particles is attempted. Here, a parameter of the number of small particles comprising an agglomerate,  $R_A$ , was obtained from micrographs. In this parameter the entrapped liquid fraction could be reflected indirectly, and also Mori's number of quasi-spherical aggregates could be obtained. In Fig. 4.17, the comparison of these three parameters is presented. From Fig.4.3, the values of  $R_A$  were 4.1 and 2.8 in the continuously solidified samples at 0.075 K/s with shear rates of 180 and 900  $s^{-1}$ , respectively; for a slowly cooled sample (0.0083 K/s at 180  $s^{-1}$ ) the value was 2.8, which suggests that slower cooling resulted in less agglomeration than faster cooling, and hence lower viscosity. Hence, the larger  $R_A$  is, the more agglomeration that occurs and the higher the viscosity the slurry exhibits. In chapter 6, this method is applied to composite slurries and the parameters were compared with each other.

#### 4.7. Summary of Results

For alloy slurries in the semi-solid state, the rheological behavior and microstructure were investigated and the results are as follow.

- (1) In continuously cooled samples, the relationship of apparent viscosity and process parameters was expressed in the form of an exponential function of volume fraction solid. The rate of increase in the viscosity with volume fraction solid, the coefficient A, was found to be a strong function of shear rate as well as cooling rate.

- (2) In isothermally sheared samples, apparent viscosity at steady state was much lower than that from continuous cooling conditions for a given volume fraction solid.
- (3) In isothermally sheared samples, the pseudoplasticity was well identified by the sequential step-change of shear rates after an initial steady state. This method should be employed to allow the constancy of microstructure of a semi-solid slurry from which one can study the non-Newtonian behavior of such slurries.
- (4) In result 3, the Newtonian behavior was also found in both lower and higher range of shear rates.
- (5) In isothermally sheared samples, thixotropic behavior was observed and the thixotropic recovery rate of steady state was strongly related to the previous rest time.
- (6) A method to analyze the degree of agglomeration of primary solid particles was proposed:  $R_A$ , the number of single small particles comprising a large agglomerate. The larger value of this would result in higher viscosity.

## CHAPTER 5.

# RHEOLOGICAL BEHAVIOR OF COMPOSITE SLURRIES WITH THE MATRIX ALLOY IN THE MOLTEN STATE

### 5.1. Introduction

There has been no detailed report that a composite slurry of ceramic particulates in the molten metal is non-Newtonian; it was briefly mentioned by Mada and Ajersch [158] that such composites behaved as Newtonian, while Loué and Kool [140, 157] observed pseudoplasticity with similar materials. In this chapter, the rheological behavior of composite slurries were reported with the matrix alloy in the molten state. This type of slurry is different from the semi-solid slurry with the matrix alloy as the solid phase:

- (a) In this composite slurry, the ceramic particulates are much smaller than the primary solid particles of the matrix, and
- (b) The shape of the ceramic particulates are practically unchanged, while the primary solid particles change their shapes during a shearing process.

Hence, the composite with the matrix in the molten state is a slurry with small, non-deformable, and constant-shaped solid particles. The results for this composite slurry were also compared to those for the alloy slurry of its matrix in semi-solid state.

## 5.2. Experimental Procedures for Composite ( $T > T_L$ )

Metal matrix composites of Al-6.5 wt%Si alloy with 10, 20, and 30vol% of silicon carbide(SiC) particulates were used for this study (the preparation of this material is described in Chapter 3). Fig. 5.1 shows a microstructure of a composite with 20vol%SiC cast in a graphite mold.

All the measurements of rheological properties were conducted at 700°C. The shear rates employed were 180, 540, and 900 s<sup>-1</sup>. A sample material was initially conditioned by shearing at 540 s<sup>-1</sup> for half an hour, followed by resting for another half an hour before every measurement. The rheological behavior of the composite slurry was investigated by the following experiments.

(a) Transient stage at constant shear rate:

After a sample was pre-conditioned in the viscometer, it was sheared at a given initial shear rate. The torque was recorded from the initial peak to the eventual steady state.

(b) Steady state at constant shear rate:

The steady state values of apparent viscosity and shear stress were calculated from the torque at steady state at a given initial shear rate. Also, the equilibrium flow curves were plotted with shear stress at steady state against initial shear rate.

(c) Step change of shear rate:

After a steady state, shear rate was changed by steps without interruption of shearing, from which the flow curves which are called "structure curves" were constructed for each initial shear rate.

## 5.3. Results

### 5.3.1. Constant Shear Rate Experiments

#### (1) Transient Stage

The first group of measurements on the molten composite slurry was carried out at constant shear rates. When shearing was started after initial conditioning, the shear stress or apparent viscosity level increased immediately to the peak value and rapidly decreased in the early stage of shearing and gradually decreased to a steady state level. This transient curve is a characteristic of thixotropic materials [e.g., 53]. The time for reaching steady state was dependent on the initial shear rate and amount of silicon carbide particulates. As the initial shear rate was increased, the steady state was reached more rapidly, as shown in Fig. 5.2. For example, it took about ten minutes at  $900\text{ s}^{-1}$  to establish a steady state for a composite slurry with 20 vol%SiC, compared to 100 minutes at  $180\text{ s}^{-1}$ . It should, however, be noted that most of the drop occurs within two and ten minutes at  $900$  and  $180\text{ s}^{-1}$ , respectively. With higher concentration of ceramic particulates, it takes longer to reach the steady state at a given shear rate, as shown in Fig. 5.3. It is interesting that the composite slurry with 30 vol%SiC showed a much higher viscosity and took a longer time to reach steady state compared to composites with lower concentrations of silicon carbide.



## (2) Steady State

At the end of the transient stage, a steady state level of shear stress or apparent viscosity was reached. The apparent viscosity of a molten composite slurry at steady state was dependent on the volume fraction of the ceramic particulates and shear rate. For a given concentration of silicon carbide particulates, the change of equilibrium shear stress at steady state with shear rate is shown in Fig. 5.4 (this is often called an "equilibrium curve"). These curves are similar in shape to others for different slurries [67,159]. The corresponding apparent viscosity at steady state with shear rate is also shown in Fig. 5.5. As the composite slurry was sheared at higher shear rate, the apparent viscosity decreased consequently. There seems to be a converging value of the apparent viscosity for all samples at higher shear rates beyond the shear rates employed in this study. In some pseudoplastic materials, there can be a constant viscosity at the high shear rate limit, which is a Newtonian region at high shear rate. Each point on an equilibrium flow curve may represent an independent microstructural characteristic for pseudoplastic materials, such as degree of agglomeration of solid particles, etc. Hence, the step change of shear rate was required to find such time-independent, non-Newtonian behavior as well as time-dependent thixotropy.

In Fig. 5.6, the variation of apparent viscosity at steady state with the 10, 20, and 30 vol%SiC samples is shown with initial shear rates, and the data are listed in Table 5.1. At all shear rates, the apparent viscosity increased slowly up to 20 vol%SiC, and then rapidly increased in the samples with 30 vol%SiC.

### 5.3.2. Step Change of Shear Rate: Structure Curves

An example of step change of shear rate on a 30 vol%SiC/Al-6.5wt%Si composite slurry is shown in Fig. 5.7. After the slurry reached a steady state at an initial shear rate of  $900\text{ s}^{-1}$ , then the shear rate was dropped to  $540\text{ s}^{-1}$ . After a new steady state at the new shear rate, the initial shear rate was restored. This was repeated at another shear rate, such as  $180\text{ s}^{-1}$ , and so on. It is clear that there is time-dependency of shear stress or apparent viscosity at each shear rate. The response in shear stress with time to the new shear rate suggests that the sample shows thixotropy. The thixotropy of the sample is further confirmed in that the initial level of shear stress at steady state was restored after shearing at the initial shear rate was resumed. Assuming that the microstructure of a slurry sample be maintained within the initial period just after a change of shear rate, one can take the initial peak (down or up) values of shear stress as a set of data for the sample with the initial microstructure. Hence, from the step changes of shear rate, the structure curves starting from different initial shear rates were obtained for the molten composite slurries with different concentrations of silicon carbide particulates. For a composite slurry with 20 vol%SiC, the structure curves in Fig. 5.8(a) and 5.8(b) showed the following behavior:

- (a) If the slurry was initially sheared at higher shear rate, then it showed lower apparent viscosities at changed shear rates than the slurry initially sheared at low shear rate.

- (b) The flow curve for this composite slurry showed that there is a non-Newtonian, pseudoplastic region at lower shear rates and a Newtonian range at high shear rates.
- (c) The high shear limit Newtonian viscosity occurred over the shear rates of about 300 and about 360 s<sup>-1</sup> for the initial shear rates of 900 and 180 s<sup>-1</sup>, respectively. The high shear limit viscosity,  $\eta_{\infty}$ , was 0.035 Pa·s and 0.060 Pa·s when the initial shear rates were 900 and 180 s<sup>-1</sup>, respectively.
- (d) In the non-Newtonian range of shear rate, the relation between the viscosity and shear rate was well fitted by a power law, which indicated that the composite slurry exhibits a pseudoplasticity:

$$\eta = \eta_{\infty} + k' \dot{\gamma}^{n'} \quad (47)$$

where the measured values of  $n'$  ( $-1 < n' < 0$ ) from the log-log plot of viscosity and shear rate were - 0.90 and - 0.68 for the initial shear rates of 900 and 180 s<sup>-1</sup>, respectively. The greater the value of  $|n'|$  is, the more pseudoplastic is the slurry.

- (e) In the range of shear rates much lower than 180 s<sup>-1</sup>, there may be another Newtonian range, where a low limit viscosity can exist.

The effect of concentration of SiC particulates on the pseudoplasticity is shown in Fig. 5.9 for 10 and 20 vol%SiC at an initial shear rate of 180 s<sup>-1</sup> and Fig. 5.10 for 20 and 30 vol%SiC at an initial shear rate of 900 s<sup>-1</sup>. With a higher concentration of silicon carbide particulates, the slurry became more pseudoplastic. It was especially significant in the sample with 30 vol%SiC, and the high shear limit Newtonian viscosity was obtained at

shear rates higher than  $1200 \text{ s}^{-1}$ . In Table 5.2, the measured values of  $n$  and  $\eta_{\infty}$  are listed. The value of the low shear limit viscosity was approximated from the curve extrapolated to the origin in the plot assuming this slurry has no yield stress.

## 5.4. Discussion

### 5.4.1. Rate of Thixotropic Recovery in the Transient Stage

In the early stage of a transient curve, the apparent viscosity decreases rapidly with a rate which may be dependent on the shear rate and amount of solid phase. The rate of the decrease drops significantly after the initial large drop. It would require much more time to reach the eventual steady state.

The apparent viscosity change in this transient stage has been studied in many theoretical and experimental ways [53,55-57]. Jones and Brodkey [67] studied the rate of viscosity decrease in the initial transient stage and formulated a rate equation. Recently, Mada and Ajersch [158] presented a rate equation based on a kinetic analysis of agglomeration and breakdown of the agglomerates in a metal matrix composite slurry with the matrix in the semi-solid state.

Among the several model equations describing the early portion of transient stage, the first approximation of the decrease rate of viscosity may be tested in a log-log plot of the viscosity and shearing time. In the case of a composite slurry with 20 vol%SiC, the following relation can be applied, which was proposed by Jones and Brodkey [67]:

$$\eta_a = \eta_p t^b \quad (50)$$

where  $\eta_p$  is the peak viscosity at the start of shearing after the pre-conditioning rest,  $t$  time in seconds and  $b$  a constant ( $b < 0$ ) for a given shear rate. The rate of decrease in viscosity is then expressed as:

$$\frac{d\eta}{dt} = b \eta_p t^{b-1} = c t^{b-1} \quad (51)$$

where a constant  $c$  is defined as  $b\eta_p$ . Hence, the decay rate is dependent on the  $\eta_p$ . For the 20 vol%SiC/Al-6.5wt%Si composite slurry, the values of the power index,  $(b-1)$  were measured as -1.034, -1.067, and -1.121, and the values of the coefficient  $c$  were calculated as -0.0056, -0.0064, and -0.007 for shear rates of 180, 540, and 900 s<sup>-1</sup>, respectively.

Another simple relationship was derived by Mada and Ajersch [158]:

$$\frac{\eta - \eta_{\text{steady}}}{\eta_{\text{peak}} - \eta_{\text{steady}}} = \exp(-k_t t) \quad (49)$$

where  $\eta_{\text{steady}}$  is the viscosity at steady state, and  $\eta_{\text{peak}}$  that at the initial peak. In the early stage of resumed shearing after a rest, this relation also fits well the data for the slurries with 20 vol%SiC at different shear rates (Fig. 5.11) and also for the composites with 30 vol%SiC at 900 s<sup>-1</sup> (Fig. 5.12). The composite with 10 vol%SiC did not exhibit noticeable thixotropy. Compared with the matrix slurry in Fig. 4.15, these relationships could not be extended to longer shearing times.

#### **5.4.2. Comparison with Semi-Solid Alloy Slurry**

The apparent viscosity of the composite slurry with 20vol%SiC above the liquidus temperature was much larger than that of the equivalent matrix slurry with 0.2 volume fraction of isothermally sheared primary particles, Fig. 5.13. The question is why the composite slurry with much finer particulates of silicon carbide exhibits a higher viscosity than the other slurry with larger particles. As discussed in the background chapter, the most reasonable explanation can be to compare the ratio of the surface area per unit volume of solid particles. The viscosity is higher when the solid particles in a slurry have a higher surface area to volume ratio of the solid phase(s) [108]. At the same volume fraction, the finer particles, such as in the composite slurry of 8.5  $\mu\text{m}$  silicon carbide, have a higher ratio of surface area to volume than the coarser ones such as the primary solid particles in the matrix slurry, for which the size range is several hundred microns.

#### **5.4.3. Comparison of Experimental Data with Theoretical Models**

As discussed in the chapter 2, a number of theoretical and semi-empirical relationships of relative viscosity with concentration of solid phase in suspensions have been proposed. To compare the present experimental data with those theoretical relationships, one should take data from the Newtonian range of shear rate, such as the high shear limit or low shear limit viscosity.

Fig. 5.14 is a plot of curves from some theories and the high shear limit data obtained from the step change experiments. Among these

theoretical equations, the Mori-Ototate equation, eqn.(9) [15] seems to be worth mentioning. In this equation, one can include the non-spherical shape factor and size of solid particles, as well as the maximum packing volume fraction. For the silicon carbide of F600 grit used in this study, the surface area per unit weight was measured as  $0.87 \times 10^3 \text{ m}^2/\text{kg}$  by the provider. Then the surface area per unit volume was calculated to be  $2.78 \times 10^6 \text{ m}^{-1}$ , with the density of the silicon carbide particle assumed to be  $3.2 \times 10^3 \text{ kg/m}^3$ . The average diameter of F600 grit particles is  $8.5 \times 10^{-6} \text{ m}$ . Hence, the coefficient of the second term in the Mori-Ototate equation for the relative viscosity and concentration of solid was determined as 11.8:

$$\eta_r = 1 + 11.8 \left( \frac{1}{\phi_{\text{SiC}}} - \frac{1}{\phi_m} \right)^{-1} \quad (51)$$

where  $\phi_{\text{SiC}}$  is the volume fraction of silicon carbide. The maximum packing factor,  $\phi_m$ , was taken as 0.55, which was experimentally determined from the pressure infiltrated composite of SiC/Al-6.5wt%Si. Comparing these two Newtonian viscosities to the Mori-Ototate relation, the high shear limit viscosities obtained for  $\dot{\gamma}_0 = 180 \text{ s}^{-1}$  were very close to those predicted by the relation with the coefficient of 11.8. When the particles are all monosized spheres, the coefficient is equal to 3. In Fig. 5.14, the high limit viscosities for  $\dot{\gamma}_0 = 900 \text{ s}^{-1}$  seem to follow this line for spheres.

## 5.5. Summary of Results

For the composite slurries of Al-6.5wt%Si with 10, 20, and 30 vol%SiC particulates, the rheological behavior was investigated at  $700^\circ\text{C}$ .

(1) Pseudoplasticity:

The step change of shear rate was employed to study the dependence of viscosity on shear rate. The composites exhibited non-Newtonian behavior of pseudoplasticity: the apparent viscosity was lower as the slurry was sheared at higher shear rate. In the composite with 10 vol%SiC, the pseudoplasticity was weak compared to composites with higher concentrations.

(2) Steady State Viscosity:

The viscosity of a composite slurry was higher than that of an alloy slurry with the equivalent volume fraction solid. In particular, the composite with 30 vol%SiC exhibited much higher viscosity than others with lower concentrations.

(3) Thixotropy:

This was also observed in these slurries: again, the composite with 10 vol%SiC did not exhibit a noticeable time-dependent viscosity change.



## CHAPTER 6.

# RHEOLOGICAL BEHAVIOR OF COMPOSITE SLURRIES WITH THE MATRIX ALLOY IN THE SEMI-SOLID STATE

### 6.1 Introduction

In this chapter, the rheological behavior of a particulate-reinforced composite was investigated in the solid-liquid mixture range of the matrix. The experimental methods to study this were the same as those described in the previous chapters. In the semi-solid range, the material system consists of three phases: the liquid (L) and primary solid ( $\alpha$ ) of the matrix and the particulate silicon carbide (SiC). The present composite slurry differs from the previous metallic slurry or the composite slurry above the liquidus in some aspects as follows:

a) Size of solid phase:

The silicon carbide used in this experiment is about 10 microns while the size of the primary solid of matrix, Al-6.5wt%Si, ranges up to several hundred microns, which is determined by the processing condition. Hence, the difference of sizes of these two solid phases is a factor of  $10^2$ , which gives a polydispersity of the size of solid particles.

b) Shape of solid phase:

While the irregular shape of silicon carbide particulates does not change (i.e., non-deformable), the primary solid particles change their shape during processing (i.e., deformable).

Hence, the objectives of this chapter are to investigate the effect of the presence of the smaller, non-deformable silicon carbide particulates on the apparent viscosity of a composite slurry with the matrix in the semi-solid state, as well as on the microstructure of the deformable primary solid phase.

## **6.2. Experimental Procedures for Composites ( $T_E < T < T_L$ )**

The composite used in this experiment was the same as that used in chapter 5: Al-6.5wt%Si with 10 and 20 vol% of silicon carbide particulates (8.5  $\mu\text{m}$ ).

### **(1) Continuous Cooling Conditions**

The composite was completely remelted and rested for half an hour before starting a new shearing at 650°C ( $T > T_L$ ). Then it was sheared at a given shear rate of 180, 540, or 900  $\text{s}^{-1}$  during solidification through the semi-solid range of the matrix alloy at a given cooling rate (0.075 or 0.0083 K/s). It was sheared until the slurry was fully solidified below the eutectic temperature. The whole crucible and rotor were removed from the viscometer and quenched in water. The final microstructures were compared with those of the unreinforced matrix.

### **(2) Isothermal Conditions**

In each run, a charge of the composite was completely remelted and rested for half an hour. Then it was cooled to a temperature in the semi-

solid range of the matrix under shearing at a given initial shear rate of 180, 540, or 900 s<sup>-1</sup>. The shearing was continued at a specific temperature in the semi-solid range of the matrix until a steady state in the torque level was reached. The corresponding steady state viscosity was obtained in this way and compared with data for the unreinforced alloy slurry.

After a steady state was established at a given initial shear rate and at a primary solid fraction as described above, the step change of shear rate was applied to obtain the structure curve for the initial shear rate. Also, the effect of the rest time was investigated in the same way as described in chapter 4. One temperature at which primary solid fraction is 0.2 was selected for a composite with 20 vol%SiC (the total volume fraction solid of this composite slurry is 0.36, calculated by the eqn. (53)) to compare with i) the previous results for an unreinforced alloy slurry, and ii) a composite slurry with the matrix in the fully molten state with equivalent volume fractions of solid phase(s). The total volume fraction of solid phase(s) in a slurry is calculated by the following relation.

$$g_{s(\text{total})} = g_{s(\text{SiC})} + g_{s(\alpha)} [1 - g_{s(\text{SiC})}] \quad (53)$$

## 6.3. Results

### 6.3.1. Continuous Cooling of Composite Slurry

#### (1) Apparent Viscosity

The change of the apparent viscosity with solidification is shown in Fig. 6.1, in terms of primary solid fraction for a composite with 20 vol%SiC.

Again, the viscosity of the composite slurry was dependent on the shear rate. To compare the effect of the volume concentration of the silicon carbide particulates, the change of viscosity at shear rate of  $180 \text{ s}^{-1}$  with temperature, or the primary solid fraction, was plotted in Fig. 6.2. At the same temperature, the viscosity increased as the concentration of silicon carbide particulates increased until the temperature reached the volume fraction of the primary particles of about 0.3, above which the viscosity was lower for the slurries with more SiC particulates than that for the unreinforced alloy slurry. Such a cross-over was also observed in other continuously cooled slurries sheared at  $180 \text{ s}^{-1}$ .

Since the composite slurry contains some content of solid particles of SiC, it was appropriate to express the apparent viscosity with the total volume fraction solid of primary solid and silicon carbide using eqn.(53). Then, an interesting plot was made, as shown in Fig. 6.3 and Fig. 6.4. In Fig. 6.3, at a given total fraction solid, the apparent viscosity was lower when the concentration of silicon carbide was higher relative to total fraction solid. Fig. 6.4 shows the difference in viscosities of the alloy slurry and a composite slurry, sheared at 180 and  $540 \text{ s}^{-1}$ . Also, it was observed that the rate of increase in viscosity with increasing fraction solid becomes slower as the concentration of silicon carbide particulates increases.

## **(2) Microstructures**

The microstructure of a continuously cooled composite was compared with that of the unreinforced matrix alloy, Fig. 6.5. Using a criterion to express the degree of agglomeration of solid particles, one can measure the  $R_A$ , which was defined as the number of single particles in an

agglomerate (see section 4.6 (c)). The measured values of  $R_A$  from the microstructures in Fig. 6.5 were 2.8 and 2.5 for the matrix without SiC and the composite with 20 vol%SiC, respectively. Hence, the degree of agglomeration of the primary particles was lower when the slurries contained the smaller, non-deformable silicon carbide particulates. Comparing the microstructures of composites in Fig. 6.5 with alloys in Fig. 4.3, it seems that the presence of the small, non-deformable ceramic particulates modified the shape of the primary solid particles of matrix alloy of Al-6.5wt%Si. The role of the ceramic particulates was supposed to block the agglomeration of primary solid particles of an alloy [157].

In the composite slurries, the size and shape of primary solid particles were also dependent on the shear rate and cooling rate, as in the alloy slurries. The effect of cooling rate on the microstructure is shown in Fig. 6.6 for a composite with 20 vol%SiC. In the more rapidly cooled sample, more entrapped liquid between the primary particles was observed while there was a much smaller amount of entrapped liquid in the slowly cooled sample. This is the same tendency as in the metallic slurries. The measured values of  $R_A$  were 3.6 and 2.8 in the sample sheared at  $180\text{ s}^{-1}$  and cooled at  $0.075\text{ K/s}$ , and in the sample sheared at the same rate and cooled at  $0.0083\text{ K/s}$ , respectively. It is interesting to find some single ceramic particulates inside a quasi-round primary solid particle in the slowly cooled sample, Fig. 6.6 (b). This suggests that the coarsening between the single particles in an agglomerate caused a complete surrounding of the ceramic particulate(s).

The effect of shear rate on the microstructure is shown in Fig. 6.7. Compared with the unreinforced alloy slurry, as in Fig. 4.3, it is clear from these figures that the primary solid particles were much refined

when the composite slurry was sheared at higher rate. Also, the degree of agglomeration of primary solid particles was much less with the higher shear rate. Again, in terms of  $R_A$ , they were 3.6 and 2.7 in the samples sheared at  $180 \text{ s}^{-1}$  and  $900 \text{ s}^{-1}$ , respectively.

### 6.3.2. Isothermal Shearing of Composite Slurry

#### (1) Isothermal Steady State

A composite with 20 vol%SiC was isothermally held at a temperature where the volume fraction of primary solid is 0.2 (i.e.,  $g_{s(\alpha)} = 0.2$  in the matrix alloy). Hence, the composite slurry contained a total of 0.36 in volume fraction of solid phases—SiC and primary solid ( $\alpha$ ). It was sheared at different shear rates until the steady state. In Fig. 6.8, the data for these composite slurries are compared to those for the unreinforced matrix alloy at  $g_{s(\alpha)} = 0.36$ . It is interesting that the matrix alloy slurry showed a higher viscosity than the composite slurry. And the difference between two viscosities decreased with higher shear rate. These observation suggest that microstructures of the slurries are strongly controlled by the presence of the smaller, non-deformable SiC particulates. The microstructures of the composite slurries sheared at  $180$  and  $900 \text{ s}^{-1}$  are shown in Fig. 6.9. It seems to be difficult to analyze the size and shape of primary solid. The primary solid particles at  $g_{s(\alpha)} = 0.2$  are much smaller than at  $g_{s(\alpha)} = 0.4$ . From the effect of polydispersity of solid particles in a slurry, as in eqns. (10) - (12), it was presumed that the bimodal distribution of particles in the composite slurries contributed to the decrease in viscosity of such slurries lower than that of slurries with monosized distribution of solid particles.

## **(2) Pseudoplasticity of Composite in the Semi-Solid Range**

The pseudoplasticity of the composite slurry with  $g_{s(\text{SiC})}=0.2$  and  $g_{s(\alpha)}=0.2$  in the matrix alloy was compared to an unreinforced matrix alloy slurry with  $g_{s(\alpha)}=0.4$ . The initial shear rate dependence of the composite slurry is shown in Fig. 6.10. The viscosity of a slurry, sheared at higher initial shear rate, was lower than that of a slurry sheared at lower shear rate. In terms of apparent viscosity, as in Fig. 6.11, these slurries exhibit high shear limit viscosities. Compared with an alloy slurry with the equivalent volume fraction solid, the composite slurry showed lower viscosity, as shown in Fig. 6.12 and 6.13. The high shear limit Newtonian viscosity was lower in the composite slurry than the matrix alloy slurry with the same amount of solid phase.

## **(3) Thixotropy of Composite in the Semi-Solid Range**

Fig. 6.14 shows a thixotropic effect of resting on the initial peak viscosity of a composite slurry, which was initially sheared at  $180 \text{ s}^{-1}$  for two hours at a temperature for  $g_{s(\alpha)}=0.2$  and followed by different resting periods. Again, the peak viscosity was increasing with longer resting period. The increase in the viscosity, however, seems very small, even with a resting for  $10^4 \text{ s}$ . Comparing the microstructure of a sample taken after the isothermal shearing, as shown in Fig. 6.9(a), with the one rested for  $10^4 \text{ s}$ , Fig. 6.15, there was not noticeable agglomeration of the primary solid particles of the matrix during the resting. This indicates that the composite slurry would be less thixotropic than the matrix alloy slurry because the agglomeration

of primary solid particles may be blocked by the silicon carbide particles between the primaries [157].

## **6.4. Discussion**

Silicon carbide particulates in the samples taken from the top, middle, and bottom of the gap did not show noticeable settling after about eight hours at a temperature above the liquidus of the matrix alloy. However, the concentration of the particulates was often found to vary along the radial direction. The concentration on the inner side was lower while it became higher toward the outer side of the viscometer. Since only the inner rotor was rotating and the outer cylinder was stationary, the induced centrifugal force transferred the smaller silicon carbide particulates toward the outer cylinder [160]. However, this segregation of SiC particulates did not occur in many experiments. Also, such segregation is not considered to determine the cross-over of viscosity shown in Figures 6.2.

## **6.5. Summary of Results**

For the SiC/Al-6.5wt%Si composites, the rheological behavior and microstructure were investigated in the semi-solid range of the matrix alloy and the following results were obtained:

- (1) The presence of non-deformable silicon carbide particulates contributed to a reduction in the viscosity of the composite slurry at a given total volume fraction of solid phases.



- (2) It also contributed to the modification of the microstructure of such composites so that the primary solid particles were more refined at high shear rate and became more rounded, compared with those in the unreinforced matrix alloy.
- (3) The high shear limit viscosity was also reduced in the composite slurry at a given total solid fraction.
- (4) Thixotropy was reduced in the composite slurry by the presence of the non-deformable, ceramic particulates, which may act as obstacles to the agglomeration of the primary solid particles during the rest period.

## CHAPTER 7.

### CONCLUSION

The rheological behavior and microstructure were investigated using a concentric-cylinder viscometer for three different slurries: a) semi-solid alloy slurries of a matrix alloy, Al-6.5wt%Si, i.e., ( $\alpha$ +L), b) composite slurries, SiC<sub>p</sub>(8.5  $\mu$ m)/Al-6.5wt%Si, with the same matrix alloy in the fully molten state, i.e., (SiC<sub>p</sub>+L), and c) composite slurries of the same composition with the matrix alloy in the semi-solid state, i.e., (SiC<sub>p</sub>+ $\alpha$ +L). The pseudoplasticity (or shear-thinning behavior) of these slurries was obtained by step changes of shear rate from a given initial shear rate. To study the thixotropic behavior of the system, a slurry was allowed to rest for different periods of time, prior to shearing at a given initial shear rate. The major conclusions are the following:

- (1) In the continuous cooling experiments, the viscosity of these slurries was dependent on shear rate, cooling rate, volume fraction of solid, including silicon carbide particulates and/or primary solid of matrix alloy. The addition of the small, non-deformable ceramic particulates contributed not only to reduce the viscosity of such composite slurries, but also to refine the primary solid particles and act as an obstacle to the agglomeration of the primary phase of the matrix alloy.

- (2) In the isothermal experiments, all three kinds of slurries exhibited non-Newtonian shear-thinning (or pseudoplastic), and thixotropic properties depending on the volume fraction of solid particles.
- (3) The composite slurries with 20 and 30vol%SiC and a matrix alloy slurry with 40vol% of primary solid exhibited clear pseudoplasticity up to a critical shear rate, above which they showed high shear limit Newtonian viscosities. The viscosity of a slurry when it was sheared at higher initial shear rate, was lower than that of a slurry sheared at lower initial shear rate.
- (4) When a slurry sample was sheared after a period of rest, the viscosity displayed a characteristic transient stage, i.e., a gradual decrease from an initial peak value to a steady state. The rate of viscosity decrease in the transient stage was dependent on the initial shear rate, rest time, and material variables such as the volume fraction and the kind of solid phase, i.e., non-deformable ceramic particulate or deformable, shape-changing primary solid of the matrix alloy.
- (5) The steady state viscosity was also dependent on the initial shear rate and the amount and size of the solid phase. A composite slurry in the fully molten state showed higher viscosity than an alloy slurry with an equivalent solid fraction. This can be explained in terms of surface area per unit volume of solid particles which affects the resistance of particles to flow under shearing: the smaller silicon carbide would have much larger surface area per unit volume than the larger primary solid particles.

The composite slurry with the matrix in the semi-solid state, however, exhibited a lower viscosity than the matrix alloy slurry with an equivalent total volume fraction of solid. This composite slurry contains two sizes of particles, which could contribute to reduction in the viscosity of such a polydispersed slurry.

## CHAPTER 8.

### SUGGESTIONS FOR FUTURE RESEARCH

#### (1) Data in the Lower Shear Rate Range:

The range of shear rate employed in this study is somewhat higher than those used in other works. Even though the present shear rates are considered to be more effective in the practical processing of these composites, it is still required to collect data from the low shear rate ranges, such as shear rates below  $100 \text{ s}^{-1}$ . In the present research, the low shear limit viscosity was not obtained in structure curves because the present shear rate was too high to reveal it.

#### (2) Microstructures:

Since every rheological behavior is directly related to the actual microstructure, more intensive study on the microstructure is suggested. More combinations of the volume fractions of ceramic particulates and primary solid particles are required to elucidate the role of ceramic particulates.

#### (3) Kinds and Sizes of Ceramic Particulates:

The physical and chemical interactions of a ceramic particulate with the matrix alloy in the liquid or in the semi-solid state are very important factors which affect the rheological behavior as well as the microstructure of a slurry. Hence, it is recommended to study several material systems of ceramic particulates and matrix alloys.

# APPENDICES

## APPENDIX 1.

### CALCULATION OF FRACTION SOLID OF MATRIX ALLOY

The phase diagram of aluminum-silicon shown in Fig. 3.1(a) was reproduced from an enlargement of a published phase diagram [162]. The liquidus of the aluminum-rich region of the diagram is rather curved than straight. Hence, a regression analysis was applied to find the equation for the liquidus as follows.

$$T_L = 660.15 - 5.74 C_L^* - 7.09 \times 10^{-2} C_L^{*2} \quad (A-1)$$

where  $C_L^*$  is the liquidus composition in wt%Si between 0 and 12.64.

On the other hand, the solidus of the diagram was quite straight, so that we have:

$$T_S = - 53.3 C_S^* + 660.15 \quad (A-2)$$

where  $C_S^*$  is the solidus composition, ranging from 0 to 1.56 wt%Si.

#### By The Equilibrium Lever Rule

Weight fraction of the solid phase can be given directly by the lever rule from the equilibrium phase diagram:

$$f_s = \frac{C_L^* - C_o}{C_L^* - C_S^*} \quad (A-3)$$

**By The Scheil Equation:**

$$(C_L - C_S^*) df_s = (1 - f_s) dC_L \quad (A-4)$$

$$df_s / (1 - f_s) = dC_L / (C_L - C_S^*) \quad (A-5)$$

From (A-4) and (A-5),

$$C_L - C_S^* = aC_L + bC_L^2 \quad (A-6)$$

where  $a = 0.892$  and  $b = -1.33 \times 10^{-3}$ . Integrating from  $f_s = 0$  to  $f_s$  and  $C_0$  to  $C_L$ , then we obtain

$$f_s = 1 - \left\{ \left( \frac{a+bC_L}{a+bC_0} \right) \left( \frac{C_0}{C_L} \right) \right\}^{1/a} \quad (A-7)$$

The results of the two calculations of weight fraction solid by eqns. (A-3) and (A-7) are shown in Fig. A.1. The difference between these two fractions solid of Al-7wt%Si alloy ranges from 0 at melting point of the alloy to a maximum of about 4 % at the eutectic temperature.

If the volume fraction of the solid phase ( $g_s$ ) is needed, a density correction should be applied as follows.

$$g_s = \frac{\rho_L f_s}{\rho_L f_s + \rho_S (1-f_s)} = \frac{\rho_L f_s}{\rho_S + (\rho_L - \rho_S) f_s} \quad (A-8)$$

From a rough estimation of densities, 2.5 for liquid phase and 2.8 for solid phase, the difference of  $g_s$  and  $f_s$  is about 10%: for example, when  $f_s = 0.20$ ,  $g_s = 0.18$ . Since we do not have exact data on densities of the alloy solid and liquid phases with temperature, it would be quite reasonable to use weight fraction as volume fraction with a small error.



## APPENDIX 2.

### COUETTE CONCENTRIC CYLINDER VISCOMETRY

#### A2.1. Exact Solution of Navier-Stokes Equations

For flow between two concentric rotating cylinders, both of which move at different but steady rotational speeds, the following assumptions are made for an ideal system :

- the fluid is incompressible
- the flow of the fluid is not turbulent
- circular streamlines on the horizontal planes perpendicular to the axis of rotation
- no relative motion between the cylinders and the material in immediate contact with the cylinders
- the motion of the liquid is the same on each plane perpendicular to the axis of rotation, that is, the motion is two dimensional
- neglect of gravitational force and pressure differences
- no wall slippage
- negligible end effects.

Then, there remains only one velocity component,  $u_\theta$ , in cylindrical coordinates. The Navier-Stokes equation is reduced to:

$$0 = \frac{\partial}{\partial r} \left[ \frac{1}{r} \frac{\partial}{\partial r} (ru_\theta) \right] \quad (\text{A-9})$$

or

$$u_\theta = \frac{1}{2} C_1 r + \frac{C_2}{r} \quad (\text{A-10})$$

The boundary conditions are:  $u=R_1\Omega_1$  for  $r=R_1$ , which is the peripheral velocity of the inner cylinder, and  $u=R_2\Omega_2$  for  $r=R_2$ , which is the peripheral velocity of the outer cylinder. Letting  $u_0=u$ , one can obtain the solution for eqn. (A-9) is

$$C_1 = 2 \frac{R_2^2 \Omega_2 - R_1^2 \Omega_1}{R_2^2 - R_1^2}$$

$$C_2 = - \frac{R_2^2 R_1^2}{R_2^2 - R_1^2} (\Omega_2 - \Omega_1)$$

$$u(r) = \frac{1}{R_2^2 - R_1^2} [r(\Omega_2 R_2^2 - \Omega_1 R_1^2) - \frac{R_1^2 R_2^2}{r} (\Omega_2 - \Omega_1)] \quad (\text{A-11})$$

### Velocity Distribution

The velocity distribution in the annulus between the two cylinders is shown in Fig. A2 [1]. Denoting the ratio of the two radii by  $\beta=R_1/R_2$ , the gap of the annulus by  $d=R_2-R_1$ , and the current relative radius by  $x=r/R_2$ , we obtain

$$(I) \quad \frac{u}{u_1} = \frac{\beta}{1 - \beta} \frac{1 - x^2}{x} \quad (\Omega_1 \neq 0, \Omega_2 = 0: \text{Searle type}) \quad (\text{A-12})$$

$$(II) \quad \frac{u}{u_2} = \frac{\beta}{1 - \beta} \left( \frac{x}{\beta} - \frac{\beta}{x} \right) \quad (\Omega_1 = 0, \Omega_2 \neq 0: \text{Couette-Hatschek type}) \quad (\text{A-13})$$

From these distributions, we find that:

- the velocity is very strongly dependent on  $\beta$  in case I, whereas nearly independent of  $\beta$  in case II,

- when the value of  $\beta$  is close to 1, both curves tend to the linear velocity distribution of Couette flow,
- and for case II, there are two asymptotic curves, for  $\beta = 0$  and 1.

### Shear Stress

$$\tau_{r\theta} = -\eta \left[ r \frac{\partial}{\partial r} \left( \frac{u_\theta}{r} \right) \right] \quad (\text{A-14})$$

$$\tau_{r\theta} = \frac{2\eta}{r^2} C_2 \quad (\text{A-15})$$

With the boundary conditions, the solution for the shear stress is:

$$\tau_{r\theta} = -\frac{2\eta}{r^2} \frac{R_2^2 R_1^2}{R_2^2 - R_1^2} (\Omega_2 - \Omega_1) \quad (\text{A-16})$$

### Torque Measurement

When the inner cylinder is at rest while the outer cylinder rotates, the torque transmitted by the outer cylinder to the fluid becomes, when  $\Omega_1=0$ ,  $\Omega_2 \neq 0$ ,

$$M_2 = (2\pi R_2 h \tau_{r\theta}) R_2 = -4\pi h \eta \frac{R_1^2 R_2^2}{R_2^2 - R_1^2} \Omega_2 \quad (\text{A-17})$$

where  $h$  is the length of contact between the inner cylinder and the sample along the  $z$ -axis. The moment  $M_1$  with which the fluid acts on the inner

cylinder has the same magnitude as  $M_2$ . By measuring  $M_1$  and  $\Omega_2$ , viscosity,  $\eta$ , can be obtained.

When the outer cylinder is at rest while the inner cylinder rotates, the torque transmitted by the inner cylinder to the fluid becomes

$$M_1 = (2\pi R_1 h \tau_{r\theta}) R_1 = 4\pi h \eta \frac{R_1^2 R_2^2}{R_2^2 - R_1^2} \Omega_1 \quad (\text{A-18})$$

when  $\Omega_1 \neq 0$ ,  $\Omega_2 = 0$  at  $r = R_1$ . In the special case of a single cylinder rotating in an infinite fluid ( $R_2 \rightarrow \infty$ ,  $\Omega_2 = 0$ ), eqn. (A-11) gives  $u = R_1^2 \Omega_1 / r$ , and the torque to the cylinder becomes  $M_1 = 4\pi \eta h R_1^2 \Omega_1$ .

### Shear Rate

Assuming Newtonian fluid flow, we have the viscosity of the fluid as the ratio of the shear stress to the shear rate:

$$\tau_{r\theta} = -\eta \dot{\gamma}$$

From eqn. (A-16),

$$\dot{\gamma}(r) = -\frac{2R_1^2 R_2^2}{R_2^2 - R_1^2} \frac{\Omega_2 - \Omega_1}{r^2} \quad (\text{A-19})$$

Hence,

$$\dot{\gamma} = \frac{2}{1 - \beta^2} \Omega_1 \quad \text{at } R_1 \text{ when } \Omega_1 \neq 0, \Omega_2 = 0 \quad (\text{A-20})$$

$$\dot{\gamma} = -\frac{2\beta^2}{1-\beta^2} \Omega_2 \quad \text{at } R_2 \text{ when } \Omega_1 = 0, \Omega_2 \neq 0 \quad (\text{A-21})$$

The average shear rate through the gap is calculated as:

$$\begin{aligned} \dot{\gamma}_{\text{avg}} &= \int_{R_1}^{R_2} \dot{\gamma}(r) dr / (R_2 - R_1) \\ &= -\frac{2\beta}{1-\beta^2} (\Omega_2 - \Omega_1) \end{aligned} \quad (\text{A-22})$$

$$\text{Or, when } (R_2 - R_1)/R_1 \ll 1, \quad = -\frac{\beta}{1-\beta} (\Omega_2 - \Omega_1) \quad (\text{A-23})$$

### Newtonian Viscosity

Finally, the Newtonian viscosity of a Newtonian fluid can be given by combining eqns. (A-17) with (A-20), and (A-18) with (A-21):

$$\eta = \frac{R_2^2 - R_1^2}{4\pi h R_2^2 R_1^2} \frac{M_1}{\Omega_1} \quad \text{when } \Omega_1 \neq 0, \Omega_2 = 0 \quad (\text{A-24})$$

$$\eta = \frac{R_2^2 - R_1^2}{4\pi h R_2^2 R_1^2} \frac{M_2}{\Omega_2} \quad \text{when } \Omega_1 = 0, \Omega_2 \neq 0 \quad (\text{A-25})$$

The rheological constants of these equations are summarized in Table A1 for various rotor dimensions.

### A2.2 Calibration

#### End Effect Correction

The theoretical derivation of the apparatus constant,  $K$ , in  $\eta_a = K \cdot \Omega$  assumes that the cylinders are of infinite length. Hence, in practice, the

effect of the ends of the cylinders must be taken into consideration. The end effects can be found experimentally by immersing the inner cylinder to different depths in the liquid to find whether the apparatus constant changes. The effective length,  $h$ , in eqns. (A-24) and (A-25) is  $h_0 + (h_1 + h_2)$ , where  $h_1$  is the end effect due to bottom and  $h_2$  that due to the top [148]. Generally, it is required that the length  $h$  be at least twenty times as long as the shearing gap to exclude the end effects.

### **No slip condition**

An assumption in the derivation of the equation is that there be no slip between the liquid medium and the cylinder. One of the methods to confirm the no-slip condition is to plot torque vs. revolutions per unit time. If there is no slip, the relation is linear and the line passes through the origin. If, however, there is slip, then the straight portion of the graph would not extrapolate back to the origin.

### **A2.3 Stability of Couette Flow**

The stability of laminar flow in Couette flow is largely governed by the centrifugal forces. In case I, eqn. (A-12), the layers at the rotating inner wall experience larger centrifugal forces than those near the outer wall. Hence the case turns out to be highly unstable. It was investigated early by G.I. Taylor [161] for viscous fluids. He discovered the existence of a secondary flow, which is three-dimensional, in the form of ring-like vortices, in excellent agreement between theory and experiment. Such vortices were named Taylor-vortices, and are shown in Fig. A.3. In case II, eqn. (A-12), the larger centrifugal forces occur in the fluid layers at the

outer wall, and this has a stabilizing effect on the flow. Assuming the kinematic viscosity to be 0.01 and 0.1 for the molten matrix alloy and molten composite, respectively, stability conditions in Couette flow are as summarized in Table A2 for various rotor dimensions.

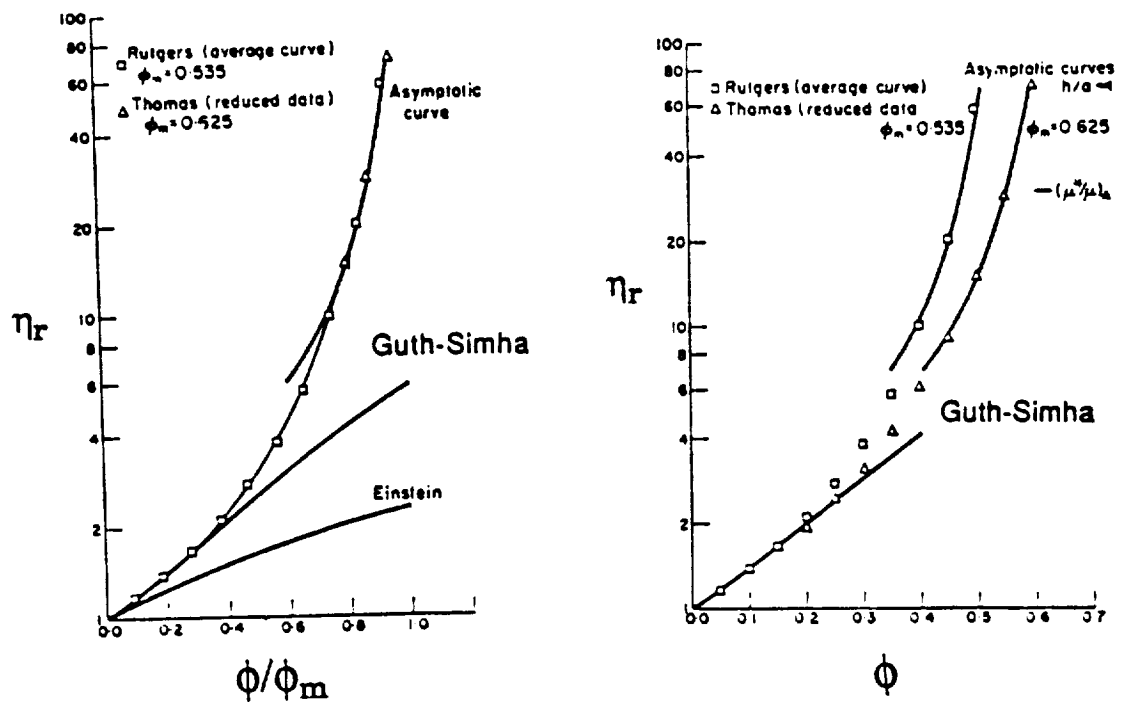


Fig. 2.1 Comparison of an asymptotic relation for the relative viscosity by Frankel-Acrivos [14] with various models of Rutgers [12], Thomas [13], Einstein [8], and Guth-Simha [31]. (a) relative viscosity versus reduced concentration,  $\phi/\phi_m$ , (b) relative viscosity versus concentration.



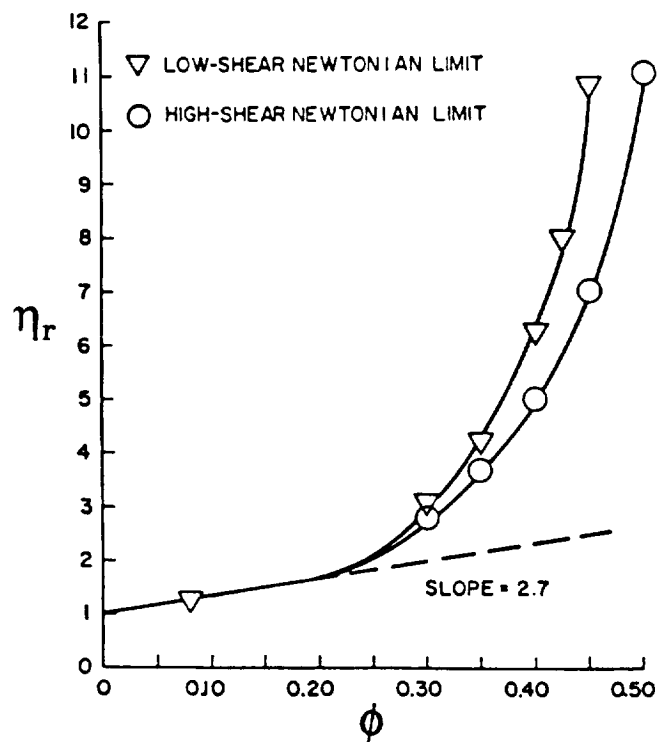


Fig. 2.2 At high concentrations, suspensions may have viscosities between the low shear limiting and high shear limiting values, depending on applied shear rate. The suspension shown here has a pseudoplasticity in which the relative viscosity decreases with increasing shear rate. The difference between the two limiting values may become greater as the concentration of a suspension is higher [37].

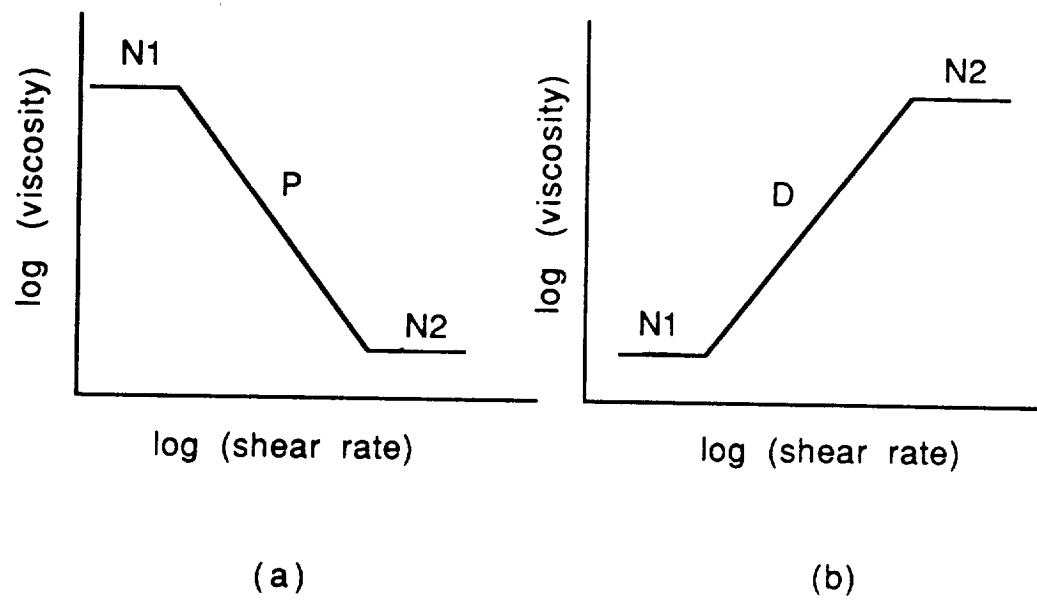


Fig. 2.3 Schematic flow curve at steady state,  $\log \eta$  versus  $\log \dot{\gamma}$ : (a) for a pseudoplastic (shear-thinning) suspension, and (b) for a dilatant (shear-thickening) suspension. N1 and N2 are Newtonians in the low and high shear rate ranges, respectively. P denotes pseudoplasticity and D is for dilatancy.

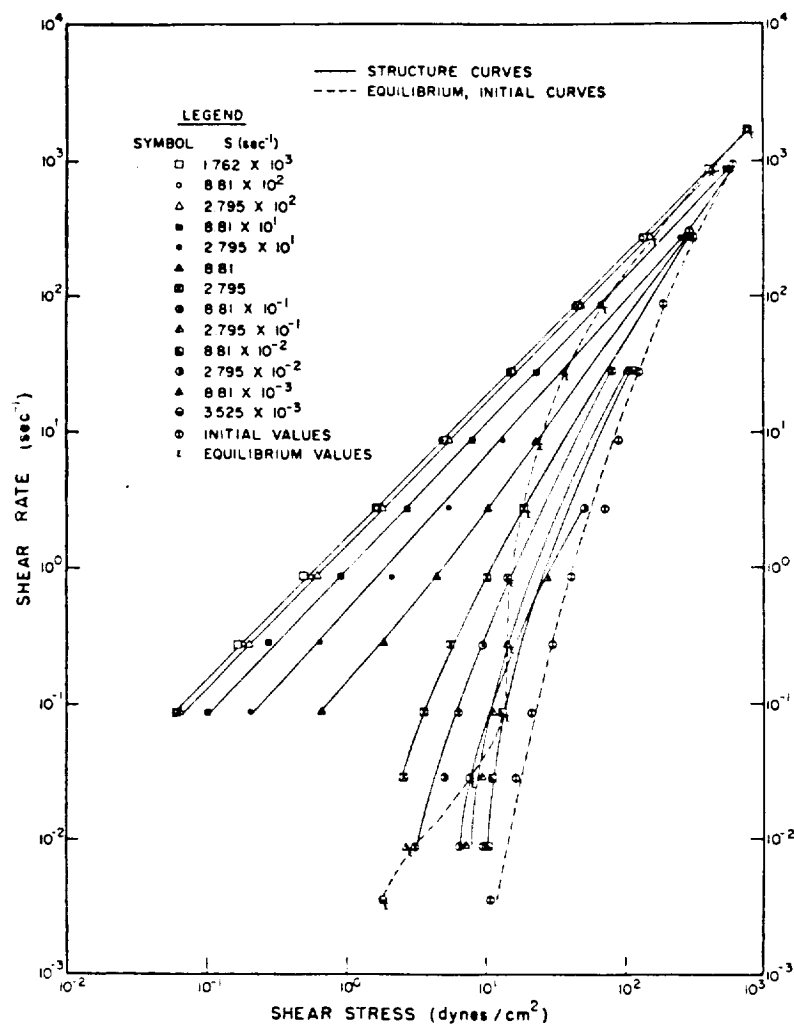


Fig. 2.4 Equilibrium, structure, and initial shear stress curves for a thixotropic suspension of colloidal alumina [67]. All these curves, together with time dependent parameters, are required to understand fully the complicated rheological behavior of thixotropic suspensions.

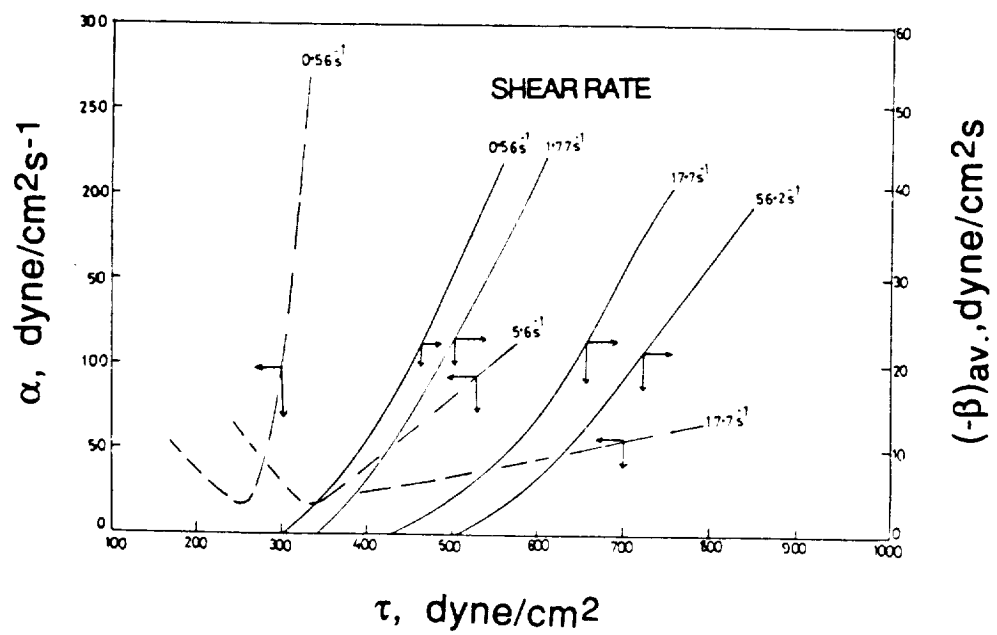


Fig. 2.5 The functional forms of  $\alpha$  and  $\beta$  in Cheng's structural equations can be obtained by experiments [53].

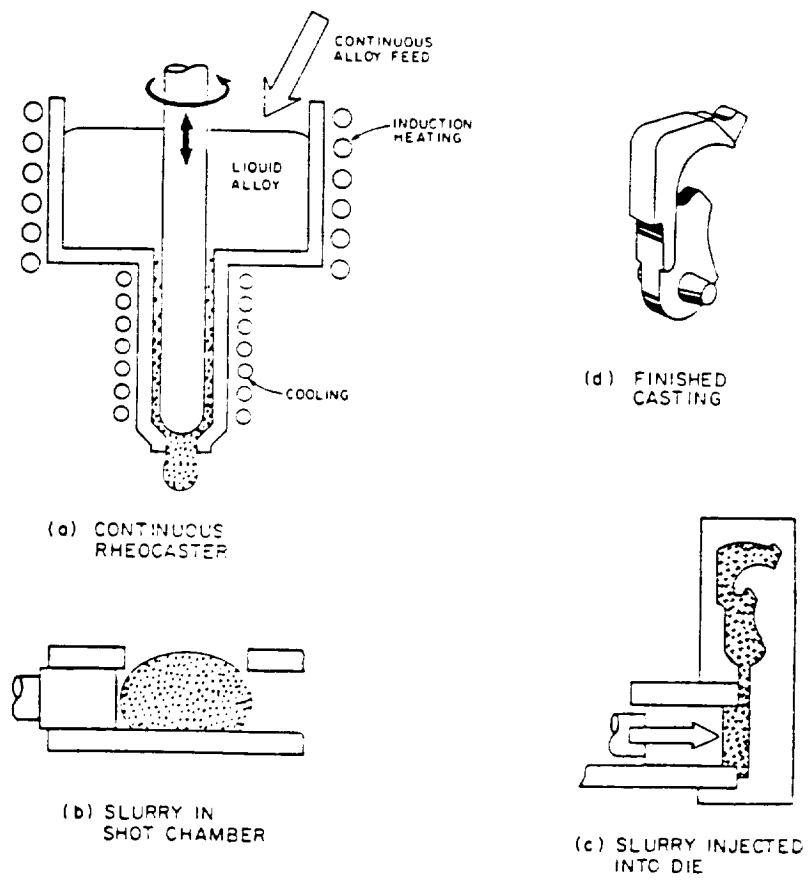


Fig. 2.6 Rheocasting process [71].

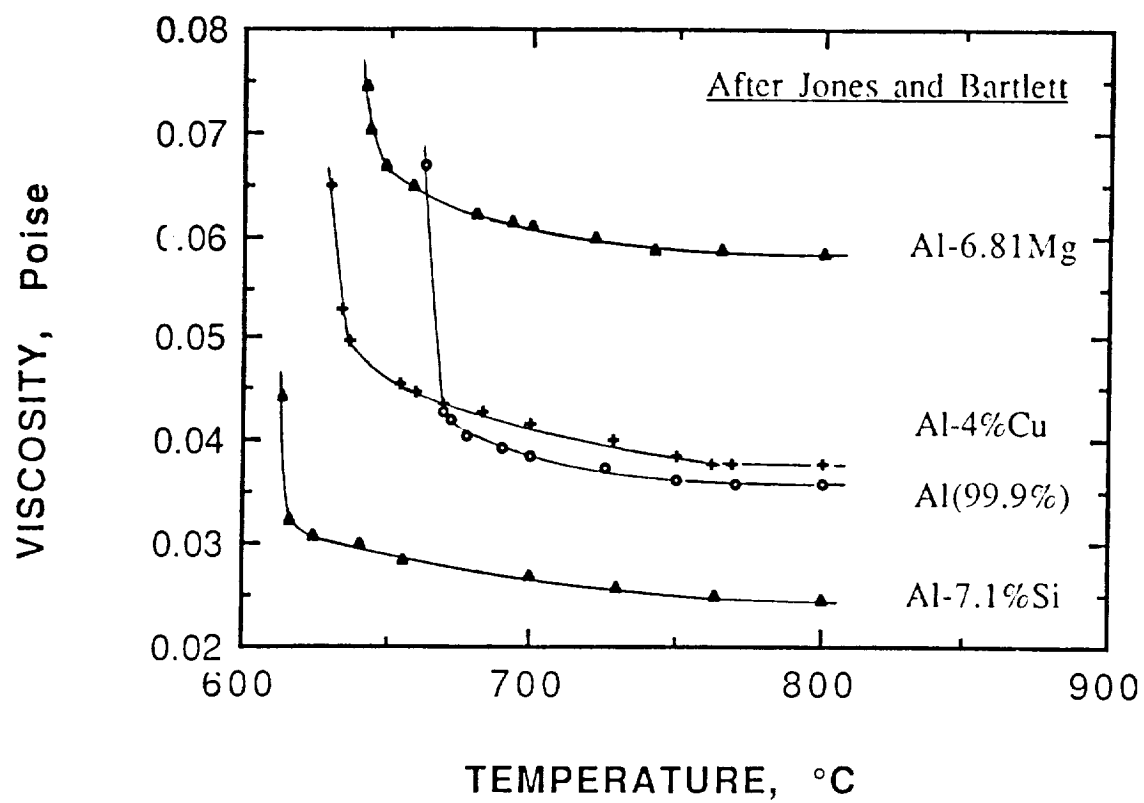


Fig. 2.7 Viscosity of some aluminum alloys in liquid state [148].

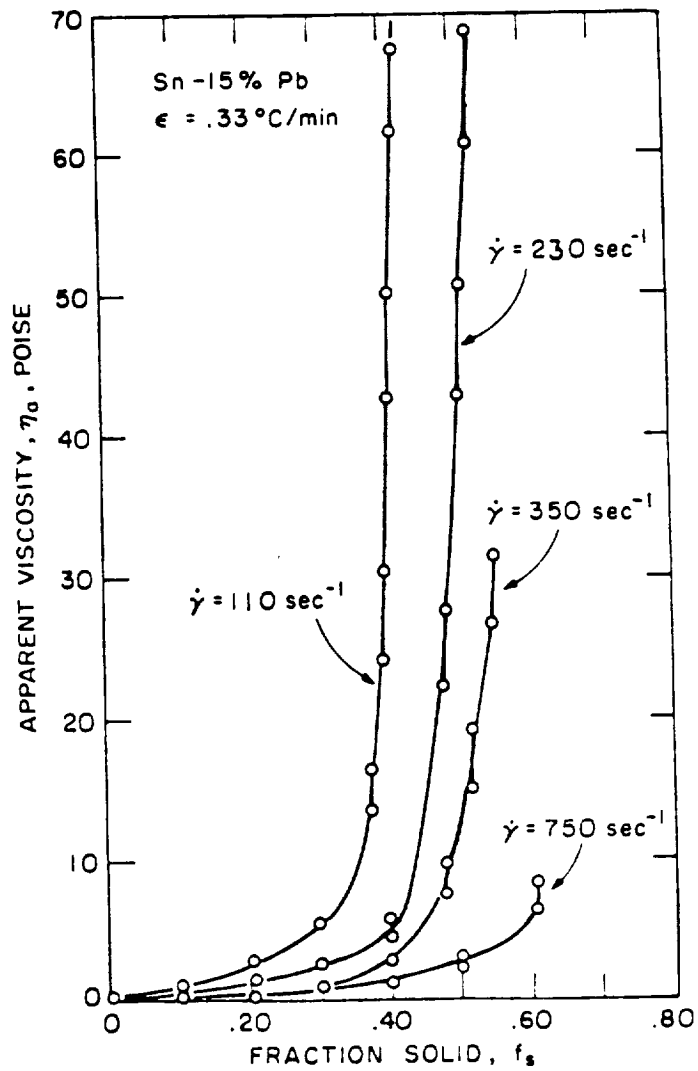


Fig. 2.8 Effect of shear rate on viscosity [72].

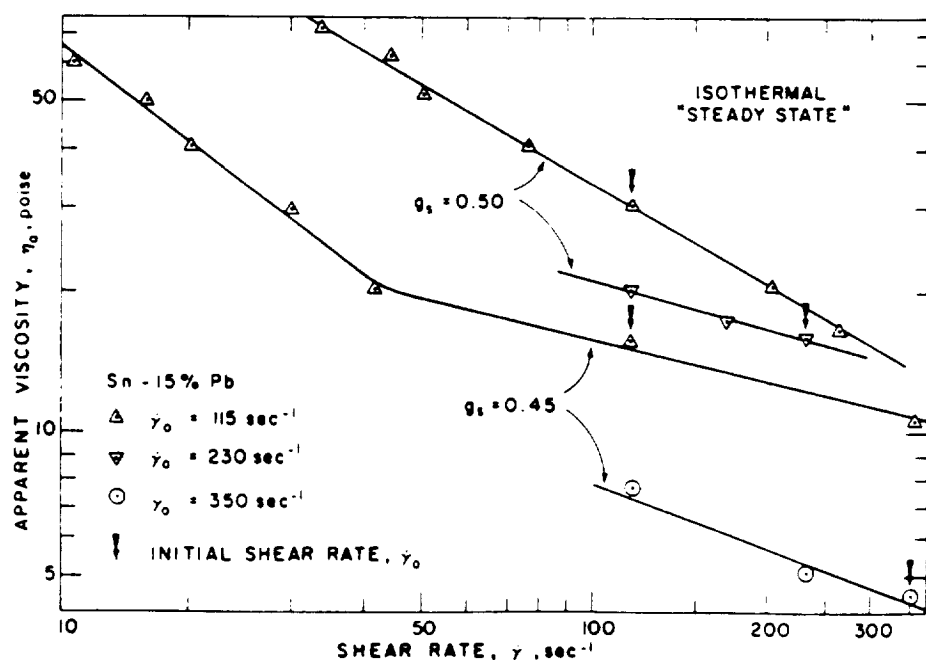


Fig. 2.9 Shear-thinning behavior of a semi-solid alloy slurry. Note the effect of the initial shear rate on viscosity [72].



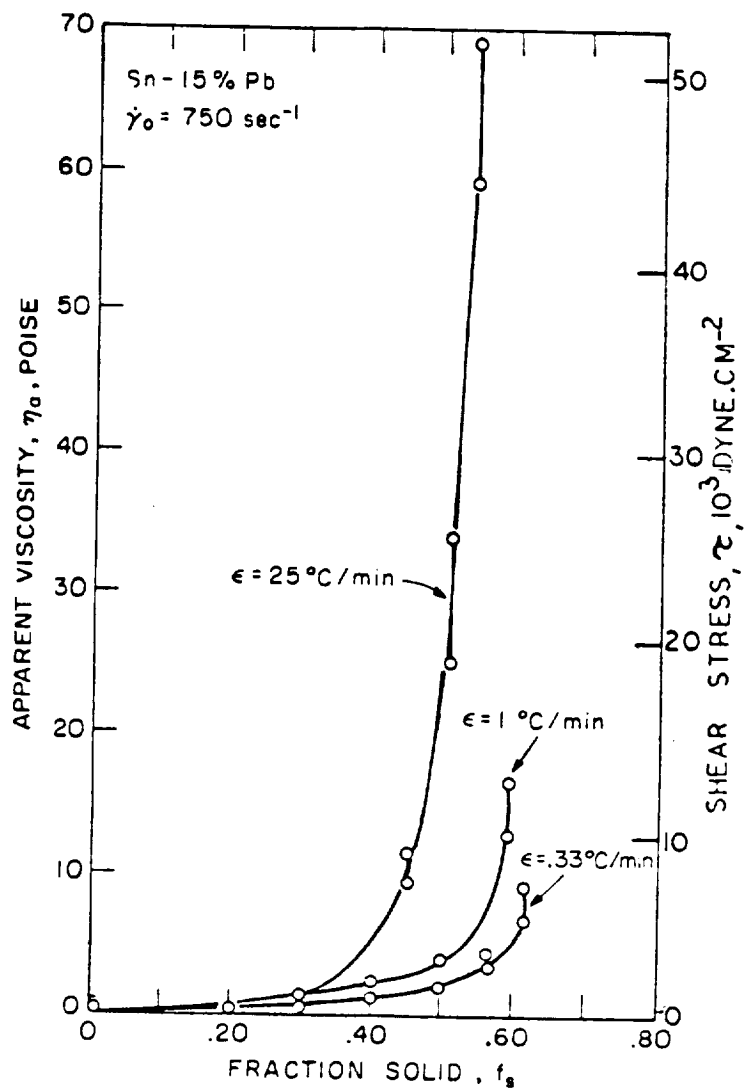


Fig. 2.10 Effect of cooling rate on viscosity [72].

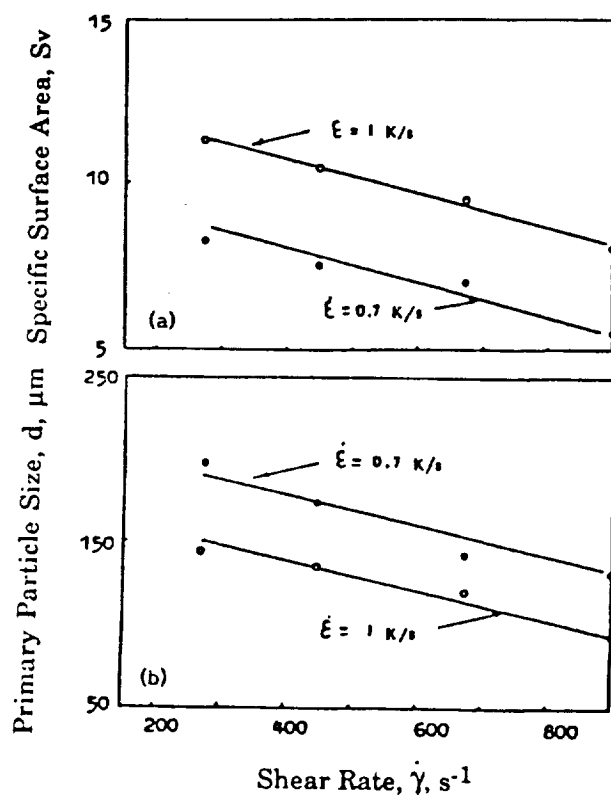


Fig. 2.11 Effect of shear rate and cooling rate on the solid-liquid surface area and primary particle size,  $d$  [108].

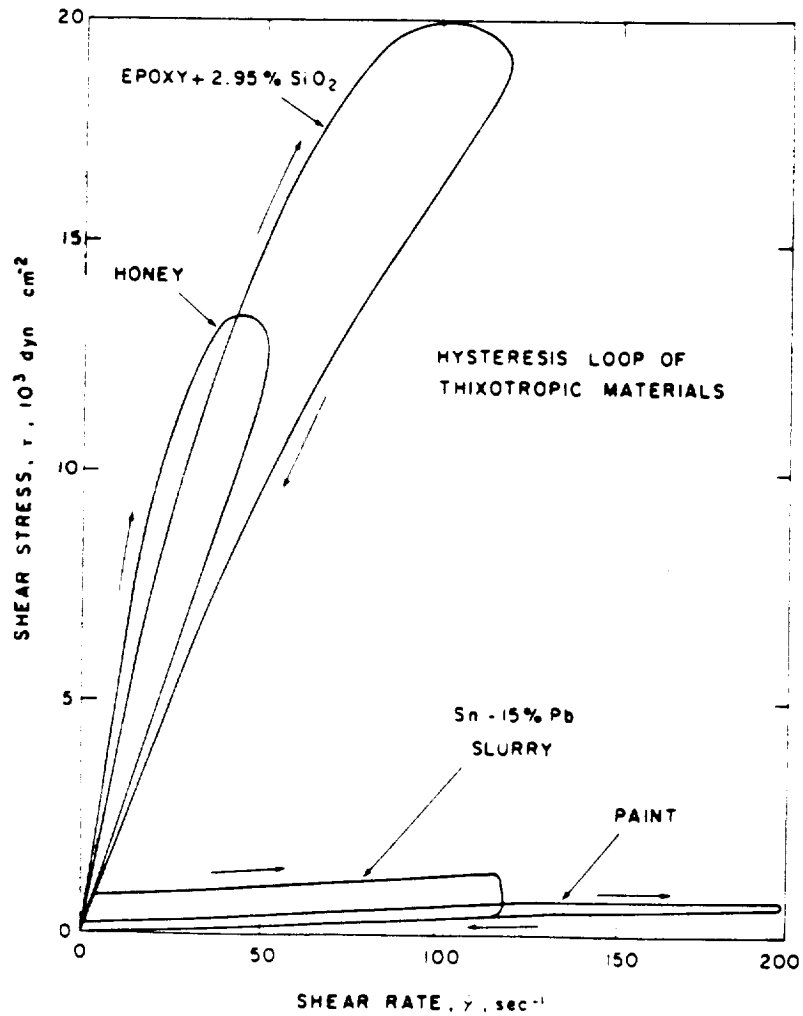


Fig. 2.12 Experimentally determined hysteresis loops of 0.45 volume fraction solid slurry of Sn-15%Pb alloy and some well-known nonmetallic thixotropic materials [72].

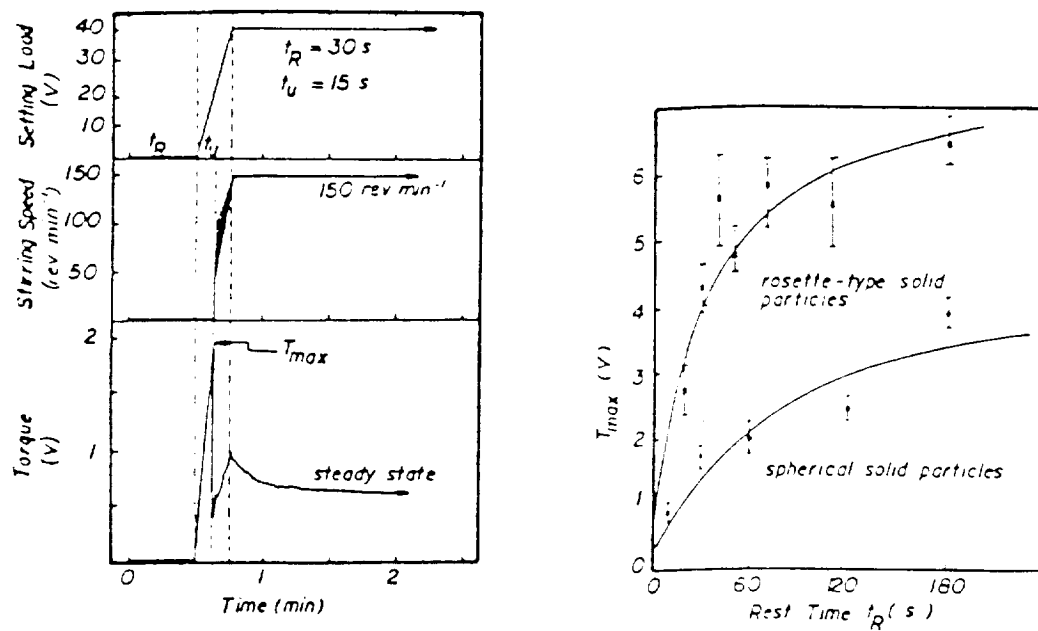


Fig. 2.13 (a) Time dependence of shear stress after a time of rest for Al-15%Cu at  $f_s = 0.4$ . The alloy slurry exhibits the "ultimate shear strength,"  $T_{max}$ , before a new steady state. (b) The shape of primary solid of the alloy affects the value of the maximum stress. Also stress is a strong function of the rest time [94].

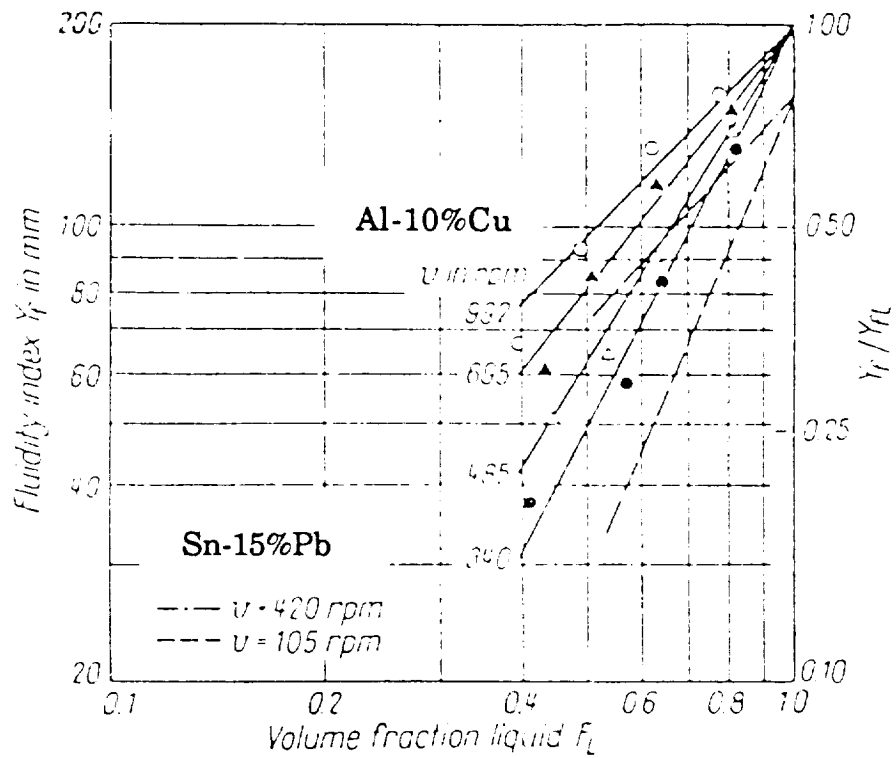


Fig. 2.14 The fluidity of an alloy in semi-solid state decreases with increase of volume fraction solid and decrease in shear rate: (1) Al-10%Cu [86], and (2) Sn-15%Pb [85].

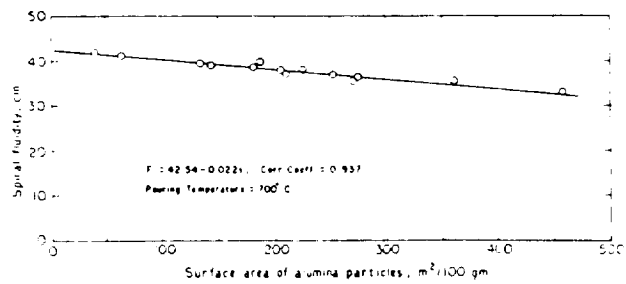
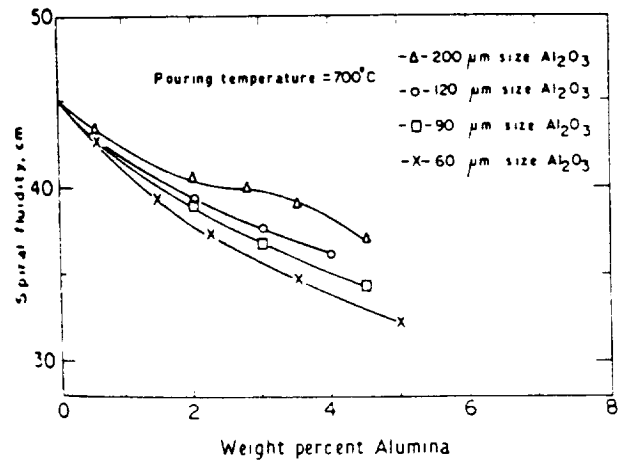
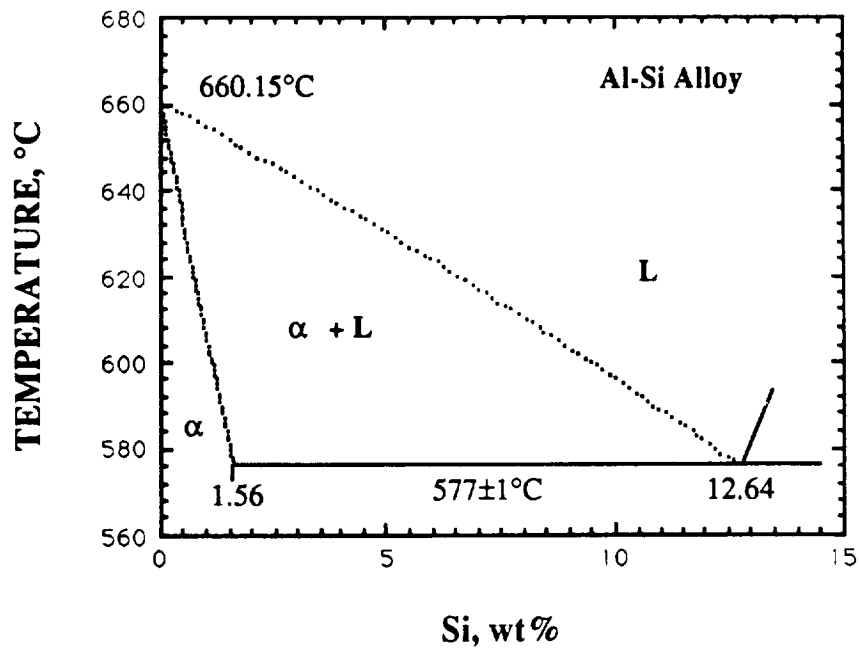
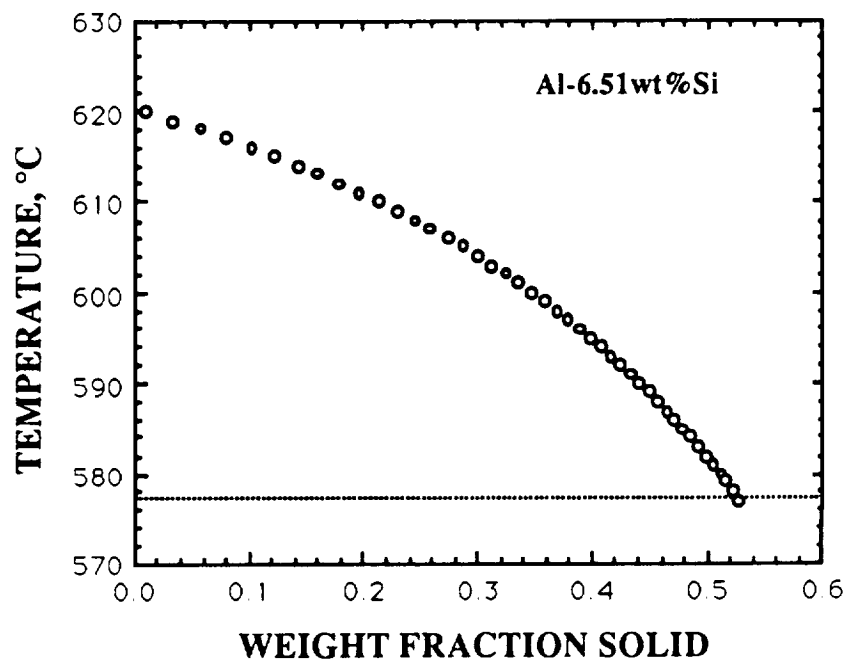


Fig. 2.15 Spiral fluidity of alumina particulate/Al-11Si composite slurry [144].



(a)



(b)

Fig. 3.1 (a) Phase diagram of Al-Si alloy.

(b) Weight fraction solid of primary phase for Al-6.51wt%Si calculated by the Scheil equation.

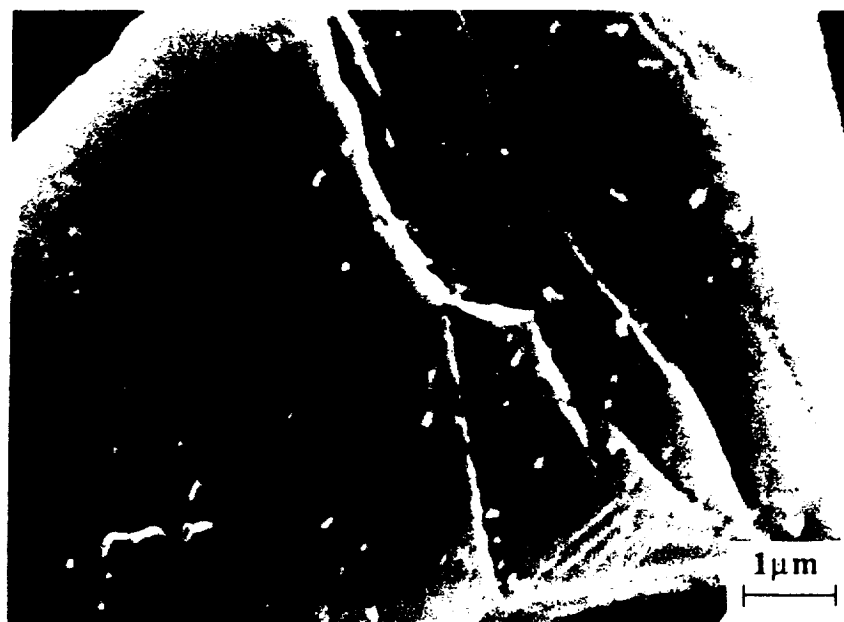


Fig. 3.2 Scanning electron micrograph of high purity silicon carbide (SiC) particulates at different magnifications.



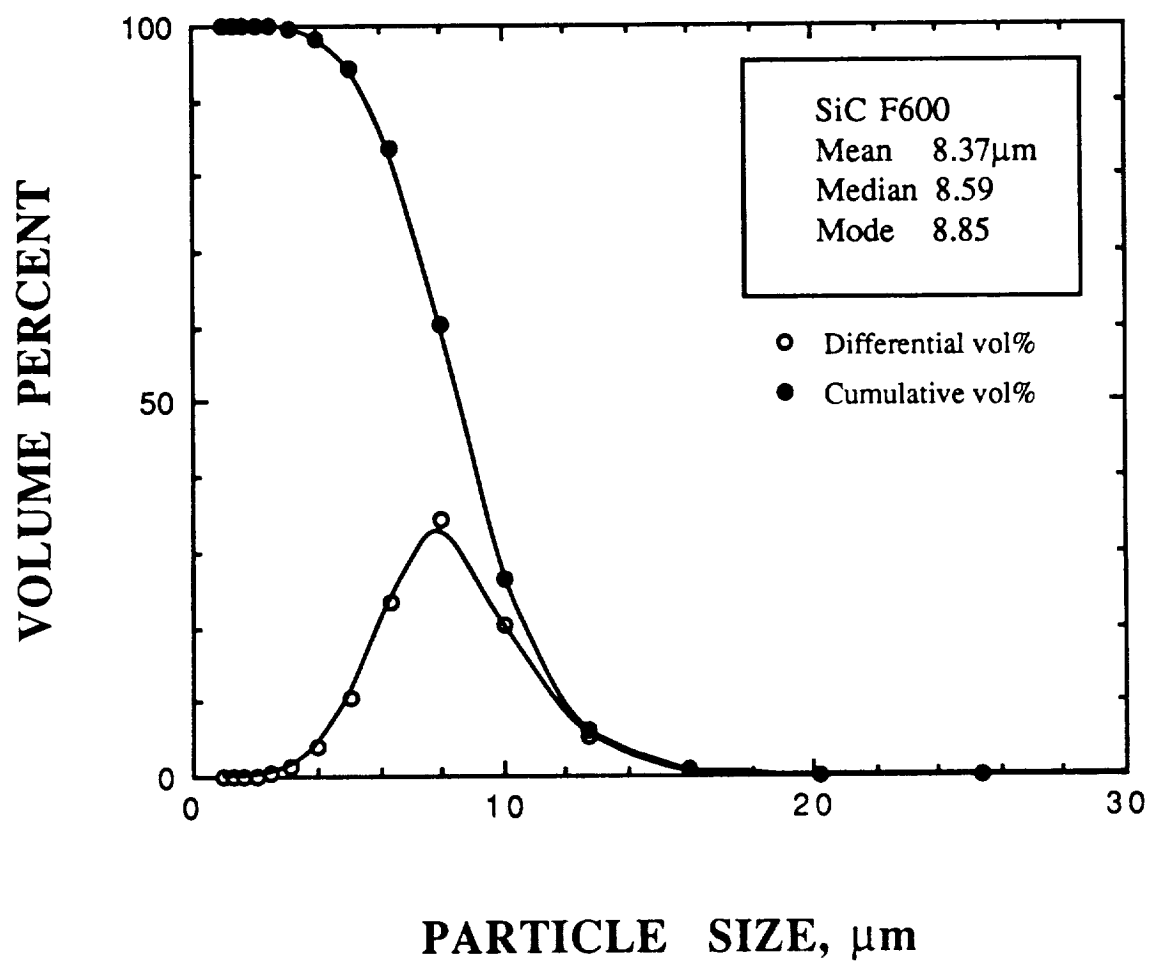


Fig. 3.3 Size distribution of silicon carbide particulates analyzed by a Coulter counter. The average size of the batch is 8.6  $\mu\text{m}$ .

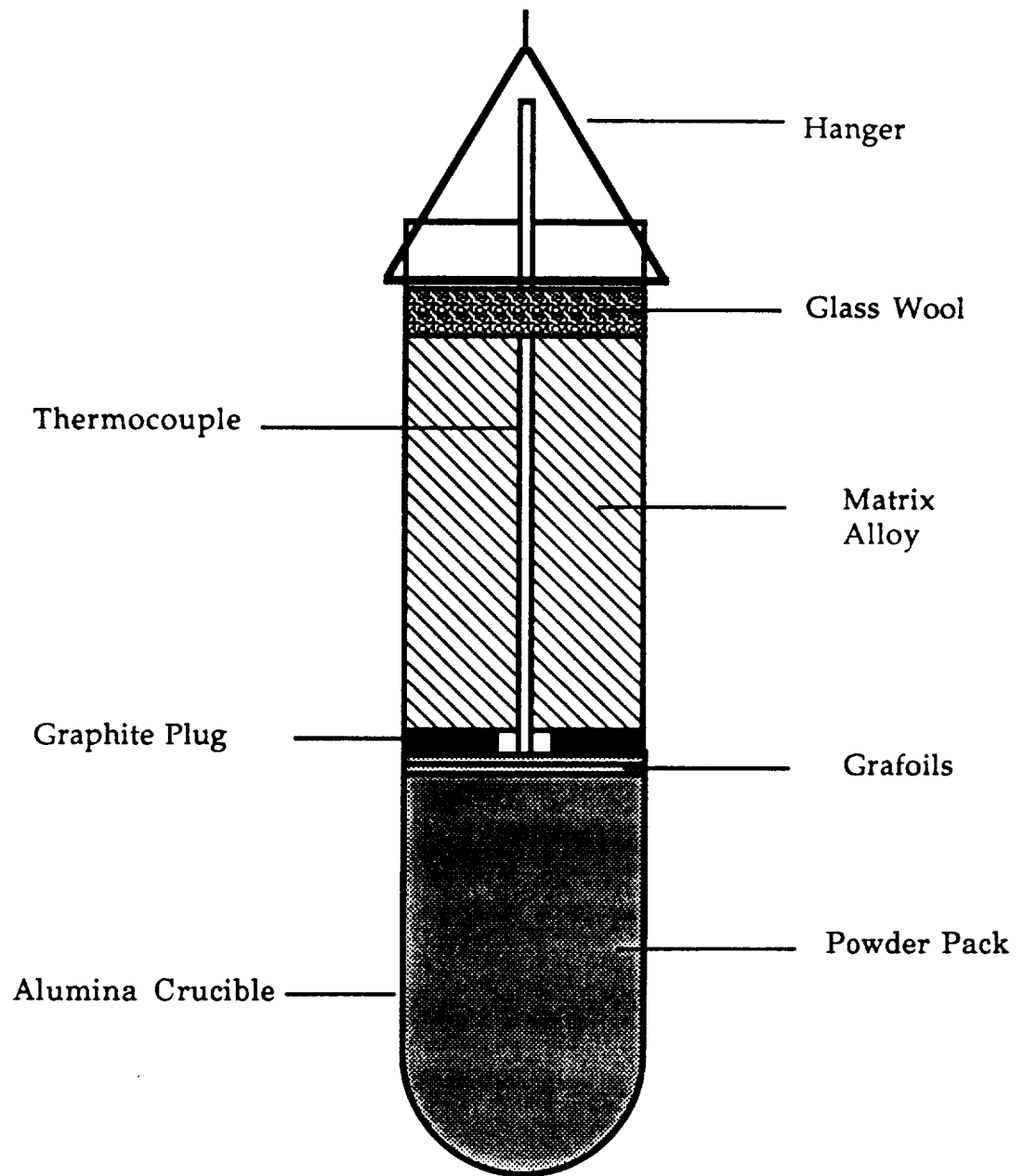


Fig. 3.4 Ceramic particulates and matrix alloy packed into an alumina crucible for pressure infiltration

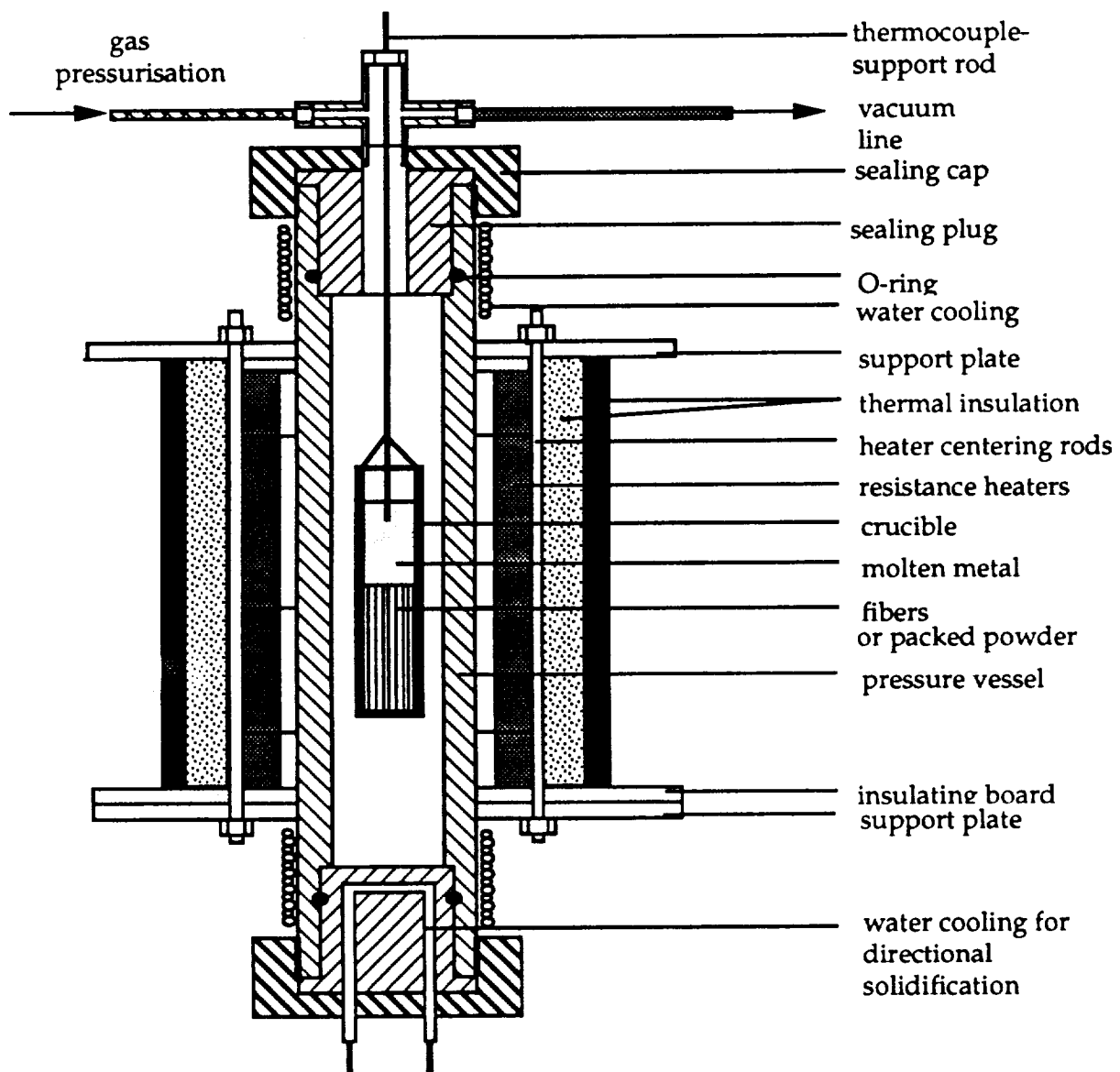


Fig. 3.5 Pressure-infiltration equipment used for the preparation of high density composite compact.

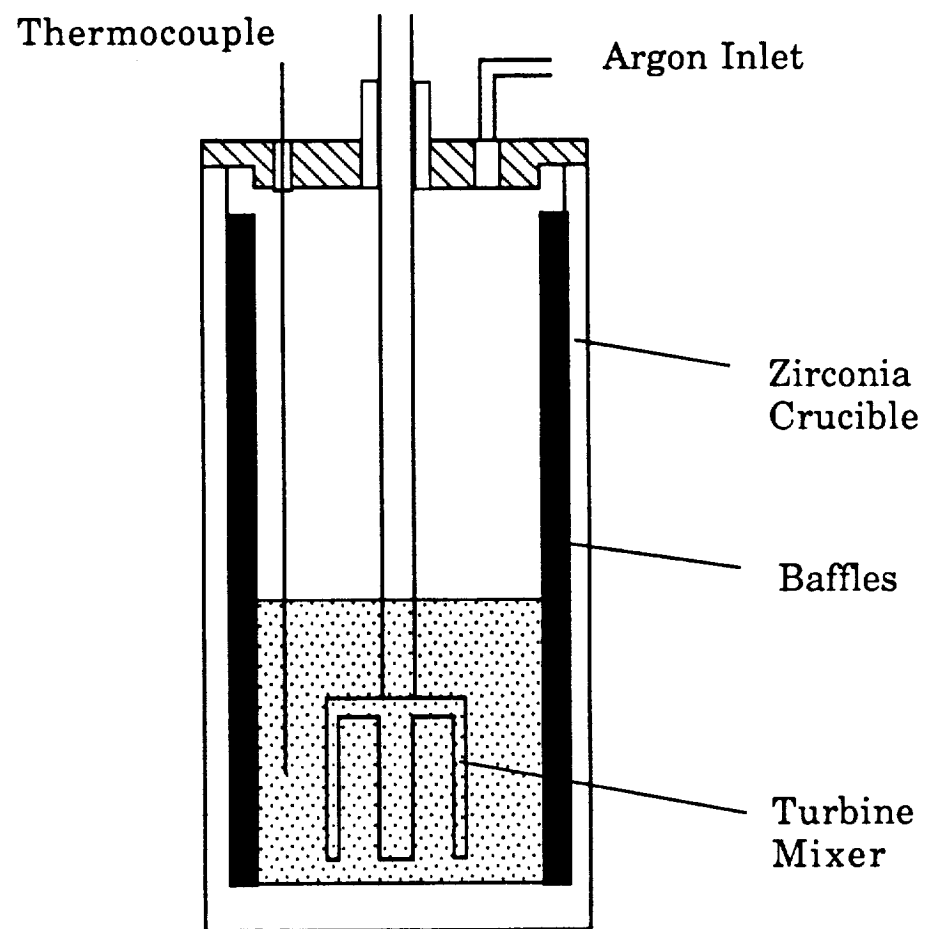
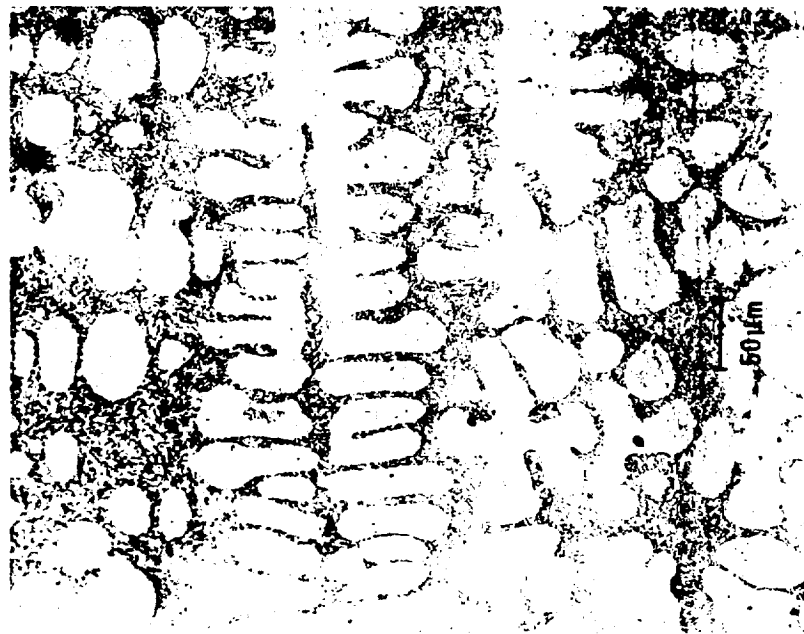
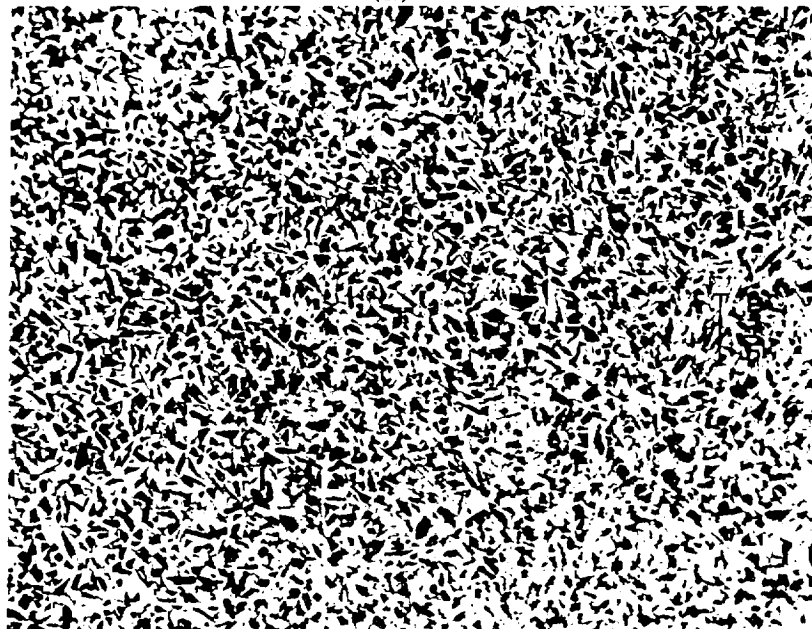


Fig. 3.6 Sketch of an apparatus for the dilution of composite compact.



(a)



(b)

Fig. 3.7 (a) Optical micrograph of Al-6.5wt%Si alloy, conventionally cast without stirring during solidification  
(b) Optical micrograph of a pressure-infiltrated SiC<sub>p</sub>/Al-6.5 wt%Si composite compact.

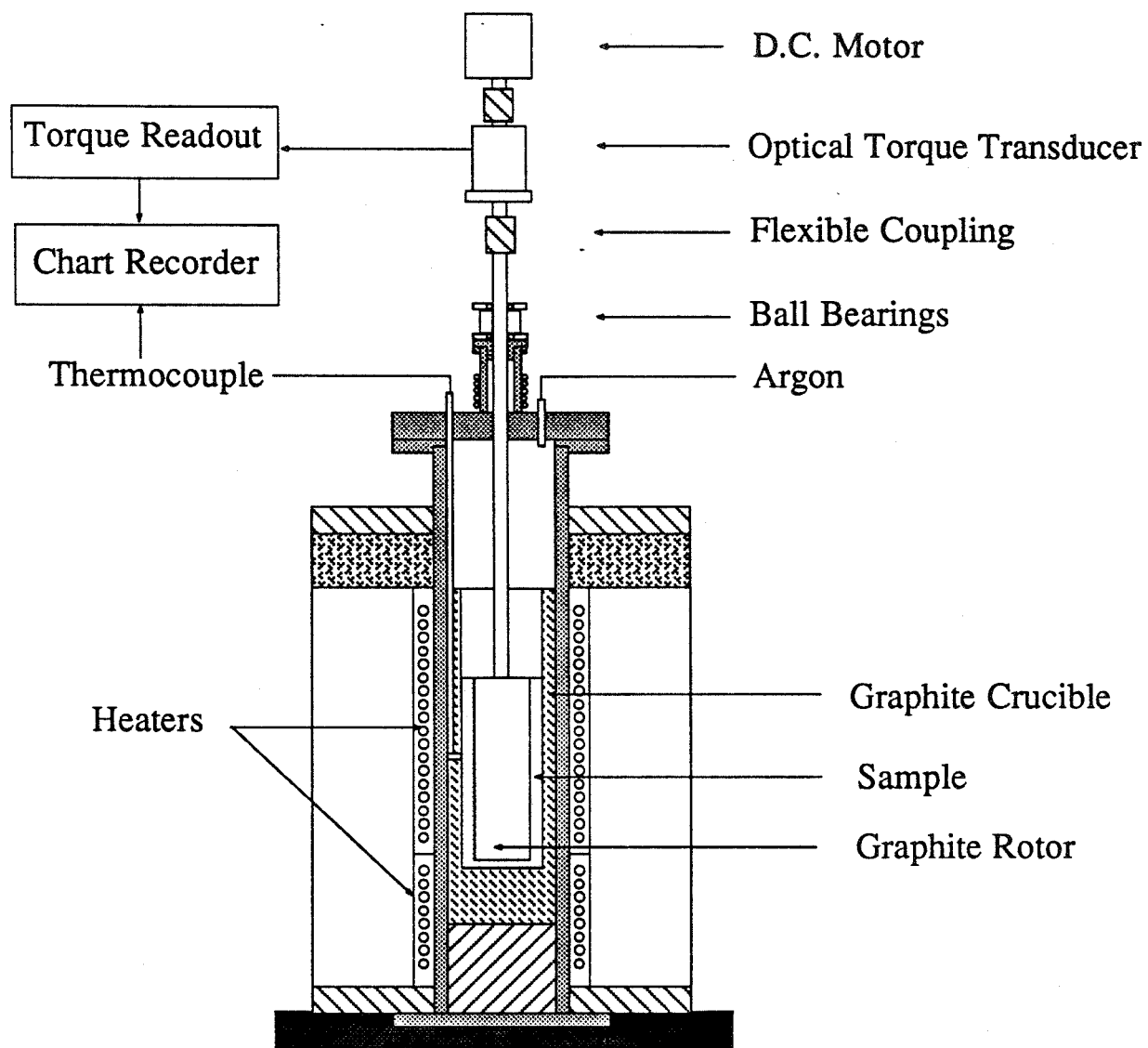


Fig. 3.8 Sketch of experimental apparatus for the rheological study of metallic and composite slurries.

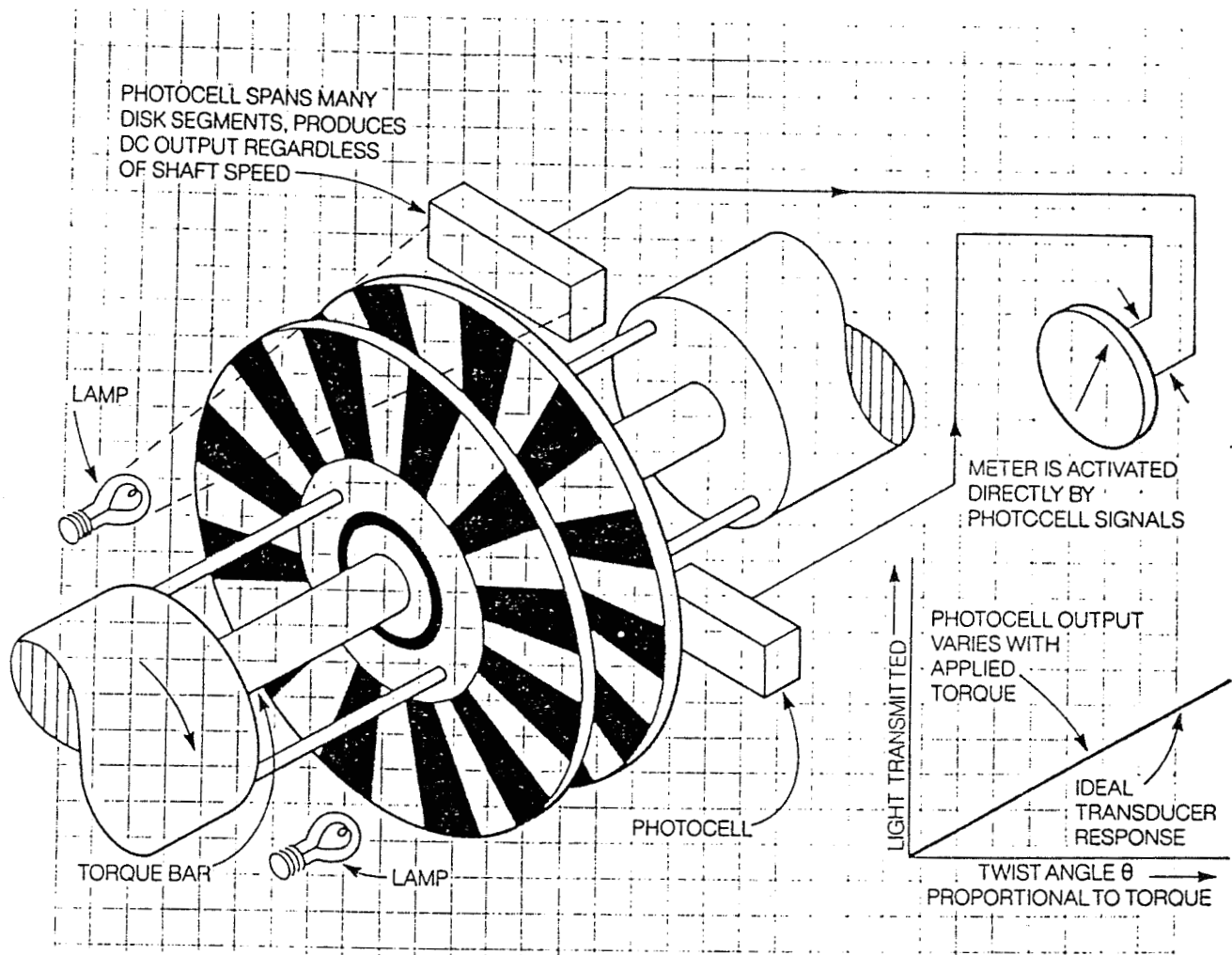


Fig. 3.9 Optical torque transducer: Vibrac® model T3.

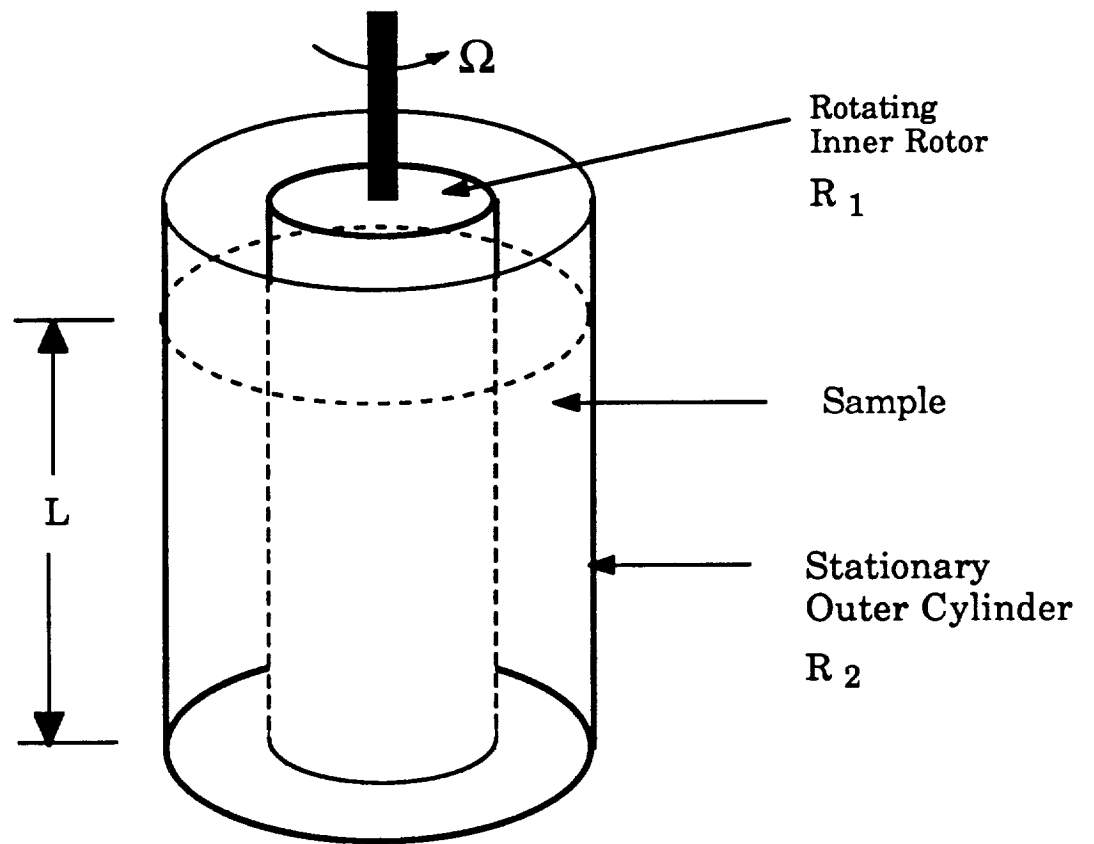


Fig. 3.10 Rotating concentric cylinder viscometer used in this study, often called the Searle-type viscometer.



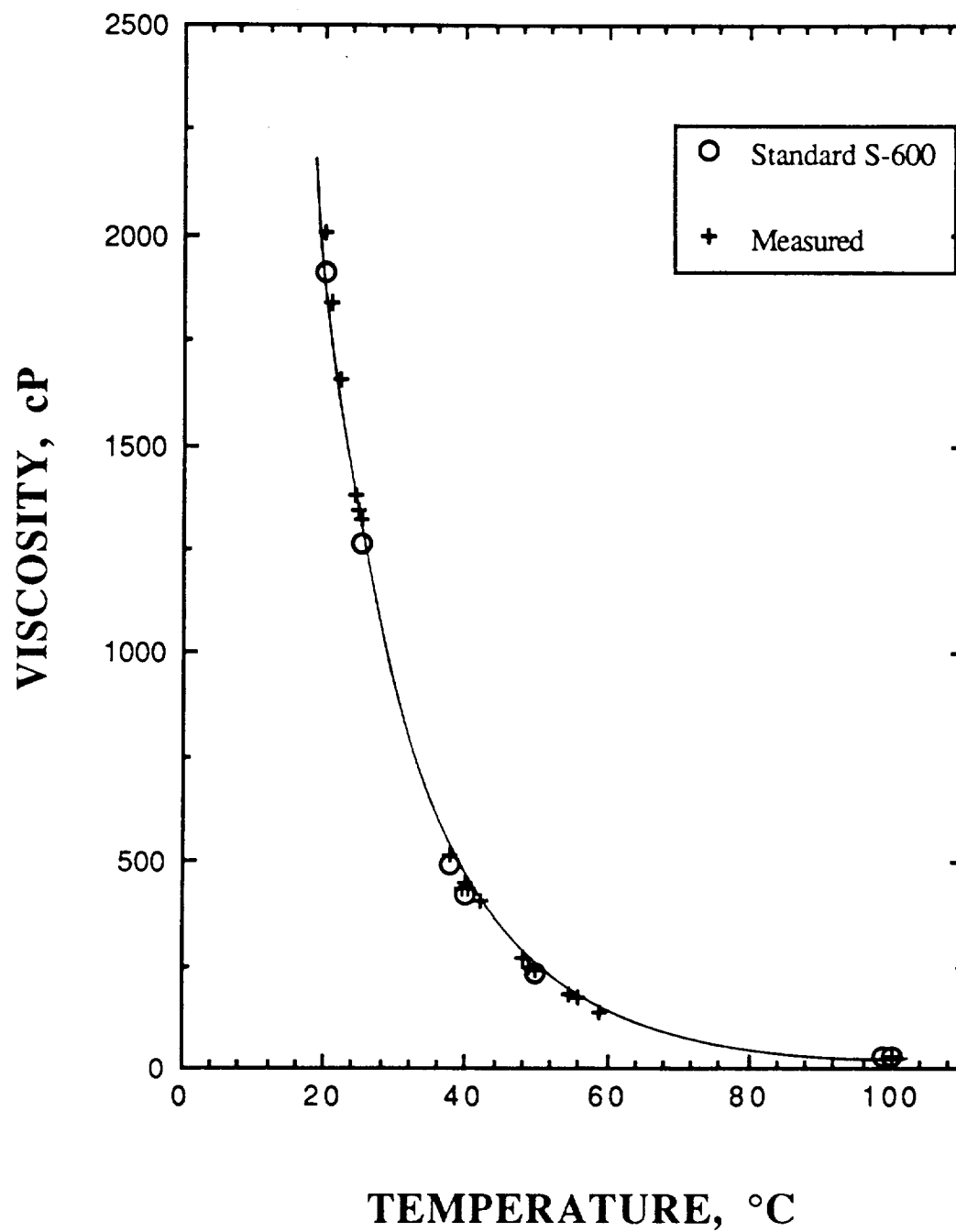
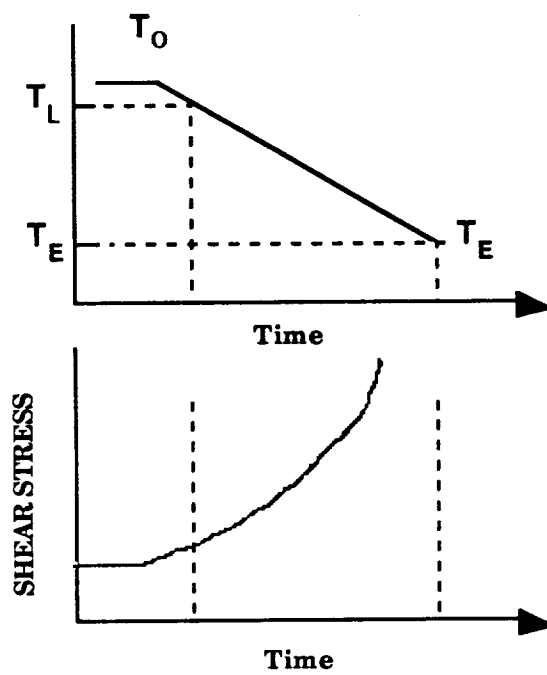
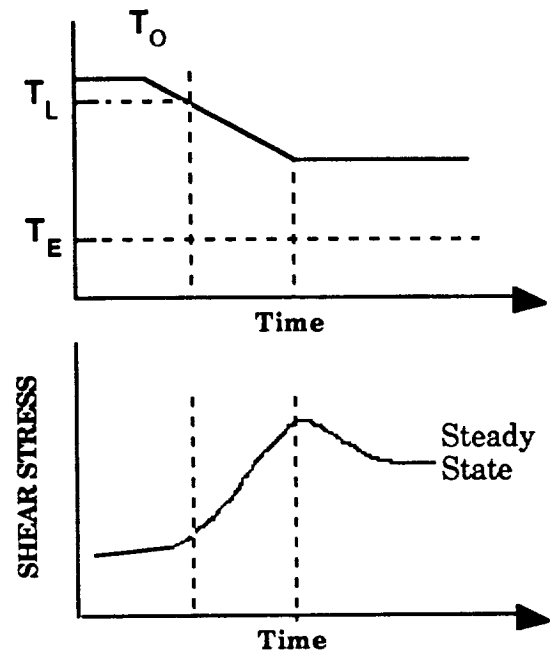


Fig. 3.11 Plot of measured apparent viscosity of S-600 standard oil and standard values.



(A) CONTINUOUS COOLING



(B) ISOTHERMAL CONDITION

Fig. 3.12 Experimental procedures for (a) Continuous cooling and (b) Isothermal experiments

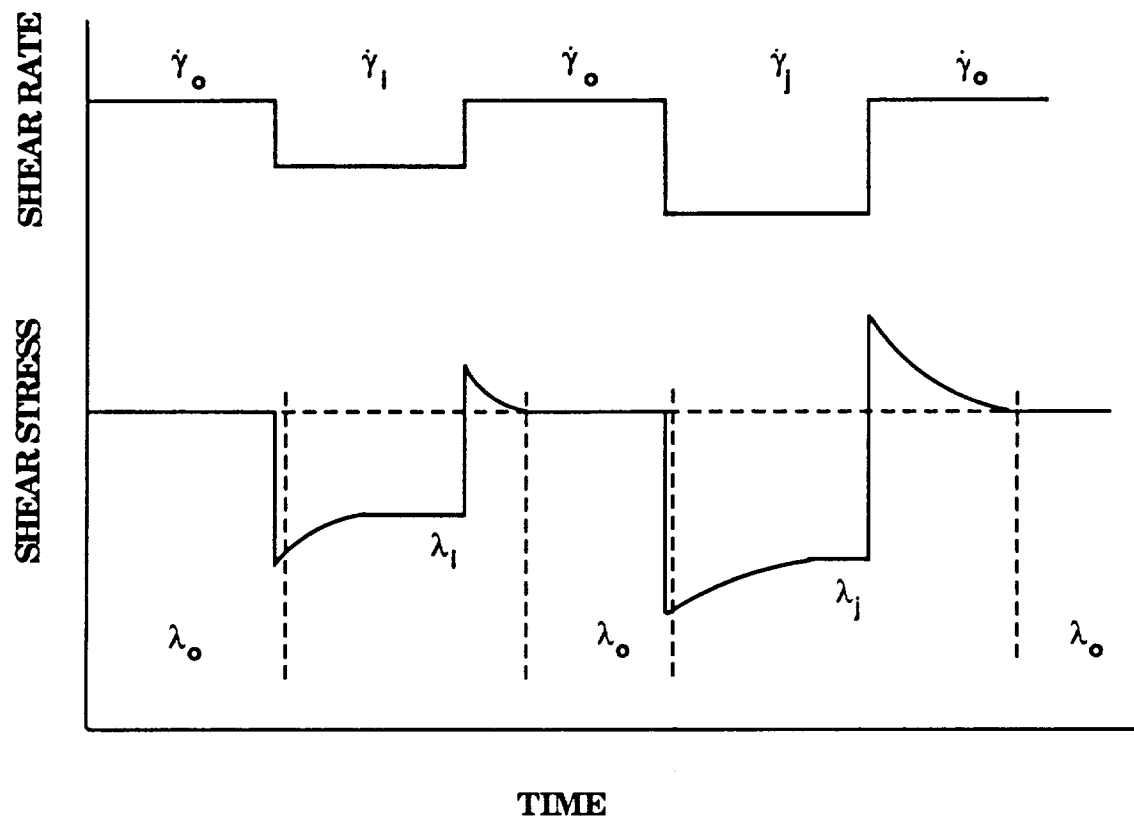


Fig. 3.13 Step change method to obtain structure curves.  $\lambda_0$ ,  $\lambda_i$ , and  $\lambda_j$ , are the individual structures corresponding to the shear rates  $\dot{\gamma}_0$ ,  $\dot{\gamma}_i$ , and  $\dot{\gamma}_j$ , respectively.

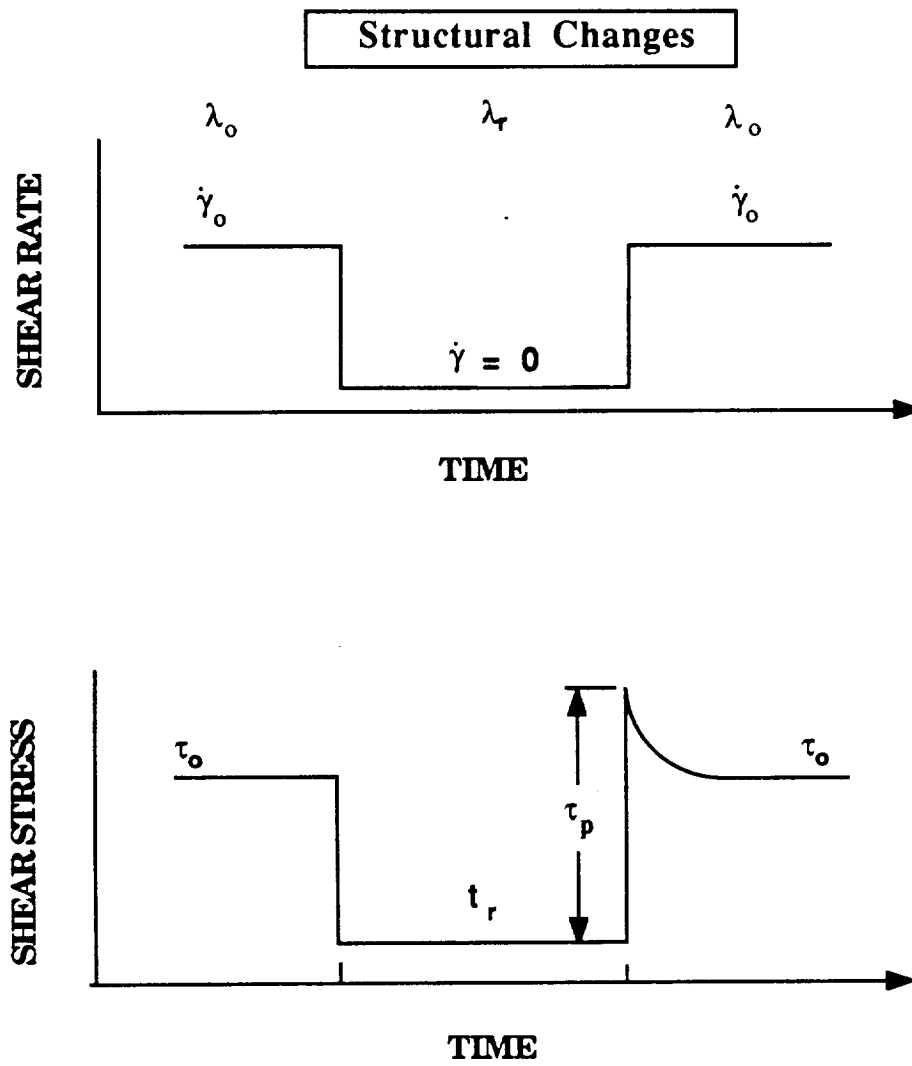


Fig. 3.14 Experimental procedure for measuring the effect of rest time on the transient curve and microstructure.

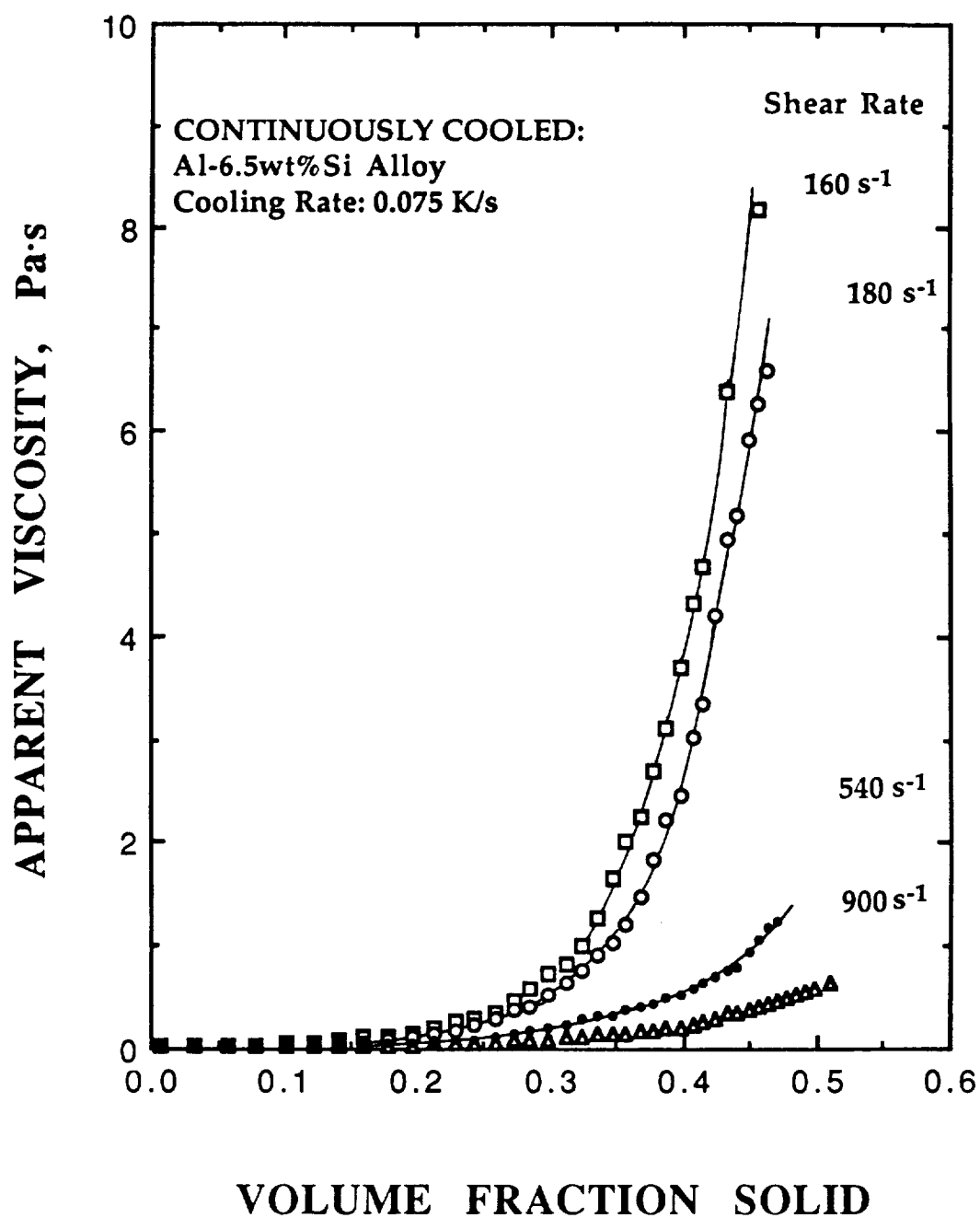


Fig. 4.1 Plot of apparent viscosity of Al-6.5wt%Si alloy versus volume fraction solid at cooling rate 0.075 K/s with shear rates of 180, 540, and 900 s<sup>-1</sup>.

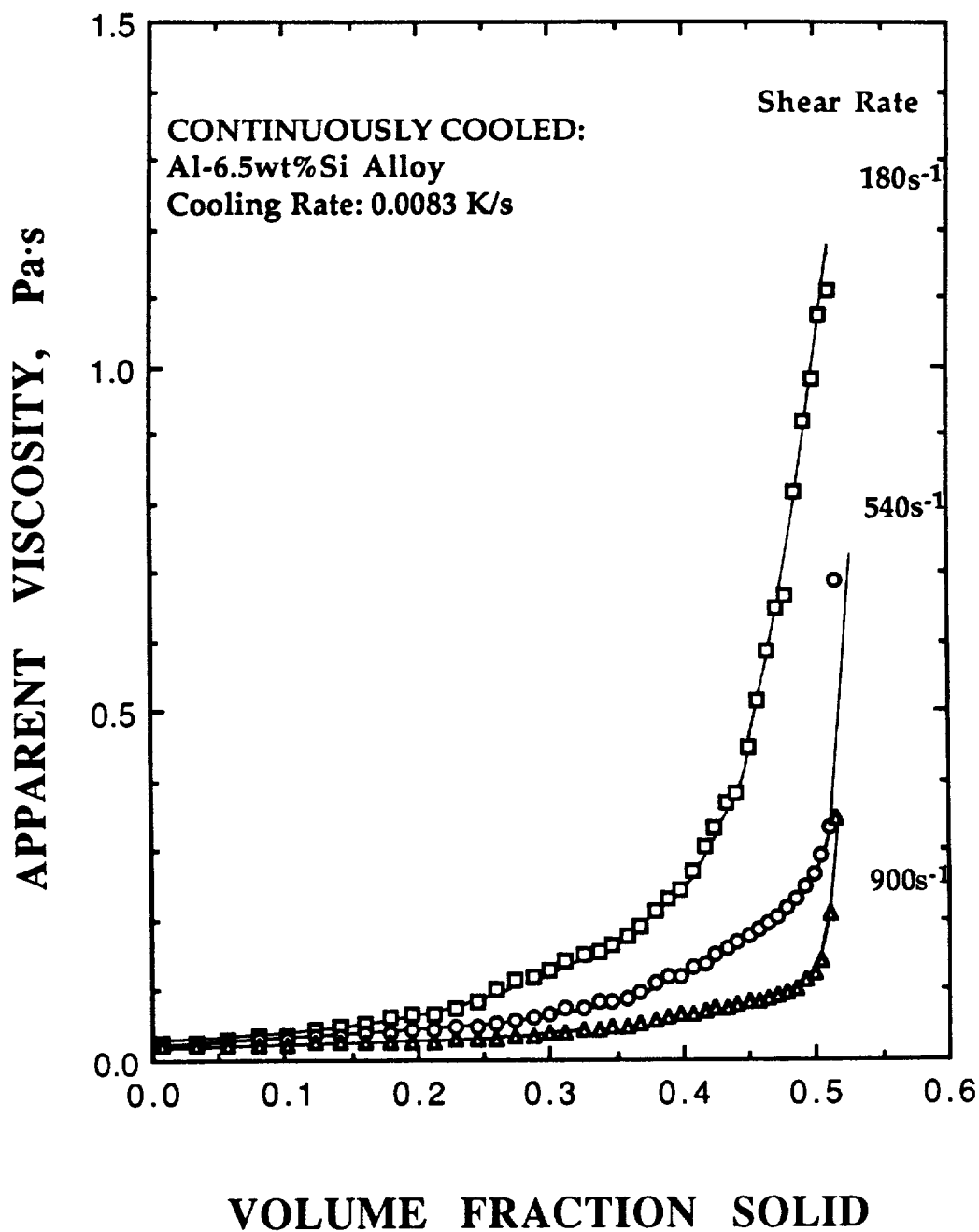
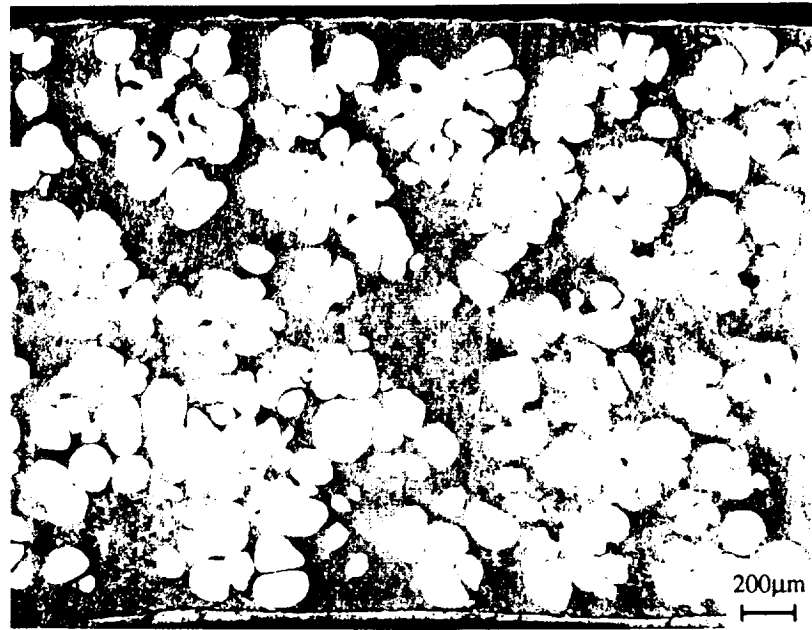
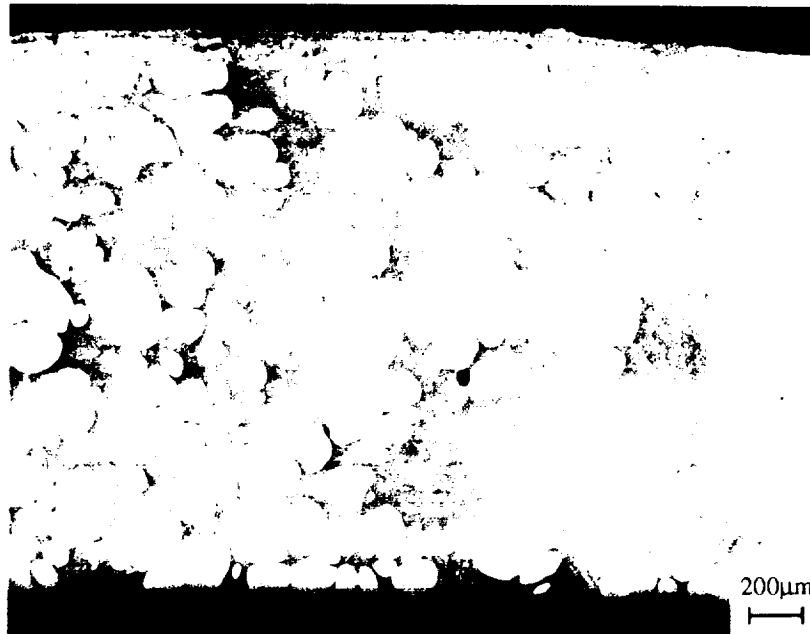


Fig. 4.2 Plot of apparent viscosity of Al-6.5wt%Si alloy versus volume fraction solid at cooling rate of 0.0083 K/s with shear rates of 180, 540, and 900 s<sup>-1</sup>.



(a)



(b)

Fig. 4.3 Cross-sectional microstructures of continuously cooled samples of Al-6.5wt%Si alloy in the gap of the viscometer: the average shear rates were (a) 180 and (b) 900 s<sup>-1</sup> and the average cooling rate was 0.075 K/s for both. The final volume fraction solid is 0.52, calculated by the Scheil equation.

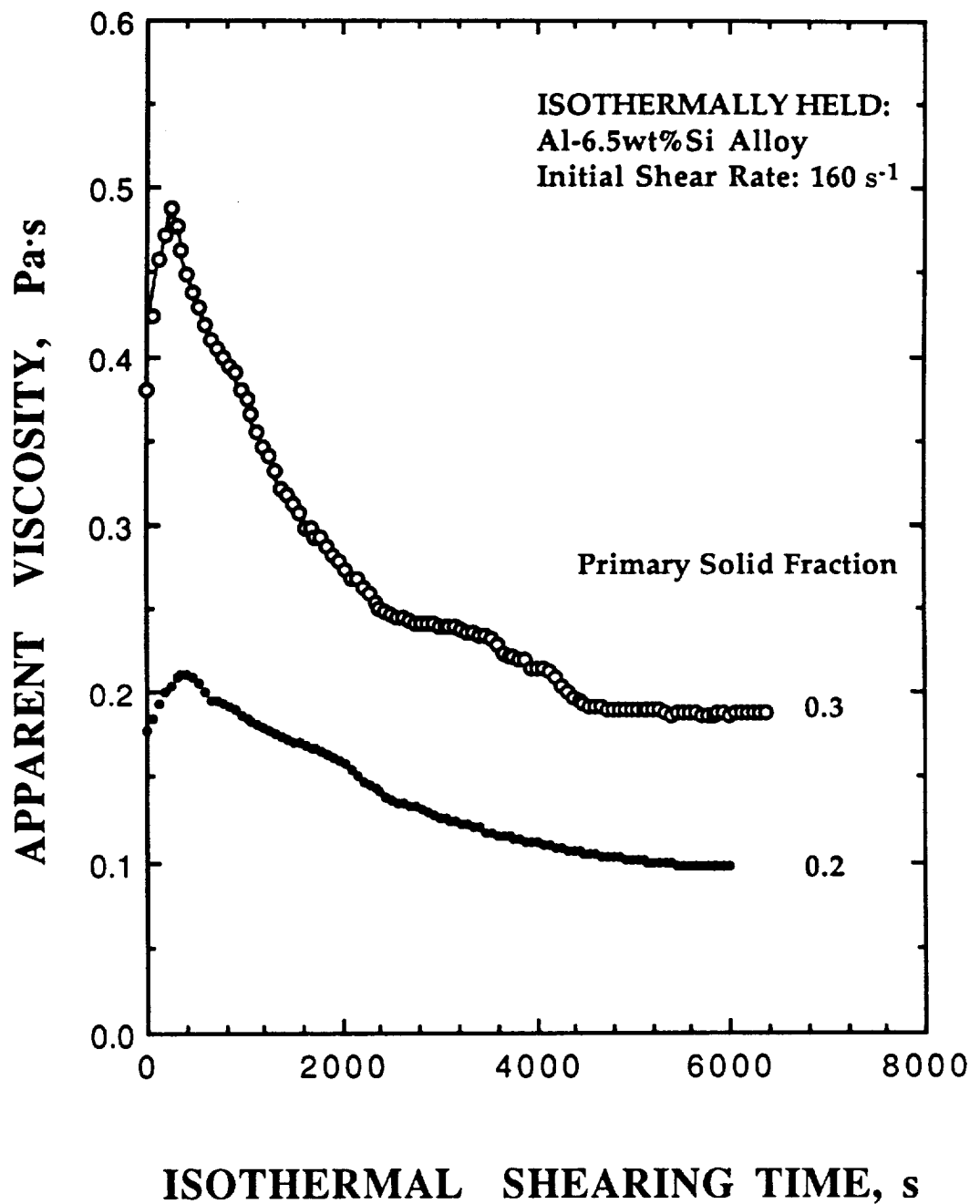


Fig. 4.4 Change in apparent viscosity of Al-6.5wt%Si alloy during isothermal shearing: apparent viscosity was increasing to a maximum level in the early period of isothermal shearing, and then slowly decreased to a steady state level.



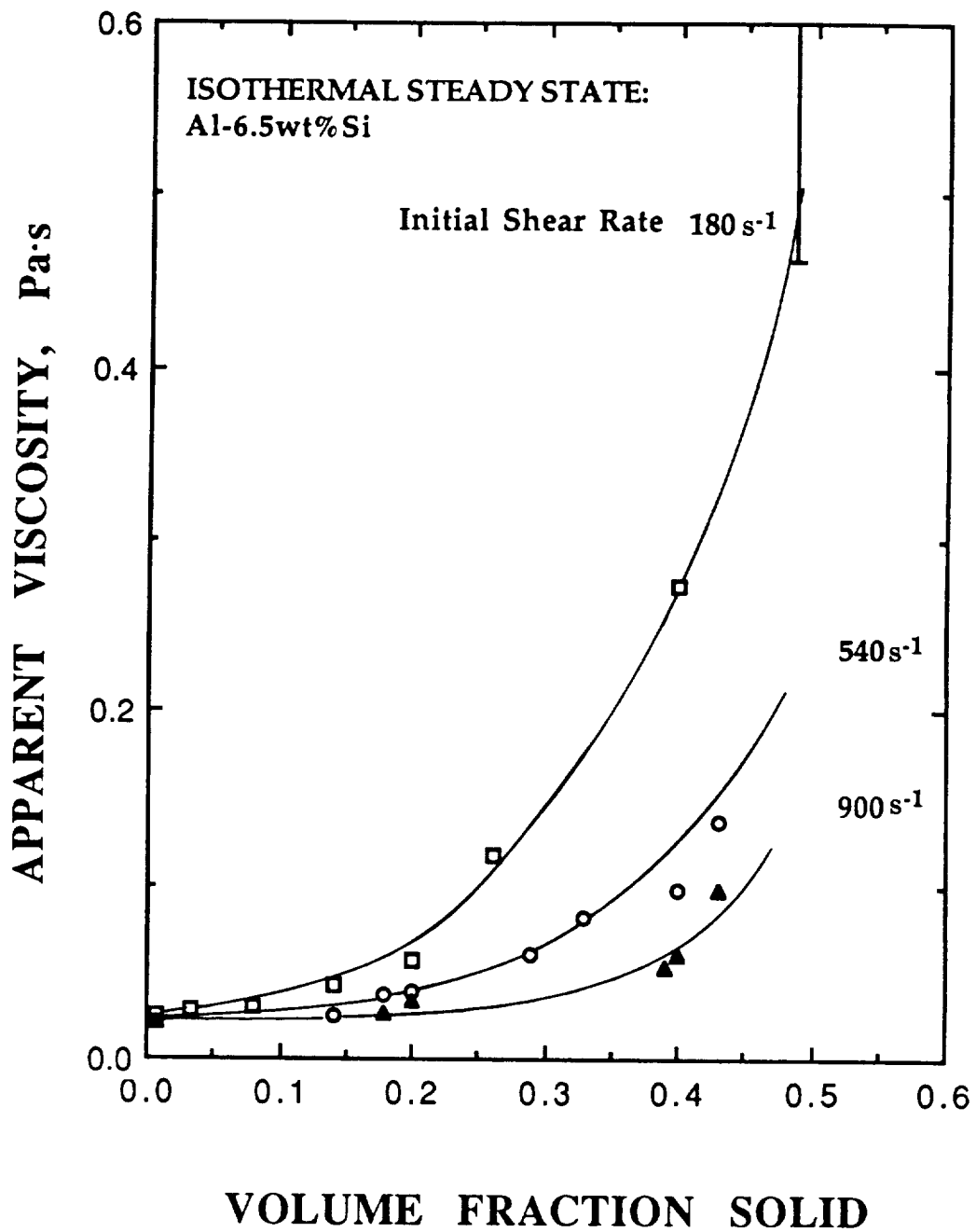


Fig. 4.5 Plot of apparent viscosity of Al-6.5wt%Si alloy at an isothermal steady state versus volume fraction solid of the primary solid phase under different initial shear rates,  $\dot{\gamma}_0$ .

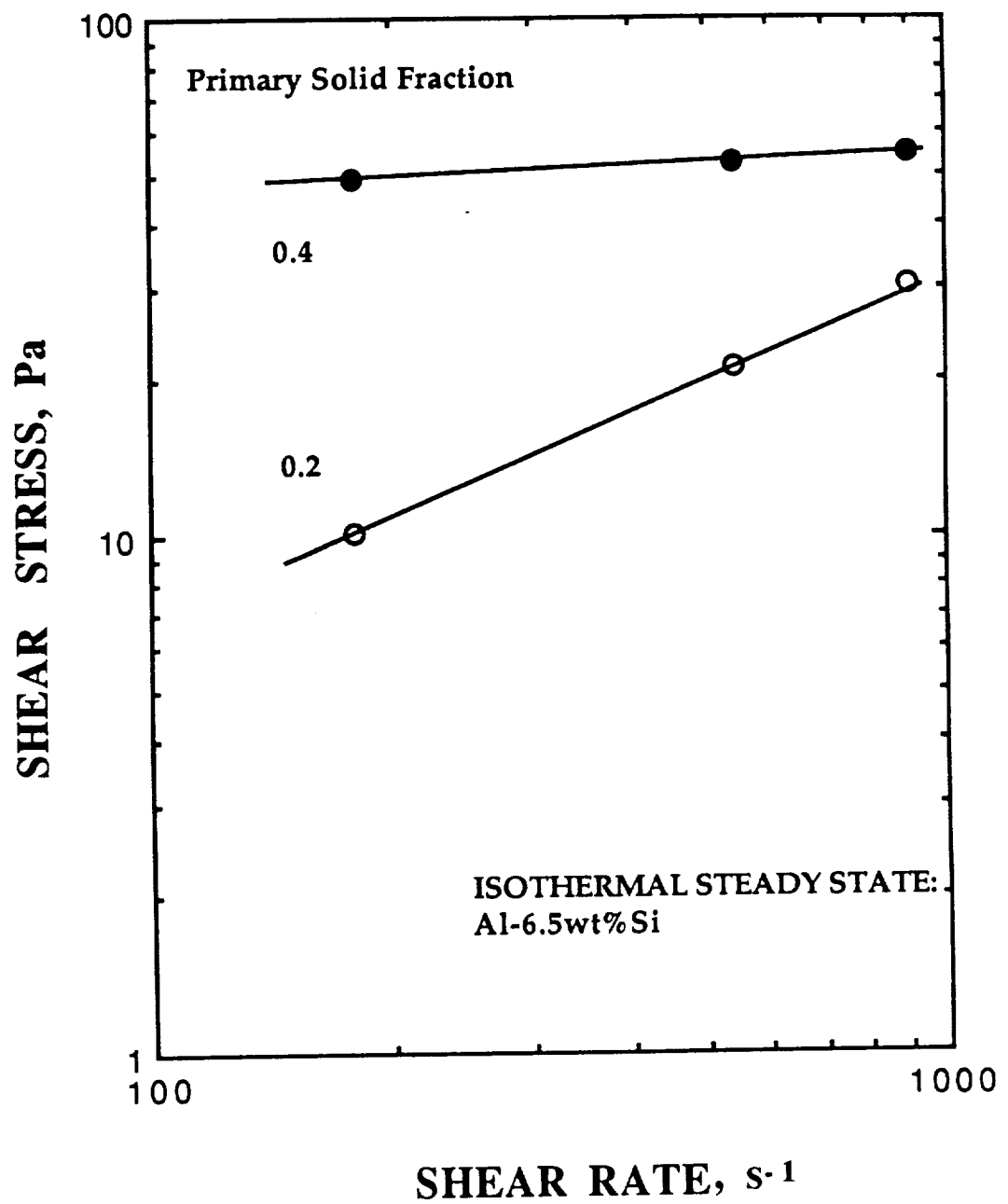


Fig. 4.6 (a) Plot of isothermal shear stress at steady state versus initial shear rate for volume fractions solid of 0.2 and 0.4 in Al-6.5 wt %Si alloy.

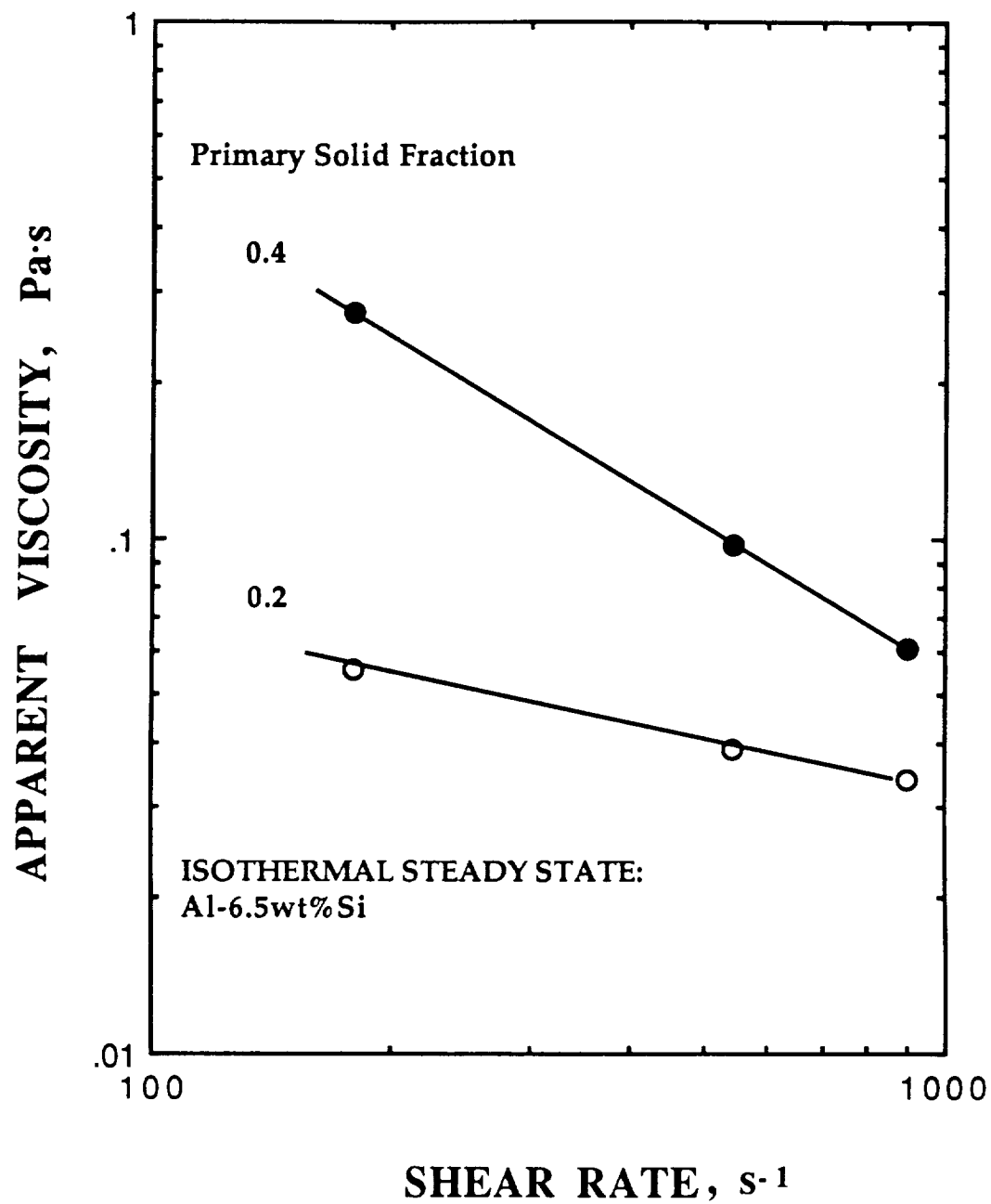


Fig. 4.6 (b) Plot of isothermal apparent viscosity at steady state versus initial shear rate for volume fractions solid of 0.2 and 0.4 in Al-6.5wt%Si alloy.

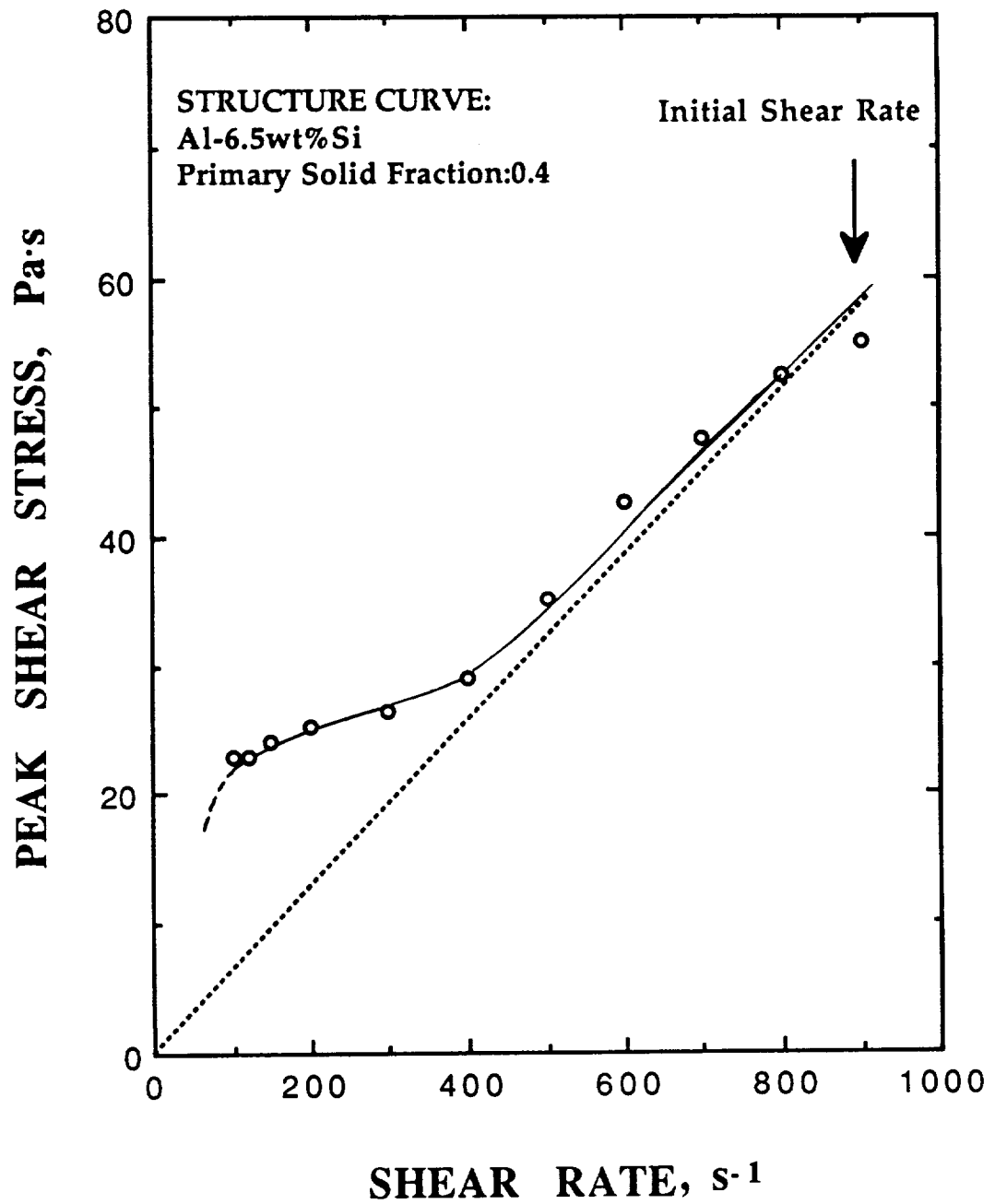


Fig. 4.7 (a) Pseudoplasticity of an alloy slurry with volume fraction solid of 0.4, sheared at an initial shear rate of  $900 s^{-1}$ . (a) plot of shear stress versus shear rate,

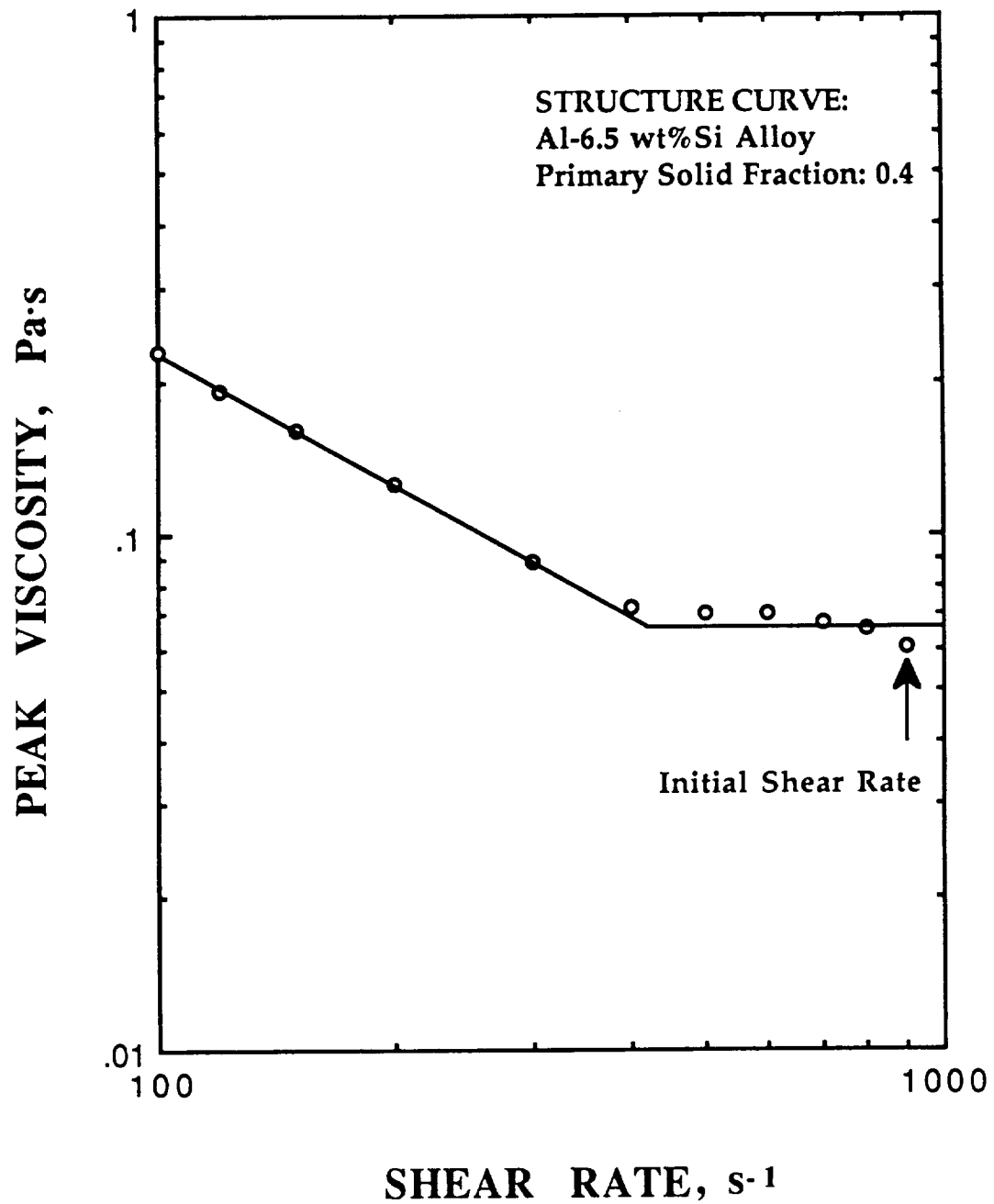
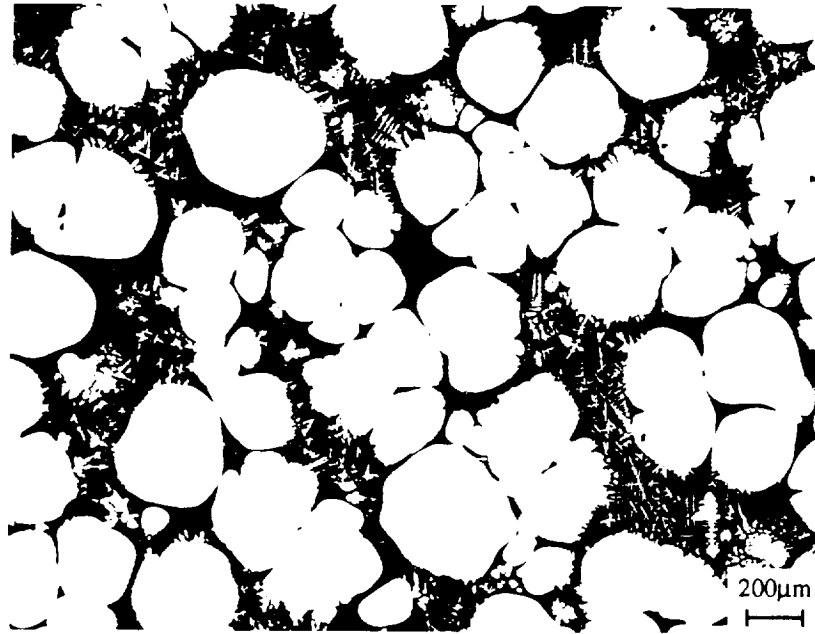
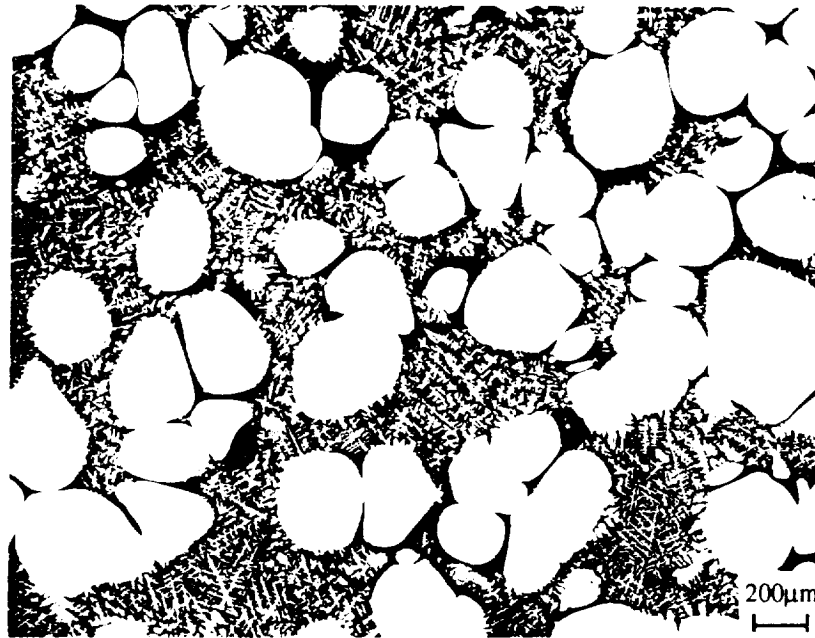


Fig. 4.7 (b) Pseudoplasticity of an alloy slurry with volume fraction solid of 0.4, sheared at an initial shear rate of 900 s<sup>-1</sup>. (b) plot of apparent viscosity versus shear rate.

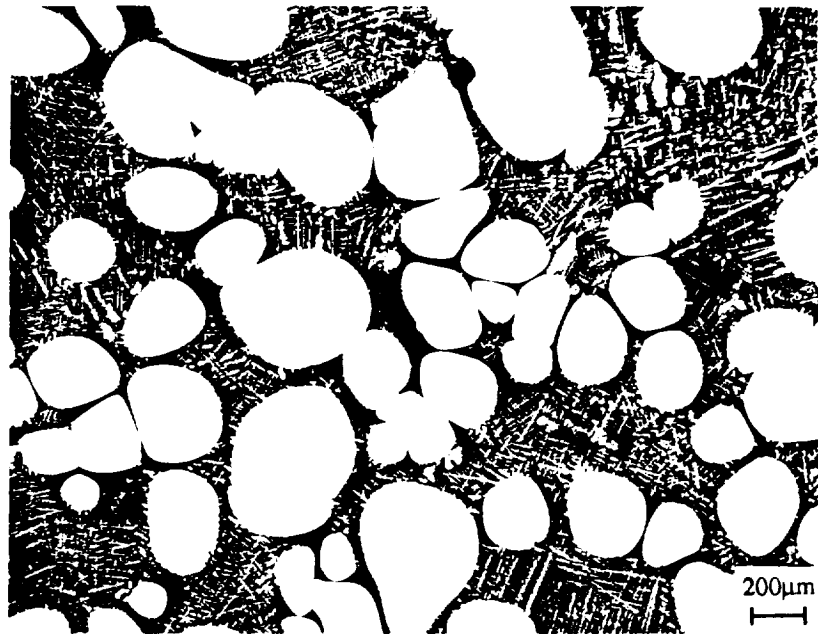


(a)

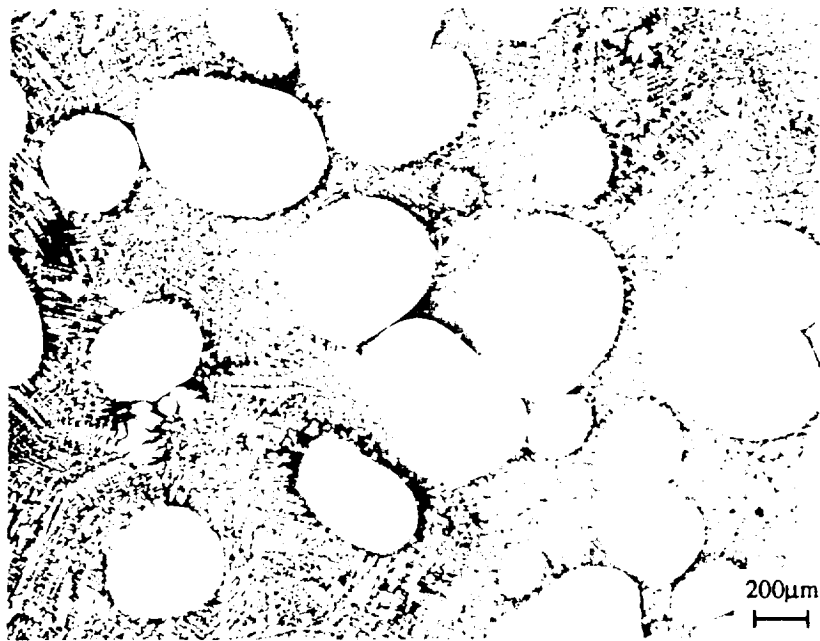


(b)

Fig. 4.8(a,b) Microstructural evolution during the rest of a slurry of Al-6.5wt%Si with  $g_{s(\alpha)}=0.4$ : The initial microstructure was formed by shearing isothermally at the initial shear rate of  $180 \text{ s}^{-1}$  for two hours. The rest time was (a) 0 (the initial structure), and (b) 3 hours, respectively.



(c)



(d)

Fig. 4.8(c,d) Microstructural evolution during the rest of a slurry of Al-6.5wt%Si with  $g_{s(\alpha)}=0.4$ : The initial microstructure was formed by shearing isothermally at the initial shear rate of  $180 \text{ s}^{-1}$  for two hours. The rest time was (c) 6 hours, and (d) 24 hours, respectively.

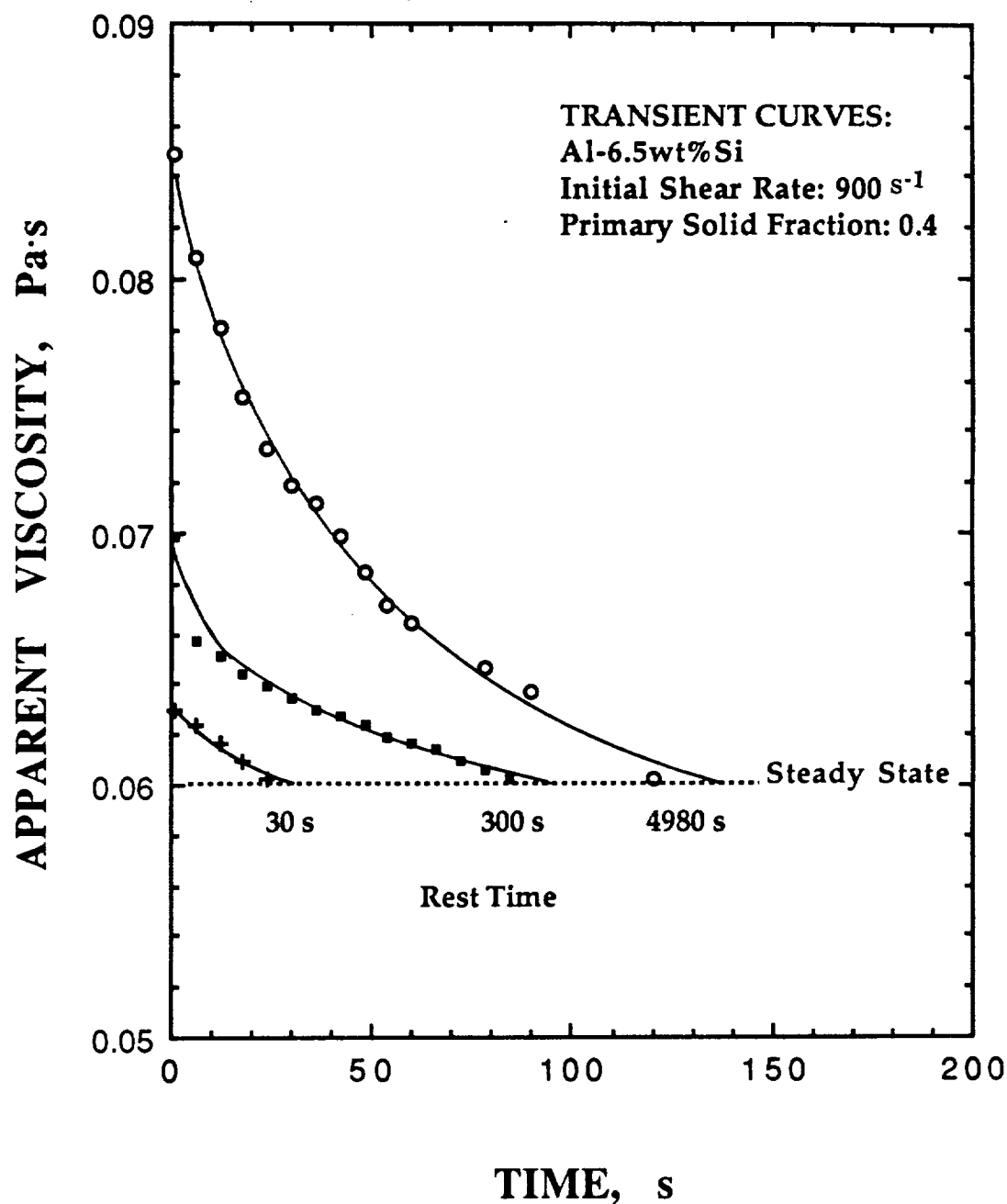


Fig. 4.9 Transient curves of apparent viscosity with time when shearing of a slurry of Al-6.5wt%Si alloy was resumed after a rest.



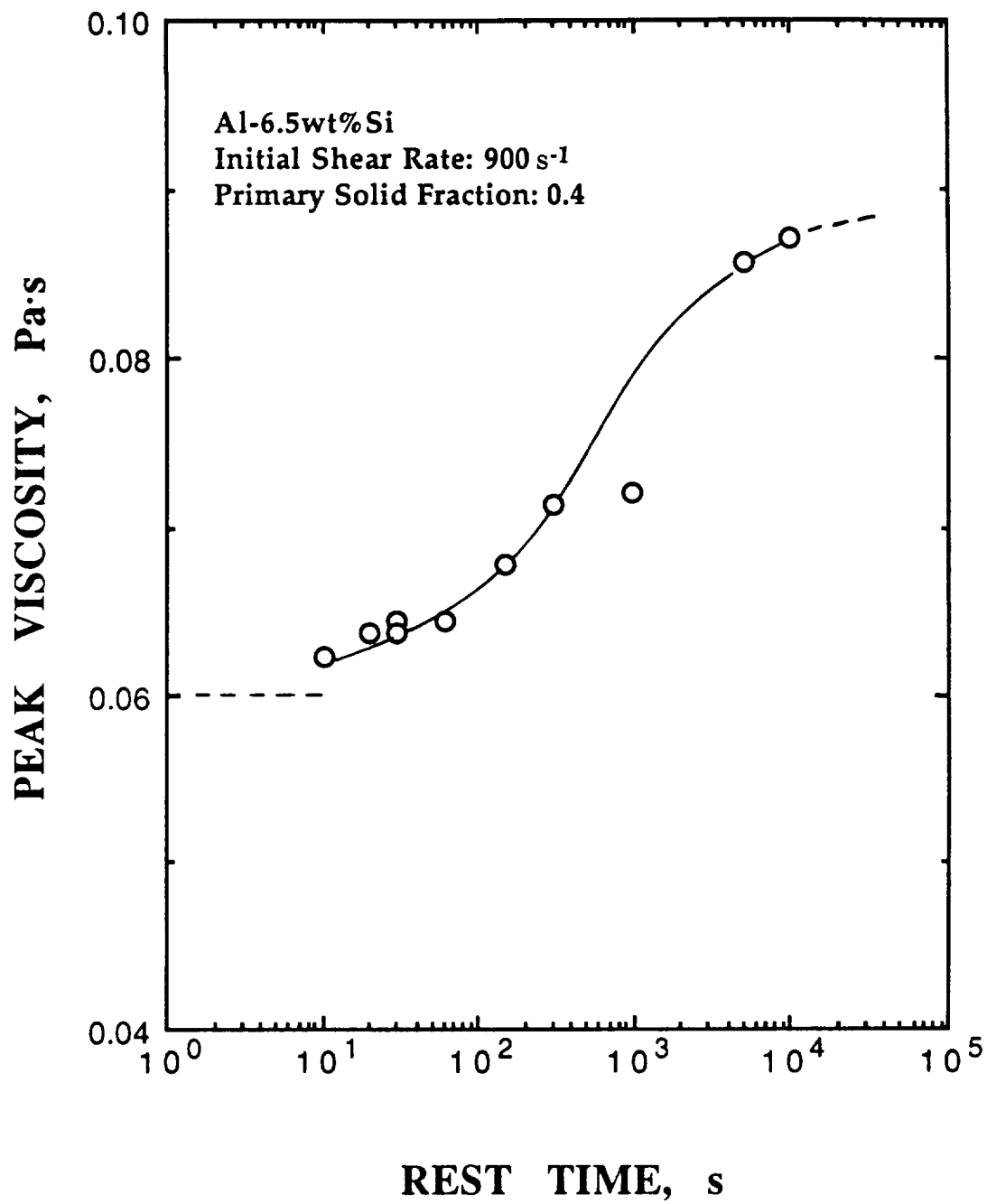


Fig. 4.10 Plot of initial peak viscosity after resumption of shearing versus rest time.

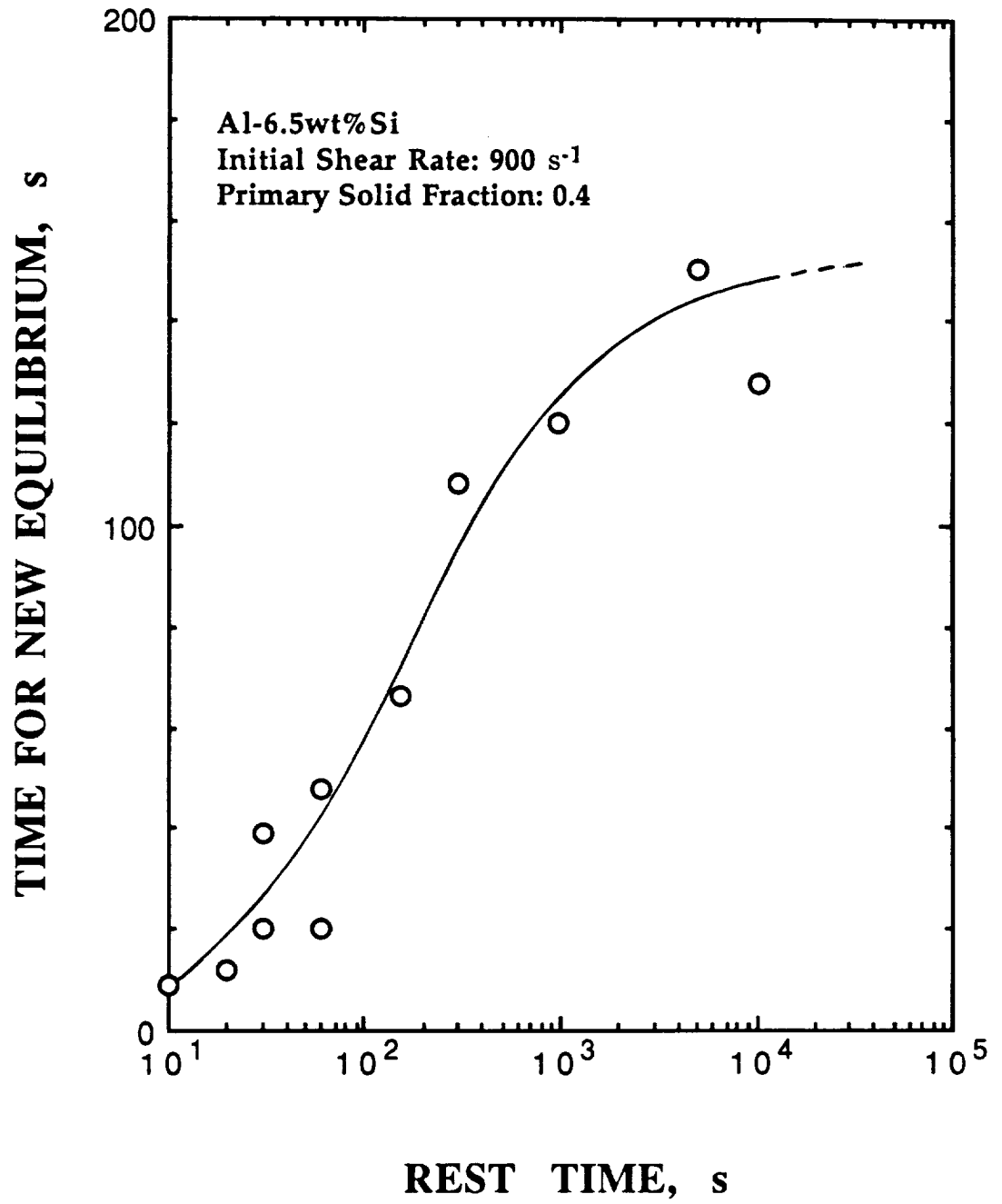


Fig. 4.11 Plot of time for new equilibrium versus rest time.

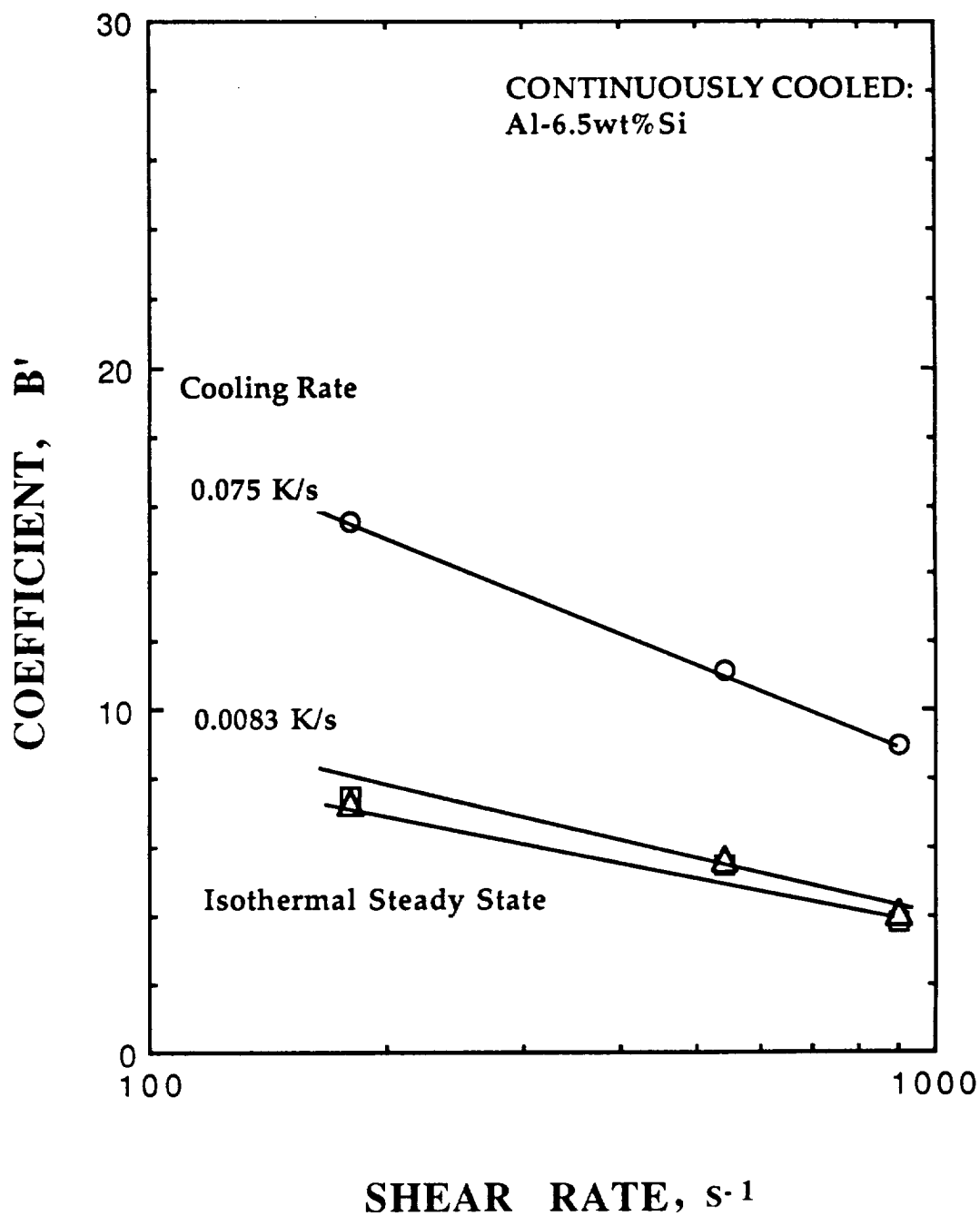


Fig. 4.12 The coefficient  $B'$  in eqn.(48) of Al-6.5wt%Si alloy versus shear rate at cooling rates of 0.075 and 0.0083 K/s.

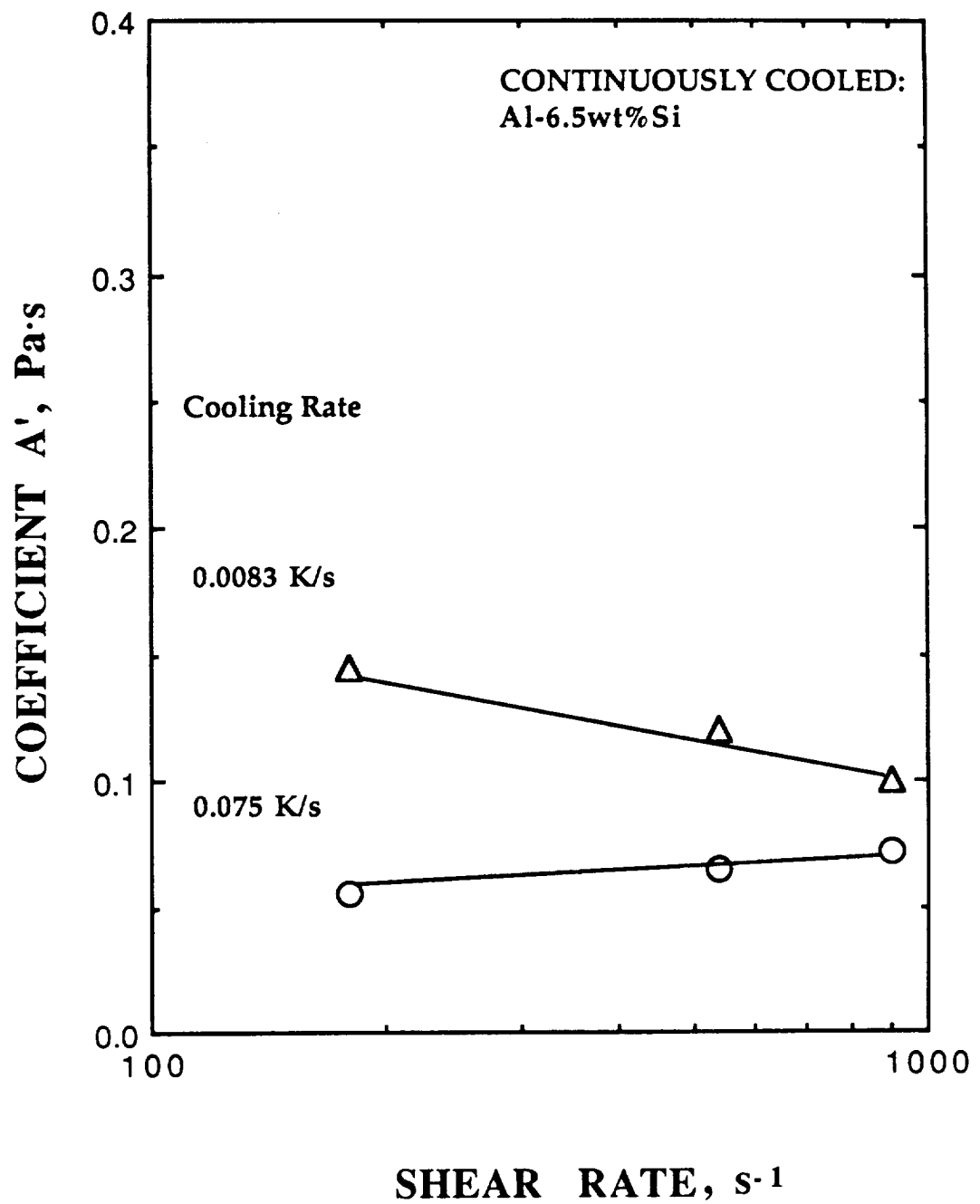


Fig. 4.13 The coefficient A' in eqn.(48) of Al-6.5wt%Si alloy versus shear rate at cooling rates of 0.075 and 0.0083 K/s.

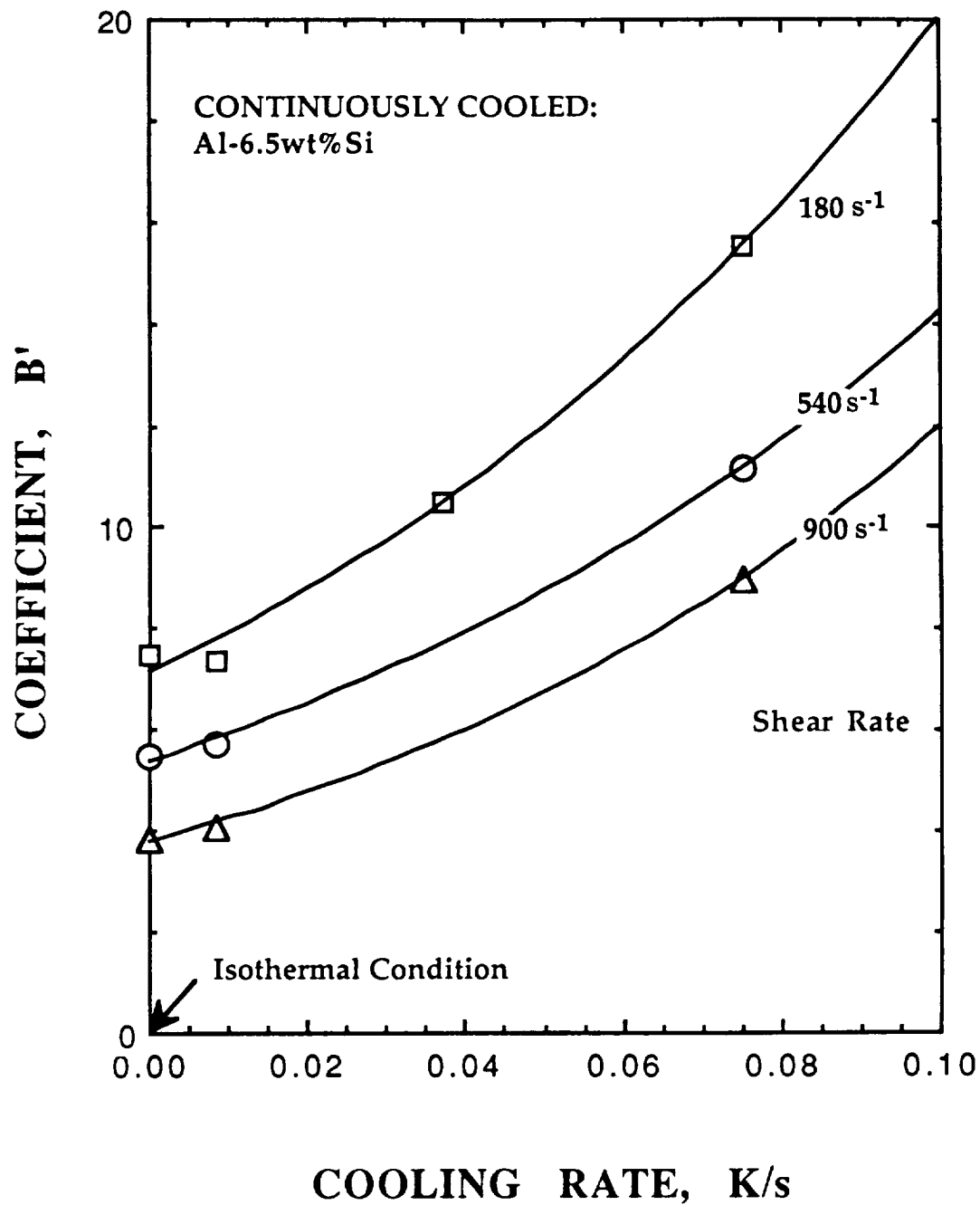


Fig. 4.14 The coefficient  $B'$  in eqn.(48) of Al-6.5wt%Si alloy versus cooling rate at shear rates of 180, 540, and  $900 \text{ s}^{-1}$ .

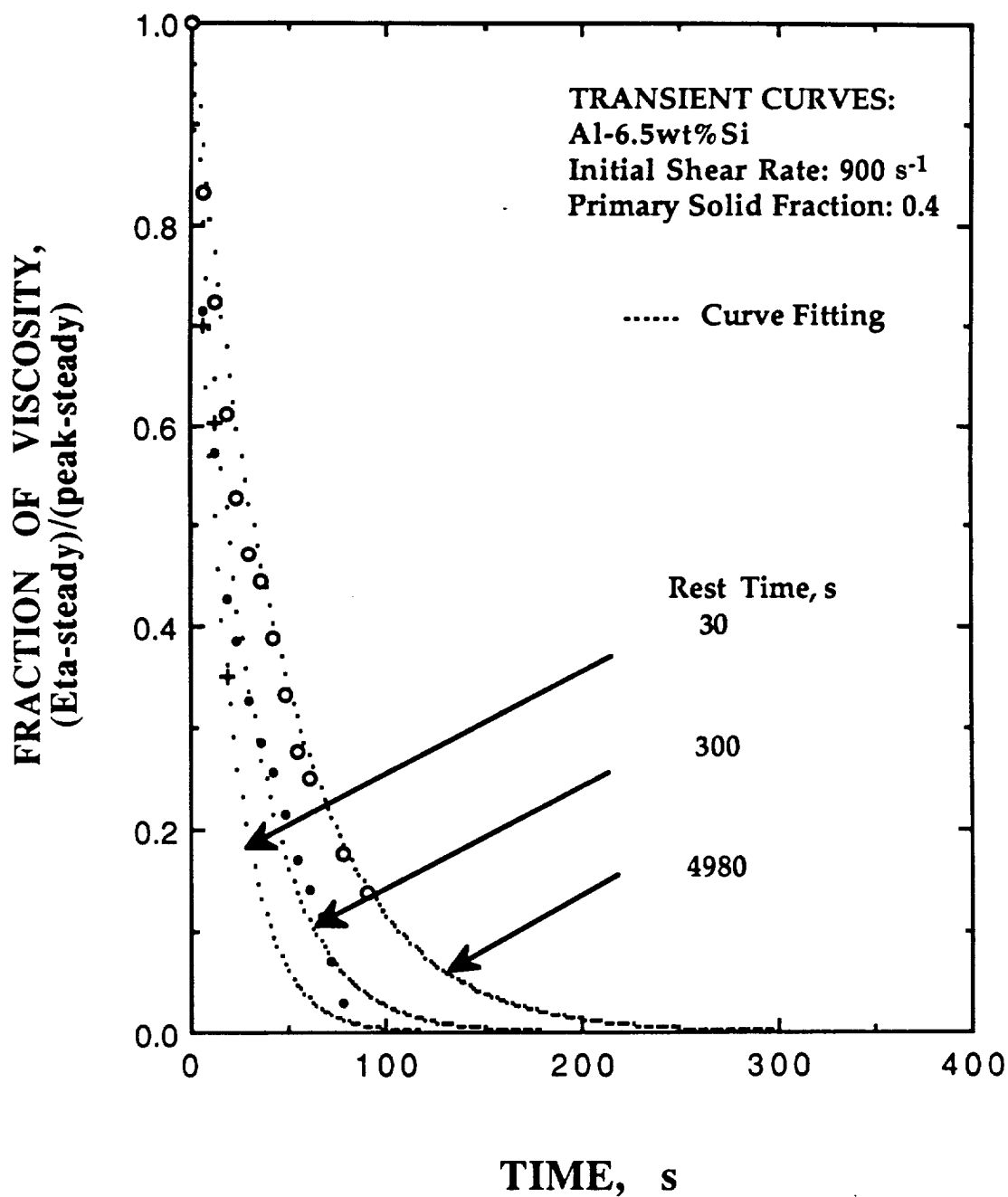


Fig. 4.15 Plot of change of viscosity relative to the steady state and shearing time after different periods of rest: 30, 300, and 4980 seconds.

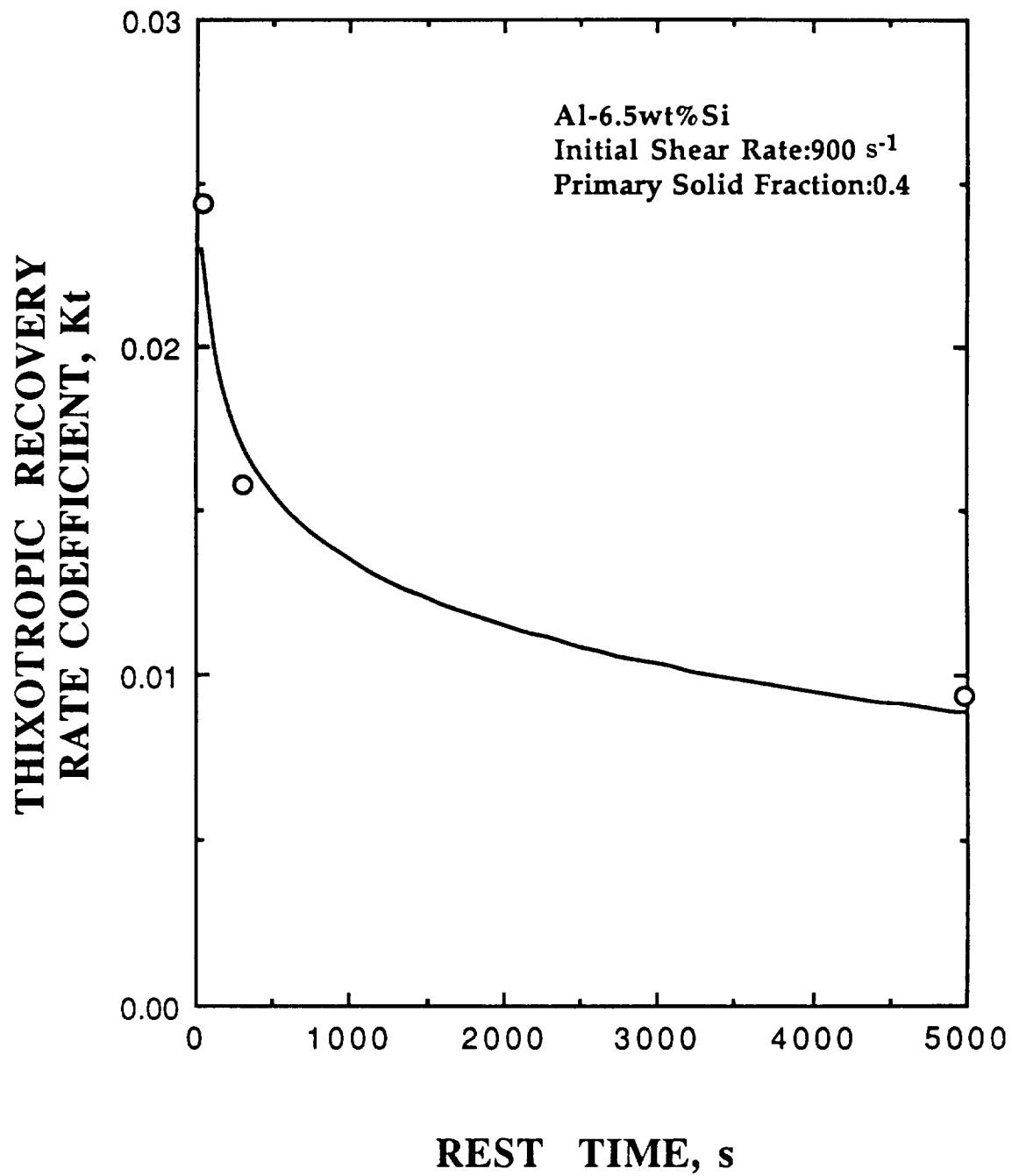


Fig. 4.16 Plot of thixotropic recovery rate and rest time.

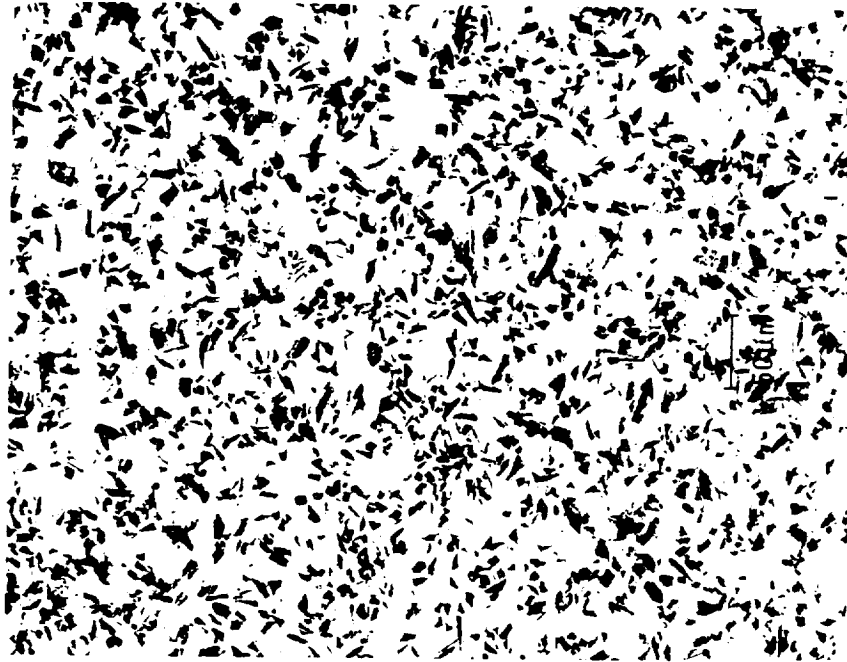


Fig. 5.1      Optical micrograph of 20vol%SiC/Al-6.5wt%Si composite cast in a graphite mold.



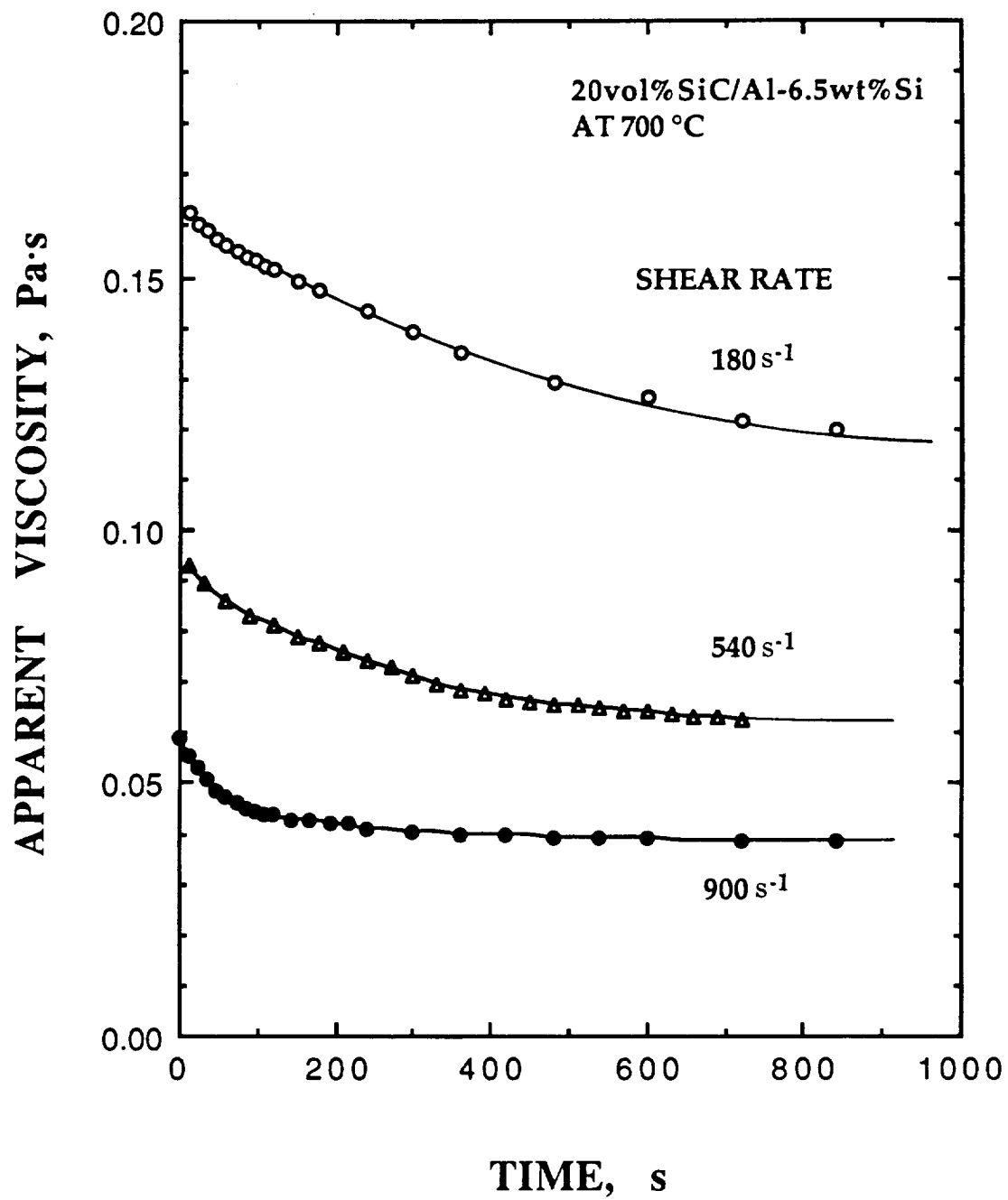


Fig. 5.2 Change of apparent viscosity of 20vol%SiC/Al-6.5wt%Si composite with time, sheared at different shear rates after a rest at 700°C (transient curves).

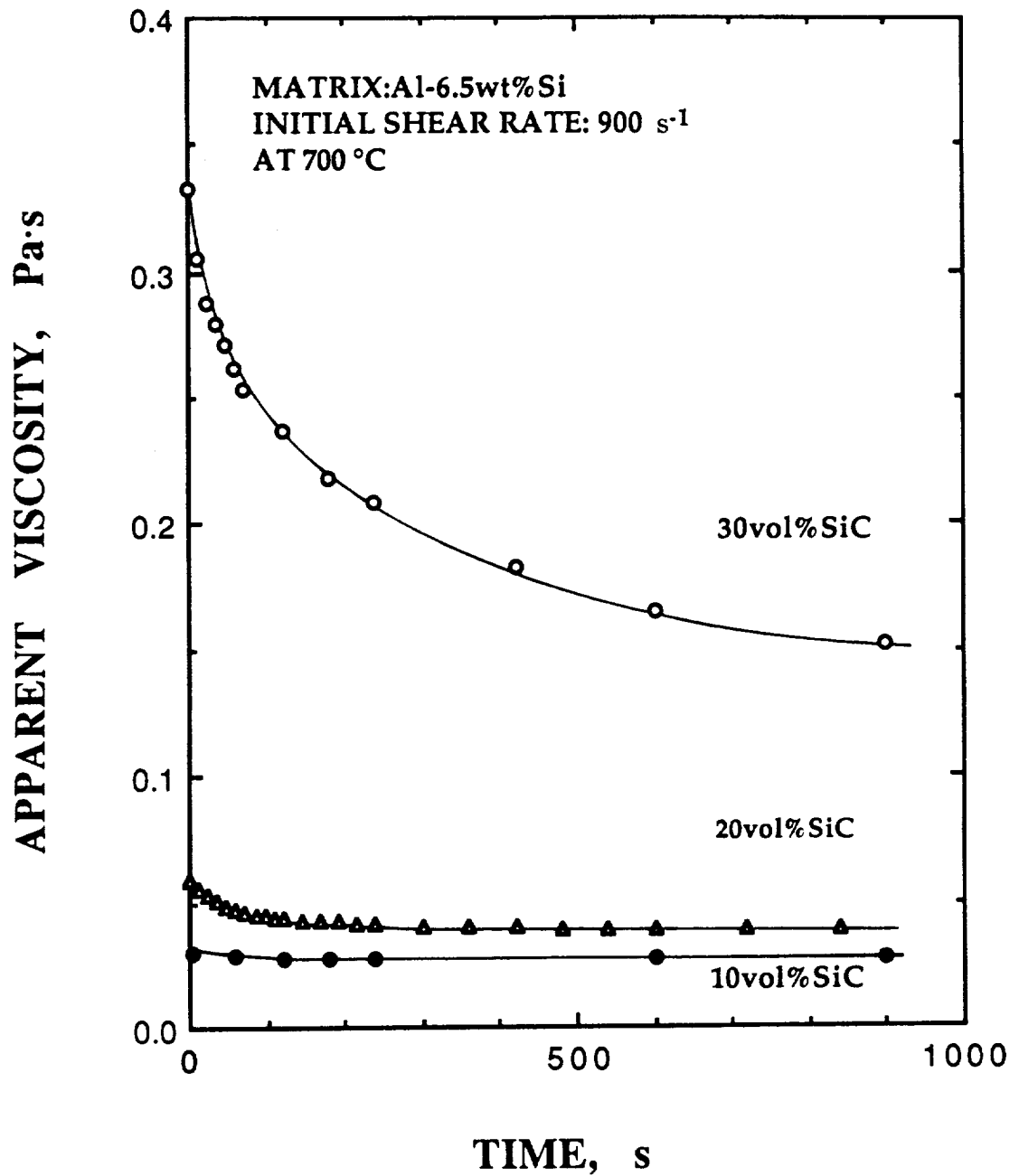


Fig. 5.3 Changes of apparent viscosity of 10, 20 and 30 vol%SiC/Al-6.5 wt%Si composite with time, sheared at 900 s<sup>-1</sup> after a rest at 700 °C (Transient curves).

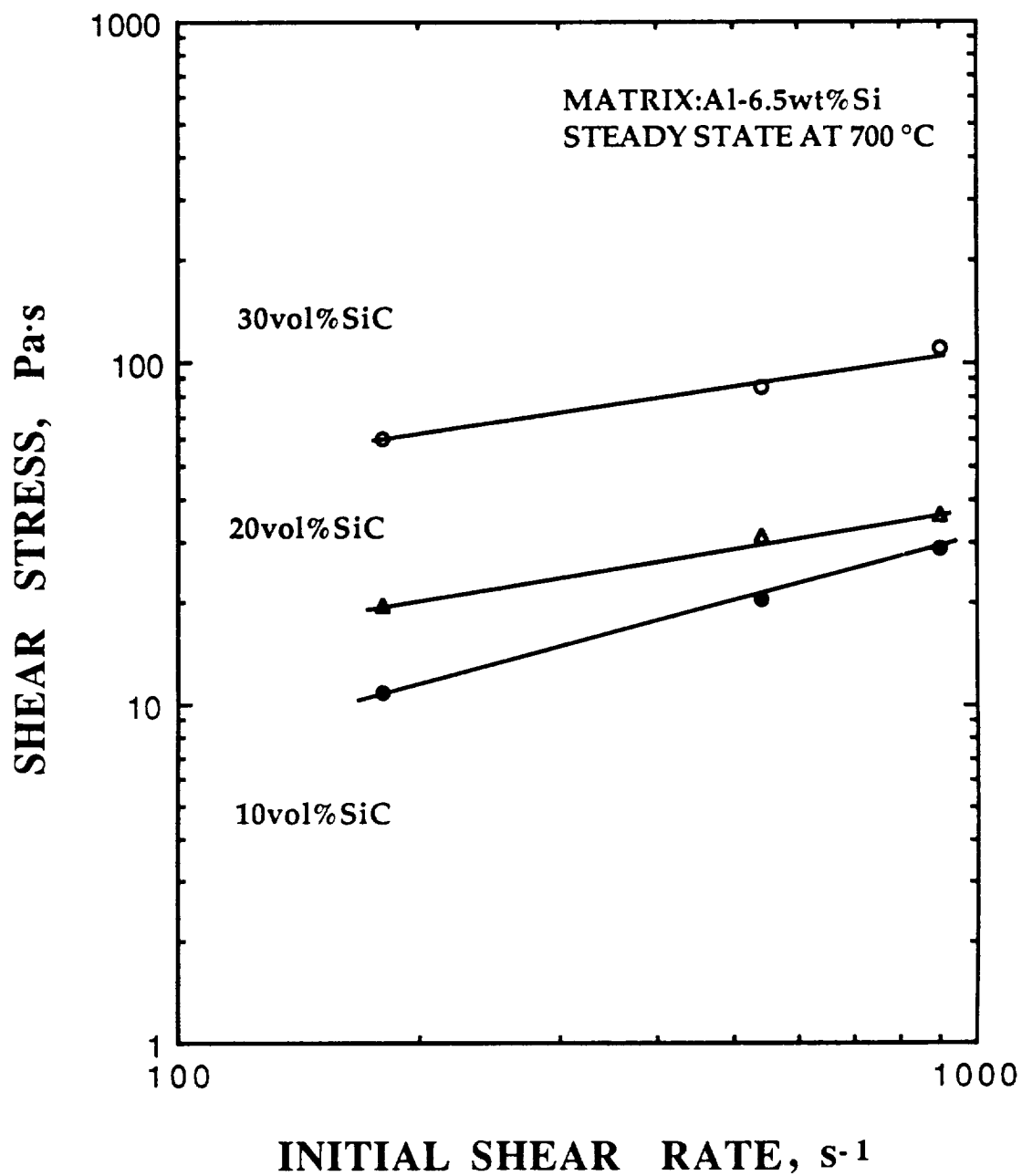


Fig. 5.4 Plot of shear stress at steady state and initial shear rate for composite slurries with 10, 20, and 30 vol% SiC/Al-6.5 wt%Si at 700°C (equilibrium curves).

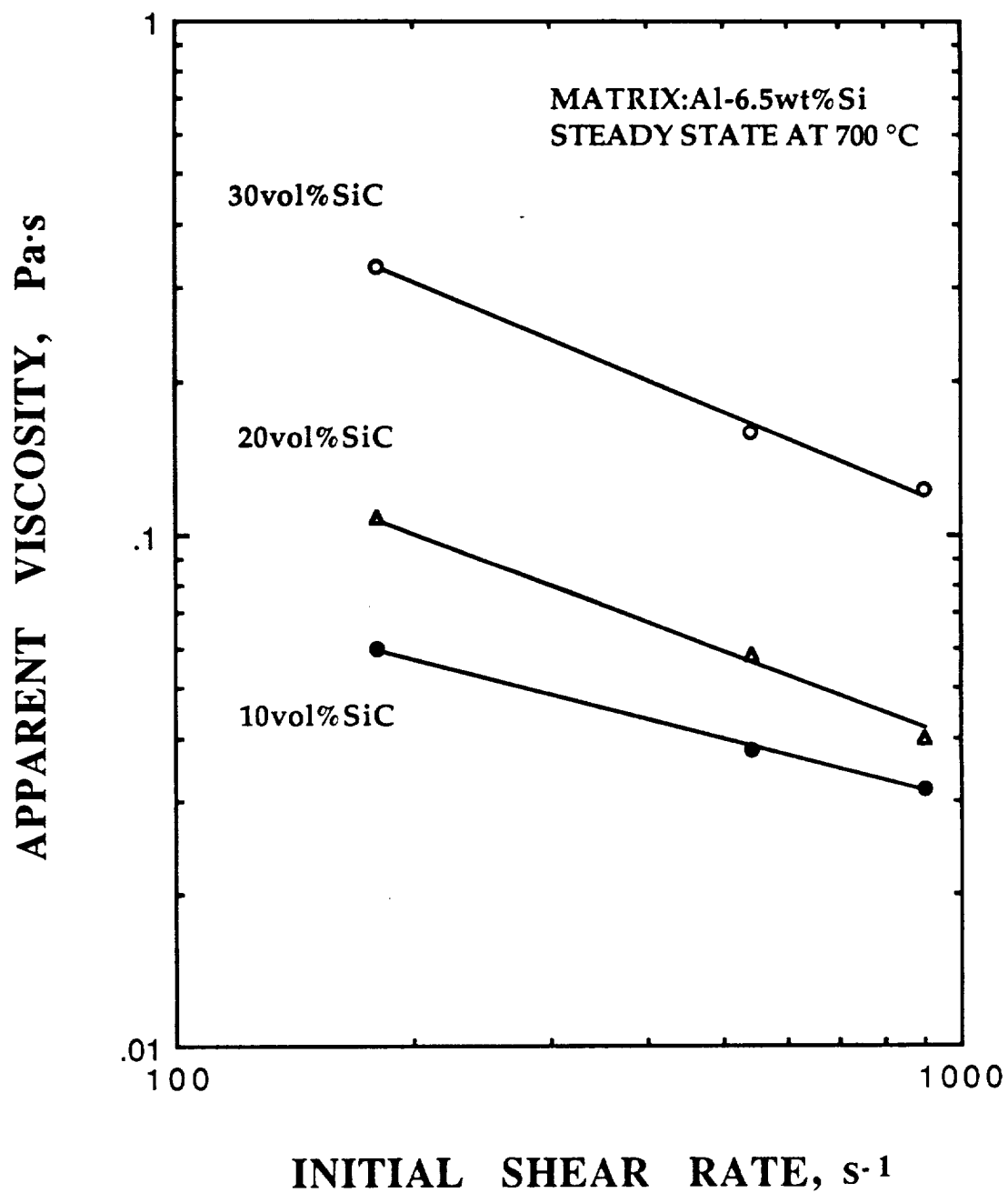


Fig. 5.5 Plot of apparent viscosity at steady state and initial shear rate for composite slurries with 10,20 and 30vol% SiC/Al-6.5 wt%Si at 700 °C (equilibrium curves).

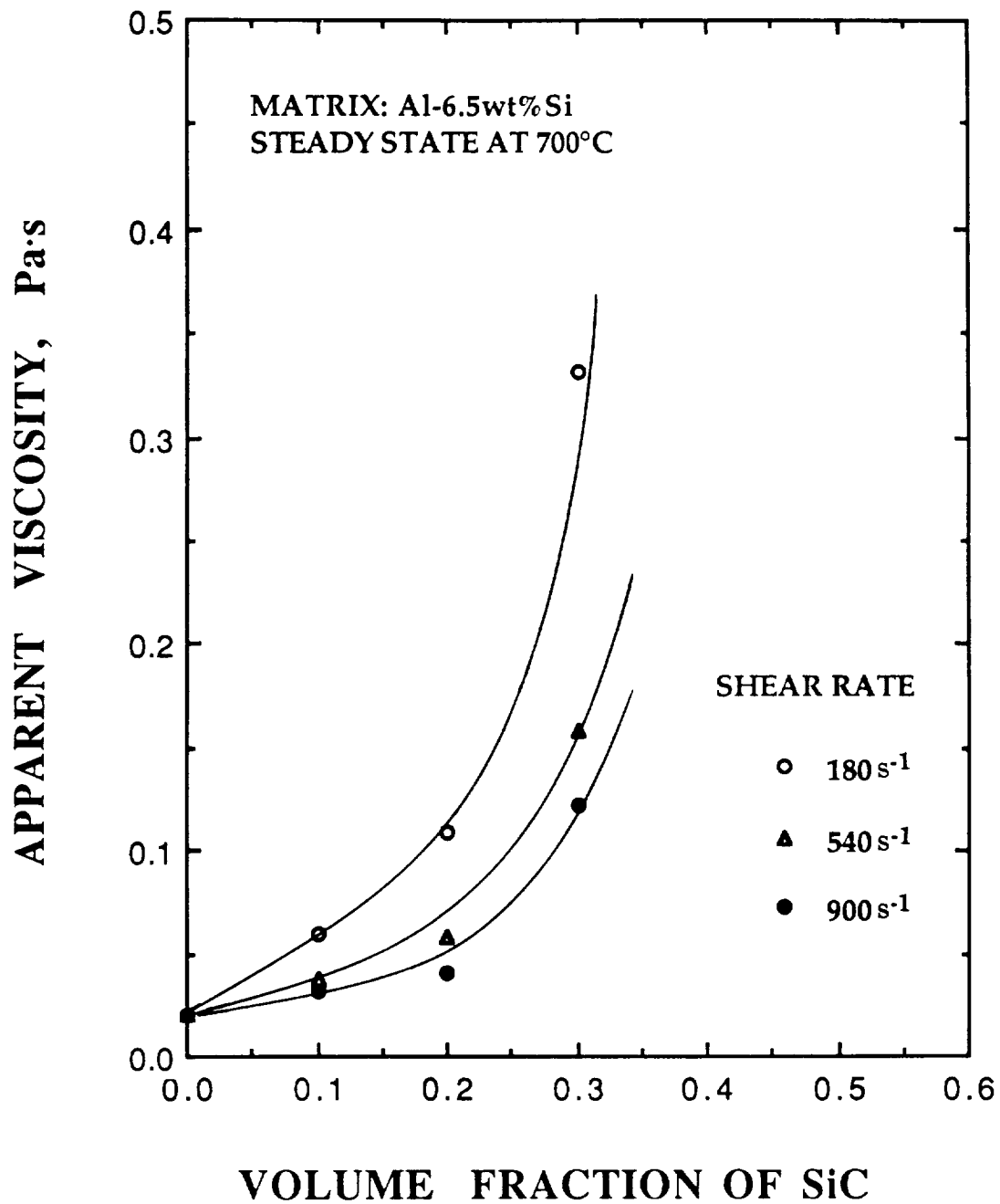


Fig. 5.6 Plot of apparent viscosity at steady state vs. volume fraction of SiC for composite slurries with 10, 20, and 30 vol% SiC/Al-6.5 wt%Si at 700 °C.

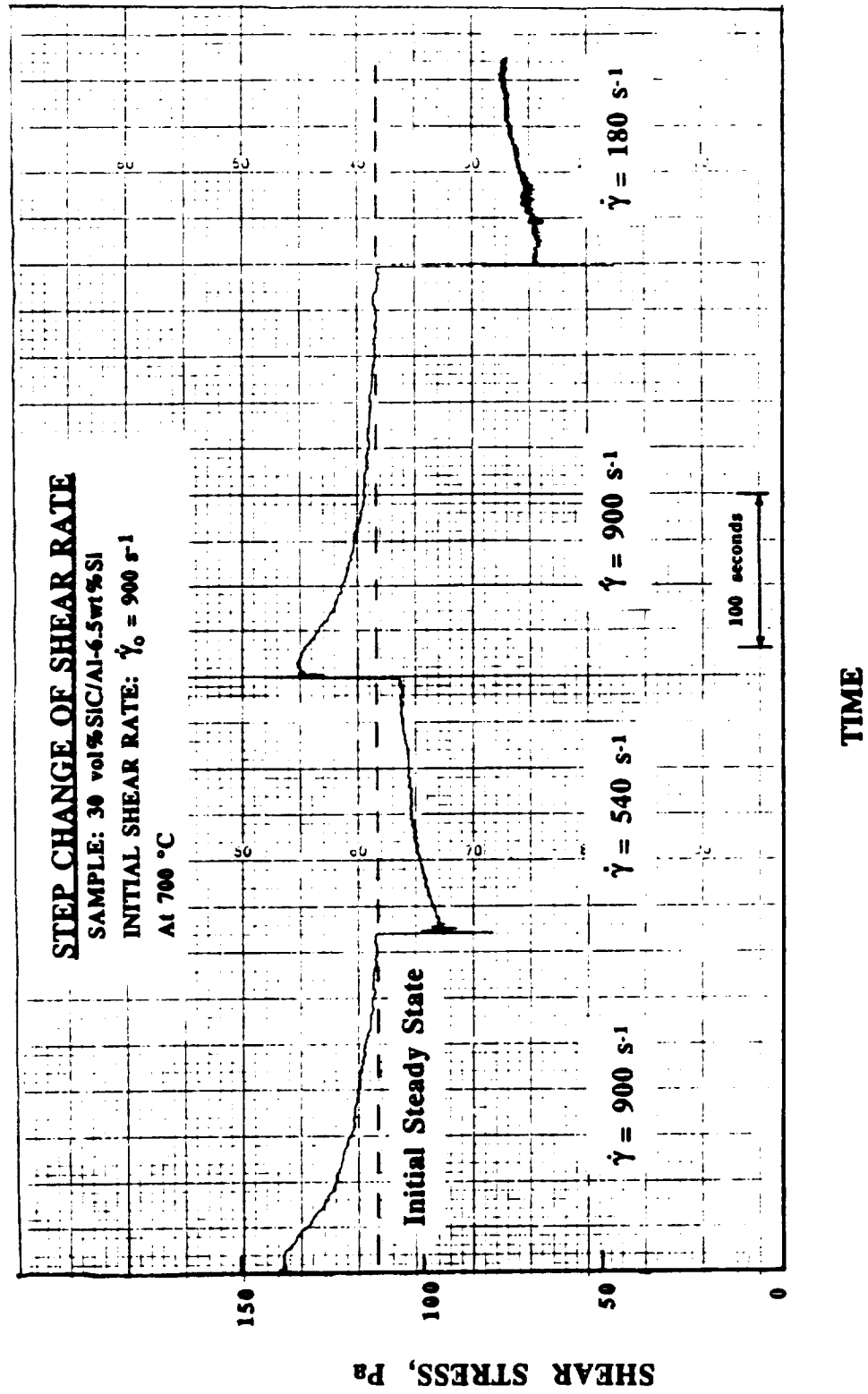


Fig. 5.7 Step change of shear rate: a composite slurry of 30 vol%SiC/Al-6.5 wt%Si at 700 °C, initial shear rate at 900 s<sup>-1</sup>.

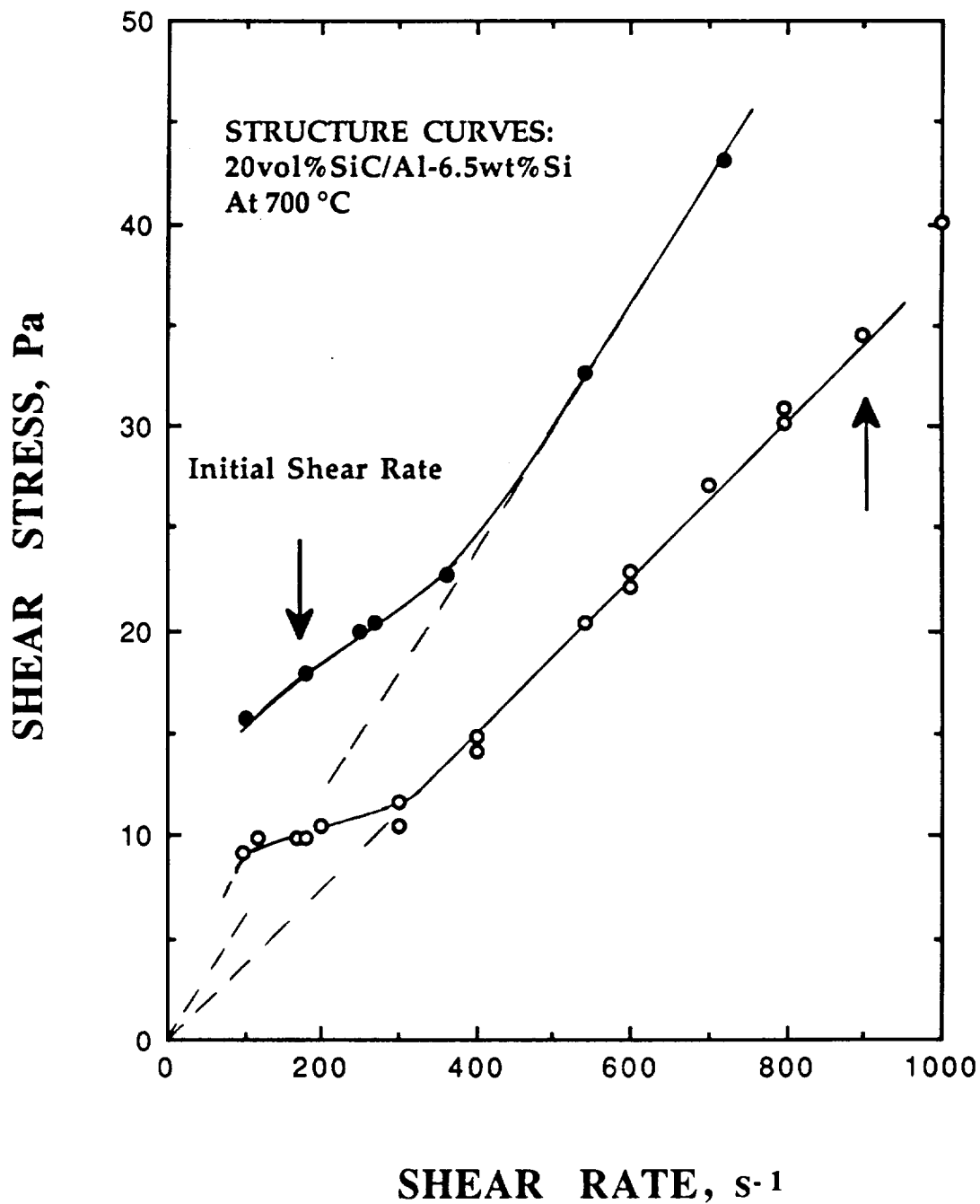


Fig. 5.8 (a) The plot of shear stress and shear rate of 20 vol%SiC/Al-6.5 wt%Si composite slurry at 700 °C. Each sample was initially sheared at 180 and 900  $s^{-1}$  (Structure curves).

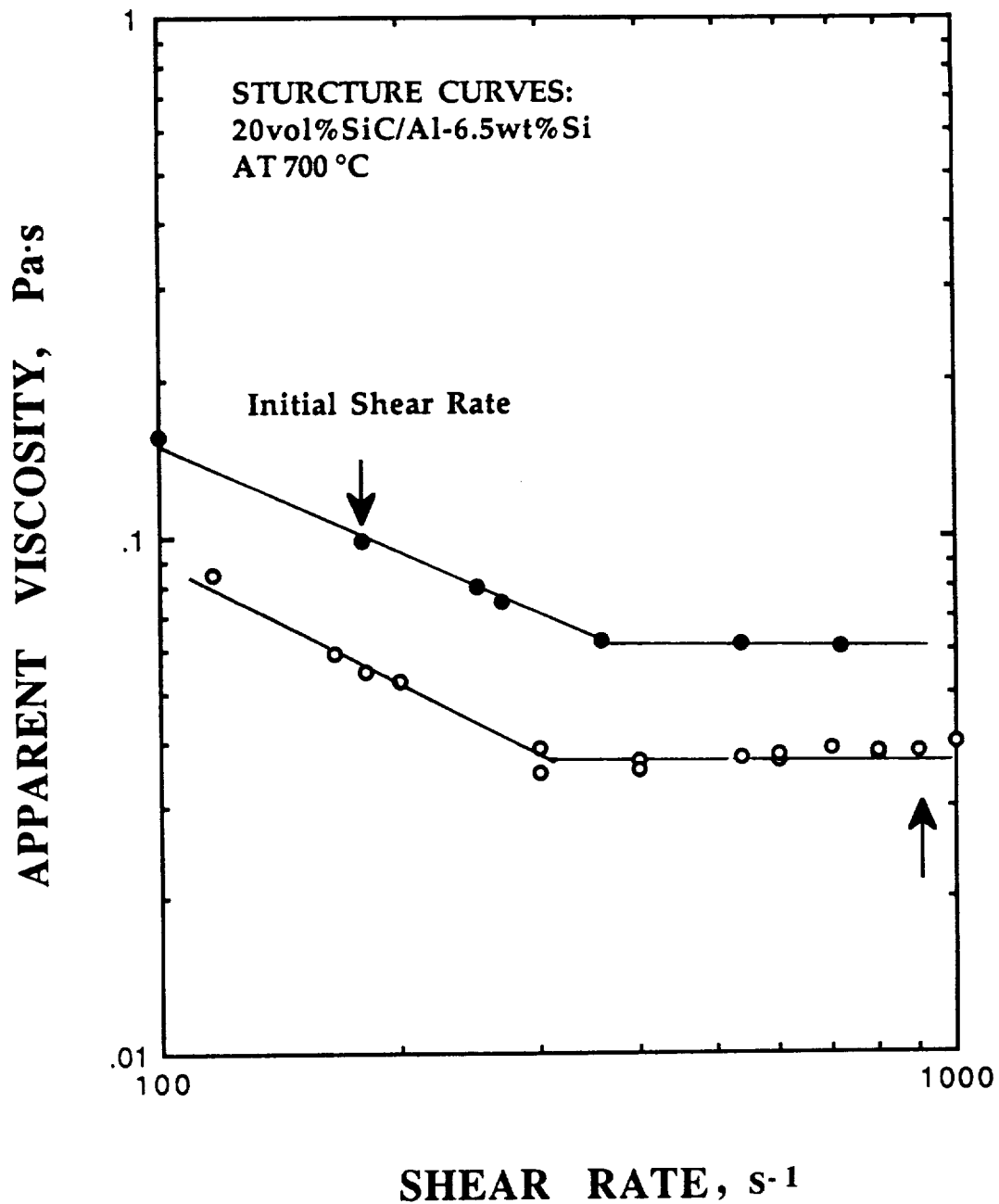


Fig. 5.8 (b) The plot of apparent viscosity and shear rate of 20 vol%SiC/Al-6.5 wt%Si composite slurry at 700 °C. Each sample was initially sheared at 180 and 900 s<sup>-1</sup>.



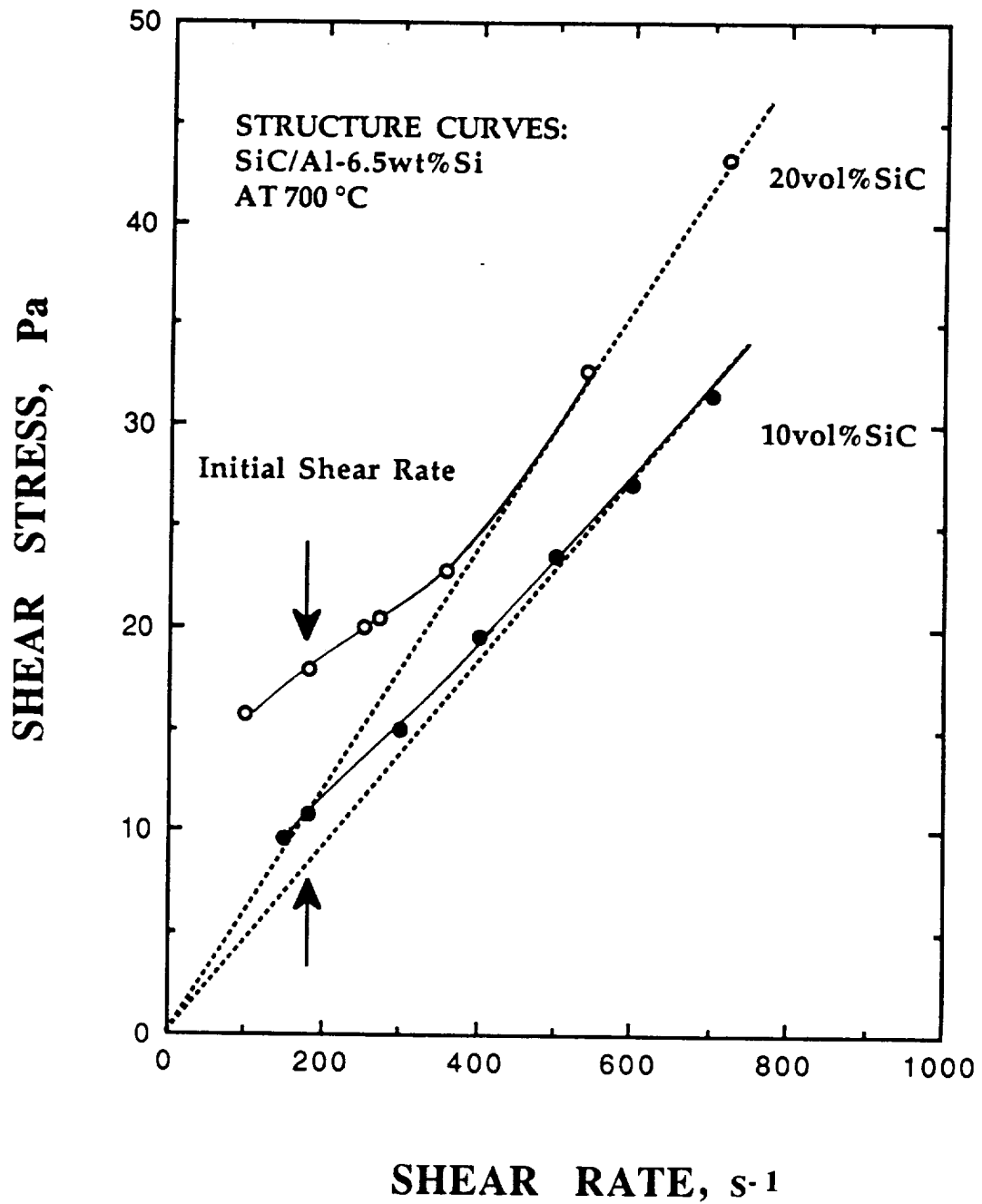


Fig. 5.9 (a) The plot of shear stress and shear rate of 10 and 20 vol%SiC/Al-6.5 wt%Si composite slurry at 700 °C. Both samples were initially sheared at 180 s<sup>-1</sup>.

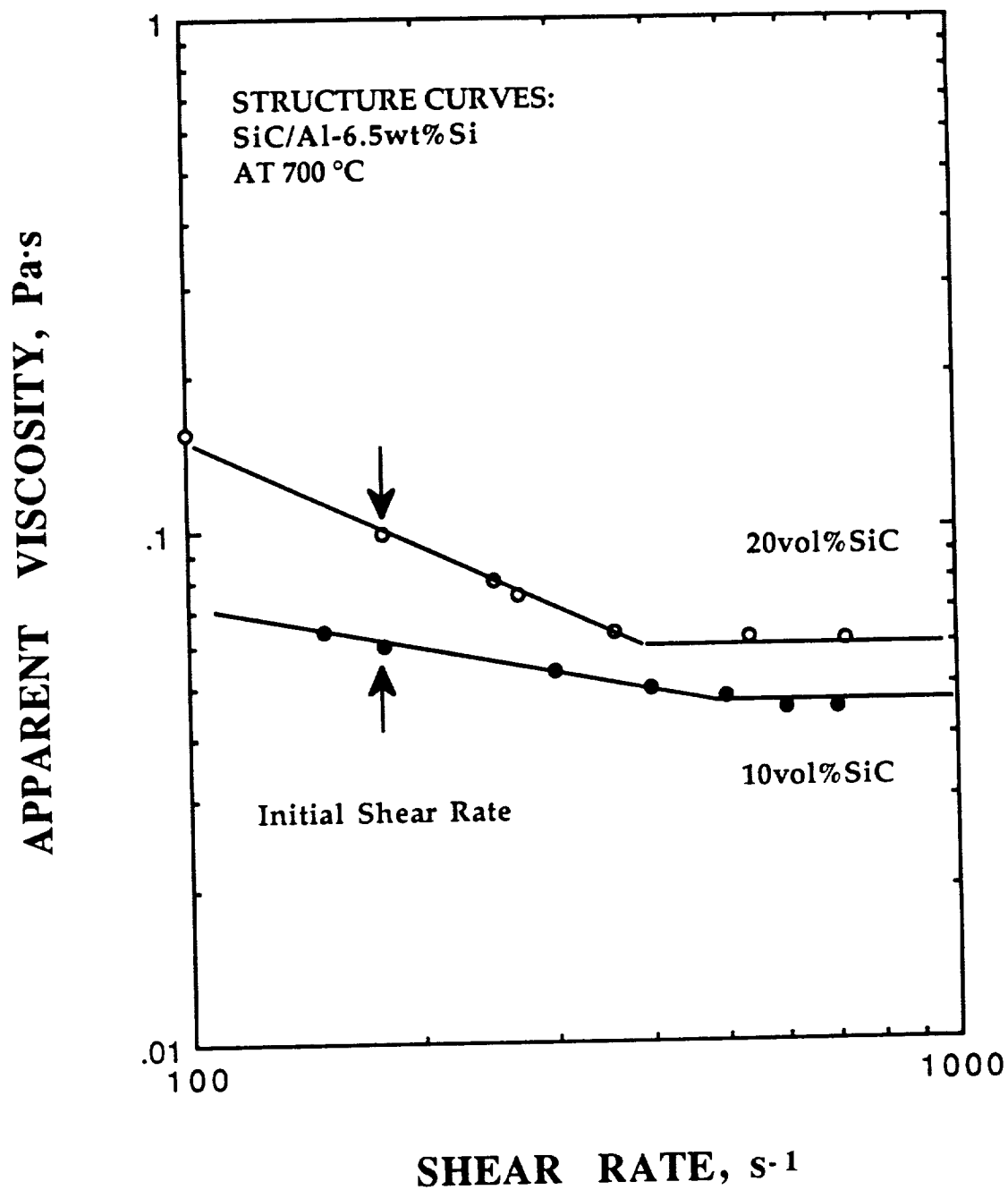


Fig. 5.9 (b) The plot of apparent viscosity and shear rate of 10 and 20 vol%SiC/Al-6.5 wt%Si composite slurry at 700 °C. Both samples were initially sheared at 180 s<sup>-1</sup>.

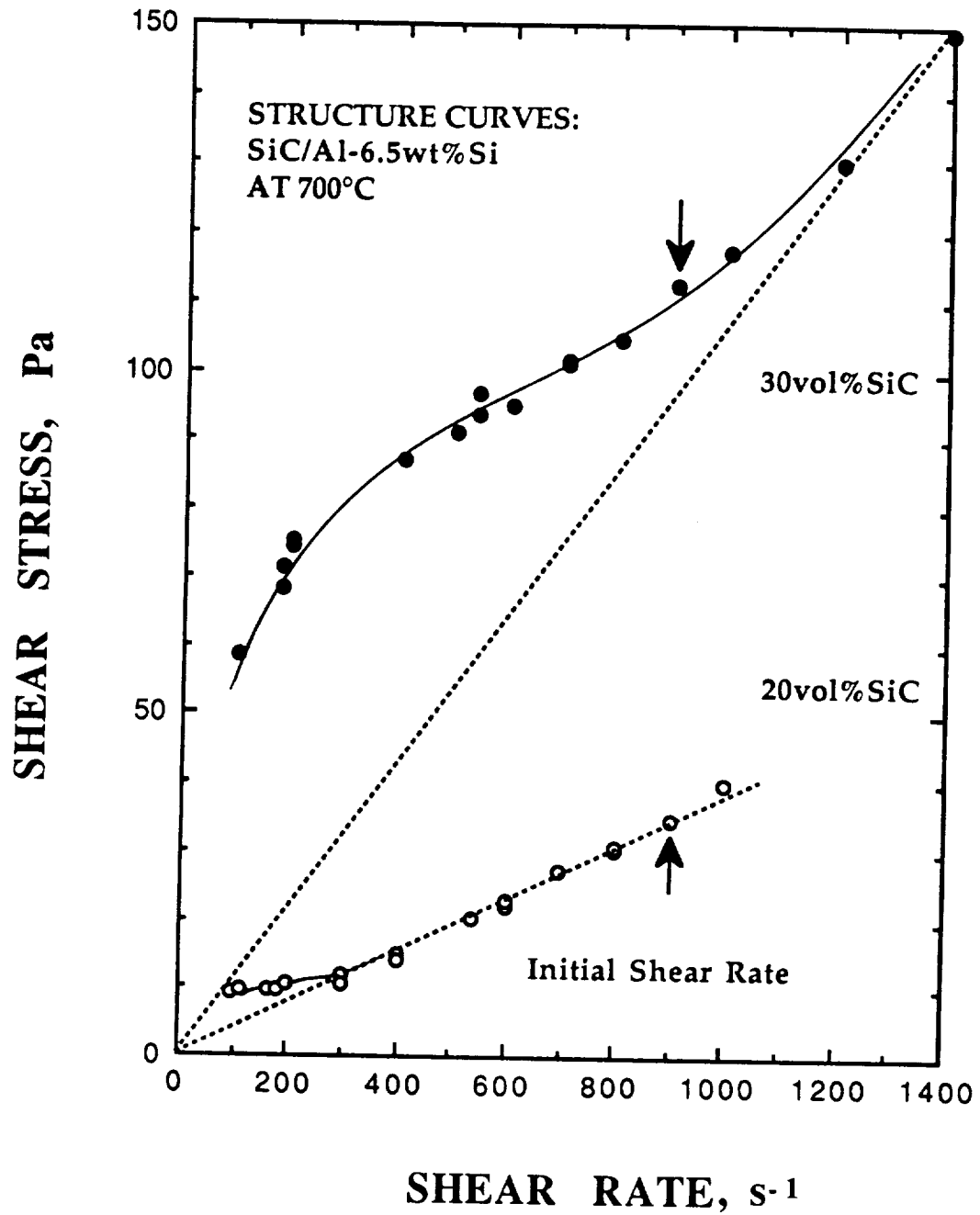


Fig. 5.10 (a) The plot of shear stress and shear rate of 20 and 30 vol%SiC/Al-6.5 wt%Si composite slurry at 700 °C. Both samples were initially sheared at 900  $s^{-1}$ .

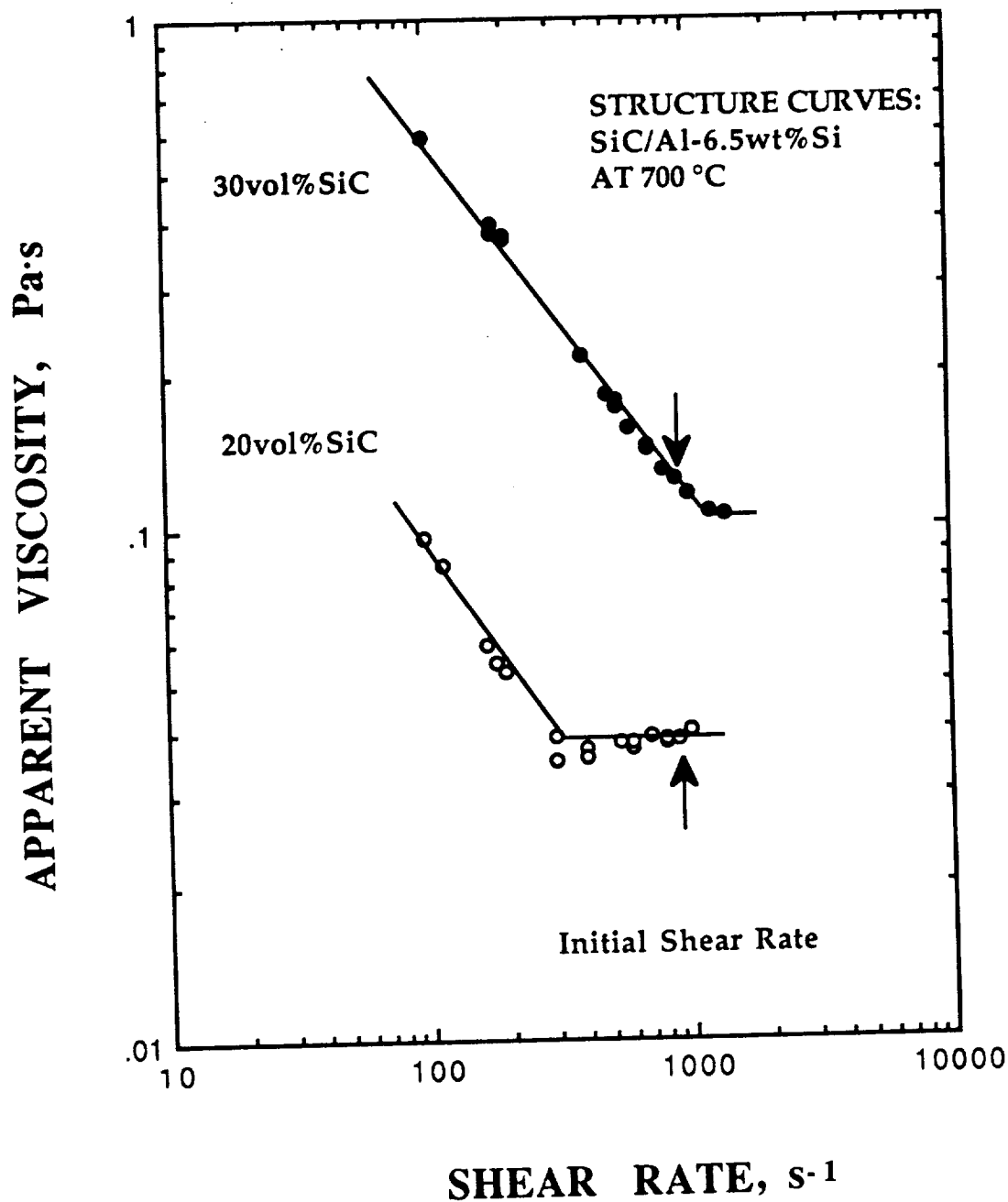


Fig. 5.10 (b) The plot of apparent viscosity and shear rate of 20 and 30 vol%SiC/Al-6.5 wt%Si composite slurry at 700 °C. Both samples were initially sheared at 900 s<sup>-1</sup>.

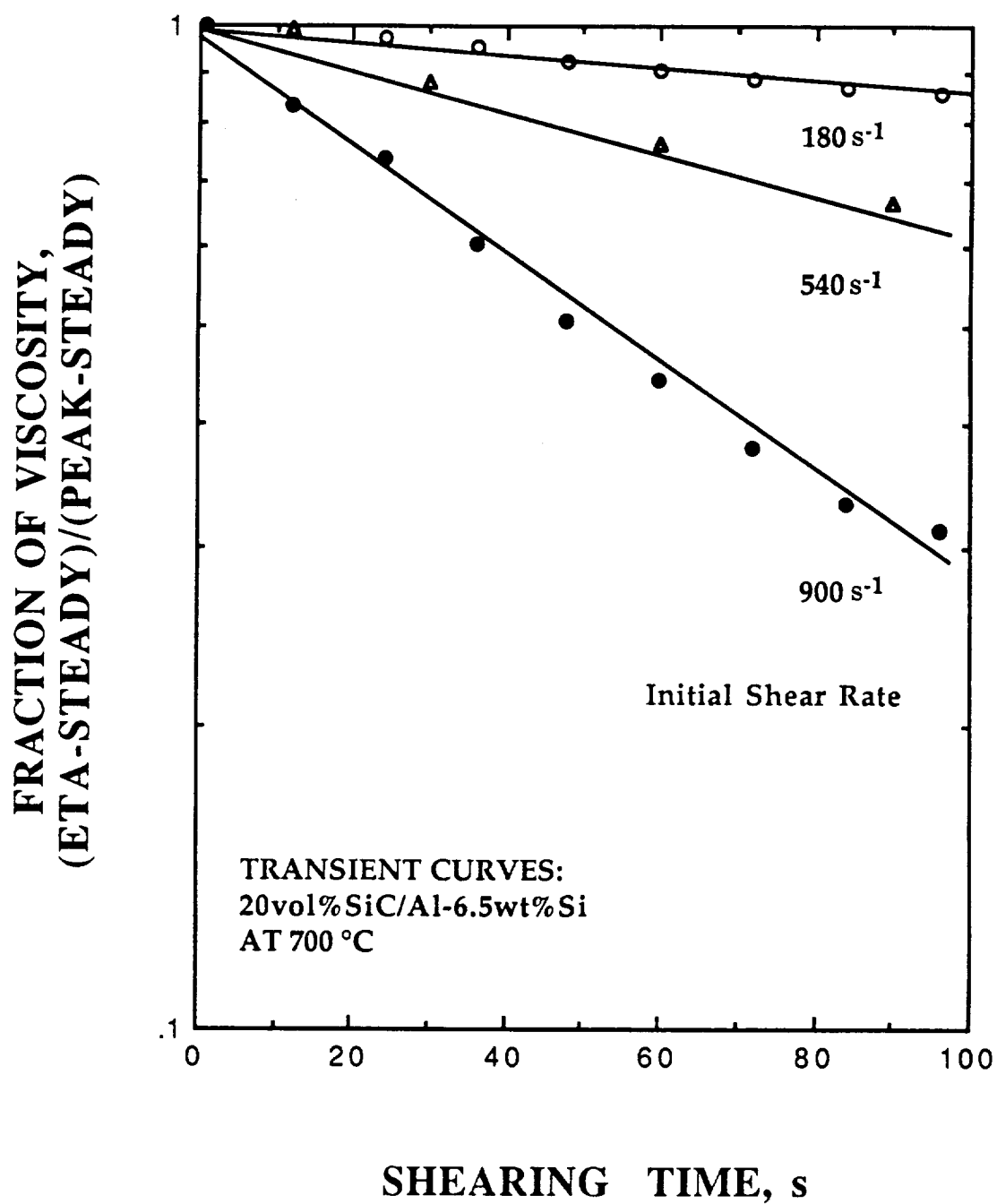


Fig. 5.11 Plot of change of viscosity relative to the steady state and shearing time after a rest, sheared at different shear rates for 20vol%SiC/Al-6.5wt%Si composite slurry at 700°C.

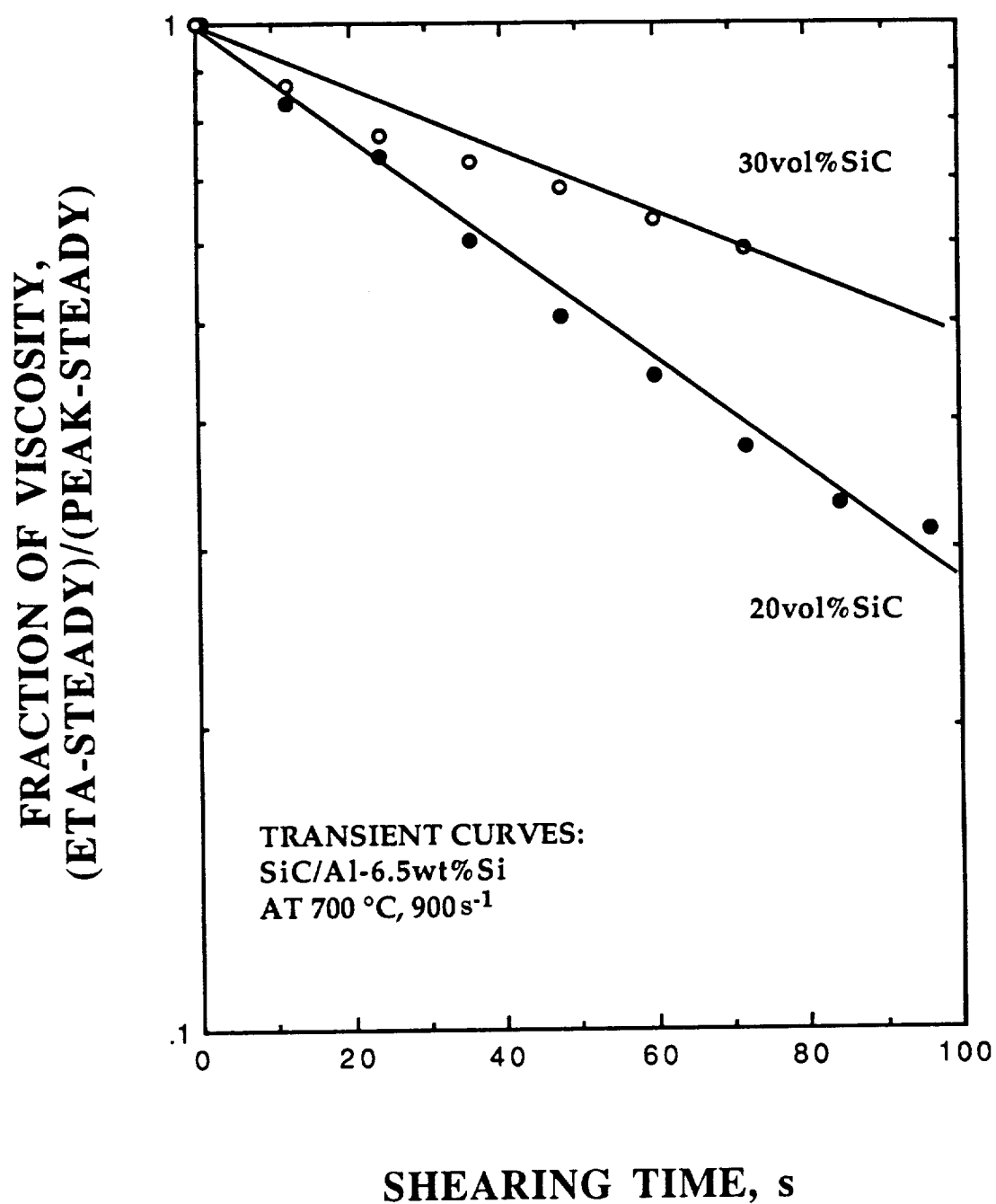


Fig. 5.12 Plot of change of viscosity relative to the steady state and shearing time after a rest, sheared at 900 s<sup>-1</sup> for 20 and 30 vol%SiC/Al-6.5wt%Si composite slurries at 700°C.

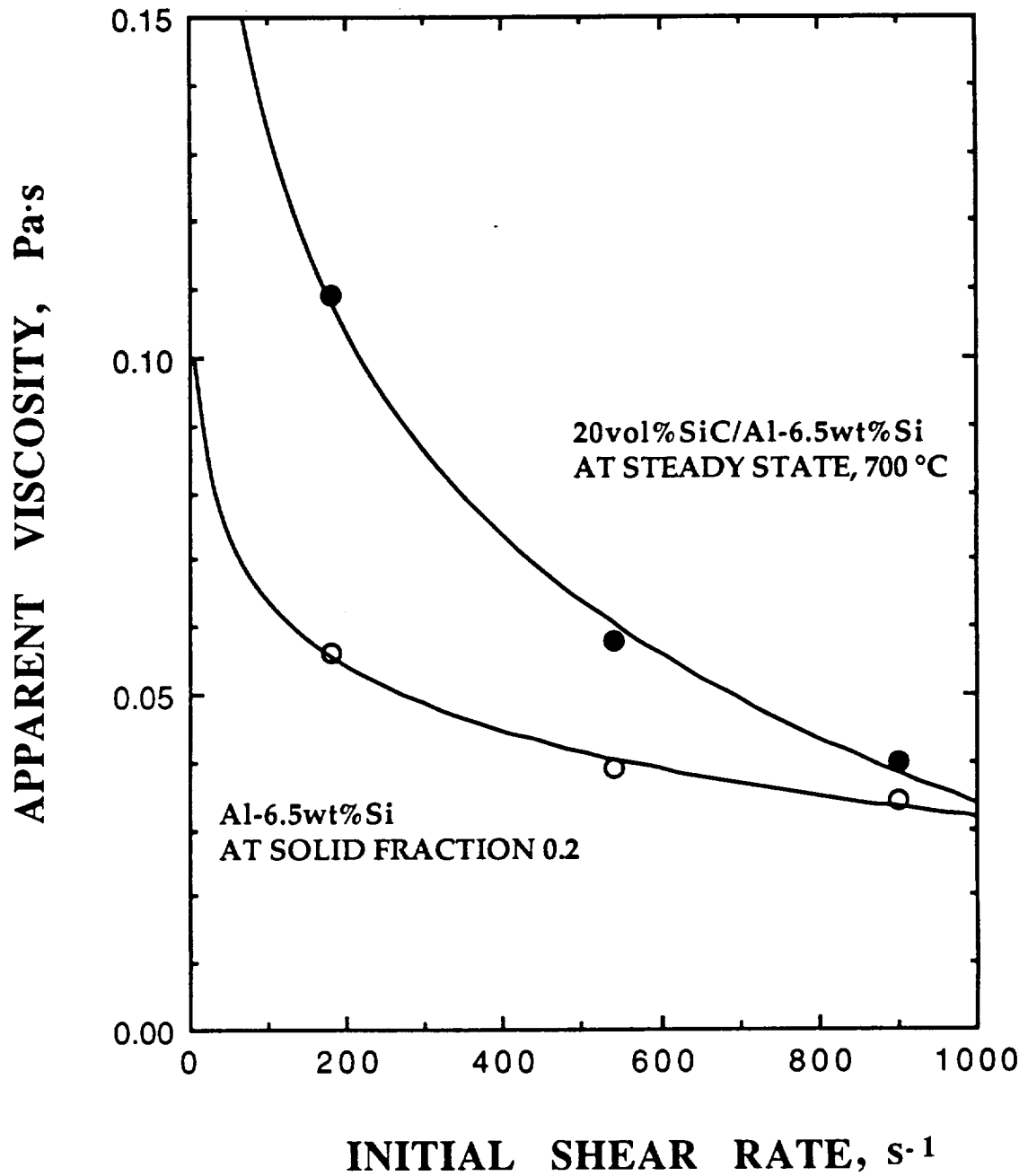


Fig. 5.13 Comparison of apparent viscosity of an alloy slurry with  $g_{s(\alpha)}=0.2$  in the semi-solid state and a composite slurry with  $g_{s(\text{SiC})}=0.2$  at 700°C.

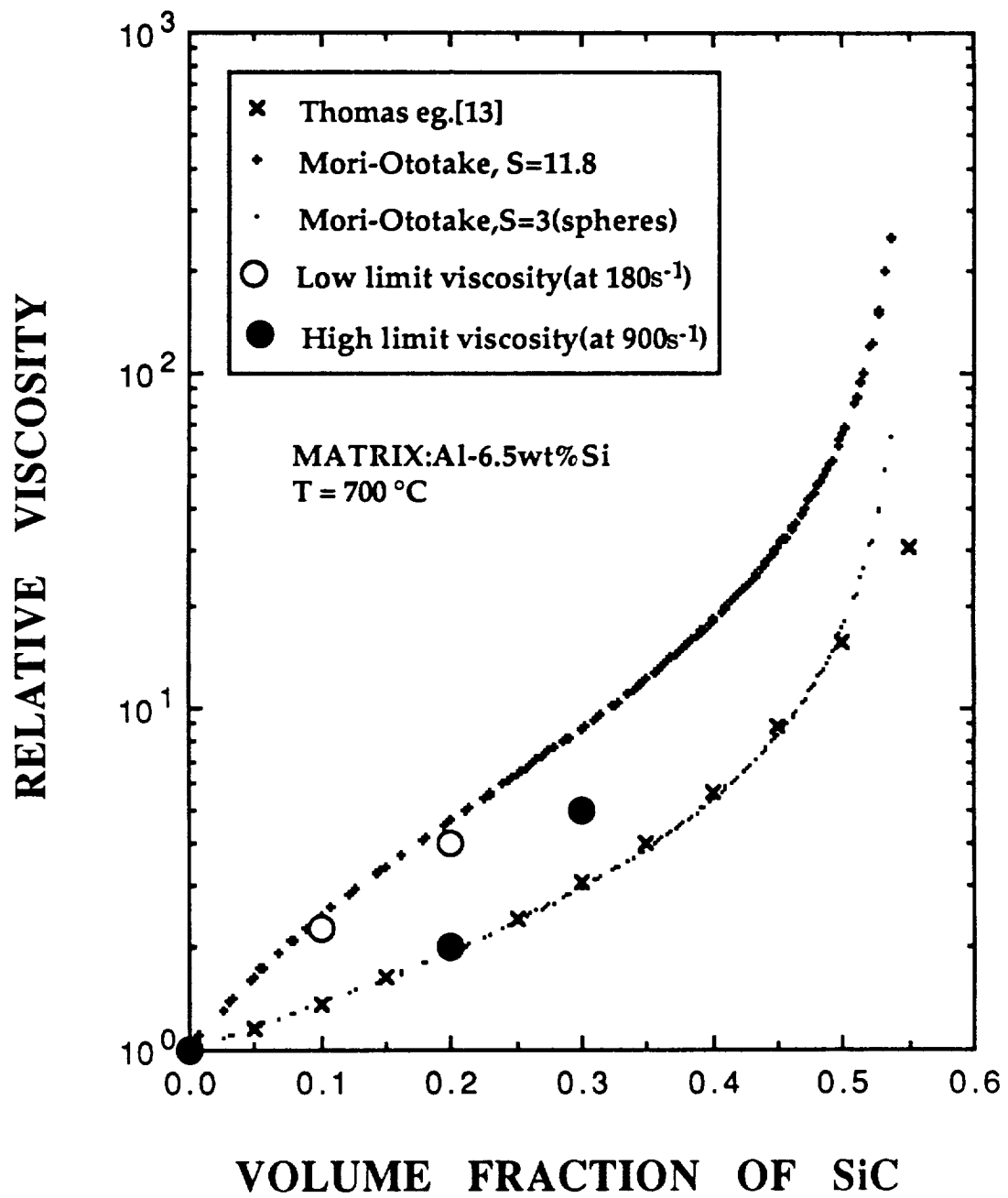


Fig. 5.14 Plot of low shear limit viscosity and high shear limit viscosity and volume fraction of SiC.



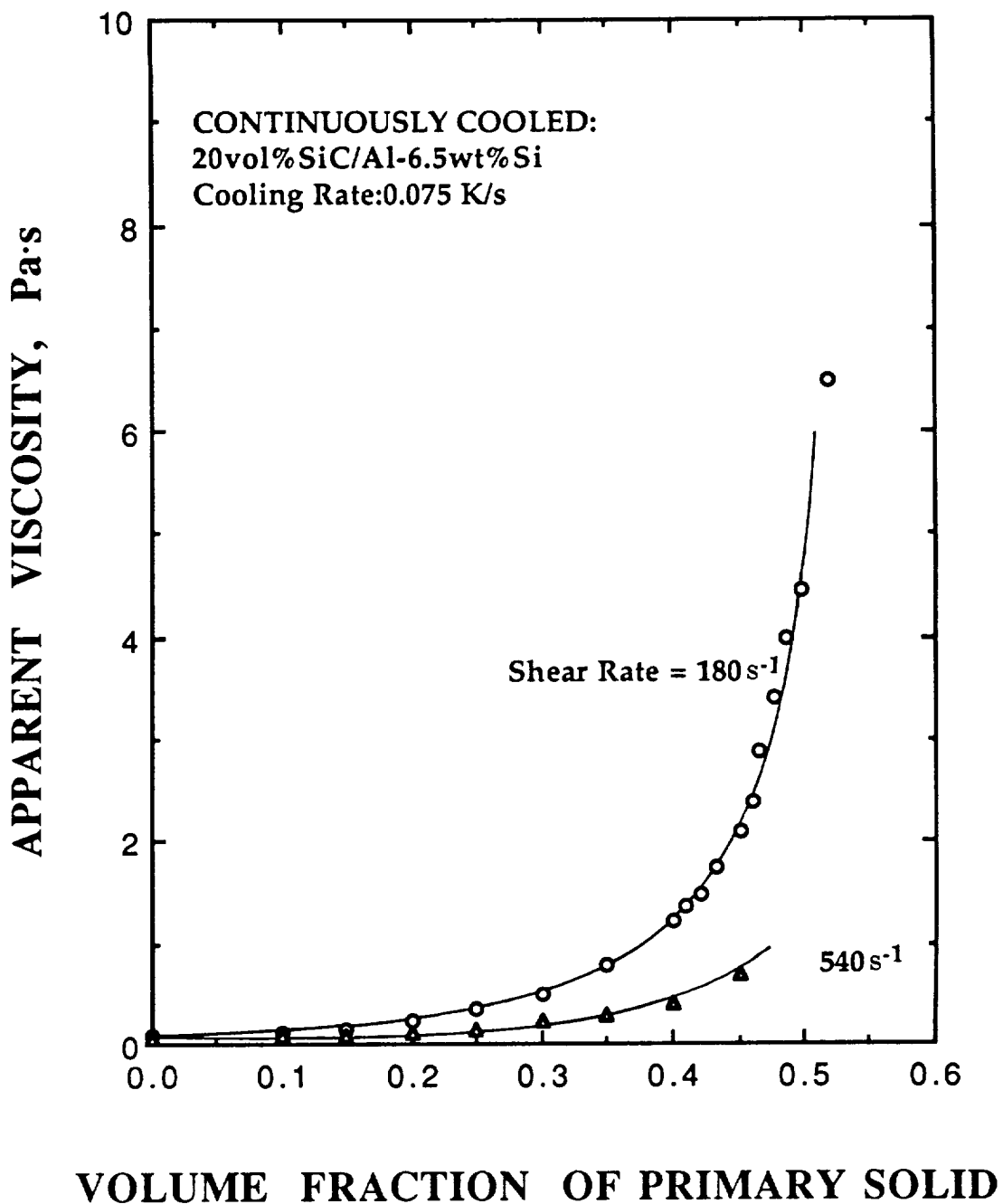


Fig. 6.1 Change of apparent viscosity of a composite with 20 vol%SiC, continuously cooled at 0.075 K/s at shear rates of 180 and  $540 \text{ s}^{-1}$ . The fraction solid is from the primary solid of the matrix alloy, equivalent to the temperature.

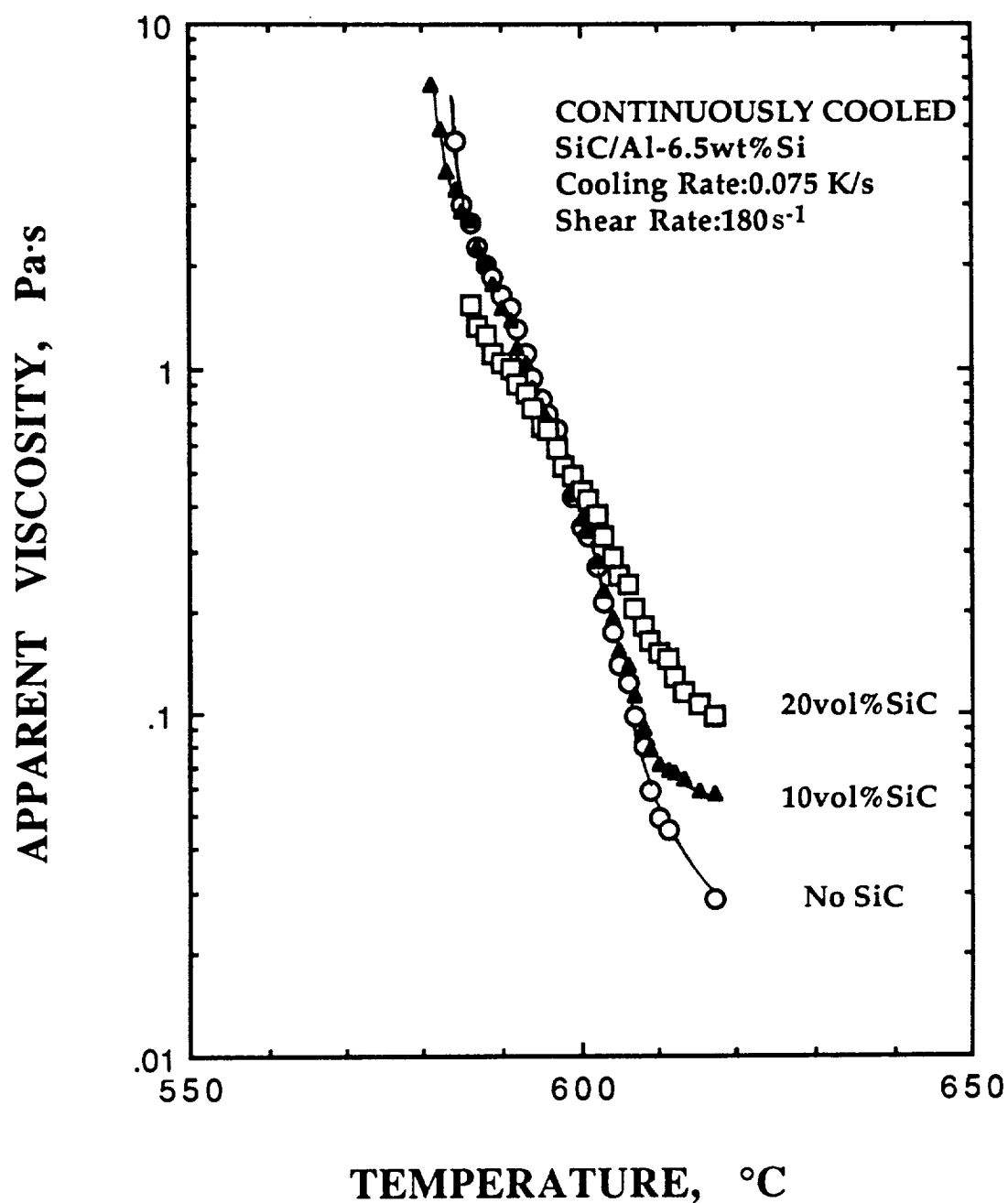


Fig. 6.2 Change of apparent viscosity of composite slurries with 0, 10, and 20 vol%SiC, continuously cooled at 0.075 K/s at shear rates of 180 s<sup>-1</sup>. Note that there is a clear cross-over in temperature for a composite with 20 vol%SiC, below which the viscosity of the composite is lower than that of the matrix alloy.

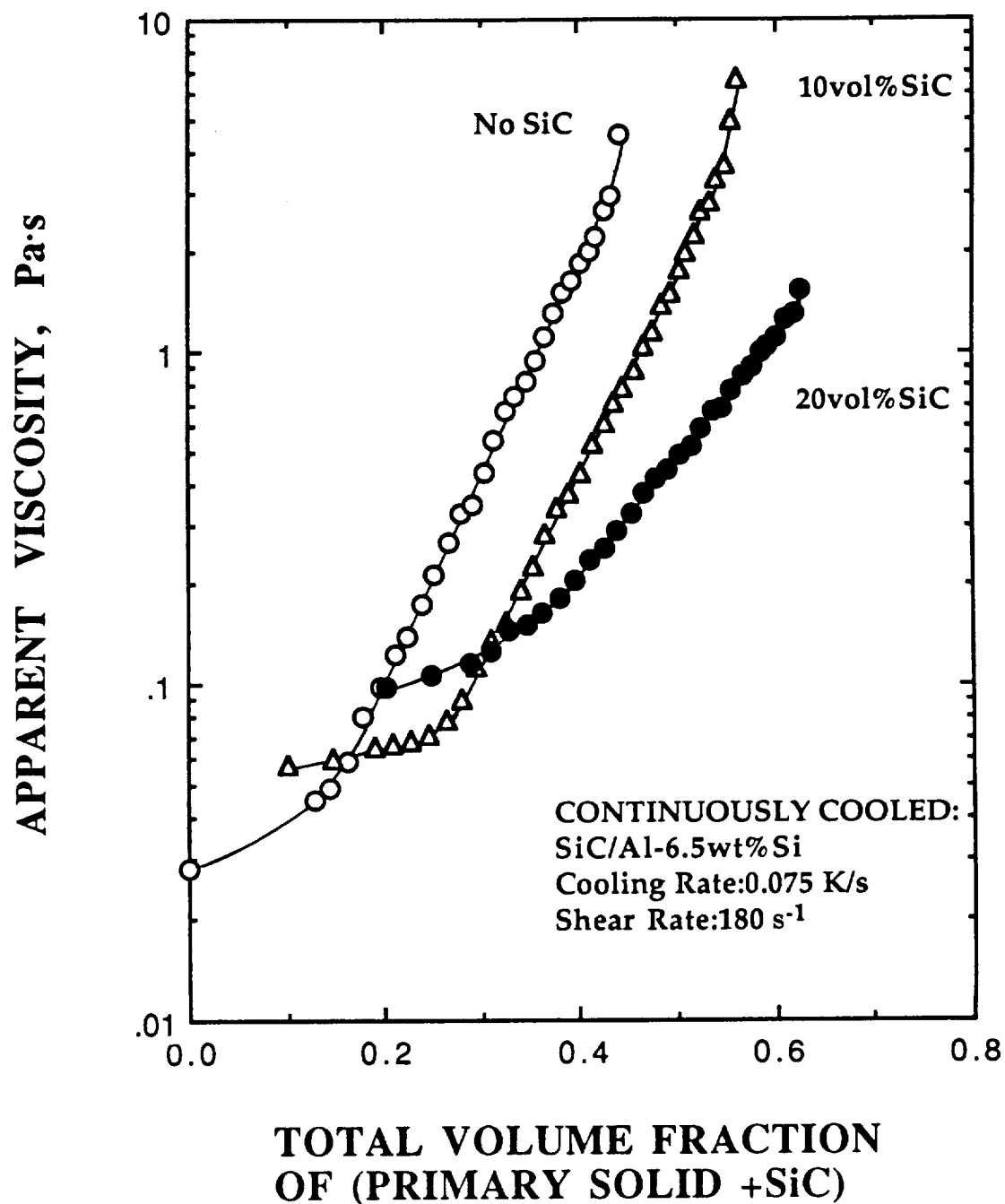


Fig. 6.3

Change of apparent viscosity of composite slurries with 0, 10, and 20 vol%SiC, continuously cooled at 0.075 K/s at shear rates of 180 s<sup>-1</sup>. Note that volume fraction solid is expressed in total solid amount, including SiC and primary solid, calculated by eqn. (53).

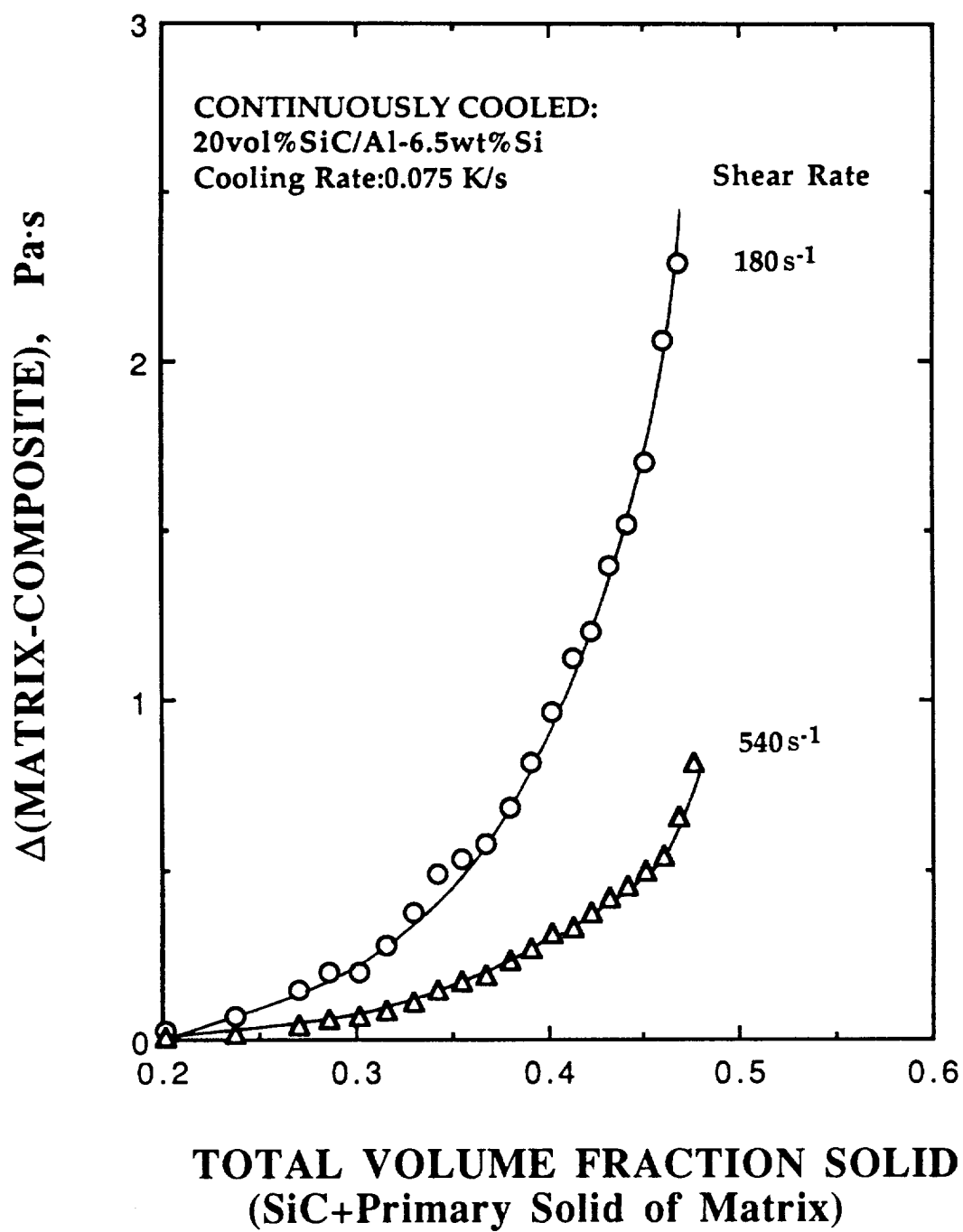
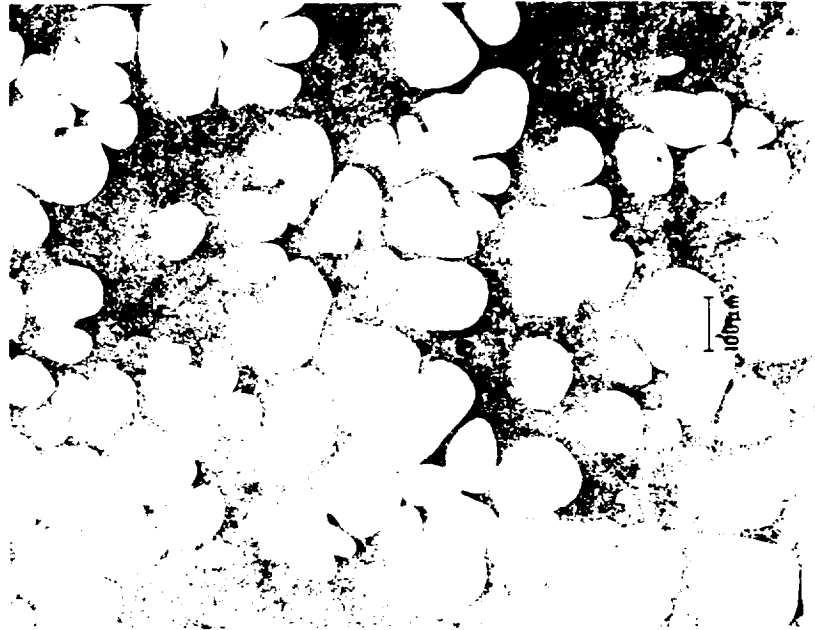
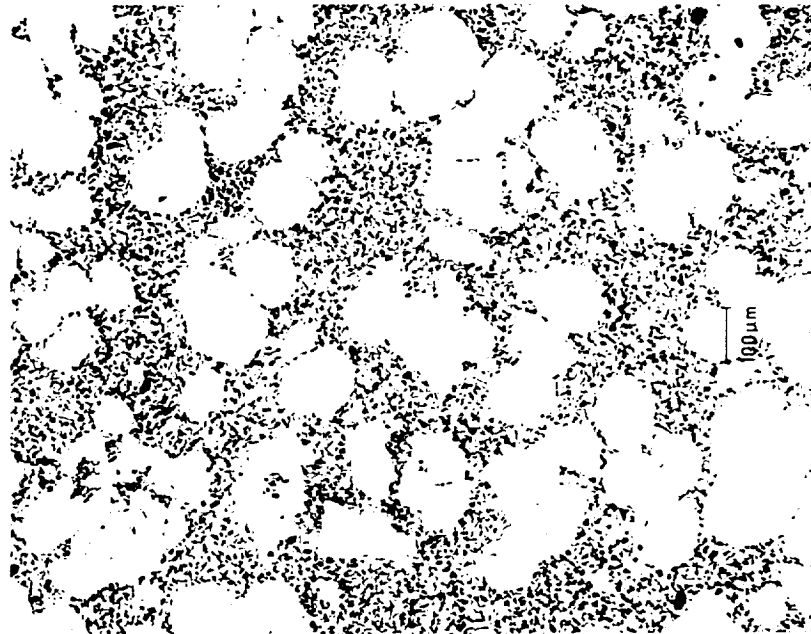


Fig. 6.4

Comparison of difference in the viscosities of a composite slurry with 20 vol%SiC and the matrix alloy of the composite, both sheared at 180 and 540 s<sup>-1</sup>.



(a)



(b)

Fig. 6.5 Optical micrographs of samples, continuously cooled at 0.075 K/s, and sheared at  $900 \text{ s}^{-1}$  (x75):  
 (a) Al-6.5wt%Si matrix alloy ( $R_A=2.8$ ),  
 (b) 20 vol%SiC/Al-6.5wt%Si composite ( $R_A=2.5$ ).

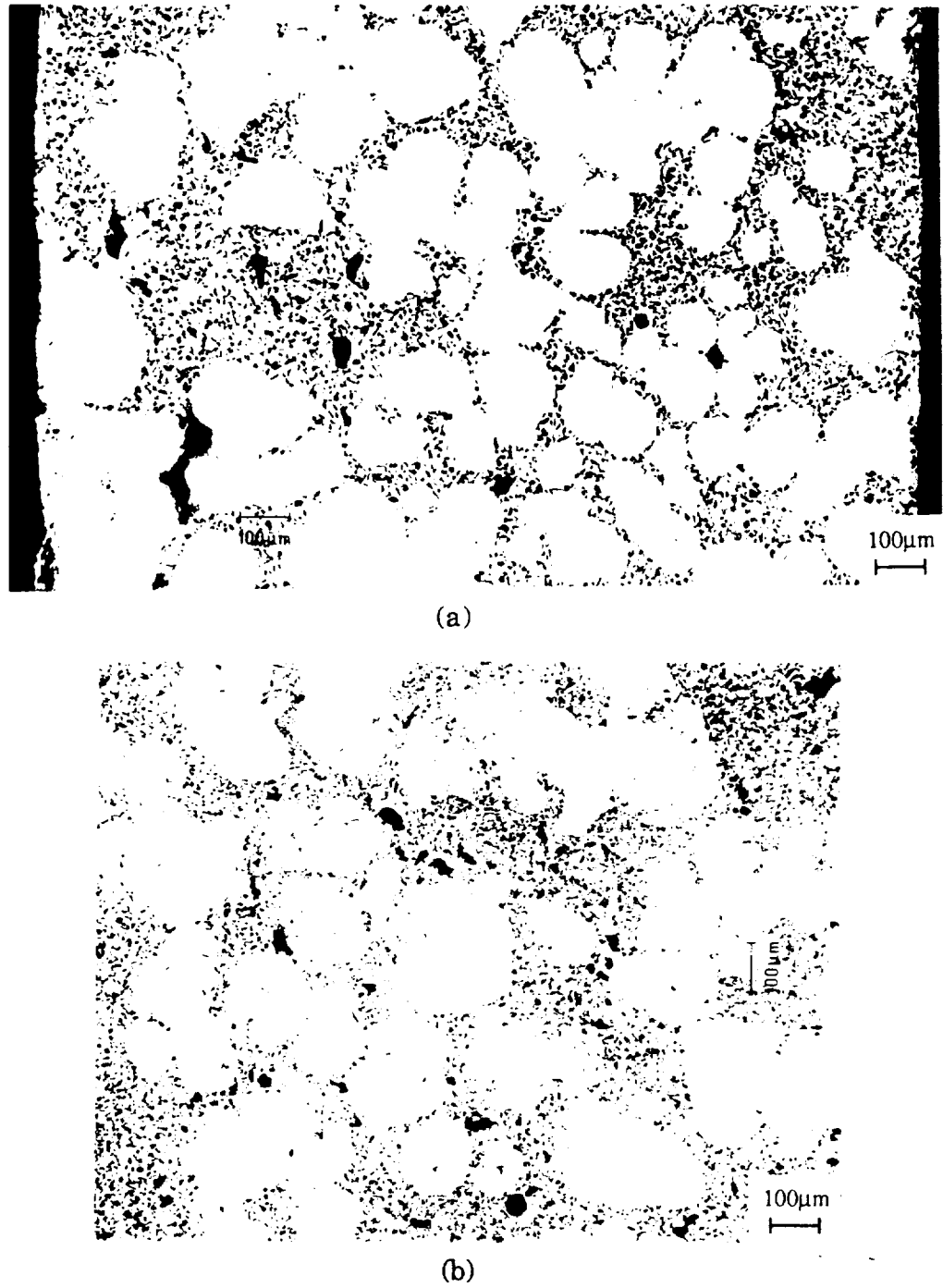


Fig. 6.6 Effect of cooling rate on the microstructures of composites (20 vol%SiC/Al-6.5wt%Si), sheared at  $180 \text{ s}^{-1}$ , and continuously cooled at (a)  $\epsilon = 0.075 \text{ K/s}$  ( $R_A=3.6$ ), and (b)  $\epsilon = 0.0083 \text{ K/s}$  ( $R_A=2.8$ ) (x75).

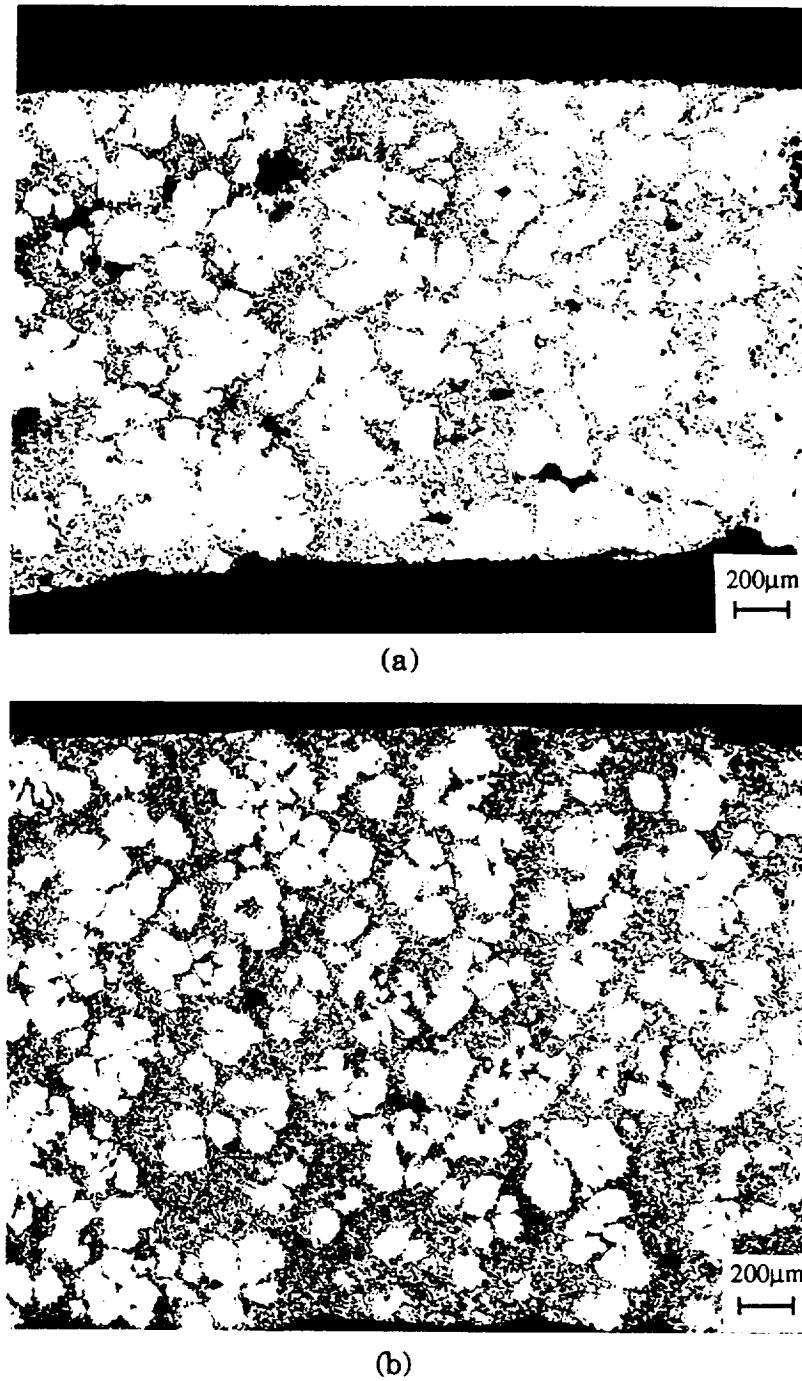


Fig. 6.7 Effect of shear rate on the microstructures of composites (20 vol%SiC/Al-6.5wt%Si), continuously cooled at 0.075 K/s (x37.5). Shear rate was (a)  $180 \text{ s}^{-1}$  ( $R_A=3.6$ ), and (b)  $900 \text{ s}^{-1}$  ( $R_A=2.7$ ), respectively.

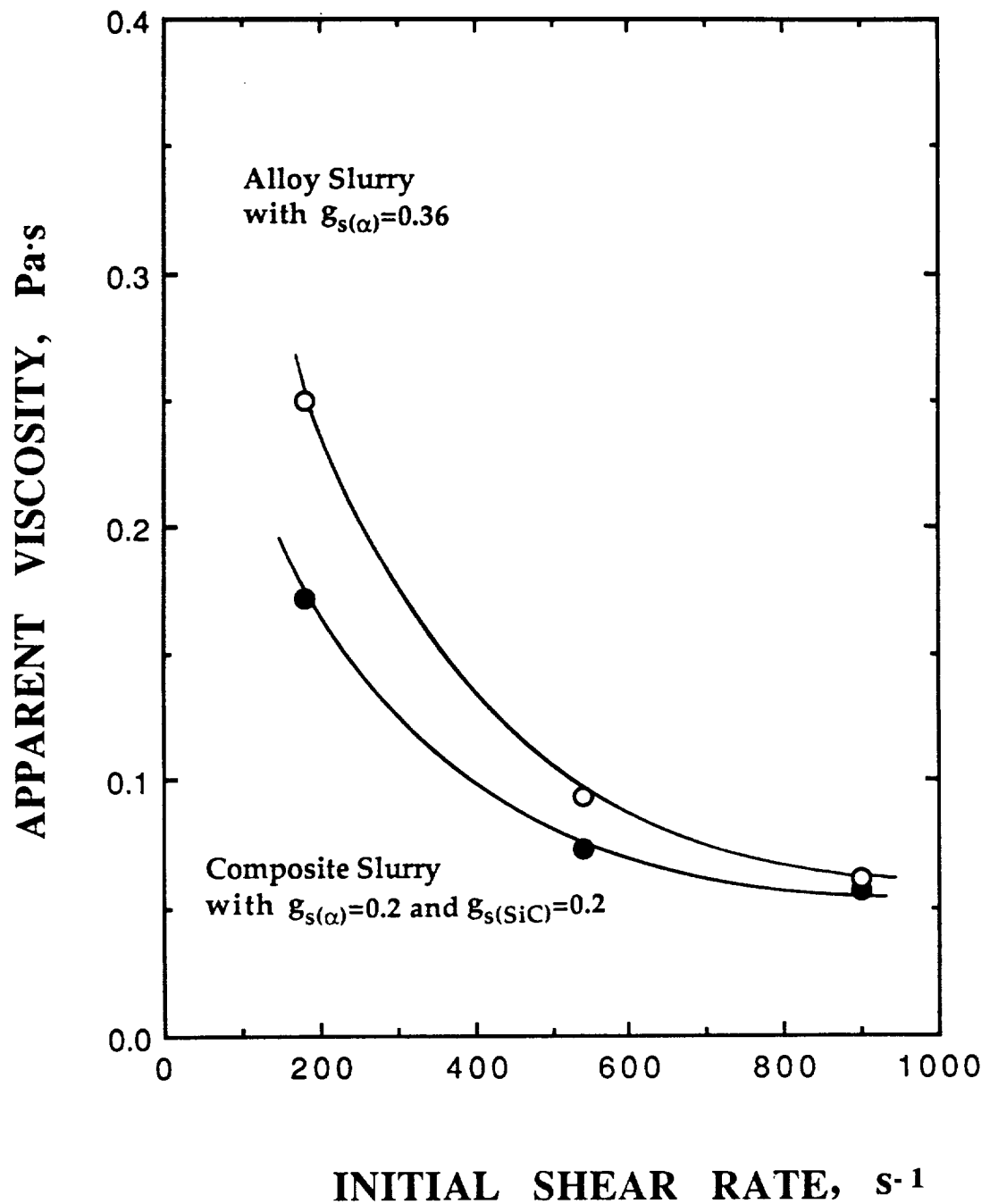
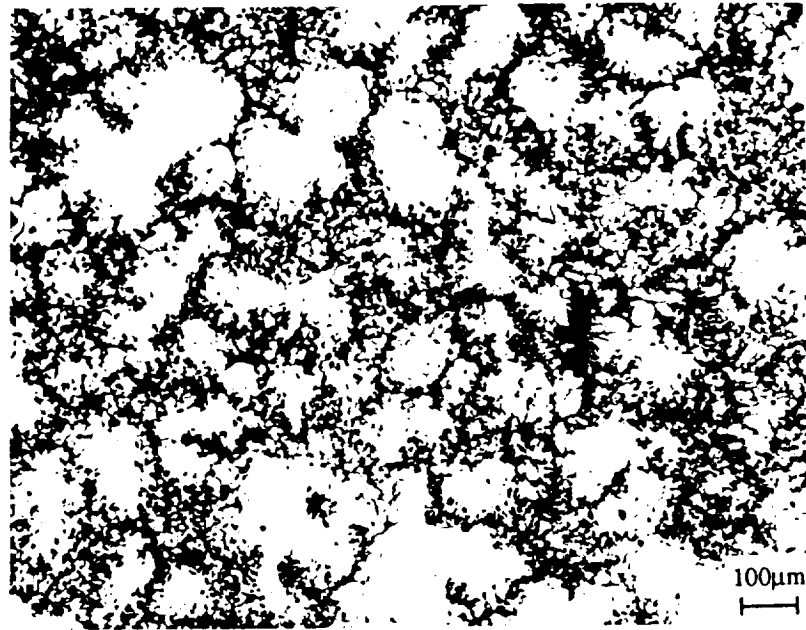
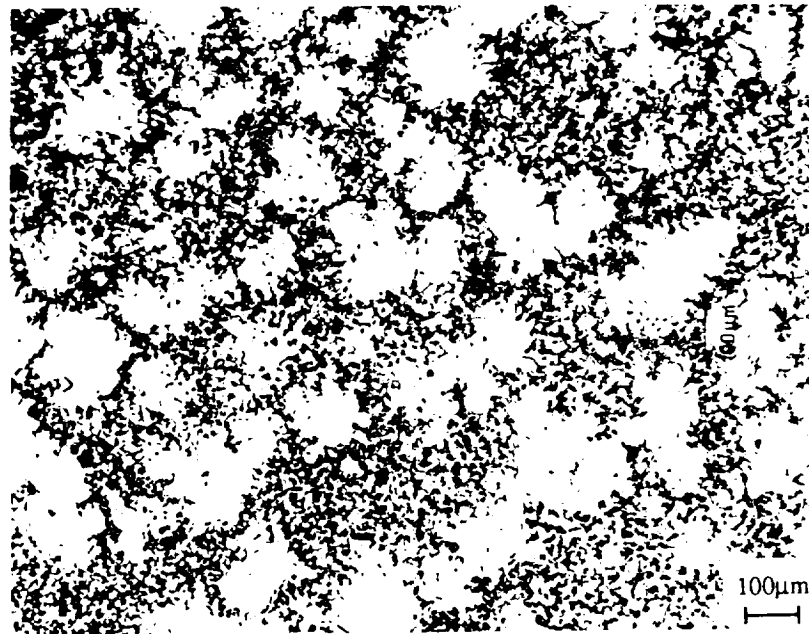


Fig. 6.8 Comparison of the apparent viscosity of a composite with total 0.36 fraction solid (i.e., a mixture of  $g_{s(\text{SiC})}=0.2$  and  $g_{s(\alpha)}=0.2$ ), and an alloy slurry with 0.36 fraction solid of primary particles only. Note that the apparent viscosity of the composite is lower than that of the alloy slurry.





(a)



(b)

Fig. 6.9 Optical micrographs of a composite with a mixture of  $\mathcal{G}_{s(\text{SiC})}=0.2$  and  $\mathcal{G}_{s(\alpha)}=0.2$ , isothermally sheared at (a)  $180 \text{ s}^{-1}$ , and (b)  $900 \text{ s}^{-1}$ , respectively, (x75).

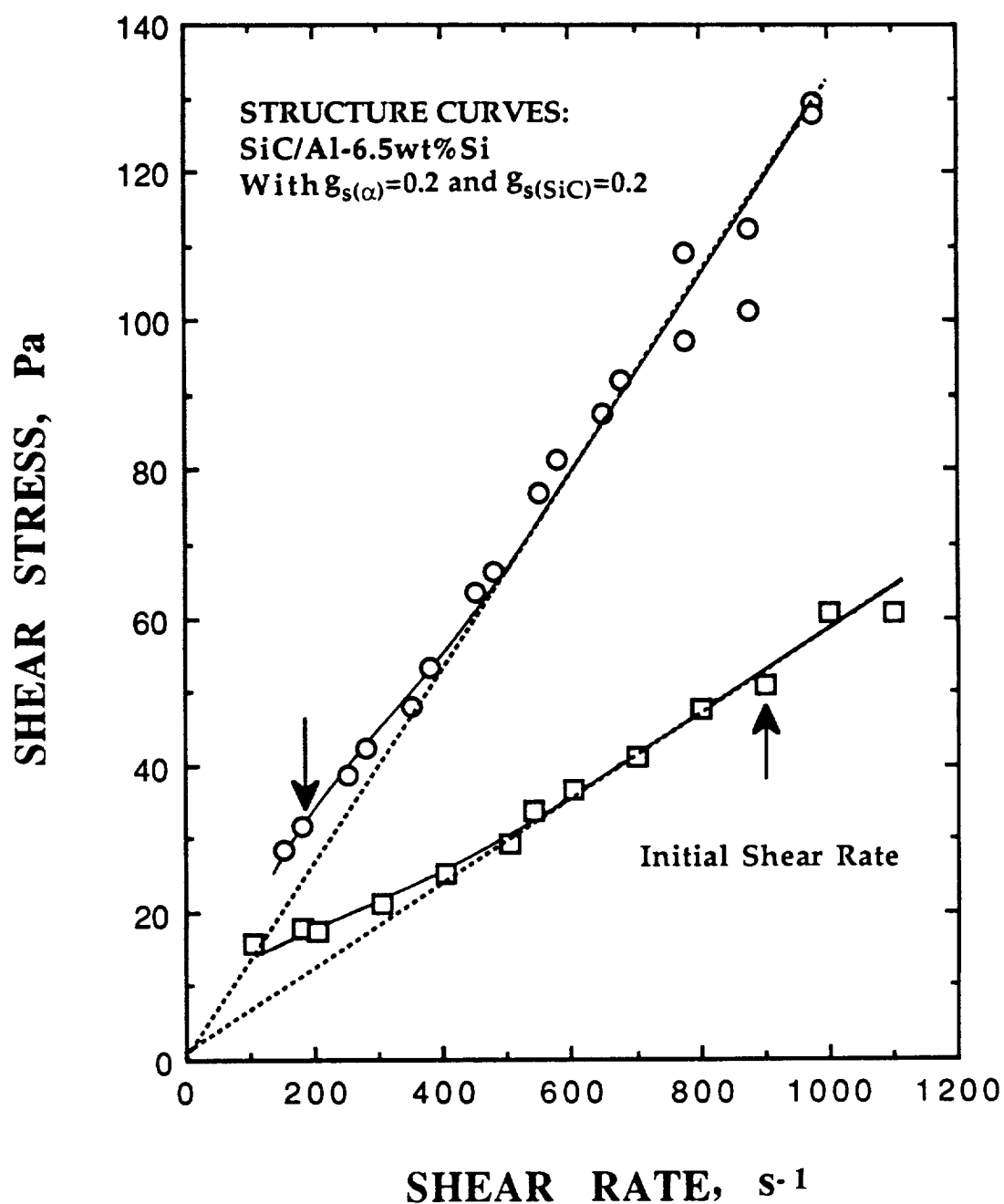


Fig. 6.10 Plot of shear stress and shear rate of 20 vol%SiC/Al-6.5wt%Si at a temperature for  $g_{s(\alpha)}=0.2$ . Each sample was initially sheared at 180 and 900  $\text{s}^{-1}$  (structure curves).

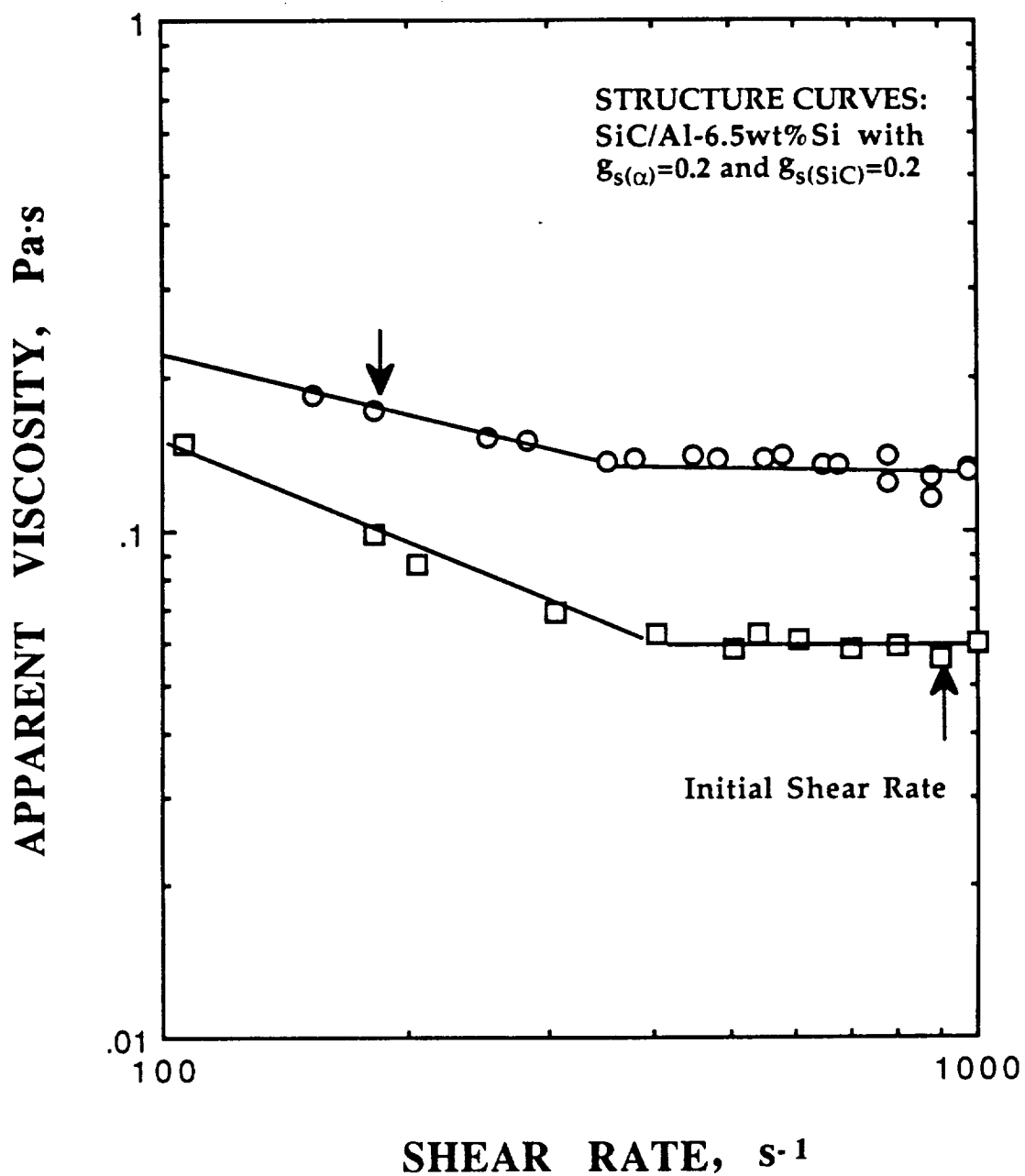


Fig. 6.11 Plot of apparent viscosity and shear rate of 20 vol%SiC/Al-6.5wt%Si at a temperature for  $g_{s(\alpha)}=0.2$ . Each sample was initially sheared at 180 and 900  $\text{s}^{-1}$  (structure curves).

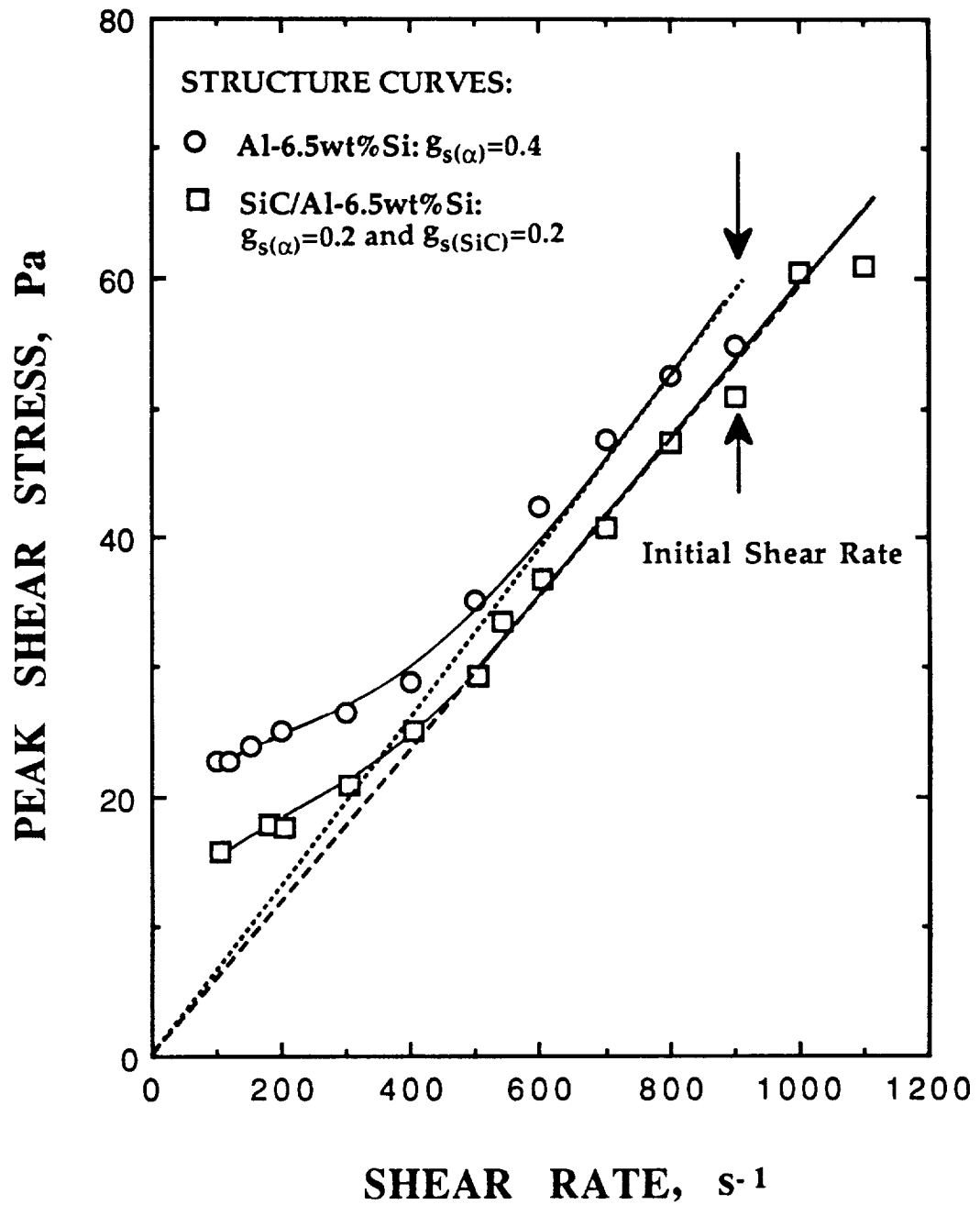


Fig. 6.12 Plot of shear stress and shear rate of 20 vol%SiC/Al-6.5wt%Si at a temperature for  $g_{s(\alpha)}=0.2$  and a matrix alloy with  $g_{s(\alpha)}=0.4$ . Both samples were initially sheared at  $900 \text{ s}^{-1}$  (structure curves).

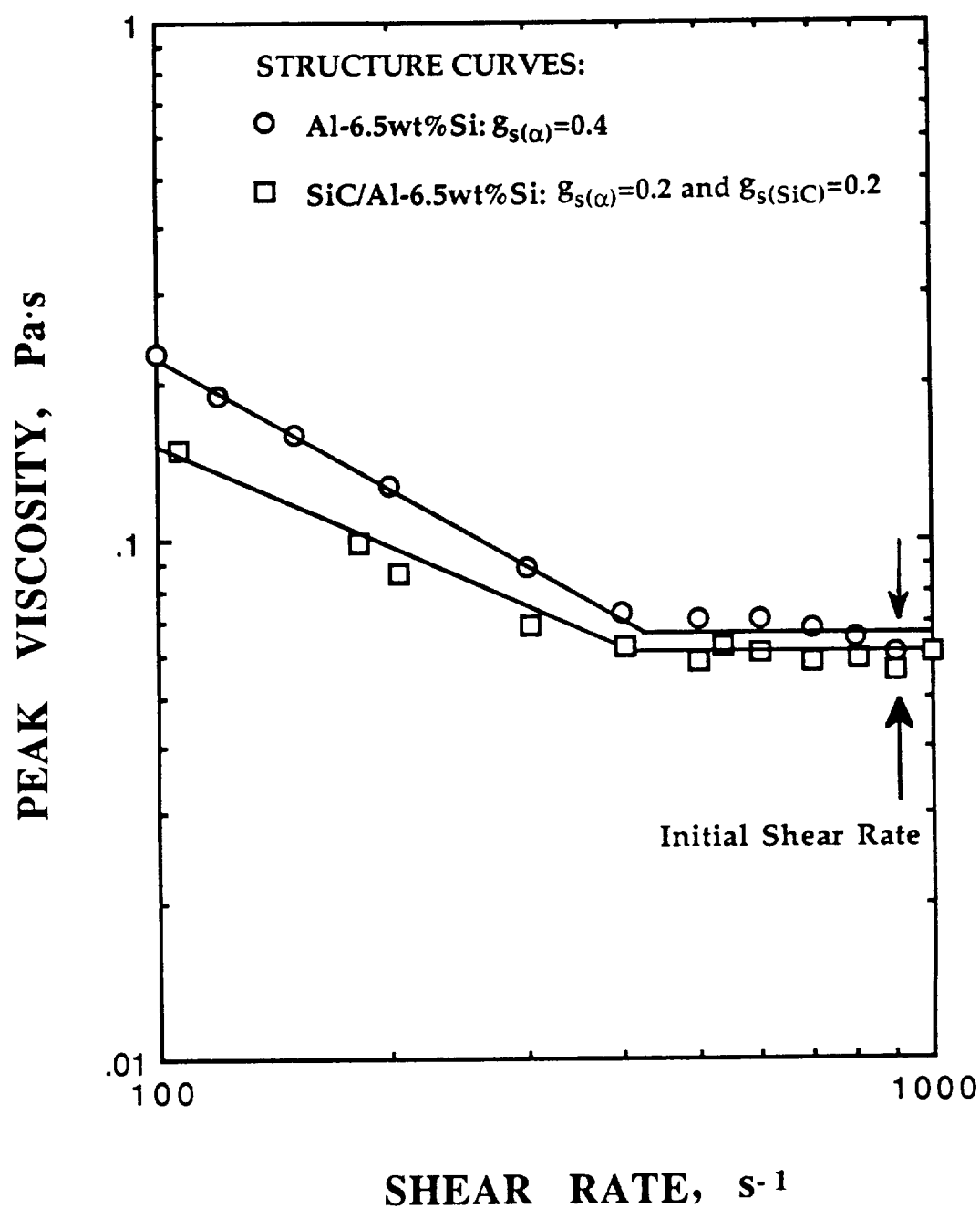


Fig. 6.13 Plot of apparent viscosity and shear rate of 20 vol%SiC/Al-6.5wt%Si at a temperature for  $g_{s(\alpha)}=0.2$  and a matrix alloy with  $g_{s(\alpha)}=0.4$ . Both samples were initially sheared at  $900 \text{ s}^{-1}$  (structure curves).

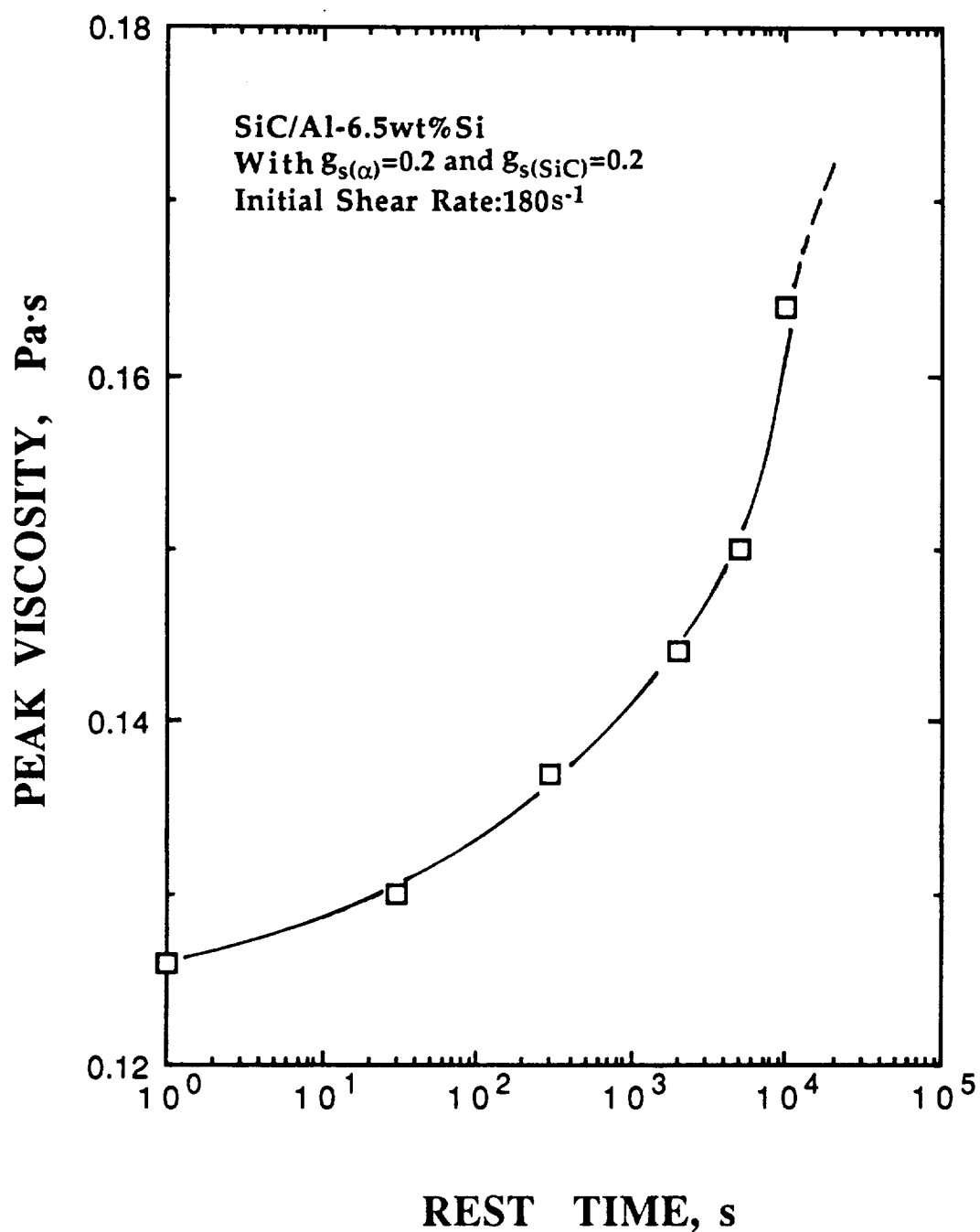


Fig. 6.14 Plot of peak viscosity after resumption of shearing versus rest time for 20 vol%SiC/Al-6.5wt%Si at a temperature for  $g_{s(\alpha)}=0.2$ . The initial shear rate was  $180\text{ s}^{-1}$ .

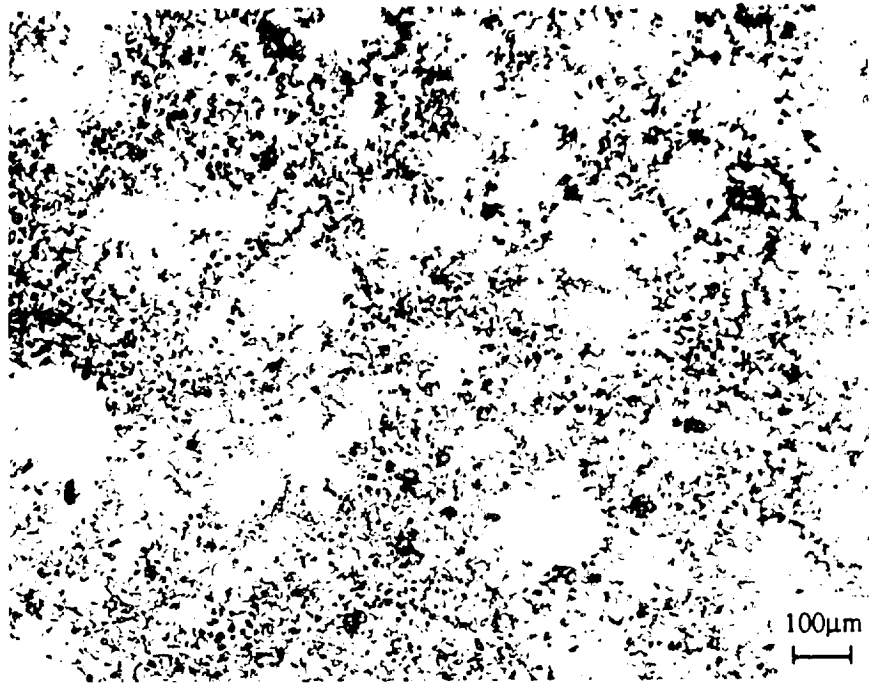


Fig. 6.15 An optical micrograph of 20 vol%SiC/Al-6.5wt%Si at a temperature for  $g_{s(\alpha)}=0.2$ , initially sheared at  $180 \text{ s}^{-1}$  for two hours, followed by resting for  $10^4 \text{ s}$ .

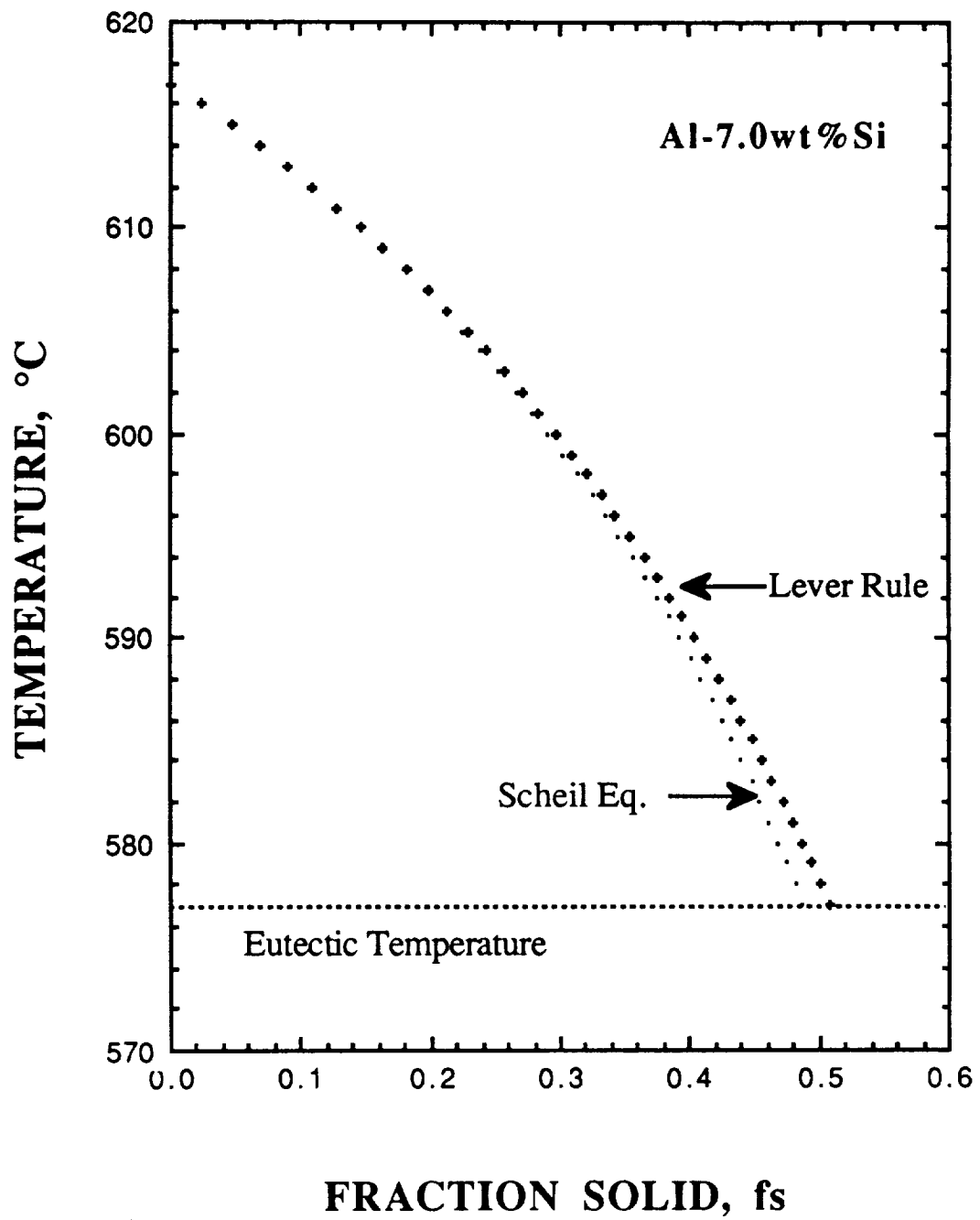


Fig. A1 Comparison of weight fractions solid calculated from the lever rule and the Scheil equation.



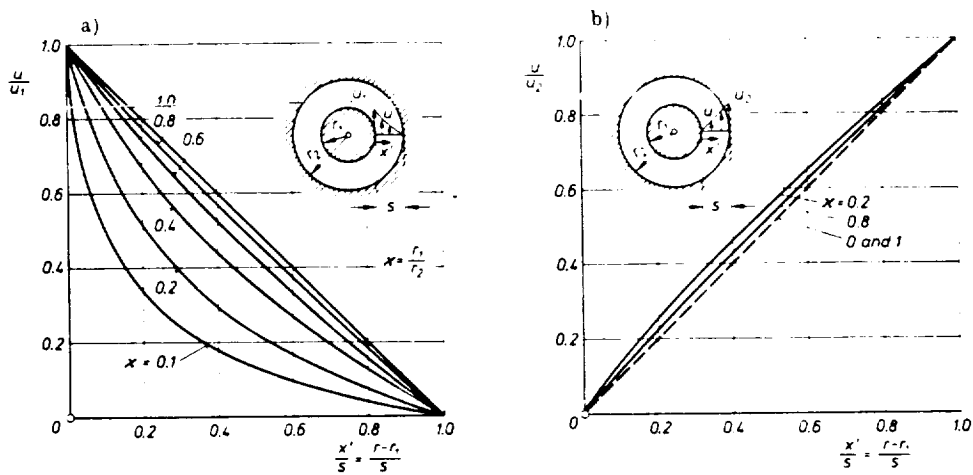


Fig. A2 Velocity distribution in the annulus between two concentric, rotating cylinders [160].  
 (a) Case I : inner cylinder rotating; outer cylinder at rest  
 (b) Case II: inner cylinder at rest; outer cylinder rotating

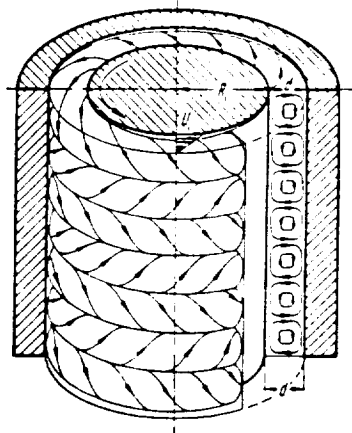


Fig. A3 Taylor vortices between two concentric cylinders: inner cylinder rotating, the outer cylinder at rest [160].

Table 2.1 Relationship Between Relative Viscosity and Concentration of Suspension

Ref.	Authors	Formula	Comments
8	Einstein (1906,1911)Theo.	$\eta_r = (1+\phi/2)/(1-2\phi) = 1 + 2.5\phi$	For spheres, $\phi < 0.01$
25	Eilers (1941)Empirical	$\eta_{r,\infty} = [1 + 1.56\phi/(1-\phi\phi_m)]^2$	
16	Vand (1948) Theo.	$\eta_r = \exp [k_1\phi + \gamma_2(k_2 - k_1)\phi^2/(1-Q\phi)]$	For spheres, $k_1=2.5$ , $k_2=3.175$ , $\gamma_2=4$ , $Q=39/64$
17	Robinson(1949) Semi-theo	$\eta_r = 1 + k [\phi/(1-s'\phi)]$	$k$ =material constant, $s'$ =relative sedimentation volume
18	Roscoe(1950) Theo.	$\eta_r = (1 - 1.35\phi)^{-2.5}$	For higher concentration, equal size
10	Mooney (1951)Semi-theo.	$\eta_{r,o} = \exp [2.5\phi/(1-k\phi)]$ , $k=1/\phi_m$	For spheres; $k$ =Crowding factor
9	Simha (1952) Empirical	$\eta_{r,o} = 1 + (54/4f^3) (\phi^2/(1-\phi/\phi_m)^3)$	$1 < f < 2$ ;empirical
19	Brinkman(1952) Theo.	$\eta_r = (1 - \phi)^{-2.5}$	For higher concentration, very diverse sizes
15	Mori-Ototake(1956)Theo.	$\eta_r = 1 + (dSr/2)/\phi$ , $\phi = 1/\phi - 1/\phi_m$	Robinson Type, $d$ =size, $Sr$ =volume specific surface
20	Maron-Pierce(1956)Semi-theo	$\eta_{r,\infty} = (1 - \phi/\phi_m)^{-2}$	In Newtonian region, $\phi < 0.25$ ,Synthetic latex data, $\phi_m=0.68$
11	Brodnyan(1959)	$\eta_{r,o} = \exp \{ [2.5 + 0.399(p-1)^{1.48}] \phi / (1-k\phi) \}$	Modified Mooney'e eq. for ellipsoids
21	Krieger-Dougherty(1959)	$\eta_r = (1 - \phi/\phi_m)^{-[\eta]\phi_m}$	$[\eta]$ and $p$ are shear-dependent
22	Maude(1960)	$\eta_{r,\infty} = (1 - 1.25\phi)^{-1}$	
23	Landel-Moser-Bauman(1963)	$\eta_{r,\infty} = (1 - \phi/\phi_m)^{-2.5}$	
13	Thomas(1965)Empirical	$\eta_{r,\infty} = 1 + 2.5\phi + 10.05 \phi^2 + A \exp(B\phi)$	$A=0.00273$ , $B=16.6$ ; Reduced curve, $\phi_m=0.625$
14	Frankel-Acrivos(1967) Theo	$\eta_{r,\infty} = 1 + C'\beta$ , $\beta = (\phi/\phi_m)^{1/3} / [1 - (\phi/\phi_m)^{1/3}]$	$C'=9/8$ ;Uniform sized spheres
24	Sengun-Probstein(1988)	$\eta_{r,\infty} = 1 + C f(\beta)$	$C$ is empirical, $\beta$ is the same as in Frankel-Acrivos

\*Theo.=Theoretically derived, Semi-theo.=Semi-theoretical

\*\*  $\eta_{r,o}$  = relative viscosity at low shear limit and  $\eta_{r,\infty}$  = relative viscosity at high shear limit

Table 2.2 Maximum Packing Volume Concentration in Suspensions of  
Uniform Hard Spheres [1,p.489]

Arrangement	$\phi_m \times 10^3$	Comments
Cubical	523.6	Theoretical
Single-staggered(Cubical tetrahedral)	604.5	Theoretical
Double-staggered	698.0	Theoretical
Pyramidal(face-centered cubical)	740.5	Theoretical
Hexagonal close-packed	740.5	Theoretical
Random-loose	601	Experimental limits
Random-dense	637	for steel spheres
Random-loose	596	Experimental limits
Random-dense	641	for nylon spheres
Average random-loose	$589 \pm 14$	Average of published
Average random-dense	$639 \pm 32$	experimental data
Most probable random	620	Experimental average

Table 2.3 Effects of Processing Parameters on Rheocast Structure and Viscosity

Processing Variables (increasing)	Primary Solid Particle			Segregation		Eutectic Phase			Viscosity
	size	sphericity	Sv	macro	micro	size	amount	uniform distribution	
Shear rate	↓	↑	↓	↓	—	↓	—	↑	↓
Isothermal shearing time	↓	↑	↓	↓	↓	—	↓	↑	decrease to steady state
Volume fraction solid	↓	↑	↓	↓	↓	—	↓	—	↑
Cooling rate	↓	↓	↑	↑	↑	↓	—	↑	↑
Rest time after shearing	↑	↓	↑	N.A.	N.A.	N.A.	N.A.	N.A.	↑

Note: ↑ = increasing, ↓ = decreasing, — = no change, N.A. = No Available report

\* The sphericity can be defined as  $F = 4 \pi A / p^2$ , where A = the area of a particle and p = its perimeter.

\*\* Sv = (Area of Liquid-Solid Interface)/(Volume of particle)

**Table 3.1      Chemical Composition of Aluminum-Silicon Alloys (wt.%)**

Ingot #	Al	Si	Other Elements	Charge Metals
1	93.5	6.38	0.12	#5 + 99.9Al
2	93.5	6.51	Fe<0.001	99.9Al + 99.9Si
3	-	7.0	-	#1 + 99.9Si
4	-	12.7	-	#5 + 99.9Al
5	-	48.1	-	Al-Si master alloy

Table 3.2 Chemical analysis of high purity silicon carbide particulates \*.

Element	wt%
Free Si	0.51
SiO <sub>2</sub>	0.43
Total C	28.61
Free C	0.24
SiC	94.70
Fe	0.07
B	0.02
Al	0.015
Mg	0.01
Ca	0.007

\* Provided by the Norton Company, Worcester, M.A., U.S.A.

Table 4.1 Effect of cooling rate, initial shear rate and volume fraction solid on the apparent viscosity of continuously cooled Al-6.5wt%Si alloy slurries ( viscosity unit in Pa.s )

Volume Fraction Solid (Primary Solid), $\xi_s(\alpha)$	Cooling Rate: $\epsilon = 0.0083$ K/s			$\epsilon = 0.075$ K/s		
	Initial Shear Rate:			Initial Shear Rate:		
	180	540	900	180	540	900
0.06	0.031	0.029	0.023	0.029	0.029	0.024
0.10	0.037	0.033	0.024	0.038	0.033	0.026
0.16	0.054	0.038	0.026	0.068	0.045	0.035
0.20	0.065	0.042	0.028	0.130	0.068	0.044
0.26	0.102	0.054	0.033	0.298	0.148	0.072
0.30	0.129	0.069	0.038	0.522	0.236	0.099
0.35	0.163	0.086	0.047	1.036	0.386	0.144
0.40	0.245	0.119	0.065	3.00	0.72	0.24
0.45	0.449	0.176	0.082	5.92	1.04	0.39
0.50	0.979	0.266	0.124	-	-	0.60

Table 4.2 Effect of shear rate and volume fraction solid on the apparent viscosity at "steady state" of isothermally held Al-6.5%Si alloy slurries. (viscosity unit in Pa·s)

Volume Fraction Solid (Primary Solid)	Initial Shear Rate, $\dot{\gamma}_o, \text{s}^{-1}$		
	180	540	900
0.01	0.024	0.022	0.021
0.03	0.029	-	-
0.08	0.031	-	-
0.10	0.035	0.024	0.023
0.14	0.043	0.025	-
0.18	-	0.038	0.026
0.20	0.056	0.039	0.034
0.26	0.117	-	-
0.30	0.150	0.060	0.038
0.33	-	0.082	-
0.39	-	-	0.053
0.40	0.273	0.097	0.061
0.43	-	0.136	0.097
0.50	0.718	-	-



Table 5.1. Apparent Viscosity and Shear Stress at Steady State for Molten Composite Slurry  
and Molten Matrix at 700 °C.

Shear Rate, s <sup>-1</sup>	Apparent Viscosity, Pa·s				Shear Stress, Pa			
	180	540	900		180	540	900	
0 vol%SiC	0.020±0.010	0.020±0.05	0.020±0.03		3.6	10.8	18.0	
10 vol%SiC	0.055±0.010	0.031±0.003	0.027±0.002		10.8	20.52	28.8	
20 vol%SiC	0.109±0.020	0.058±0.005	0.040±0.002		19.6	31.3	36.4	
30 vol%SiC	0.331±0.064	0.158±0.037	0.122±0.010		59.6	85.3	109.8	

Table 5.2 The measured values of  $n$  and high shear limit viscosity of SiC/Al-6.5wt%Si composites at 700 °C

vol%SiC	$\dot{\gamma}_0 = 180 \text{ s}^{-1}$		$\dot{\gamma}_0 = 900 \text{ s}^{-1}$	
	$n'$	$\eta_{\infty}$	$n'$	$\eta_{\infty}$
10	-0.153	0.045	-	-
20	-0.680	0.060	-0.850	0.035
30	-	-	-0.670	0.107

Table 6.1 The comparison of the apparent viscosities for a metallic slurry and a composite slurry with the same total solid fraction(at steady state, isothermally sheared for two hours).

Samples with total $g_s = 0.4$	Apparent viscosity, Pa·s, at initial shear rate of		
	$180 \text{ s}^{-1}$	$540 \text{ s}^{-1}$	$900 \text{ s}^{-1}$
<u>Primary Solid (<math>\alpha</math>)</u> $g_{s(\alpha)} = 0.4$	0.273	0.097	0.061
<u>20vol%SiC+Primary Solid</u> $g_{s(\alpha)} = 0.2$ , and $g_{s(\text{SiC})} = 0.2$	0.172	0.073	0.057

Table A1. Dimensions of Rotors and Constants for Rheological Equations

Rotor	R <sub>1</sub> , cm	R <sub>2</sub> , cm	β	L, cm	B	C	C'	D
X-9	1.8	2.0	0.9	9.0	12.34	1.102	0.992	12.44
X-5				5.0	22.20			22.44
Y-9	1.6	2.0	0.8	9.0	15.61	0.582	0.466	33.50
Y-5				5.0	28.10			60.38

### Rheological Equations

1. Shear Stress [Pa] :

$$\tau = \left[ \frac{2.26 \times 10^{-3}}{2\pi R_1^2 L} \right] (\% \text{Torque}) = B (\% \text{Torque})$$

2. Shear Rate [s<sup>-1</sup>] :

$$\dot{\gamma}_{R_1} = \left[ \frac{4\pi}{60(1-\beta^2)} \right] n = C n \quad \text{at } R = R_1$$

Average Shear Rate [s<sup>-1</sup>]

$$\dot{\gamma}_{\text{average}} = \beta \dot{\gamma}_{R_1} = (\beta C) n = C' n$$

3. Apparent Viscosity [Pa·s] :

$$\eta_a = \frac{\tau}{\dot{\gamma}_{\text{average}}} = \left[ \frac{B}{C'} \right] \frac{(\% \text{Torque})}{n} = D \frac{(\% \text{Torque})}{n}$$

Table A2. Stability Criteria for the Flow in Concentric Cylinder Viscometer (Searle-type viscometer)

Material	$v, \text{cm}^2/\text{s}$	$T_a$	Rotor	$[E]$	Critical Parameters		
					Re	n	$\dot{\gamma}$
Matrix	0.01	41.3	X	1.26	124	33	36
			Y	3.35	83	12	7
		400	X	1.26	1200	318	351
			Y	3.35	800	120	70
Composite	0.10	41.3	X	0.126	124	330	361
			Y	0.335	83	123	72
		400	X	0.126	1200	3180	3500
			Y	0.335	800	1200	700

· Rotor X: 3.8 cm dia. 9.0 cm long      · Rotor Y: 3.6 cm dia. 9.0 cm long

### Criteria for Flow Stability

1. Reynolds Number : 
$$Re = \frac{R_1 \Omega d}{v} = \frac{2 \pi n R_1 d}{60}$$

2. Taylor Number : 
$$Ta = Re \sqrt{\frac{d}{R_1}} = \left[ \frac{2 \pi R_1^{1/2} d^{3/2}}{60 v} \right] n = [E] n$$

$Ta < 41.3$  : Laminar Couette Flow  
 $Ta < 400$  : Laminar Flow with Taylor Vortices

# BIBLIOGRAPHY

1. L.A. Utracki, *Rheological Measurement*, A.A. Collyer and D.W. Clegg, ed., Elsevier, London (1988) 479
2. J. Mewis, *Proc. 8th International Congress on Rheology*, v.1 (1980) 149
3. D.J. Jeffrey and A. Acrivos, *AIChE*, 22 (1976) 417
4. G.K. Batchelor, *Ann. Rev. of Fluid Mechanics*, 6 (1974) 227
5. H. Brenner, *Progress in Heat and Mass Transfer*, v.5, W.R. Schowalter et al., ed., Pergamon Press, Oxford (1972) 89
6. M. Reiner, *Advanced Rheology*, H.K. Lewis London (1971)
7. J.C. Van der Werff and C.G. De Kruif, *J. Rheol.*, 33 (1989) 421
8. A. Einstein, *Ann. Phys.*, 19 (1906) 289; 34 (1911) 591
9. R. Simha, *J. Appl. Phys.*, 23 (1952) 1020
10. M. Mooney, *J. Colloid Sci.*, 6 (1951) 162
11. J.G. Brodnyan, *Trans. Soc. Rheol.*, 3 (1959) 61
12. R. Rutgers, *Rheol. Acta*, 2 (1962) 202, 305
13. D.G. Thomas, *J. Colloid Sci.*, 20 (1965) 267
14. N.A. Frankel and A. Acrivos, *Chem. Eng. Sci.*, 22 (1967) 847
15. Y. Mori and N. Ototake, *Kagaku Kogaku*(Chemical Eng., Japan), 20 (1956) 488
16. V. Vand, *J. Phys. Colloid Chem.*, 52 (1949) 277
17. J. Robinson, *J. Phys. Colloid Chem.*, 53 (1949) 1042
18. R. Roscoe, *Brit. J. Appl. Phys.*, 3 (1952) 267
19. H. Brinkman, *J. Chem. Phys.*, 20 (1952) 571
20. S.H. Maron, and P.E. Pierce, *J. Colloid Sci.*, 11 (1956) 80

21. I.M. Krieger and T.J. Dougherty, *Trans. Soc. Rheol.*, 3 (1959) 137
22. A.D. Maude, *J. Fluid Mech.*, 7 (1960) 230
23. R.F. Landel, B.G. Moser and A. Bauman, *Proc. IV Int'l Congress on Rheology*, USA (1963) 663
24. M.Z. Sengun and R.F. Probstein, *PCH PhysicoChemical Hydrodynamics*, 11 (1988) 229
25. H. Eilers, *Kolloid Z.*, 97 (1941) 313
26. S.G. Ward, *Brit. J. Appl. Phys.*, 1, Nov. (1950) 286 (part I), 325 (Part II)
27. R.K. McGeary, *J. Amer. Ceram. Soc.*, 44 (1961) 513
28. C. Parkinson, S. Matsumoto and P. Sherman, *J. Colloid Interface Sci.*, 33 (1970) 150
29. R.J. Farris, *Trans. Soc. Rheol.*, 12 (1968) 281
30. T.G.M. van de Ven, *Polym. Comp.*, 6 (1985) 209
31. R. Simha, *J. Colloid Sci.*, 5 (1950) 386
32. R. Simha, *J. Phys. Chem.*, 44 (1960) 25
33. H.L. Goldsmith, S.G. Mason, *Rheology-Theory and Applications*, F.R. Eirich ed., Academic Press, New York, v.4 (1967)
34. S. Harber and H. Brenner, *J. Colloid Interface Sci.*, 97 (1984) 496
35. R.O. Maschmeyer and C.T. Hill, *Trans. Soc. Rheol.*, 21 (1977) 183, 195
36. H. Brenner, *J. Fluid Mech.*, 4 (1970) 641
37. I.M. Krieger, *Adv. Colloid Interface Sci.*, 3 (1972) 111
38. H.A. Barnes, *J. Rheol.*, 33 (1989) 329
39. M.M. Cross, *J. Colloid Sci.*, 20 (1965) 417; 33 (1970) 30; 44 (1973) 175
40. R.V. Williamson, *J. Rheol.*, 1 (1930) 283
41. D. Quemada, P. Flaud and P.H. Jezequel, *Chem. Eng. Comm.*, 32 (1985) 61
42. T. Matsumoto, A. Takashima, T. Matsuda and S. Onogi, *Trans. Soc. Rheol.*, 14 (1970) 617

43. L.A. Utracki, B.D. Favis and B. Fisa, *Polym. Compos.*, 5 (1984) 277
44. T.B. Lewis and L.E. Nielsen, *Trans. Soc. Rheol.*, 12 (1968) 421
45. S.G. Ward, *Brit. J. Appl. Phys.*, 10 (1959) 317
46. B. Clarke, *Trans. Instr. Chem. Engrs.*, 45 (1967) 251
47. D. Eagland, The Colloid State, *Contemp. Phys.*, 14 (1973) 119
48. E.J.W. Verwey and J.Th.G. Overbeek, *The theory of the stability of lyophobic sols*, Elsevier, Amsterdam, (1948)
49. W. Haller, *Kolloid Z.*, 56 (1931) 257
50. R.J. Morgan, *Trans. Soc. Rheol.*, 12 (1968) 511
51. W.H. Bauer and E.A. Collins, *Rheology-Theory and Applications*, F.R. Eirich ed., Academic Press, New York, v.4 (1967) 423
52. J. Mewis, *J. Non-N. Fluid Mech.*, 6 (1979) 1
53. V.V. Chavan, A.K. Deysarkar and J. Ulbrecht, *The Chemical Engineering J.*, 10 (1975) 205
54. A. Slibar and P.R. Paslay, *Proc. Int. Sym. on Second-Order Effects in Elasticity Plasticity and Fluid Dynamics*, M. Reiner and D. Abir (eds.), Pergamon Press, Oxford (1964) 314
55. D. C.-H. Cheng and F. Evans, *Brit. J. Appl. Phys.*, 16 (1965) 1599
56. D. C.-H. Cheng, *Rheol. Acta*, 12 (1973) 228
57. D. C.-H. Cheng, *Nature*, 245 (1973) 93
58. M. Mooney, *J. Colloid Sci.*, 1 (1946) 195
59. C.E. Chaffey, *J. Colloid Interface Sci.*, 56 (1976) 495
60. A.F. Gabysh, T. Ree, H. Eyring and I. Cutler, *Trans. Soc. Rheol.*, 5 (1961) 67
61. M. Comina and C.G. Roffey, *Rheol. Acta*, 10 (1971) 606
62. T. Alfrey Jr., *Mechanical Behavior of High Polymers*, Interscience Publishers (1948) 45
63. H. Green and R.N. Weltmann, *Ind. & Eng. Chem. An. Ed.*, 15 (1943) 201



64. H.A. Mercer and H.D. Weymann, *Trans. Soc. Rheol.*, 18 (1974) 199
65. D.J. Doherty and R. Hurd, *J. Oil Colour Chem. Assoc.*, 41(1958) 42
66. N.F. Astbury and F. Moore, *Rheol. Acta*, 9 (1970) 124
67. L.G. Jones and R.S. Brodkey, *Proc. 5th International Congress on Rheology*, v.2, S. Onogi, ed., Univ. of Tokyo press (1970) 267
68. K.K. Triliskii, Yu. L. Ishchuk and A. Ya. Malkin, *Colloid J. USSR*, 50 (1988) 464
69. W.-Y. Chiu and T.-M. Don, *J. Appl. Polym. Sci.*, 37 (1989) 2973
70. D.B. Spencer, R. Mehrabian and M.C. Flemings, *Met. Trans.*, 3 (1972) 1925
71. M.C. Flemings, R.G. Riek and K.P. Young, *Rheocasting, Mat. Sci. Eng.*, 25 (1976) 103
72. P.A. Joly and R. Mehrabian, *J. Mat. Sci.*, 11 (1976) 1393
73. M.P. Kenney et al., *Casting*, Metals Handbook, v.15, ASM International (1988) 327
74. A. Namba and K. Ichikawa, *Heat Treatment (Japan)*, 28 (1988) 254
75. K. Ichikawa, *Tetus-to-Hagane (Japan Iron and Steel)*, 74 (1988) 51
76. K. Chijiiwa and S. Fukuoka, *J. Faculty Eng., U. Tokyo (B)*, 23, no.2 (1975) 149
77. E. Kayama, K. Murai, M. Sato and S. Kiuchi, *Imono (Japanese J. Casting)*, 47 (1975) 485
78. J.M. Oblak and W.H. Rand, *Met Trans. B*, 7B (1976) 699
79. A. Vogel, R.D. Doherty and B. Cantor, *Proc. Conf. on Solidification and Casting of Metals*, Sheffield, July 1977, Metals Soc., London (1979) 518
80. R. Ichikawa and K. Miwa, *J. Japan Inst. Metals*, 42 (1978) 1023
81. S.D.E. Ramati, G.J. Abbäschián and R. Mehrabian, *Met. Trans. B*, 9B (1978) 241
82. M. Kiuchi, S. Sugiyama and K. Arai, *J. Japan Soc. Tech. Plasticity*, 20 (1979) 762

83. V. Laxmanan and M.C. Flemings, *Met. Trans. A*, 11A (1980) 1927
84. A. Shibutani, K. Arihara and Y. Nakamura, *Tetsu-to-Hagane* (Japan Iron and Steel), 66 (1980) 1550
85. B.C. Pai, and H. Jones, *Proc. Conf. on Solidification Technology in the Foundry and Cast-House*, Univ. of Warwick, Coventry, U.K., Sept. (1980) 126
86. A. Assar, N. El-Mahallawy and M.A. Taha, *Aluminium*, 57 (1981) 807
87. R. Ichikawa and K. Miwa, *J. Japan Inst. Metals*, 45 (1981) 189
88. T. Matsumiya and M.C. Flemings, *Met. Trans. B*, 12B (1981) 17
89. K. Miwa and R. Ichikawa, *J. Japan Inst. Metals*, 45 (1981) 853
90. N. Apaydin, *J. Mat. Sci., Lett.*, 1 (1982) 39
91. A. Assar, N. El-Mahallawy and M.A. Taha, *Metals Tech.*, 9 (1982) 165
92. P.R. Prasad, S. Ray, J.L. Gaindhar and M.L. Kapoor, *Z. Metall.*, 73 (1982) 714
93. M. Suery and M.C. Flemings, *Met. Trans. A.*, 13A (1982) 1809
94. R.D. Doherty, H.-I. Lee and E.A. Feest, *Mat. Sci. Eng.*, 65 (1984) 181
95. K. Ichikawa, Y. Kinoshita and S. Shimamura, *J. Japan Inst. Metals*, 48 (1984) 626
96. N. Mori, K. Ogi and K. Matsuda, *J. Jap. Inst. Metals*, 48 (1984) 936
97. H. Lehuy, J. Masounave and J. Blain, *J. Mat. Sci.*, 20 (1985) 105
98. K. Ichikawa and S. Ishizuka, *J. Japan Inst. Metals*, 49 (1985) 1093
99. K. Miwa, G. Yoshinari and T. Ohashi, *J. Japan Inst. Metals*, 49 (1985) 483
100. K. Miwa, T. Kakamu and T. Ohashi, *Trans. Japan Inst. Metals*, 26 (1985) 549
101. K. Miwa, T. Ohashi and R. Ichikawa, *J. Japan Inst. Metals*, 49 (1985) 546
102. K. Miwa, T. Ohashi and T. Fukusako, *J. Japan Inst. Metals*, 49 (1985) 1002

103. J.M.M. Molenaar, L. Katgerman, W.H. Kool and R.J. Smeulders, *J. Mat. Sci.*, 21 (1986) 389
104. K. Ichikawa and S. Ishizuka, *J. Jap. Inst. Metals*, 50 (1986) 416
105. K. Ichikawa, S. Ishizuka and Y. Kinoshita, *Trans. Japan Inst. Metals*, 28 (1987) 135
106. K. Ichikawa and S. Ishizuka, *Trans. Japan Inst. Metals*, 28 (1987) 434
107. K. Miwa and T. Ohashi, *Solidification Processing*, Sheffield Univ. (1987) 401
108. M.A. Taha, N.A. El-Mahallawy, A.M. Assar and P.R. Sahm, *Solidification Processing*, Sheffield Univ. (1987) 431
109. K. Ichikawa, S. Ishizuka and Y. Kinoshita, *Trans. Japan Inst. Metals*, 29 (1988) 598
110. N. Fat-Halla, P. Secordel and M. Suery, *J. Mat. Sci.*, 23 (1988) 2419
111. K. Ichikawa and S. Ishizuka, *J. Japan Inst. Metals*, 52 (1988) 588
112. K. Ichikawa, S. Ishizuka and Y. Kinoshita, *Trans. Japan Inst. Metals*, 29 (1988) 598
113. M.A. Taha, N.A. El-Mahallawy and A.M. Assar, *J. Mat. Sci.*, 23 (1988) 1379; *Ibid.*, 1385
114. S.B. Brown, presented at 1989 ASM/TMS Conf., Indianapolis, Indiana.
115. P.R. Prasad, S. Ray, J.L. Gaindhar and M.L. Kapoor, *Z. Metall.*, 80 (1989) 425
116. M. Hirai et al., Conference Extended Abstract on "Semi-Solid Processing of Alloys and Composites", April (1990), Ecole Nationale Supérieure des Mines de Paris
117. S.A. Metz and M.C. Flemings, *Trans. AFS*, 77 (1969) 329
118. M.C. Flemings and K.P. Young, paper no. G-T77-092, Ninth SDCE Inter. Die Casting Expo. Congr., 1977
119. J. Campbell, *Foundry Trade J.*, 138 (1975) 291
120. C.Y. Chen, J.A. Sekhar, D.G. Backman and R. Mehrabian, *Mat. Sci. Eng.*, 40 (1979) 265

121. C.C. Law, J.D. Holstetler and L.F. Schulmeister, *Mat. Sci. Eng.*, 38 (1979) 123
122. K.P. Young, R.G. Riek and M.C. Flemings, *Met. Tech.*, 6 (1979) 130
123. P.S. Frederick, N.L. Bradley and S.C. Erickson, *Adv. Mat. Processes*, (1988) 53
124. R. Mehrabian, R.G. Riek and M.C. Flemings, *Metall. Trans.*, 5 (1974) 1899
125. R. Mehrabian, A. Sato and M.C. Flemings, *The Light Metals*, II (1975) 175
126. A. Sato and R. Mehrabian, *Metall. Trans. B*, 7B (1976) 443
127. C.G. Levi, G.J. Abbaschian and R. Mehrabian, *Metall. Trans. A*, 9A (1978) 697
128. A. Munitz, M. Metzger and R. Mehrabian, *Metall. Trans. A*, 10A (1979) 1491
129. W.K. Choo, K.H. Han and Y.M. Koo, *J. Korean Inst. Metals*, 18 (1980) 11
130. F.M. Hosking, F.F. Portillo, R. Wunderlin and R. Mehrabian, *J. Mater. Sci.*, 17 (1982) 477
131. P.R. Gibson, A.J. Clegg and A.A. Das, *Foundry Trade J.*, 152 (1982) 253
132. K.J. Bhansali and R. Mehrabian, *J. Metals*, Sept. (1982) 30
133. F. Girot, Doctoral Thesis, L'Université De Bordeaux I (1987)
134. F. Girot, L. Albingre, J.M. Quensset and R. Naslain, *J. Metals*, Nov. (1987) 18
135. J.W. McCoy, C. Jones, and F.E. Wawner, *SAMPE Quart.*, Jan. (1988) 37
136. M. Kiuchi and S. Sugiyama, *Metallurgical Processes for the Year 2000 and Beyond*, H.Y. Sohn and E.S. Geskin, eds., TMS (1988) 83
137. A. Watanabe, H. Watanabe, K. Ohmori and Y. Takeuchi, *Keikinzoku* (J. Japan Inst. Light Metals), 38 (1988) 626
138. S. Abis and V. Pellegrini, *J. Less-Common Metals*, 139 (1988) 203

139. K. Yamada, S. Sekiuchi and T. Matsumiya, presented in 34th International SAMPE sym. exhib., Reno, Nevada, May 8-11 (1989)
140. W.R. Loué and W.H. Kool, Extended Abstract, Conference, Inst. Metals, London (1989)
141. M. Mada and F. Ajersch, Abstract, TMS Annual Meeting, Anaheim, CA, USA, Feb. 20, 1990
142. P.L. Antona and R. Moschini, *Metall. Sci. Tech.*, 4, no.2 (1986) 49
143. A.C. Fonseca de Arruda and M. Prates de Campos Filho, *Solidification Technology in the Foundry and Casthouse*, Coventry, England, 15-17 Sept. (1980) 143
144. M.K. Surappa and P.K. Rohatgi, *Met. Trans. B*, 12B (1981) 327
145. M.K. Surappa and P.K. Rohatgi, *J. Mat. Sci.*, 16 (1981) 983
146. A. Banerji, M.K. Surappa and P.K. Rohatgi, *Met. Trans. B*, 14B (1983) 273
147. P.K. Ghosh and S. Ray, *Trans. Jap. Inst. Metals*, 29 (1988) 509
148. W.R.D. Jones and W.L. Bartlett, *J. Inst. Metals*, 81(1952-53) 145
149. L. Battezzati and A.L. Greer, *Acta Metall.*, 37 (1989) 1791
150. R.N. Weltmann and H. Green, *J. Appl. Phys.*, 14 (1943) 569
151. A.S. Michaels and J.C. Bolger, *I.&E.C. Fundamentals*, 1 (3) (August, 1962) 153
152. S. Nagata, *Mixing: Principles and Applications*, John Wiley & Sons, New York (1975) 1
153. D.J. Llyod, *Composites Sci. & Tech.*, 35 (1989) 159
154. L.L. Oden and R.A. McCune, *Met. Trans. A*, 18A (1987) 2005
155. T. Oki, T. Choh and A. Hibino, *J. Jap. Inst. Metals*, 49 (1985) 1131
156. E. Klier, S.M. Thesis, MIT (1988)
157. W.R. Loué, E. Nava Vazquez and W.H. Kool, Intern. Conf. on Semi-Solid Processing of Alloys and Composites, CEMEF, Sophia-Antipolis, France, April 4-6 (1990)

158. M.Mada and F. Ajersch, *Metals & Ceramic Matrix Composites: processing, modeling & mechanical behavior*, Proc. Intern. Conf., Anaheim, California, USA, TMS, Feb. 19-22 (1990) 337
159. D.C.-H. Cheng, *Proc. 8th Intern. Congress on Rheology*, Naples, v.2 (1980) 575
160. H. Schlichting, *Boundary-Layer Theory*, 7th ed., transl. by J. Kestin, McGraw-Hill (1979) 87
161. G.I. Taylor, *Phil. Trans.*, Royal Soc. London A, 223 (1923) 289
162. J.L. Murray and A.J. McAlister, *Bulletin of Alloy Phase Diagrams*, v.5, no.1 (1984)

## BIOGRAPHICAL NOTE

Mr. Hee-Kyung Moon was born in [REDACTED] on [REDACTED]. He was graduated from Kyungbok High School in 1976, and then attended Seoul National University, Seoul, Korea. He graduated from Seoul National University in 1980 with a B.S. in Metallurgy. He was awarded for the top of his class. He continued his graduate study at the graduate school of Seoul National University, graduating in 1982 with a Master of Science in Metallurgy. He served military duty as a cadet, and became a reserved officer. He had worked in the Research Laboratories of Pohang Iron & Steel Co. Ltd., Pohang, Korea, for three years until he entered the graduate school of Massachusetts Institute of Technology to work on a Doctorate in September 1985. He is a joint-student member of ASM International and TMS-AIME. He married Jeong-Hae Lee in July 1987. He now has a son, Michael Han-Gi, born in Boston.